# EXPERIMENTAL CHARACTERIZATION OF ELASTIC STIFFNESS AND DELAMINATION TOUGHNESS IN THERMAL BARRIER COATING SYSTEMS

by
Jalil Alidoost

A dissertation submitted to Johns Hopkins University in conformity with the requirements for the degree of Doctor of Philosophy

Baltimore, Maryland
October 2021

**Abstract**

Reliable high-temperature propulsion materials are crucial to improved engine efficiency, reduced fuel costs and decreased life cycle costs. Multilayered thermal barrier coatings (TBC) are an effective way of extending the temperature capabilities of gas turbine engines, but accurate assessment and life prediction of these disparate material systems requires detailed knowledge of the constitutive behavior of each layer and the adhesion between layers. The focus of this study is to measure the properties relevant to thermal barrier coatings and elucidate how variations in the processing affect the mechanical response.

Working closely with industrial suppliers at General Electric (GE) and Pratt & Whitney (P&W), novel Compression Edge Delamination (CED) tests were used to measure the Mode II interfacial toughness of two TBCs. GE's standard diffusion aluminide bond coat/yttria stabilized zirconia (YSZ) topcoat TBC system was characterized at various stages of gradient thermal cycle life and compared to previous results for furnace cycled specimens with the same TBC. Both sets of samples exhibited comparable interfacial toughness and a decrease in interfacial strength with thermal cycling. The drop in interfacial strength was correlated with TGO and bond coat rumpling and found to be greater in the thermal gradient test, in part because these specimens experienced higher bond coat temperatures.

CED testing was also performed on P&W's low-pressure plasma sprayed NiCoCrAlY bond coat/YSZ topcoat TBC system at various stages of furnace cycle life. The delamination of this TBC resulted in the spallation of the topcoat in one large piece, facilitated by the absence of rumpling. The interfacial toughness of these specimens decreased with thermal cycling and was attributed to thickening of the thermally grown oxide (TGO), which in the absence of rumpling leads to increased stored strain energy that promotes delamination. A parallel investigation with

P&W investigated the influence of off normal processing conditions on the intrinsic microstructure and mechanical properties of YSZ topcoats manufactured via electron-beam physical vapor deposition. Microstructural variations were subtle, but 3-point bend experiments on free-standing topcoats showed a strong tension/compression asymmetry and variations in modulus as a function of processing conditions.

Advisor: Professor Kevin J. Hemker

Readers: Professors Kevin J. Hemker and Jaafar El-Awady and Dr. Elisa Zaleski of Pratt & Whitney

# Acknowledgements

There are a multitude of people I need to thank for helping complete this stage of my life. First and foremost I would like to thank my Ph.D. advisor, Professor Kevin Hemker, for all the help and guidance he has given me over the last five years. The support he has provided me on both a personal and professional level has been immensely invaluable. The lessons I have learned from him over the years have helped me grow as a student, scientist, professional and as a person. I am happy to finish off this chapter of my life working with Professor Hemker with such positive memories, even if Michigan never beat Ohio State in football while I was here.

I would like to express my gratitude to the countless number of people who have helped me along my professional path during this time as well. Special thanks must be given to Professor Jaafar El-Awady and Dr. Elisa Zaleski for taking the time to read my thesis as members of my defense committee. I would also like to acknowledge the support I have been lucky enough to receive from our industrial collaborators at both GE Aviation and Pratt & Whitney. The research insights provided to me by Dr. Ming Fu, Dr. Doug Konitzer and Jeff Williams at GE, along with Dr. Eliza Zaleski, Dr. Rob Hutchinson and Brian Hazel at Pratt & Whitney have been invaluable. I would also like to thank Dr. Kevin Schlichting for giving me the opportunity to intern in the Coatings & Light Alloys Development Group at Pratt &Whitney, as well as Dr. Kaylan Wessels for being an incredible mentor during my internship.

My most sincere thanks goes to my family, who have supported for my entire life before graduate school and I know will continue to do so afterwards. My parents, Susan Thomas and Yadollah Alidoost, along with my brother Kazem, sisters Marjan & Leila, and sister-in-law Maggie were my biggest fans throughout this entire process. They have been there for me

whenever I have needed to talk, needed a laugh, or wanted a nice home-cooked meal. I love you all so much and could not have done any of this without you.

My time at Johns Hopkins would not have been anything close to what it was if it was not for the amazing lab-mates I have had these last five years. The collaborative efforts of our group have been essential to the work I have done, but more importantly you all have shaped my time in Baltimore and helped make it so much fun. The list of people I need to thank includes Mo-Rigen He, Gi-Dong Sim, Kelvin Xie, Ankur Chauhan, Paul Rottmann, Brady Butler, David Eastman, Gianna Valentino, Luoning Ma, Betsy Congdon, David Mills, Matt Vaughn, Arunima Banerjee, Ojaswi Agarwal, Sam Present, Kate Brizzolara, Catherine Barrie, Sharon Park, Mike Patullo, Daniel Magnuson, Avi Gordon and Xander LeFevre. I would also like to give a special thanks to former group members Simon Lockyer-Bratton and Binwei Zhang for their support.

Finally, I would like to thank all my friends from Baltimore, Ann Arbor, Montclair and beyond. There are too many of you to list in this dissertation, but I could not have done this without all your support, encouragement, and many Zoom calls during the COVID-19 pandemic. I cannot wait to celebrate with all of you in person.

## Table of Contents

# List of Tables

# List of Figures

## Chapter 1: Introduction and Background

Layered coating systems are a key component in aerospace systems and are notably prevalent in modern-day gas turbine engines. One example of this are multilayer systems knows as Thermal Barrier Coating (TBC) systems. Over the past several decades industrial and academic research has contributed to the continued development of these systems, resulting in ever more durable coatings that can survive at high temperatures and stresses in aggressive environments. While these developments have contributed to the improved performance of gas turbine engines, there are still a variety of TBC-related challenges that require attention. The purpose of this chapter is to provide a summary of previous research into TBC systems and to highlight the issues that have motivated the work in this study. General background is given about TBC systems, including a summary of previously established TBC testing methods. Information about the manufacturing methods of TBCs as well as the specification process used to qualify TBCs is reviewed. Finally, an overview will be given on each of the chapters in this thesis.

1.1 Motivation and Focus

The growth of the aerospace industry over the last sixty years has had a profound impact on contemporary life. The proliferation of air travel is perhaps the most evident example of this, and this growth in commercial air travel is expected to continue into the coming decades. According to a study by the International Air Transport Association (IATA) around 4 billion passengers flew in 2018, with that number projected to almost double by 2036 [1]. The current world population is roughly 8 billion people, but it has been estimated that only 2% to 4% of the global population flew in 2018 [2]. Proliferation of air travel has yet to occur globally, especially in newly industrialized economies and populous countries like China, Brazil, India and more. Figure 1-1 below shows the International Civil Aviation Organization's (ICAO) projected global growth in

air travel over the next twenty years shown in revenue passenger kilometers (RPK), which is the number of passengers traveled multiplied by their distanced travelled.
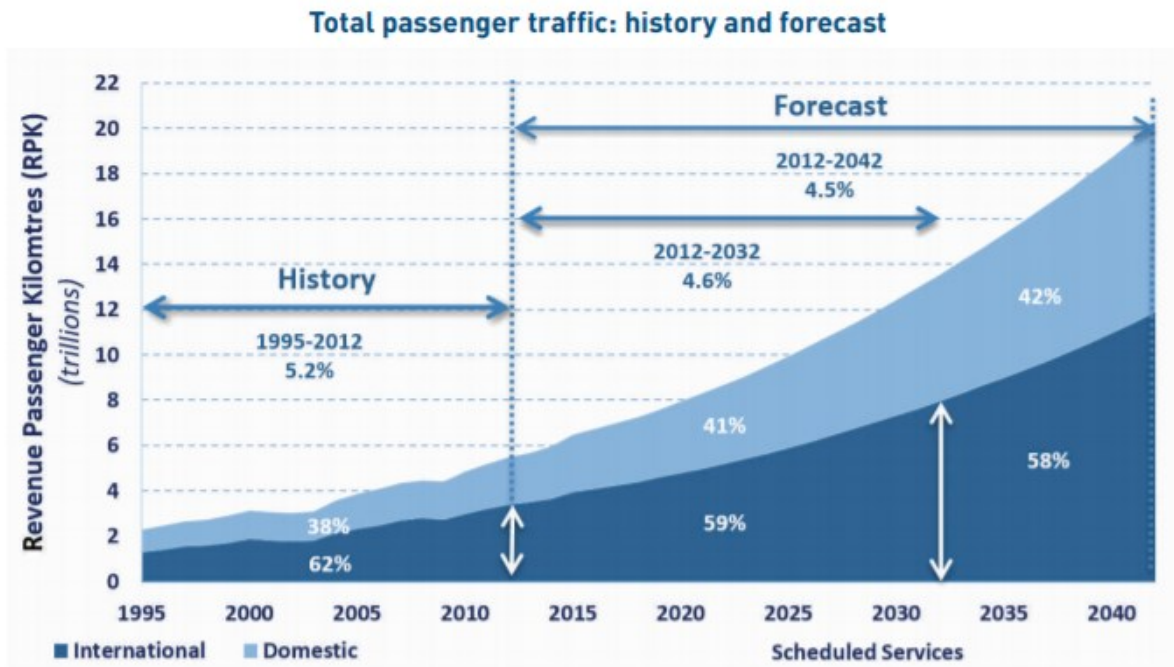


*Figure 1-1: ICAO figure showing the projected growth in air travel over the next 20 years, with the percentage of revenue coming from domestic air travel in light blue and the percentage of revenue coming from international air travel in dark blue [3].*

It is evident that there is still a large market for growth in the commercial air travel industry especially if the barrier to entry, namely cost of air travel, can be reduced. One of the primary ways this can be done is by improving the efficiency of the jet engines. Increased engine efficiency would both decrease the amount of jet fuel used per flight and increase the number of passengers able to fly on a given aircraft. Both factors correspond to an increase in revenue for the airlines, making high efficiency a desirable quality when purchasing jet engines. Thus, increasing engine efficiency directly corresponds to a competitive business advantage for the jet engine manufacturers. Furthermore, as commercial air travel continues to grow globally so will greenhouse gas emissions from jet engines. By increasing engine efficiency, jet engine manufacturers can reduce the amount of $CO_2$ and other combustion products released into the

atmosphere. Thus, increasing engine efficiency serves the dual purpose of combating climate change by using less jet fuel, while also reducing the cost of air travel.

Modern commercial passenger aircrafts are powered by gas turbine jet engines, in which air is drawn inward, mixed with fuel, and burned to drive the turbine and propel the aircraft forward. There are four main types of jet engines: turbojets, turboprops, turboshafts and turbofans [4]. Most modern-day commercial jetliners are equipped with turbofan engines, a schematic of which is shown in Figure 1-2, due to their ability to generate more thrust and operate more efficiently than the alternatives.
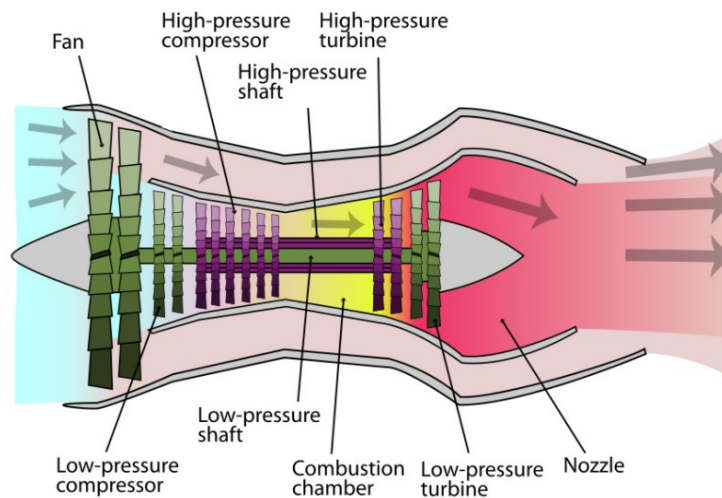


*Figure 1-2: Schematic of a turbofan engine [5].*

The thermodynamic efficiency of these engines is governed by the Brayton cycle. The efficiency of this cycle is shown below in Equation 1-1, defined in terms of temperature:

*Equation 1-1*

$$\eta_{Brayton} = 1 - \frac{T_1}{T_4}$$

Where $\eta$ is the efficiency of the cycle, $T_1$ is the inlet temperature, and $T_4$ is the operating temperature in the high-pressure turbine (HPT) region of the engine. Since the inlet temperature is governed by ambient conditions, the engine efficiency increases as its operating temperature

increases. The desire for high performance engines is not only significant in commercial applications but in military aircrafts as well, notably in hypersonics where immense engine power is necessary to generate sufficiently high speeds. Increasing engine efficiency also allows for the same amount of fuel to generate a greater amount of power. Thus, research focused on increasing engine operating temperatures is important in commercial and military applications.

1.2 Thermal Barrier Coating (TBC) Systems

The demand for structural materials with elevated temperature capabilities is critical for the further development of high-performance power generation and propulsion systems. The alloy design space for monolithic materials has not been fully explored, but prospects for significant advances appear most promising for hybrid material assemblies that capitalize on the combined properties of different material classes. This can be seen when looking at the different materials that are currently being used in various parts of a turbofan jet engine, an example of which is shown below in Figure 1-3 for a Rolls-Royce Trent turbofan engine.
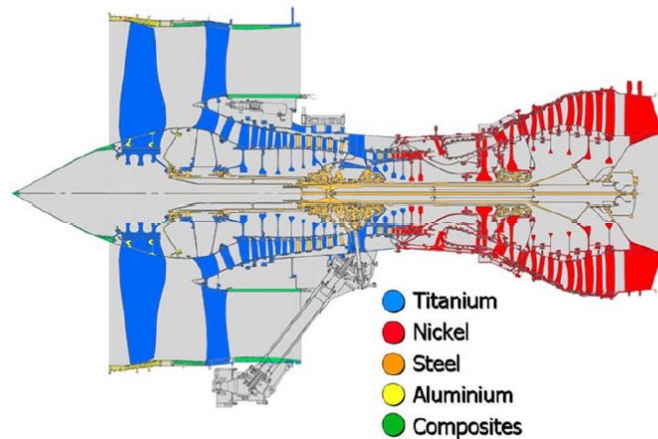


*Figure 1-3: Color-coded schematic of a Rolls-Royce Trent turbofan engine detailingF materials are used in different portions of the engine [6].*

Notable is the significant amount of nickel used in the back portion of the engine. This is the HPT region of the engine, which is exposed to the highest temperatures and as a result is built

primarily with Ni-based superalloys due to their high-temperature strength and creep resistance. Increasing the allowable temperature in the HPT would directly increase the efficiency of these engines, so research in this area is highly desirable. Figure 1-4 details how thermal protection systems in jet engines have improved in recent years.
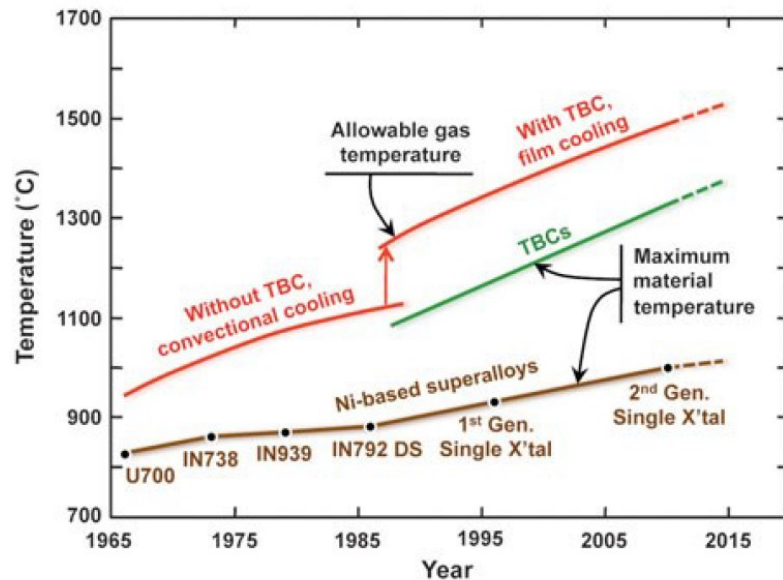


*Figure 1-4: Improvements in thermal protection systems over recent decades. The brown line shows improvements in Ni-based superalloys, the green line shows the impact Thermal Barrier Coatings had on thermal protection, and the red line highlights the effect of metal side cooling [7].*

To further increase the service temperature, beginning as early as the 1960's overlay coatings were applied to jet engine components to provide high temperature corrosion protection [8]. Overlay coatings can be deposited through plasma spray or physical vapor deposition processes and can consist of a variety of elements to provide either corrosion or oxidation resistance, depending on the application [9]. More recently however, TBCs have been used as an added thermal protection layer. Modern TBCs are a multilayer system consisting of four major layers: a) a Ni-based superalloy substrate, b) an aluminum-rich bond coat that is deposited on top of the substrate, c) a thermally grown oxide (TGO) that provides environmental protection and finally d) a low conductivity ceramic topcoat, which provides thermal protection. Figure 1-5 shows a

schematic of a TBC along with a scanning electron microscope (SEM) micrograph showing all the layers present.
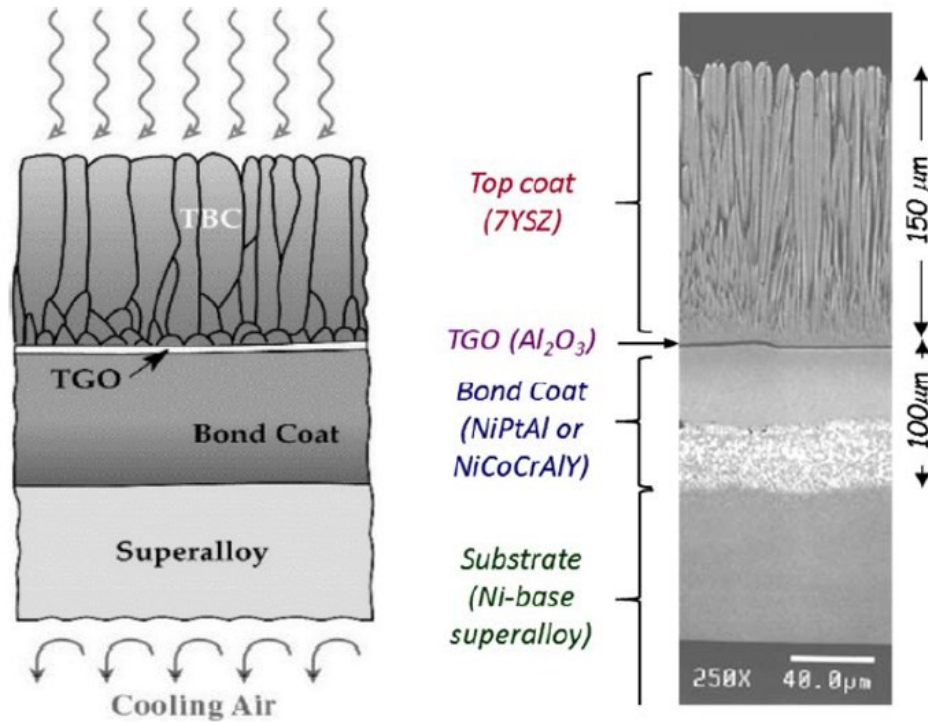


*Figure 1-5: The left shows a schematic of the four layers present in a typical TBC system along with the temperature gradient in air experienced in a jet engine [7]. The right shows an SEM micrograph of the four layers labeled with the materials present in each layer [11].*

Other inventive methods for reducing the temperature seen by the Ni-based superalloys have been developed, such as back side cooling by introducing internal cooling holes within the blades and vanes. Although highly effective, internal cooling limits engine efficiency, and TBC systems have become key to increasing jet engine service temperatures.

In TBC systems the first layer consists of the Ni-based superalloy that is the primary structural component of the blade, vane, shroud or metallic component to be thermally protected. On top of that is an aluminum-rich bond coat (varying in thickness between 50-150 µm) and is typically either: an overlay MCrAlY (M = Ni, Co or both) plasma spray bond coat or a diffusion aluminide bond coat. While bondcoats may vary, all bond coats serve two purposes. One is to act as a bonding

layer between the substrate and the topcoat, and the second is to allow for the growth of the third layer. The third layer, which is the TGO, is an aluminum oxide (preferably α-Al$_2$O$_3$) that is initially less than a micron thick but can grow to the thickness of 5-8 microns over the course of engine service. When the hot oxidizing gasses interact with the aluminum in the bond coat, the TGO is formed. The aluminum oxide is a dense layer that undergoes parabolic growth and provides environmental protection to the underlying substrate, thus mitigating oxidation and corrosion of the substrate. The final layer is the ceramic topcoat, which provides the greatest thermal protection to the system. The topcoat will is often 150-300 μm in thickness and typically consists of zirconia stabilized with 6-8% yttrium, creating a ceramic commonly known as yttria-stabilized zirconia (YSZ). YSZ is chosen as the topcoat material due to its low thermal conductivity, transformation toughening, phase stability through the full range of engine operating temperatures, as well as its high strain tolerance.

While YSZ is the most commonly used topcoat material, other ceramics are being explored either as standalone topcoats or in conjunction with YSZ as part of a multilayer system. One prominent example is gadolinium zirconate (GZ), which is an attractive alternative due to its lower thermal conductivity and increased ability to prevent the infiltration of molten calcium-magnesium-alumino-silicate (CMAS) into the TBC [12]. YSZ and GZ can both be deposited by either air plasma spray (APS) or electron beam physical vapor deposition (EBPVD) methods, but this thesis will focus on YSZ coatings deposited via EBPVD. A further discussion of the manufacturing of these coatings is provided in Section 1.2.1.

Although not addressed in this thesis, it is important to note the relevance of environmental barrier coatings (EBCs) to the TBC work discussed hereafter. While metallic HPT components are currently made from Ni-based superalloys, the transition to ceramic matrix composites (CMC),

most commonly SiC/SiC matrix composites [2], is underway. CMCs are desirable because they are lower density and can operate at higher engine temperatures than their metallic counterparts. The increased service temperature of CMCs mitigates the need for the thermal protection and instead highlights the need for environmental protection from water vapor, sand, dirt and other particulates that can be ingested during flight. EBCs are also multilayer, multi-material systems that operate in the same manner as TBCs, except to offer environmental protection from these foreign substances that might infiltrate the CMC components. The work in this thesis focuses on TBCs deposited through EBPVD methods, but most of the procedures and test methods developed are transferrable to multi-layered EBC systems.

### 1.2.1 TBC Manufacturing Methods

The method in which different TBC layers are manufactured depends on the region of the engine in which the TBC operates, as well as the projected service temperatures and conditions. There are two primary types of deposition methods used to manufacture bond coats: pack cementation for diffusion aluminum bond coats and plasma spray methods for MCrAlY bond coats [9]. Diffusion aluminide bond coats, generally a $\beta$-(Ni,Pt)Al with a B2 crystal structure, are created in a vapor deposition process called pack cementation [13]. Aluminum halide vapor is formed from a mixture of aluminum, alumina and ammonium halide at elevated temperatures. The aluminum halide vapor is very conformal resulting in a thin, even layer of aluminum deposited on the surface of superalloy parts. Rapid interdiffusion and transformation to $\beta$-NiAl forms the bond coat. Platinum can be added to facilitate the diffusion of aluminum into the substrate and to improve the oxidation resistance of the bond coat [14]. The work done with General Electric (GE) was performed on one of their standard commercial TBC coatings that contains a Pt-modified

8

diffusion aluminide bond coat, which is created by forming a β-NiAl bond coat on a superalloy substrate that have been electroplated with a thin layer of Pt [15].

MCrAlY bond coats can be formed using variety of plasma spray methods, but the most common are NiCoCrAlY bond coats formed with low-pressure plasma spray (LPPS). These overlay bond coats do not require interdiffusion with the underlying substrate, therefore a much wider family of alloys can be deposited in thicker layers than their diffusion aluminide counterparts. This allows them to be more tunable and to resist specific failure mechanisms. The work done in this thesis with Pratt & Whitney (P&W) was performed on one of their TBC coatings with an LPPS NiCoCrAlY bond coat.

YSZ topcoats can also be deposited in a variety of ways, but the two most common are APS and the previously mentioned EBPVD method. APS coatings are formed when YSZ particles are melted in a plasma and accelerated at a substrate. When the molten YSZ particles hit the substrate, they result in pancake-shaped deposits and a topcoat with broad, flat grains stacked parallel to the topcoat/bond coat interface [16]. Figure 1-6 a) shows a schematic of what an APS coating looks like. While this process is less expensive than an EBPVD process and applied to large components, the APS coatings tend to be less durable. As a result, APS coatings are generally used in power generation where the parts are bigger and longer iso-thermal temperatures are experienced. The current work focuses exclusively on EBPVD topcoats.
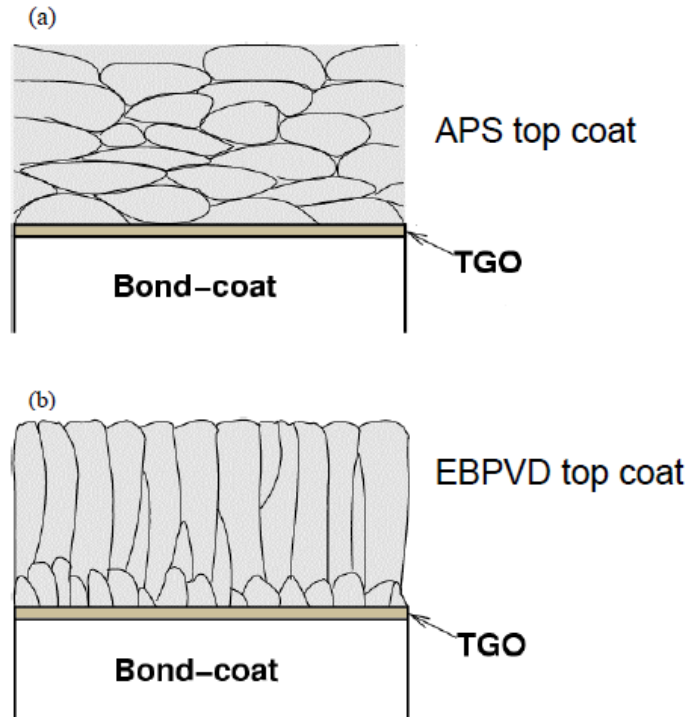
*Figure 1-6: Achematic of a) an APS topcoat and b) an EBPVD topcoat [17].*

EBPVD coatings are formed in a high energy process where an ingot of YSZ is placed in a high vacuum chamber. An electron beam is restored over the ingot to evaporate the YSZ, and the vaporized YSZ deposits onto the substrate material. The resulting coating has long, columnar grains that grow perpendicular to the topcoat/bond coat interface, in direct contrast to the pancake microstructure seen in APS coatings. A schematic of this can be seen in Figure 1-6 b). This columnar coating structure is a highly beneficial feature of EBPVD coatings, as the gaps between columns allow for higher in-plane strain tolerance as compared to the dense APS coatings.

The thermal cycling in jet engines results in large thermal stresses due to the mismatch in thermal expansion between the various layers in a TBC system, so this improved strain tolerance results in more durable coatings with longer service lifetimes. While it is known that EBPVD coatings have better cyclic [13] lifetimes than their APS counterparts, qualifying which

microstructural features of the coatings directly correlate to longer lifetimes is an important area to discuss as well.

*1.2.2 TBC Specification Process*

Although it was originally assumed and taught that topcoats made through the EBPVD deposition process have a wide processing window, highly repeatable microstructures can only be obtained through judicious control of the processing conditions. Variations between vacuum chambers, ambient operating conditions, ingot material, substrate material and more mean that topcoats made through an EBPVD deposition process can vary significantly from one sample to the next. Currently when specifying and qualifying topcoats to be used in service, the primary specification companies look for is sufficient coating thickness and sample-to-sample and run-to-run repeatability. Depending on the location along the blade and the temperature profile that location will experience, the thickness of the deposited topcoat may be varied to ensure sufficient thermal protection, while also allowing for enough strain tolerance to accommodate for the thermal stresses that develop over the course of the coating's lifetime. However, differences in topcoat density, grain size and more can all influence the durability of the coating but are not currently accounted for.

Instead of this thickness-based specification process, the goal for some commercial airline companies is to move to a process that is based on the microstructure and/or the material properties such as modulus and interfacial toughness of the topcoat. Understanding how processing related topcoat features correspond to the material properties of the topcoat is a potential key to developing more durable coatings that can be used to extend TBC life and jet engine efficiency. Current efforts with regards to topcoat variations have focused on microstructural characterization methods,

primarily through SEM imaging. Figure 1-7 below shows examples of changes in EBPVD topcoats, with 1-7 a) showing variations in topcoat grain size and coating thickness as a result of substrate curvature, while 1-7 b) shows a different coating with a much finer, more feathery columnar microstructure.
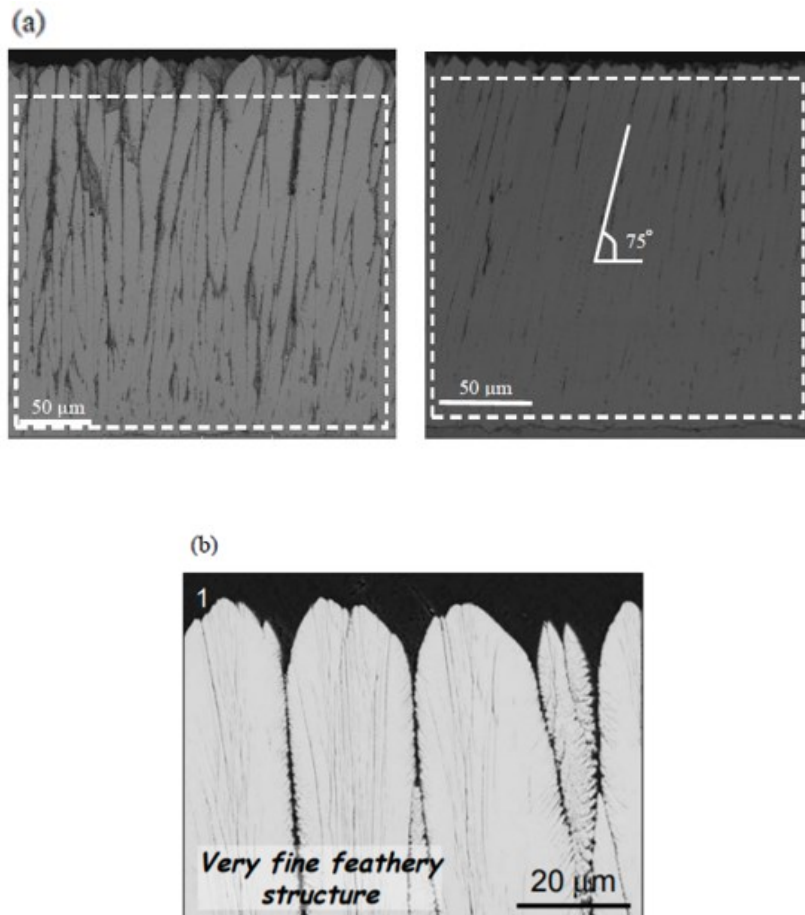


Figure 1-7: Set of EBPVD topcoat SEM images highlighting the variations that can occur in topcoat microstructure. Image a) shows two topcoat structures; on the left is a vertical, porous structure deposited on a convex curved surface and on the right is a tilted, dense structure deposited on concave surface on the same substrate [17]. Image b) shows an EBPVD topcoat that has a fine and feathery microstructure [18].

While microscopic methods can highlight the variations that are present in EBPVD runs, mechanical testing is necessary to understand what effect those variations have on topcoat properties and TBC durability. Section 1.4 below details some relevant TBC testing methods and their limitations. Because of the limitations inherent in many current TBC testing methods, as well

as the high costs of these tests both from a time and money perspective, limited work has been done on fully linking TBC microstructural variations and mechanical performance. The work discussed in Chapter 5 of this thesis focuses on measuring processing-related microstructural variations in P&W's EBPVD topcoats and then linking those variations to differences in their mechanical responses, specifically topcoat modulus.

1.3 Lifetime Assessment of TBCs

Accurately predicting the lifetime of a TBC system in service is incredibly difficult due to the fact that TBCs are disparate multilayer systems that experience complex thermal profiles in service. Successful lifetime assessment models for TBCs would result in more reliable coating systems with fewer occurrences of early part replacement. Current efforts to assess TBC lifetime have fallen under one of two categories, empirical life prediction models or mechanistic life prediction models, which are detailed below.

*1.3.1 Empirical Assessment Methods*

Historically, TBC life prediction has employed empirical life assessment methodologies, where accelerated life testing is performed to assess the failure statistics of the coating. The lifetime of the coating is then estimated as being below some accumulative probability where failure can be expected to occur. In TBC systems, one of the most common empirical life assessment methods is the furnace cycle test (FCT). FCT specimens are inserted into a furnace and heated to a maximum temperature of $T_H$, generally between 1000-1200°C [19], where they are held isothermally for a given time before being extracted from the furnace and air cooled to some minimum temperature $T_C$. This process is then repeated for $n$ cycles until the thermal exposure of

the FCT specimen has reached some desired level, or until spallation of the coating occurs. Figure 1-8 shows an example of a heating and cooling profile for a 1-hour long cycle FCT specimen, where the isothermal exposure is 45 minutes and the cooldown is 15 minutes.
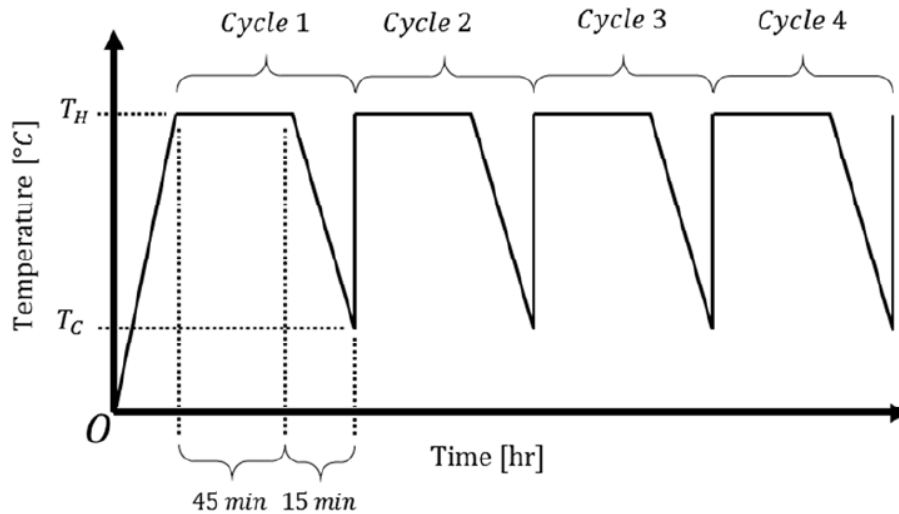


*Figure 1-8: The heating and cooling profile for a 1-hour long cycle FCT specimen, heated to $T_H$ and air cooled to $T_C$ [20].*

The popularity of the FCT stems from the fact that it is a quick and simple test method. FCT specimens can be thermally exposed to the equivalent of hundreds of cycles in a matter of days, as opposed to the months it would take for the same exposure time for coatings in a jet engine [21]. The FCT is run in a laboratory furnace with many buttons in parallel, which makes it relatively simple, easy and cheap to perform. The work described in Chapter 4 was performed on samples of P&W's TBC system that have undergone furnace cycling to various points in their lifetime.

The major drawback of the FCT test is that the entire TBC specimen is exposed to a uniform temperature as opposed to the thermal gradient that coatings experience in service, as shown in Figure 1-5. Alternative empirical life assessments that employ a thermal gradient to heat the coatings have been developed as well. The experimental setup for one common variant, the burner rig test, is shown in Figure 1-9.
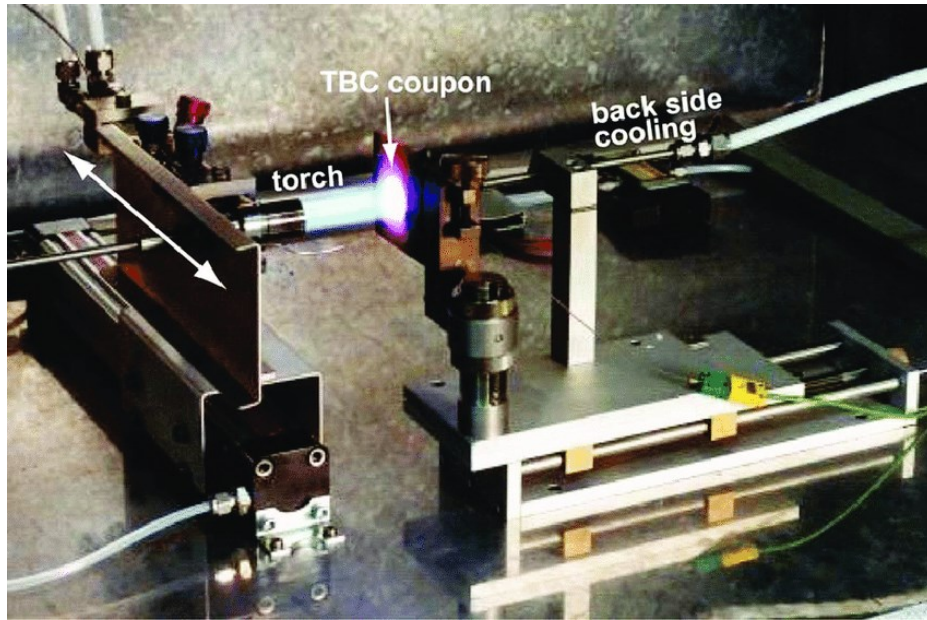
*Figure 1-9: An experimental setup for a burnet rig test, where the front side of a TBC specimen coated with ceramic is exposed to a torch while the back, uncoated side is exposed to air cooling [22].*

These thermal gradient tests normally involve the use of a bar or 1-inch diameter button that is coated on one side and uncoated on the other. The coated side of the specimen is exposed to a torch and has a surface temperature of $T_H$, while the uncoated side is exposed to backside air and has a cooling temperature $T_C$. The differences between the front and back side temperatures result in a temperature gradient through the thickness of the specimen, mimicking the thermal conditions seen during service, and the specimen can be removed and re-inserted into the path of the hot temperature at a set interval of time in order to cycle the specimen in the same manner as the FCT. The work done in Chapter 3 focuses on GE's standard commercial TBC system that has undergone a version of thermal gradient cycling known as Jet Engine Thermal Shock (JETS) cycling. The results for these JETS specimens are then compared to results previously obtained by Lockyer-Bratton on GE's same standard commercial coating that had undergone furnace cycle testing (FCT) [20]. Also discussed in Chapter 3 is work done on sections of jet engine blades provided by GE that had been thermally cycled to various fractions of life in service within jet engines.

*1.3.2 Aspirational Efforts for Mechanics-based Assessment Methods*

Empirical lifetime assessment methods are widely used by engine manufacturers but are largely limited by a key issue: they do not explain the underlying mechanisms and stresses that lead to spallation. A move to mechanistic lifetime assessment models based on coating properties and failure mechanisms would be preferred. Figure 1-10 highlights the difference between these two methods.
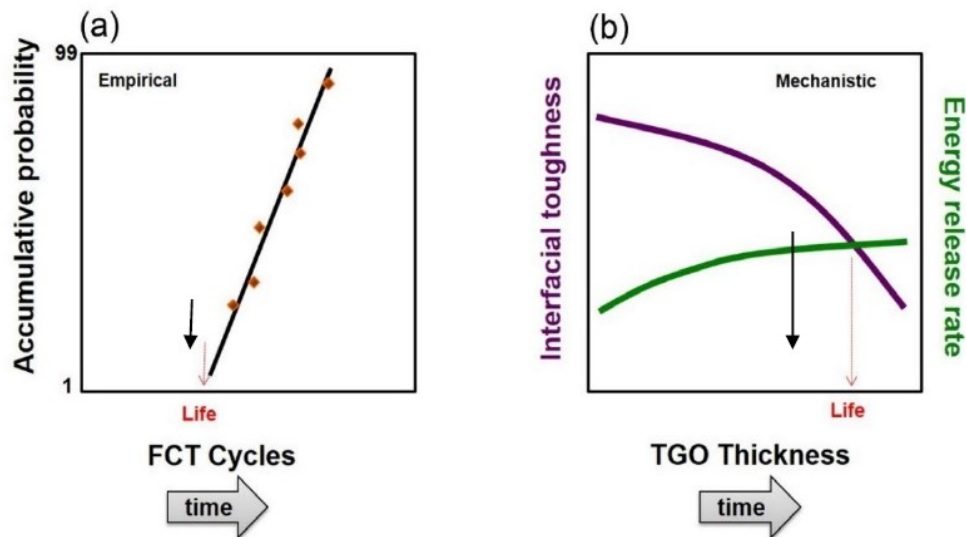


*Figure 1-10: Examples of TBC lifetime assessment models for both a) empirical methods and b) mechanistic methods [17].*

In empirical lifetime assessment methods, enough coatings are cycled to failure such that it can be accurately determined how many cycles a given coating system will remain attached to the substrate for a given FCT protocol. Such empirical lifetime assessment methods are best suited for comparing the relative efficacy of developmental coating systems and for processes control monitoring, but the number of FCT cycles to failure are not equivalent to the number of in-service cycles to failure. A mechanistic lifetime approach seeks to alleviate this issue through direct understanding of morphological and chemical changes and the evolution of stress and adhesive

16

properties in the multilayered system. This approach involves assessment of the balance between the stored strain energy in the system and the interfacial toughness between critical layers. As the lifetime of a coating increases, TGO growth occurs as a result of the flow of oxygen through the YSZ topcoat and the subsequent reaction with the Al in the bond coat. As the TGO grows, a significant amount of elastic strain energy is created in the dense $\alpha$-$Al_2O_3$ TGO. Moreover, high temperature sintering of the YSZ topcoat may lead to a stiffer, less compliant YSZ and increased strain energy in the topcoat. These lead to a net increase of total available strain energy that is available for release during coating delamination. At the same time, various damage mechanisms can occur that decrease the interfacial toughness of the interfaces. When the available strain energy release per unit crack advance is equal to the interfacial toughness, delamination of the coating in preferred. Direct measurement of the interfacial toughness is a critical and necessary component for developing a mechanistic life prediction methodology.

This desire motivates the work discussed in Chapters 3 and 4, where two different TBC systems are tested using the Compression Edge Delamination (CED) test to measure the pure Mode II interfacial fracture toughness of these systems. The CED test is a novel test first developed and employed by Lockyer-Bratton of the Hemker group [20] to measure pure Mode II interfacial toughness values. Chapter 4 details CED measurements for FCT specimens provided by P&W, while Chapter 3 focuses on CED results for JETS specimens and select engine hardware provided by GE. The blades were provided to assess the efficacy of the novel CED test on real engine hardware and to compare and contrast measured interfacial toughness values for FCT, JETS and blades. It is important to note that the blades were thermally cycled in jet engines where it is not possible to constantly monitor the temperatures of each blade. Thus, only rough thermal lifetime approximations are available for comparison.

## 1.4 TBC Fracture Toughness Testing Methods

Stemming from the fact that TBCs are complex, multilayer systems, TBC failure can occur in a multitude of ways depending on the operating conditions of the engine. These failure modes are categorized as either intrinsic or extrinsic [23]. Intrinsic failure modes occur within a layer or between layers as a result of thermal stresses and strains that develop over the course of a TBCs lifetime in service. Extrinsic failures modes occur as a result from external particles infiltrating or impacting the coating and damaging it. Figure 1-11 below shows a schematic of the different kinds of failure modes that can occur in an EBPVD TBC system.
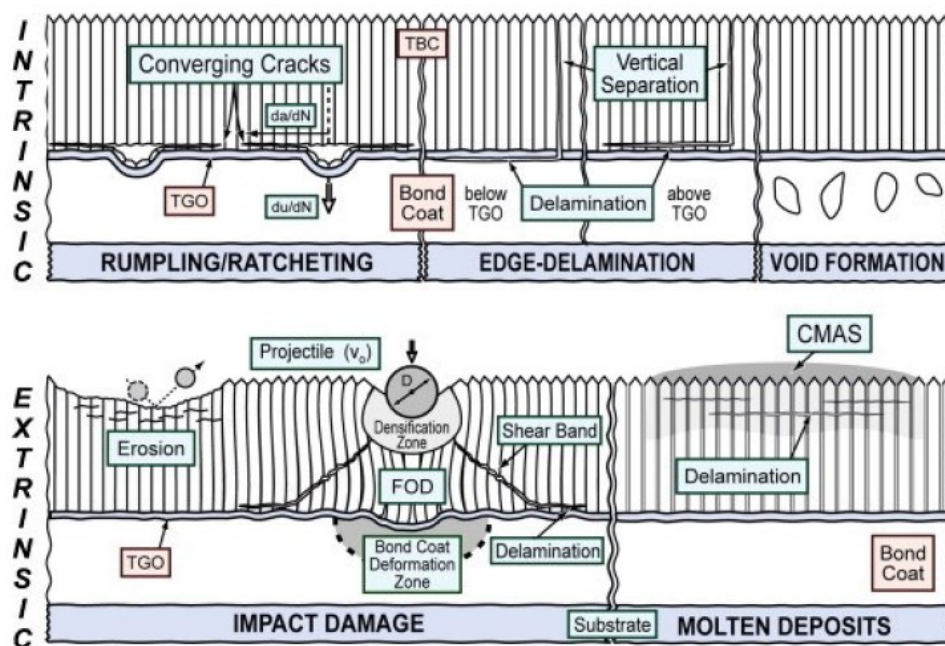


*Figure 1-11: Schematic detailing common intrinsic and extrinsic TBC failure methods [24].*

Edge-delamination of the TGO interface is deleterious to TBC life, especially in EBPVD topcoat systems. Thermal stresses develop due to the mismatch in thermal expansion between the high coefficient of thermal expansion (CTE) metallic bond coat and substrate and the relatively low CTE ceramic TGO and topcoat. When combined with pre-existing vertical cracks in the

columnar EBPVD topcoat microstructure, Mode II delamination can occur, causing the topcoat to spall and TBC failure. The work described in Chapter 3 and 4 of this dissertation was undertaken to study this edge-delamination phenomena and to experimentally measure the interfacial fracture toughness of various TBC systems.

Several experimental techniques have been previously employed to measure interfacial fracture toughness of layered material systems. Vasinonta and Beuth [25] employed a conical brale indenter to induce a circular delamination and then used the size of the delamination to estimate the interfacial toughness of as-deposited EBPVD TBC samples to be 49 J/m$^2$ with a variable mode mix, assuming a residual stress of 50 MPa and anisotropic TBC modulus of 44 GPa. Employing an indirect method, Faulhaber et al. [26] analyzed the shape and geometry of the TBC in buckled regions adjacent to spalled areas of burner rig bars, established the mechanics of ridge-cracked buckle delaminations for multilayers on curved substrates, and predicted an interfacial toughness of 75 J/m$^2$ for a mode mix of $\phi \sim 60°$ and a TBC modulus of 50 GPa. Kagawa and coworkers developed two related tests, a barb pullout test [27] and pushout tests [28] that are similar methods devised to measure interfacial toughness. Finite element (FE) analysis of the barb test by Evans et al. [29] yielded an interfacial toughness of 36 J/m$^2$ and $\phi \sim 65°$ for a Young's modulus of 44 GPa.

Beam and micro-bending tests are advantageous in testing brittle materials. More controlled loading can be imposed before and during brittle failure, and analytical solutions or FEA simulation of beam deflection can be used to extract the elastic modulus of the material. Théry et al. [30, 31] employed the double cantilever 4-point bend experiment with a stiffener to measure fracture toughness of an EBPVD TBC and reported a value of $113 \pm 11.3$ J/m$^2$ for a mode mix of $\phi \sim 40°$ and TBC modulus of 20-50 GPa. Lockyer-Bratton [20] also used the double cantilever 4-point bend experiment with a stiffener to measure interfacial toughness and reported values of

124.4 ± 11.3 J/m$^2$, matching Théry's reported values. Eberl et. al [32] developed and employed micro-bend experiments supplemented with Digital Image Correlation (DIC) to measure interfacial toughness as well. The average of these values was 57 ± 21 J/m$^2$ for a modulus of 30 GPa, mode mix of $\phi \sim$ 10-20°, and negligible residual stress.

An additional study relevant to the current study involved compression loading of the substrate and TBC in a manner that caused delamination and failure.  Johnson et al. [33] characterized the strain tolarence of various EBPVD TBCs by measuring the compressive plastic strain at delamination of a coating from an edge-initiated crack on a substrate compressively loaded beyond the yield point of the substrate. Johnson et al. did not derive an interfacial toughness from these measurement but noted that strain tolerance appears to scale inversely with the topcoat elastic modulus and with compressive residual stress in the TGO.  This work served as a precursor the work CED tests performed by Lockyer-Bratton of the Hemker group [20], the results of which will be discussed in detail in Chapter 2.

*1.4.1 Mechanical Limitations of Current Testing Methods*

In order to understand the limitations involved in current testing methods, the thermal cycling and delamination of an EBPVD TBC system in service must be discussed first. Figure 1-12 shows a detailed schematic of the edge-delamination phenomena.
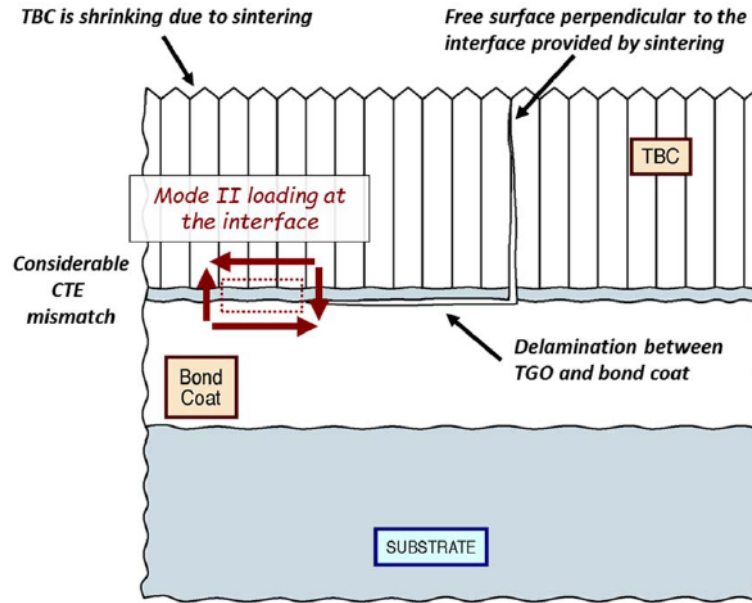
*Figure 1-12: Schematic of delamination occurring at the TGO interface of an EBPVD TBC coating system [34].*

Thermal stresses develop in the system as a result of the mismatch in the CTE's between the metallic substrate and bond coat when compared to the ceramic TGO and topcoat. At the high temperatures seen in the HPT region of a jet engine (>1000°C), high temperatures creep relaxation occurs [34] mitigating stresses and preventing failure. At ambient temperatures, however, the metallic substrate tends to compress more than the ceramic topcoat due to its larger CTE. This results in shear loading, tensile stresses in the metallic layers, and compressive stresses in the ceramic layers and creep relaxation does not occur. The mismatching stress states in the layers results in shear loading condition at the interface between the layers, which corresponds to a Mode II loading condition where the phase angle $\phi = -90°$.

In fracture mechanics, the type of fracture that occurs can be determined by the loading conditions at the crack tip. In EBPVD TBC systems, the crack tip experiences a shear loading condition or pure Mode II fracture. Functionally this means that the material at the crack tip is only displaced in the horizontal direction, with no movement occurring in the vertical direction. Thus,

for an EBPVD TBC system, the most relevant interfacial toughness values would be Mode II measured at ambient temperatures.

The experimental methods cited above all measure interfacial toughness of a TBC system at room temperature, but none of them do so in a mode mix that is close to a pure Mode II loading condition. Figure 1-13 below shows a plot of the previously mentioned test methods used to measure interfacial toughness of an EBPVD TBC system, plotted against their respective phase angles.
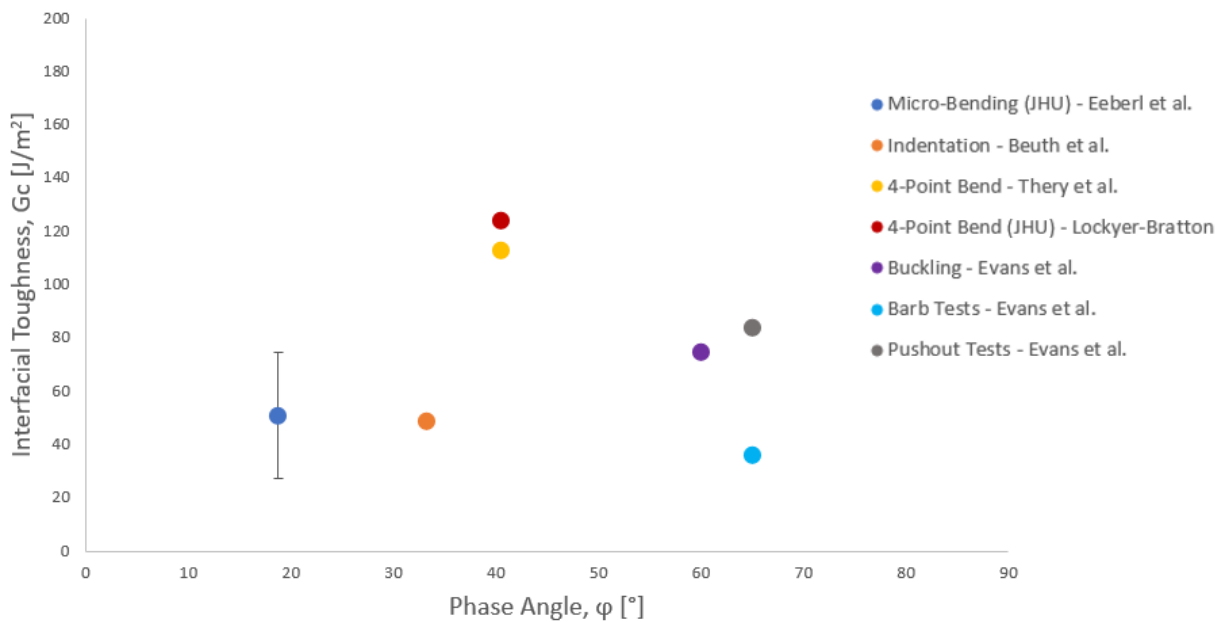


*Figure 1-13: Plot of interfacial toughness of TBC systems against the phase angle of the test used, including the 4-point bend results previously measured by the Hemker group.*

Of the tests commonly used to measure TBC interfacial toughness, the measured interfacial toughness values closest to that of Mode II were from the barb and pushout tests performed by Kagawa and Evans [29]. As stated above though, all of them are measuring some variation of mode mix as opposed to pure Mode II interfacial toughness; none of the phase angles from the previously reported experiments come close to the point of interest where the phase angle $\phi$ = -

90°. Moreover, the compilation of data does not clearly answer the question as to whether the interfacial toughness is dependent on phase angle.

This question motivated the work of Lockyer-Bratton in the Hemker group [20]. He employed the novel CED test to measure Mode II interfacial toughness values for GE's standard commercial TBC system at various stages of FCT testing. The full results for this work are covered in detail in Chapter 2, but the unmistakable conclusion of that work is that mode mix does have a significant effect on the interfacial toughness of TBCs. The current study builds upon the work of Lockyer-Bratton and expands use of the novel Mode II CED test to a wider variety of TBC systems through collaborations with colleagues at both GE Aviation and Pratt and Whitney.

*1.5* Dissertation Overview

When measuring the mechanical response of a TBC system, it is crucial to make sure that the chosen test most accurately represents the conditions experienced by that system during service in an engine. It is also crucial to understand how variations in the processing of the TBC, and the resulting microstructural variations, affect these mechanical responses. The focus of this dissertation is to develop insight into both of these topics.

The thesis is organized as follows: Chapter 1 sets the stage with motivation and a short review of salient background materials. Chapter 2 gives further detail on commonly used TBC testing methods, as well as the methods employed in this study (3-point bending and CED testing). Chapter 3 details the CED testing done in collaboration with GE Aviation on their standard diffusion aluminide bond coat/EBPVD topcoat system. CED results are shared for lab-based specimens that have undergone thermal gradient cycling, and these findings are compared with previous results for the same TBC system that underwent FCT testing. The work on GE blades is

also be presented.  Chapter 4 focuses on CED testing completed using FCT specimens of P&W's LPPS NiCoCrAlY bond coat/EBPVD topcoat system. Results of "as-deposited" and FCT specimens are presented in a manner similar to Chapter 3. The collaboration with P&W is expanded in Chapter 5 to include topcoat microstructural and mechanical property measurements for standard and off normal processing conditions. Lastly, Chapter 6 gives a comprehensive summary of all studies with conclusions and potential avenues for future work.

References:

[1]: International Air Transport Association, *2036 forecast Reveals air passengers will nearly double to 7.8 billion.* 2017. Accessed: https://www.iata.org/en/pressroom/pr/2017-10-24-01/

[2]: Tejero-Martin, D., Bennett, C., Hussain, T., *A review on environmental barrier coatings: History, current state of the art and future developments.* Journal of the European Ceramic Society, 2021. **41**(3): p. 1747-1768.

[3]: International Civil Aviation Organization, *Aviation Benefits 2017.* 2017. Accessed: https://www.icao.int/sustainability/Documents/AVIATION-BENEFITS-2017-web.pdf

[4]: NASA Glenn Research Center, *Types of Gas Turbine Engines.* Accessed: https://www.grc.nasa.gov/www/k-12/airplane/trbtyp.html

[5]: Aainsqatsi, K., *Low-Bypass Turbofan engine schematic*. T.o. lbp.svg, Editor. 2008, Wikipedia Commons: Wikipedia.

[6]: Cervenka, M., *The Rolls Royce Trent Engine.* T.R.R.T.E.-O.p.g.a.U.o. Cambridge, Editor. 2000.

[7]: Clarke, D.R., Oechsner, M., Padture, N.P., *Thermal-barrier coatings for more efficient gas-turbine engines*. MRS Bulletin, 2012. **37**: p. 891-898.

[8]: Lee, K., *Protective Coatings for Gas Turbines.* The Gas Turbine Handbook, National Energy Technology Laboratory, 2005. 4.4.2: p. 419-437.

[9]: Wing, R.G., McGill, I.R., *The Protection of Gas Turbine Blades.* Platinum Metals Rev, 1981. **25** (3):

[10]: Clarke, D.R., Levi, C.G., *Materials Design for the Next Generation Thermal Barrier Coatings.* Annual Review of Materials Research, 2003. **33**: p. 383-417.

[11]: Aviation, G. *Repair Brocure*. 2014.

[12]: Guven Gok, M., Goller, G., *State of the Art of Gadolinium Zirconate Based Thermal Barrier Coatings: Design, Processing and Characterization.* Methods for Film Synthesis and Coating Procedures, 2019.

[13]: Feuerstein, A., Knapp, J., Taylor, T., Ashary, A., Bolcavage, A., Hitchman, N., *Technical and Economical Aspects of Current Thermal Barrier Coating Systems for Gas Turbine Engines by Thermal Spray and EBPVD: A Review*. J Therm Spray Tech, 2008. **17**: p. 199-213.

[14]: Bouchet, R., Mévrel, R., *Influence of platinum and palladium on diffusion in $\beta$-NiAl phase. Defect and Diffusion Forum*. Trans Tech Publ, 2005. **237**: p.238-243.

[15]: Schilke, P.W., *Advanced Gas Turbines Materials and Coatings.* GE Energy, 2004. Accessed: https://www.ge.com/content/dam/gepower-new/global/en_US/downloads/gas-new-site/resources/reference/ger-3569g-advanced-gas-turbine-materials-coatings.pdf

[16]: Herman, H., Sampath, S., McCune, R., *Thermal spray: current status and future trends.* MRS Bulletin, 2000. **25**: p.17-25.

[17]: Zhang, B., *Experimental Characterization of Thermal Barrier Coatings Using Micro-Scale Bending Techniques.* Ph.D. Thesis, Johns Hopkins University, 2015.

[18]: Levi, C.G. et al., *Stability Issues in Thermal Barrier Coatings.* Presentation, 2006. Accessed: http://www.icmr.ucsb.edu/programs/archive/documents/Levi.pdf

[19]: Karaoglanli, A.C., Ogawa, K., Türk, A., Ozdemir, I., *Thermal Shock and Cycling Behavior of Thermal Barrier Coatings (TBCs) Used in Gas Turbines.* Progress in Gas Turbine Performance, 2013.

[20]: Lockyer-Bratton, S., *Experimental measurements of thermal barrier coating interfacial fracture toughness as a function of mode-mix.* Ph.D. Thesis, Johns Hopkins University, 2016.

[21]: Marlin Steele, *Guide to Jet Engine Maintenance.* 2020. Accessed: https://www.marlinwire.com/blog/your-guide-to-jet-engine-maintenance

[22]: Mahade, S., *Functional Performance of Gadolinium Zirconate/Yttria Stabilized Zirconia Multi-Layered Thermal Barrier Coatings.* Ph.D. Thesis, University West, 2016.

[23]: Hutchinson, J.W., Evans, A.G., *On the delamination of thermal barrier coatings in a thermal gradient.* Surface and Coatings Technology, 2002. **149**: p. 179-184.

[24]: Evans, A.G., Clarke, D.R., Levi, C.G., *The influence of oxides on the performance of advanced gas turbines.* Journal of the European Ceramic Society, 2008. **28**: p. 1405-1419.

[25]: Vasinonta, A. and J.L. Beuth, *Measurement of interfacial toughness in thermal barrier coating systems by indentation.* Engineering Fracture Mechanics, 2001. **68**(7): p. 843-860.

[26]: Faulhaber, S., et al., *Buckling delamination in compressed multilayers on curved substrates with accompanying ridge cracks.* Journal of the Mechanics and Physics of Solids, 2006. **54**(5): p. 1004-1028.

[27]: Guo, S., et al., *Measurement of interfacial shear mechanical properties in thermal barrier coating systems by a barb pullout method.* Scripta Materialia, 2005. **53**(9): p. 1043-1048.

[28]: Tanaka, M., et al., *Delamination toughness of electron beam physical vapor deposition (EB-PVD) Y 2 O 3–ZrO 2 thermal barrier coatings by the pushout method: Effect of thermal cycling temperature.* Journal of Materials Research, 2008. **23**(9): p. 2382-2392.

[29]: Liu, Y.-F., Y. Kagawa, and A. Evans, *Analysis of a "barb test" for measuring the mixed-mode delamination toughness of coatings.* Acta Materialia, 2008. **56**(1): p. 43-49.

[30]: Théry, P.-Y., et al., *Adhesion energy of a YPSZ EB-PVD layer in two thermal barrier coating systems.* Surface and Coatings Technology, 2007. **202**(4): p. 648-652.

[31]: Théry, P.-Y., et al., *Spallation of two thermal barrier coating systems: experimental study of adhesion and energetic approach to lifetime during cyclic oxidation.* Journal of Materials Science, 2009. **44**(7): p. 17-26.

[32]: Eberl, C., et al., *In situ measurement of the toughness of the interface between a thermal barrier coating and a Ni alloy.* Journal of the American Ceramic Society, 2011. **94**(s1).

[33]: Johnson, C., et al., *Relationships between residual stress, microstructure and mechanical properties of electron beam–physical vapor deposition thermal barrier coatings.* Surface and Coatings Technology, 1998. **108**: p. 80-85.

[34]: Evans, A.G., et al., *Mechanisms controlling the durability of thermal barrier coatings.* Progress in Materials Science, 2001. **46**(5): p. 505-553.

## Chapter 2: Experimental Methods for TBC Characterization

This chapter focuses on the fabrication of the specimens described in this thesis, as well as the experimental methods used to test these specimens. Specimens were provided by both GE Aviation and P&W, and the fabrication process of these specimens are summarized. A literature review, detailing previous experiments that have been employed to obtain interfacial toughness values from TBC systems is presented. Emphasis is placed on the novel CED test used on the samples described in this study, including modifications made to the test based on previous work done by Lockyer-Bratton [1]. Results from FE simulations, which indicate how these modifications effect the analytical solution for interfacial toughness and highlight how the analytical solution for interfacial toughness overestimates the true value, are shown. Following this is a literature review on previous efforts to measure constitutive properties of TBC coating layers. Special focus is given to the 3-point bend test and how it can be used to measure the elastic modulus of free-standing topcoat specimens.

## 2.1. Specimen Fabrication

The specimens tested in this study were provided by the two major American-based commercial jet engine manufactures, P&W and GE. Fabrication of these samples was performed as a result of frequent discussions between the scientists at these companies and the team at JHU. Care was taken to ensure that the specimens were fabricated using processes that mirror those used for components in jet engines, while also making sure they were viable test candidates from a mechanical standpoint. This section details the fabrication process for the studies undertaken in collaboration with both P&W and GE.

### 2.1.1. P&W Specimens

The study undertaken with P&W involved CED testing on specimens that followed their standard fabrication and coating processes. The substrates were made from P&W 1484 single crystal oriented along a <001> crystallographic orientation and coated with a NiCoCrAlY LPPS bond coat and EBPVD 7YSZ topcoat system provided by P&W. Some of these specimens were tested in the "as-deposited" state while others thermally cycled to various points of thermal exposure via the following FCT cycling conditions; $T_c$ = 38-150°C/100-300°F, $T_H$ = 1120°C/2050°F, $t_{heat\ up}$ = 15 min, $t_{max\ temp}$ = 45 min, $t_{cool\ down}$ = 7 min. A schematic for the CED specimens is given in Figure 2-1 and its geometry was based off proposed geometries by Hutchinson and Hutchinson [2] and previous work by Lockyer-Bratton [1].
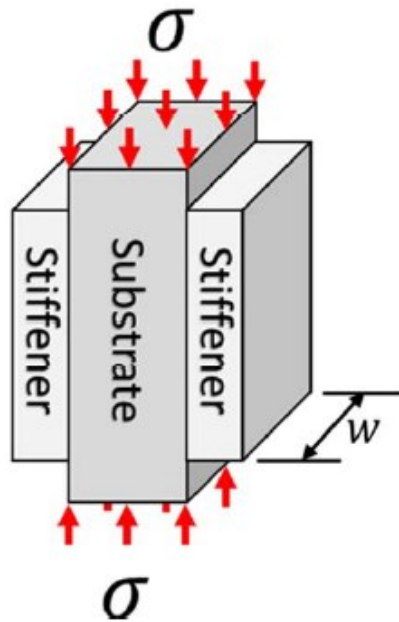


*Figure 2-1: Schematic of the compression edge delamination (CED) sample that can be used to measure the Mode II interfacial toughness of coatings. [1].*

The final dimensions ($L$ = 20 mm, $w$ = 10 mm, and $h$ = 3 mm) were chosen to avoid buckling and trigger delamination at reasonable loads. Stiffener plates that promote crack propagation before substrate yielding were also made from P&W 1484 and adhered to the TBCs on opposing

29

sides of the substrate. Lockyer-Bratton used a stiffener plate geometry of $L = 15$ mm, $w = 10$ mm, and $h = 1.5$ mm, and the same geometry was used for the current study.

Once the substrates were machined, the overlay bond coat was applied to opposing side surfaces at P&W using their LPPS processes. The topcoat was then deposited on the middle 75% of the bond coat of multiple CED specimens using a special fixture that mimicked blade dimensions and could easily be inserted in an EBPVD chamber. Coating of the CED specimens was done alongside of engine components, which assured the authenticity of the CED specimens. When turbine blades are EBPVD coated, they are held in the chamber by the base of the turbine blade. The custom frame was developed to so that it could be tack welded onto the base of a blade to allow it to be mounted in the EBPVD chamber. Figure 2-2 illustrates the protocol for that process.
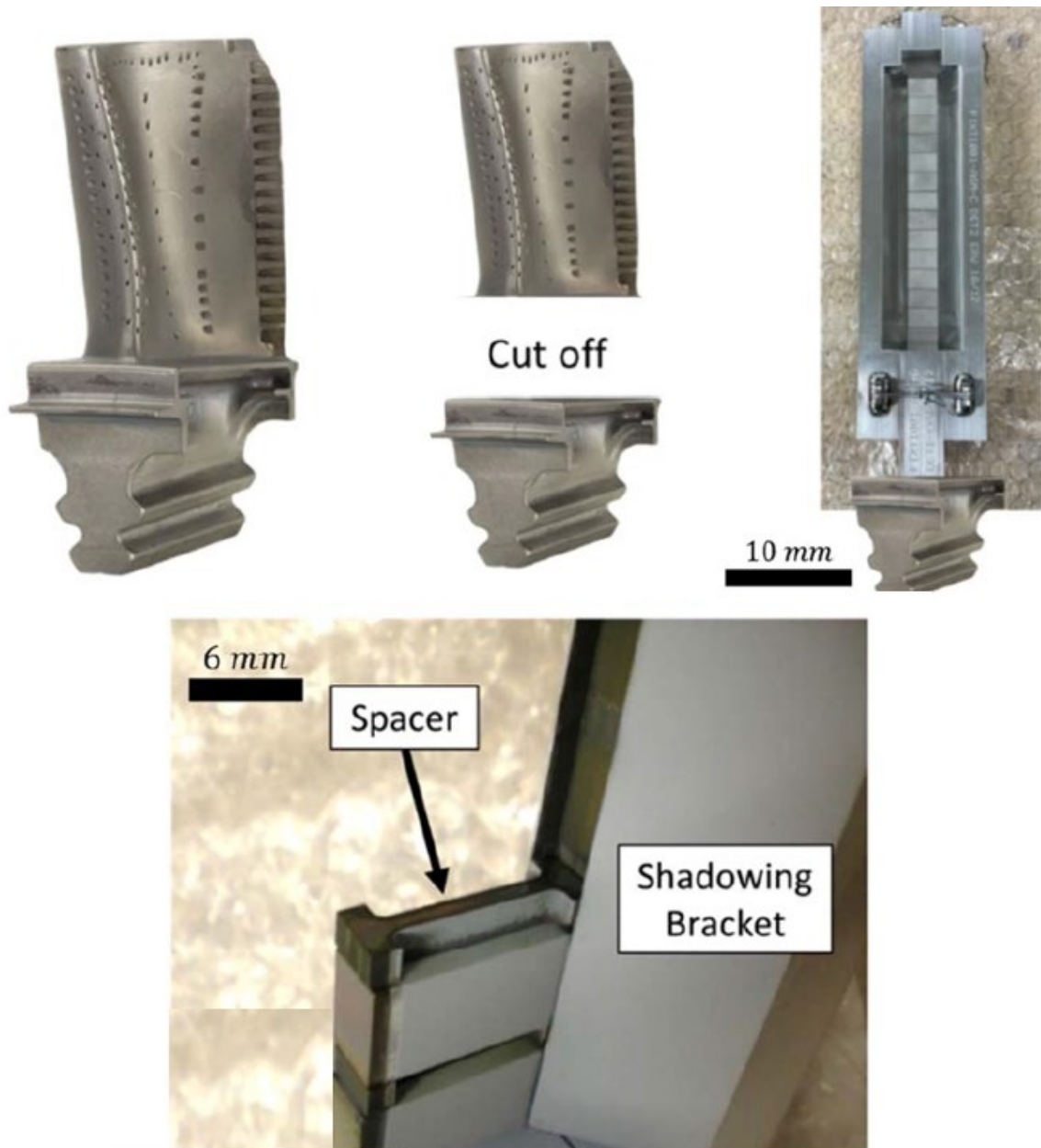
*Figure 2-2: Images of the custom fixture used to coat the CED specimens in an EBPVD coater. The top set of images shows how the fixture is tack welded to the base of a blade that can be mounted in the coater. The bottom image shows the shadow bracket used to facilitate the angle of YSZ particle deposition, as well as the spacers used to ensure the coated CED samples do not stick to one another and can be easily removed [1].*

The CED specimens in the fixture were shielded by a shadow bracket to guarantee that the angle of topcoat deposition on the flat CED specimens matched the angle of topcoat deposition normally seen by the curved blade surfaces. The thermal mass of the fixture along with the material

31

being coated also effects the coating microstructure, so the number of CED specimens coated in a single run was chosen to approximate the thermal mass of the blades coated. Spacers were added between specimens to allow for easy removal of the CED specimens without damaging the coating. After removal from the fixture, the stiffener plates and coated CED specimens and were sent from P&W to JHU to be prepped for experimentation, which is discussed in detail in Chapter 4.

A second set of specimens provided by P&W were designed to assess whether variations in topcoat microstructures and properties could be correlated with the processing conditions that were used to deposit the topcoats. Three different sets of samples, each consisting of a blade, a wedge bar and buttons, were fabricated. The substrate material and bond coat remained the same, but different topcoat processing powers were used. One set was coated with P&W's "nominal run power" YSZ topcoat, one was coated with a "low run power" YSZ topcoat, and the final was coated with a "high run power" YSZ topcoat. These run powers were controlled by variations in the processing temperature and pressure; the "high run power" specimens had a higher processing temperature and pressure and the "low run power" specimens had a lower processing temperature and pressure. Figure 2-3 below shows the "low run power" a, b) buttons, c) blade and d) wedge bar.
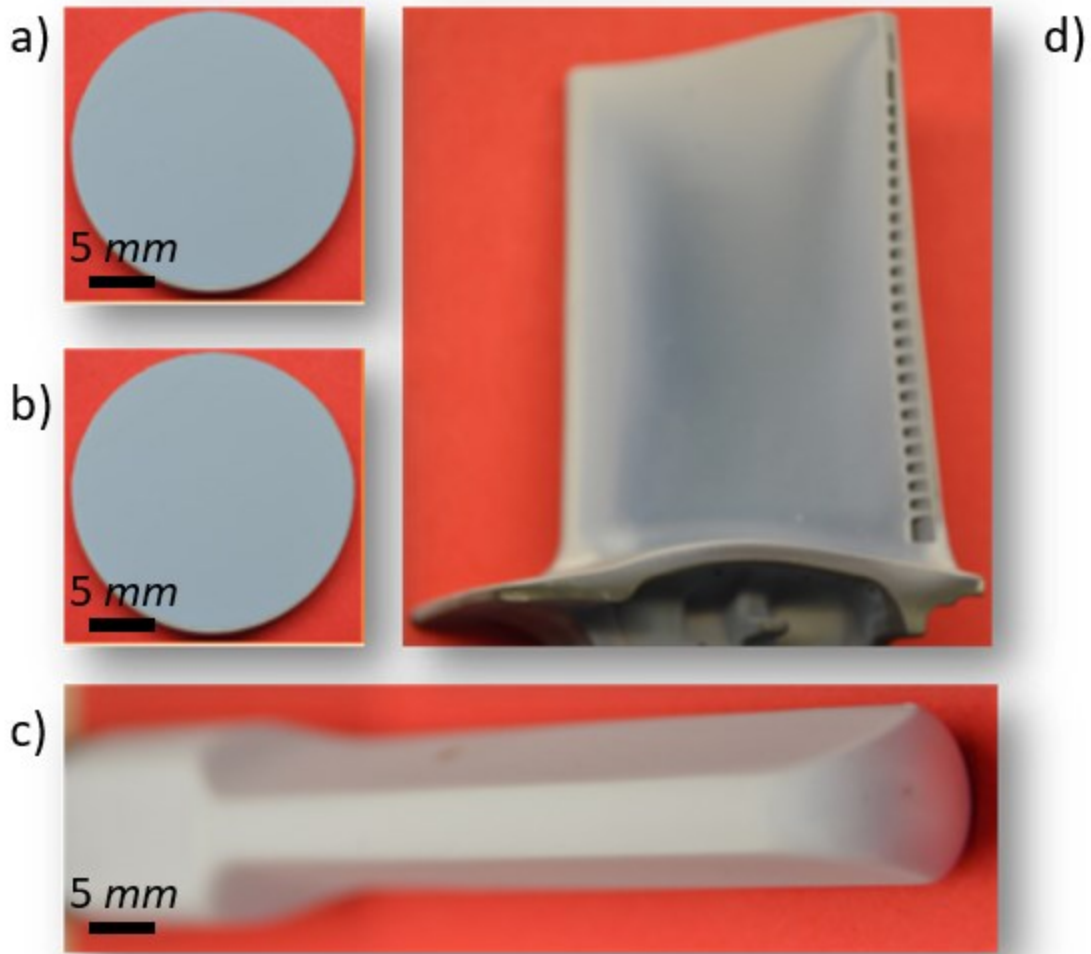
*Figure 2-3: Images of the "low run power" a, b) buttons, c) wedge bar and d) blade that was produced at Pratt and Whitney and provided to JHU for topcoat characterization.*

Cross sections of the blades and wedge bars were obtained at JHU using an STX-202a Precision Diamond Wire Saw with a 0.225 mm diameter wire for testing and SEM imaging. The cross sections of the wedge bar were also used to create free-standing topcoat samples, which were then loaded in a 3-point bending to obtain modulus values for the topcoats. The specimen preparation procedure as well as the results of this study are discussed in detail Chapter 5.

## 2.1.2.  GE Specimens

The samples provided by GE were made using René N5 single crystalline substrates oriented along a <001> crystal direction and coated with GE's standard diffusion aluminide bond coat and EBPVD YSZ topcoat system ((Ni,Pt)Al/8YSZ EBPVD TBC). Specimens were provided as 1-inch diameter buttons that were coated on one side and uncoated on the other; about half of these buttons were provided in the "as-deposited" state and the rest were thermally cycled in a thermal gradient JETS setup. In this process, the coated side of the button was exposed to a torch set at a temperature of 1316°C (2400°F), while the uncoated back side of the button was cooled with a directed stream of air at 36°C (97°F) and the bond coat experienced an estimated temperature of 1150°C (2100°F). This introduced a thermal gradient of 1280°C (2303°F) and is closer to the thermal conditions experienced in an engine than standard furnace cycle testing is. Repetition of this process allowed for the buttons to be thermally cycled to various stages in its life. For the current study, JETS buttons were examined in "as-deposited", "early-in-life", "mid-life" and "late-in-life" states.

When compared to the traditional furnace cycling method, the JETS setup is significantly more expensive and time consuming to run. As a result, only one JETS button was initially provided at each thermal lifetime point. Due to the size and shape of the buttons, as well as a desire to test multiple specimens for each thermal lifetime point, traditional CED specimens could not be made from JETS tested buttons. Instead, reduced sized CED specimens ($L = 10$ mm, $w = 6.5$ mm, and $2h = 3.2$ mm = thickness of the buttons) were designed and fabricated. Figure 2-4 below shows the coated surface of the a) "as-deposited" and b) "mid-life" buttons.  The white lines represent cut plans that were used to fabricate the reduced size CED specimens.
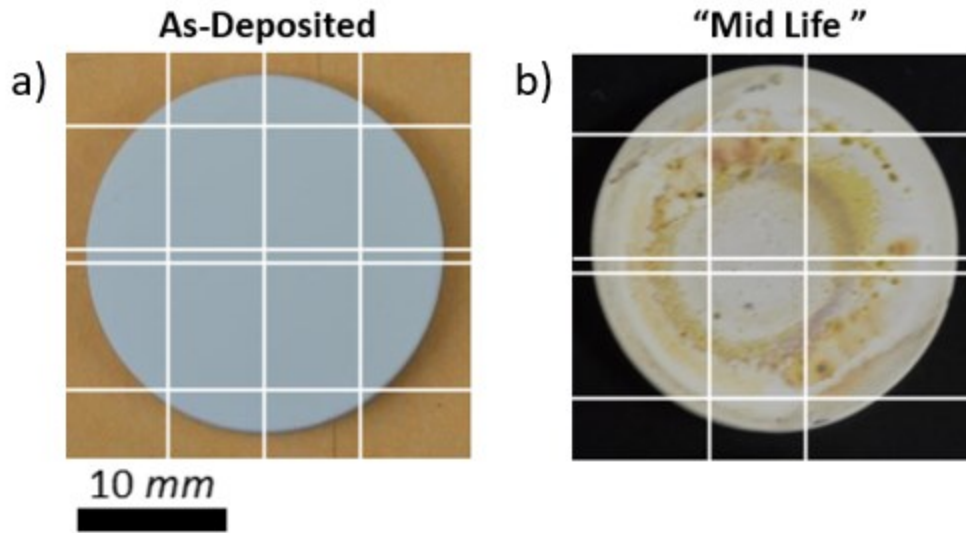
*Figure 2-4: The a) "as-deposited" button on the left and b) "mid-life" button on the right, with their cut plans for CED specimen fabrication highlighted by the white lines.*

For the "as-deposited" buttons, four specimens were fabricated from each button, but for the thermally cycled JETS samples, only two CED specimens were fabricated from each button. This was done to ensure that the specimens fabricated from the thermally cycled specimen were all taken from the "heat affected zone", or the area on the button that was most directly exposed to the torch and thus experienced the highest temperatures. Initial attempts to cut the buttons into CED specimens were done at JHU using the diamond wire saw to ensure a high-quality cut with minimal damage to the coating. However, the wire bent significantly when cutting through the substrate and the cuts took significantly longer than expected. Subsequent buttons were sent to GE Research in Niskayuna, New York to be cut with a high RPM semiconductor dicing saw by Jared Hale and Dr. Don Lipkin.

Due to the reduced size of the JETS CED specimens, the stiffener plates for these experiments were also reduced in size; the geometry for the stiffener plates was $L = 7.5$ mm, $w = 6.5$ mm, and $h = 1.6$ mm. GE provided JHU with a block of the substrate material, single crystal René N5, and fabrication of the stiffener plates was done at JHU using an electrical discharge machine (EDM).

The EDM'd surfaces were polished to remove the recast layer. The full specimen preparation as well as results of testing are discussed in Chapter 3, and comparisons are made to the preliminary work on FCT samples done by Lockyer-Bratton [1]. It is important to note that the JETS specimens were only coated on one side and were half the size of the FCT specimens, because these differences impacted the way that the interfacial toughness values were calculated, as discussed in Chapter 3.

The second set of samples provided by GE were sections of high-pressure turbine blades that had been removed from service in jet engines. Like the JETS buttons, the blade sections were identified as having been thermally cycled to various stages of their lifetime. Temperature monitoring and the exact thermal history of the blades was not available, but the blades were designated as being: "as-deposited", "early-in-life", "mid-life", and "late-in-life". Two blades for each stage were sectioned by GE and provided to JHU. An initial set of blades was cut into reduced sized CED specimens using the diamond wire saw. Care was taken to ensure that the provided blade sections were taken from flat regions of the original blade, as the geometry of the CED test requires a flat surface. Figure 2-5 shows the pressure and suction surfaces of a, b) "as-deposited" and c, d) "late-in-life" blades, with the cut planes used to fabricate reduced size CED specimens overlayed on the photos. Figure 2-5 e) shows a cross-sectional view of a blade after being cut.
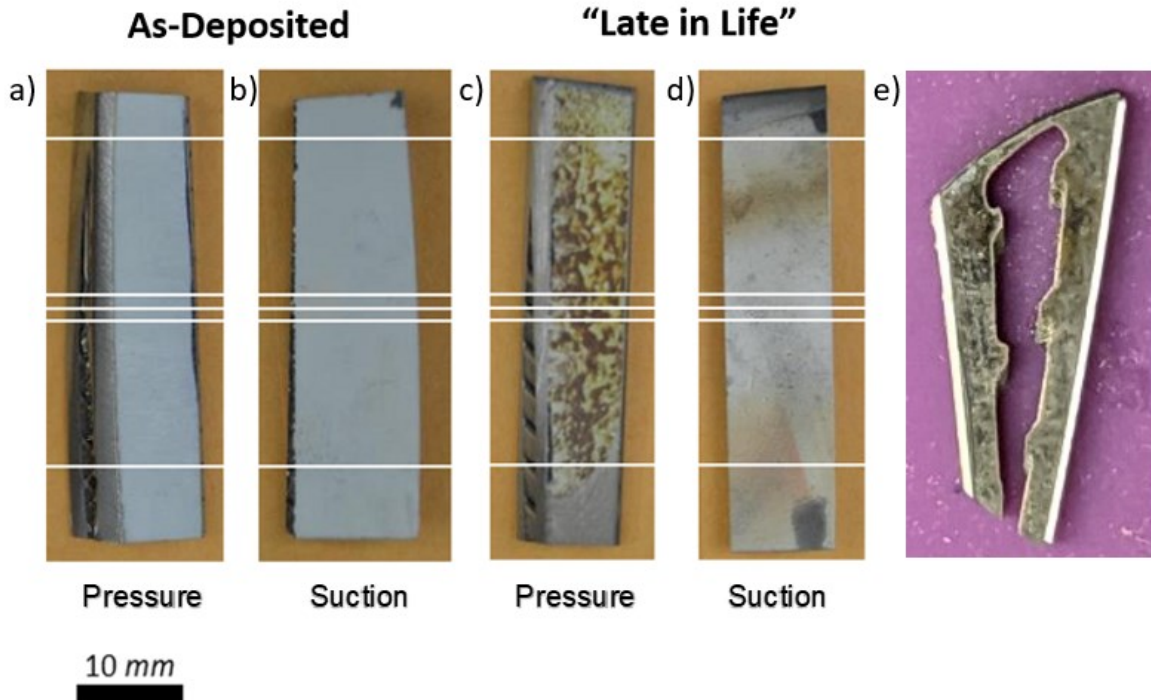
*Figure 2-5: Plane view images of the pressure and suction sides of a, b) an "as-deposited" and c, d) a "late-in-life" high-pressure turbine blades. The cut plans for CED specimen fabrication are overlayed in white. Image e) shows a cross-sectional view of a blade that was provided to JHU.*

During the cutting process, it became apparent that the first set of blade sections that GE provided could not be used for CED testing. While the provided sections were flat, they were also hollow and the substrate was only connected at one end, as seen in Figure 2-5 e). As a result, every blade split into two after being cut into CED specimens. The resultant halves were too thin ($h <1$ mm) for CED testing. Upon recognizing this, GE provided a second set of high-pressure turbine blades that were sectioned from an area with ribs that provided a more robust support between the two sides of the blade. Figure 2-6 shows the a) pressure, b) suction side and c) more robust support of a thermally cycled blade.
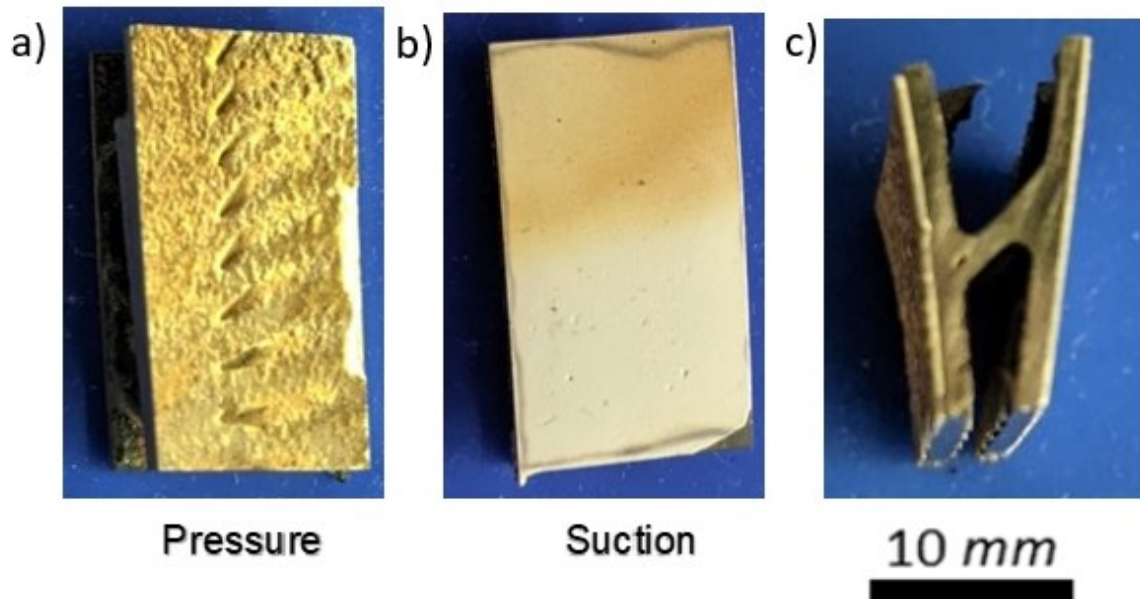
*Figure 2-6: Image of one of the thermally cycled blades from the second set of provided blades with the a) pressure and b) suction side labelled while c) shows the more reinforced connector between the two sides.*

The second set was comprised of one "as-deposited" blade and three blades that had been thermally cycled to various stages of their thermal lifetime. The geometry of these new blades was much closer to that of the standard CED specimen ($L \sim 20$ mm, $w \sim 10$ mm, and $h \sim 1$ mm), so the blades could be CED tested without any need for further sectioning. However, the surfaces of the blades had more pronounced curvature. To ensure proper adherence between the stiffener plates and the TBC surfaces, the blades were optically imaged and curved stiffener plates were custom milled at JHU. The results of the CED tests for these blades are discussed in Chapter 3.

## 2.2. Interfacial Toughness Measurement Techniques

As previously discussed in Section 1.4, a variety of test methods have been employed to measure interfacial toughness of TBC systems. However, none of these methods properly measure Mode II interfacial toughness, which is most relevant for the EBPVD TBC systems that this study

focuses on [2]. This section details the experimental methodology of both the 4-point bend and the novel CED test, the latter of which can be used to measure Mode II interfacial toughness values.

### 2.2.1. 4-Point Bend Tests

Bending tests have been widely used as a method to measure the flexural strength of ceramics and material systems [3-8]. The use of bending tests to measure the interfacial toughness of coatings and layered material systems like TBCs was limited until 1989 when Charalambides et al. [8] published a detailed mechanical analysis of a 4-point testing method, that is also commonly referred to as the "Santa Barbara test". A schematic of this test is shown in Figure 2-7.
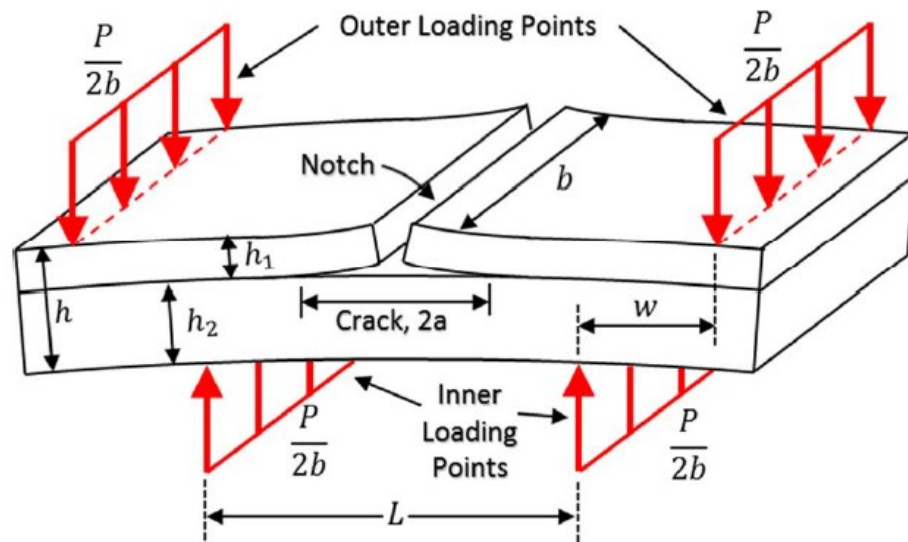


*Figure 2-7: A schematic detailing the geometry and loading conditions for a 4-point bend test on a layered material system [1].*

The setup for this test is the same as a traditional 4-point bend test where two outer pins and two inner pins are used to load the specimen. The uniqueness of this setup comes from the placement of a notch or vertical crack through the thickness of the coating or top layers of a layered material system, with the loading points placed symmetrically on either side of the crack. This

crack can be cut into the coating or grown by loading under 3-point bending. When the vertically-cracked sample is loaded in 4-point bending, the coating is placed in tension and a constant bending moment is realized between the inner loading pins. The load is increased until the crack begins to propagate and run along the weakest interface, or for TBCs between the coating and the substrate. Since the crack propagation is driven by a constant applied moment, this means that there is a constant strain energy release during delamination [8]. Thus, the plateau applied load corresponds to the crack growth, and an interfacial toughness value can be calculated using that moment without the need to monitor crack tip radius or position. The equation for interfacial toughness for this test is given in Equation 2-1.

*Equation 2-1*

$$G = \frac{21}{4} \frac{M^2}{Eh^3}$$

Where $E$ is the plane strain or plane stress elastic modulus, $M$ is the applied moment $M = Pw/2b$, and $h$ is the thickness of the substrate and coating. For systems with more than 2 layers like TBCs, analytical solutions can be derived that easily allow for the use of this test.

Despite the many benefits of the Santa Barbara 4-point bend test, there are also some drawbacks that limit its use. If sufficient strain energy is not developed in the coating, then the substrate may plastically deform before crack propagation begins. This severely complicates the analysis used to measure interfacial toughness and significantly detracts from the desired simplicity of the test. Oechsner et. al [10] mitigated this issue by epoxying stiffener plates to the outer coating, which increased the amount of strain energy in the system and facilitated crack growth before the onset of plasticity. This concept is critical to the CED test as well and revisited below in the discussion of the CED test method.

The modified 4-point bend test has a second major drawback, which is the fact that the mode-mix or phase angle of fracture for this test is $\phi = 40.9°$ [8]. For EBPVD TBC systems that are being studied for this dissertation the fracture mode mix that is most relevant is pure Mode II fracture, ($\phi = -90°$). It is important to note that with the presence of a crack and the different TBC layers, the phase angle of the CED test is slightly off pure Mode II, 89.5° as reported by Lockyer-Bratton [1], but is close enough that it will be referred to as pure Mode II in this thesis. The study undertaken here is motivated by a desire to measure the pure Mode II fracture toughness of TBC systems, the importance of which was further confirmed by Lockyer-Bratton's recent introduction of the novel CED specimen [1]. Thus, the novel CED test was chosen for this work due to its ability to directly measure the Mode II fracture toughness representative of the fracture mode seen in jet engine service for EBPVD systems.

### 2.2.2. Compression Edge Delamination (CED) Test

The CED test requires more specimen preparation and is more difficult to perform than the 4-point bend test, as interfacial toughness must be measured in the elastic region before plastic deformation, with no plateau stress or modulus change available as an indication of delamination. However, Lockyer-Bratton's recent successes with GE's standard TBC at various stages of FCT life [1] motivated its use in the current study. Here, it was expanded and used to explore different TBC coatings that have been exposed to a variety of thermal cycling.

The CED test was first theorized in a 2011 paper by Hutchinson and Hutchinson [2], where they proposed a variety of possible test methods to measure delamination toughness of TBC systems at a variety of mode mix. The CED test was specifically identified as a straightforward method to measure pure Mode II interfacial fracture toughness for multilayer systems. As

envisioned by Hutchinson and Hutchinson [2], a substrate is coated with TBC on two opposing sides and axially compressed. Taking a page from Oeschner [10], stiffener plates are epoxied on top of the TBC coating to increase the strain energy in the system. A pre-crack is introduced between the substrate and the coating and neither the coating nor the stiffener plates extend to the fixed platen. A schematic of the originally proposed test is shown in Figure 2-8.
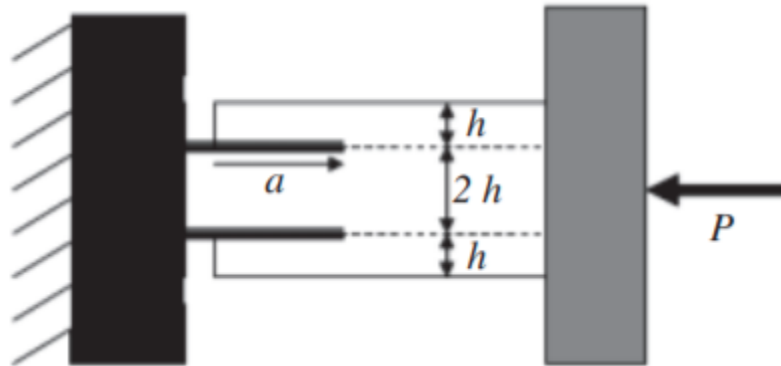


*Figure 2-8: Schematic of the original compression edge delamination (CED) test proposed by Hutchinson and Hutchinson [2].*

In this schematic, *a* represents the crack length, *h* represents the thickness of the stiffener plate (which is half the thickness of the substrate), and *P* represents the applied load to the system. The elastic strain in the substrate is transferred into the intimately attached coatings (not shown in Fig. 2-9) and stiffener plates. Resultant crack growth leads to a reduction in stress and strain in the coating and stiffener in the area above the crack and generates an energy release that promotes crack growth. FE simulations by Hutchinson and Hutchinson [2] and Lockyer-Bratton [1], defined a minimum crack length (a>1.5h) for steady-state crack growth, highlighted the need to account for friction, and reaffirmed the Mode II nature of the test. Figure 2-9 below from Lockyer-Bratton shows the normalized energy release rate plotted against normalized crack length. From this figure, it can be seen that a steady-state energy release rate is reached when the crack length *a* is ~ 1.5 larger than the thickness of the stiffener plate *h*.
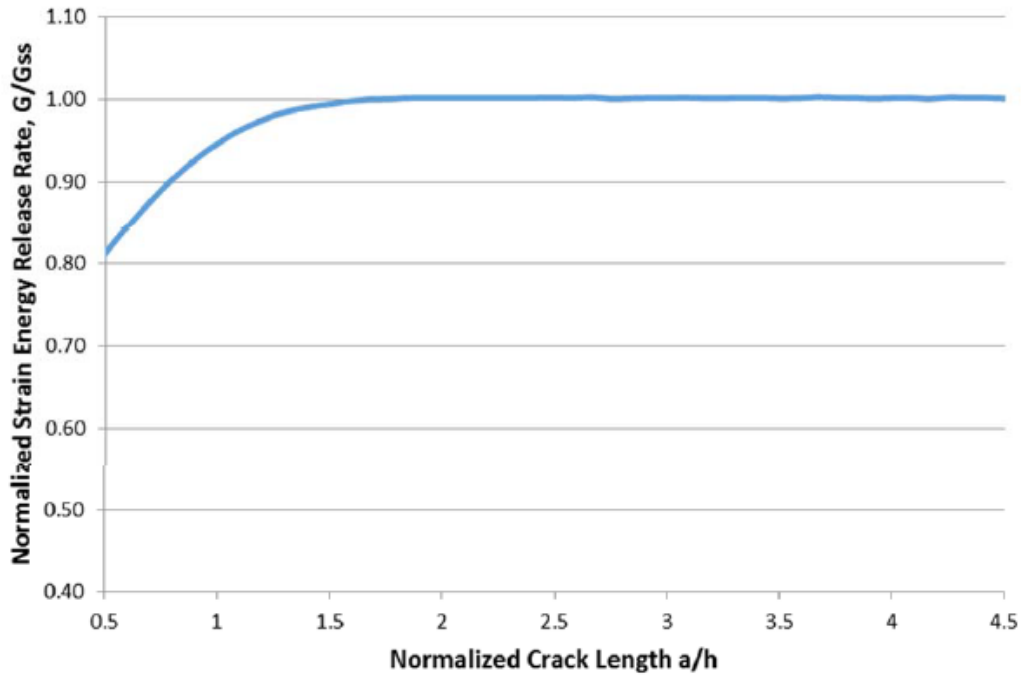
*Figure 2-9: Normalized strain energy release rate plotted against normalized crack length from FEA [1].*

The Mode II phase angle can be reimagined in Equation 2-2:

*Equation 2-2*

$$\phi = \tan^{-1}\left(\frac{\delta x}{\delta y}\right) = 90°$$

Where $\delta x$ is the horizontal displacement and $\delta y$ is the vertical displacement, while also ignoring the elastic mismatch between the layers and the crack face contact. In order for $\phi = -90°$ to be true, the horizontal displacement of the crack must equal a negative value while the vertical displacement is zero. This follows suit with the schematic shown in Figure 2-8 as the sample is being compressed in the horizontal direction with no load in the vertical direction. Thus, the loading conditions imparted by a CED test match those of pure Mode II fracture loading conditions. For simplicity, Hutchinson's analytical derivation of interfacial toughness assumes that there is no coating at the interfaces and a homogenous sample (with constant E) is being compressed. Methods like FEA must be employed to account for the effects of disparate layers

43

and friction on the crack faces between these layers, but a J-integral analysis [11] is still an insightful place to start.

The J-integral is a contour path integral that can be used to calculate the strain energy release rate for elastoplastic materials as well as materials with complicated geometries that do not have simple, analytical solutions. A typical J-integral solution takes the form shown in Equation 2-3.

*Equation 2-3*

$$J = \int_{\Gamma} (W \, dy - T_i \frac{du_i}{dx} ds)$$

Where $T_i$ are the surface tractions acting on the boundary $\Gamma$, $u$ is the displacement vector, $dx$ is the change in the $x$ position along a path, $dy$ is the change in the $y$ position along a path, $ds$ is the is an element of the arc length along $\Gamma$ and $W$ is the strain energy density shown in Equation 2-4.

*Equation 2-4*

$$W = \int \sigma_{ij} d\epsilon_{ij}$$

One benefit to the J-integral is that the analysis is independent of the path taken around the crack, and thus the path can be chosen to best simplify the calculations. This means that the J-integral result can be re-written such that the final J-integral result is the sum of $n$ different J-integrals, each one representing a subset of the total path taken around the crack, as shown in Equation 2-5.

*Equation 2-5*

$$J_{\Gamma} = J_{\Gamma}^{1} + J_{\Gamma}^{2} + \cdots J_{\Gamma}^{n}$$

Figure 2-10 shows a schematic for the breakdown of paths used for the J-integral analysis of the modified CED specimens.
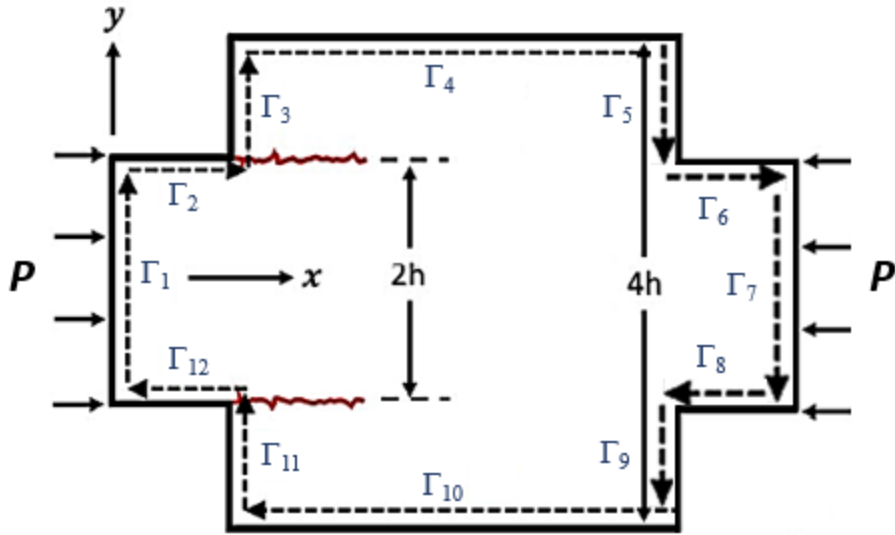
*Figure 2-10: Schematic showing the breakdown of the different paths chosen for the J-integral analysis of the modified CED specimen.*

For the path chosen for the CED specimens, the J-integral is represented by Equation 2-6.

*Equation 2-6*

$$J_\Gamma = J_\Gamma{}^1 + J_\Gamma{}^2 + \cdots J_\Gamma{}^{12} = \sum_1^{12} \Gamma_i$$

From Equation 2-3, it can be seen that $J_2, J_4, J_6, J_8, J_{10}$ and $J_{12} = 0$, since there are no surface tractions and no changes in $y$, meaning all $T$'s and $dy$'s = 0. $J_3, J_5, J_9$ and $J_{11} = 0$ since there are no surface tractions and no applied load on these faces, meaning all $T$'s and $W$'s = 0. This leaves two remaining J-integrals, $J_1$ and $J_7$. On $\Gamma_1$, the loading conditions are:

$$W = \frac{1}{2}\sigma\epsilon \qquad\qquad dy = ds$$

$$T_1 = -\sigma \qquad\qquad \frac{du_1}{dx} = \epsilon$$

Where $\sigma = \frac{P}{2h}$ is the stress applied on $\Gamma_1$ where the load $P$ is applied over a length of *2h*. And on $\Gamma_7$, the loading conditions are:

$$W = \frac{1}{2}(-\sigma)\epsilon \qquad\qquad dy = -ds$$

$$T_2 = -\sigma \qquad\qquad \frac{du_2}{dx} = -\epsilon$$

Where $\sigma = \frac{-P}{2h}$ is the stress applied on $\Gamma_2$ where the load $P$ is applied over a length of *2h*.

Plugging back into Equation 2-3, Equation 2-7 is obtained.

*Equation 2-7*

$$J_\Gamma = \int_0^h (\frac{1}{2}\sigma\epsilon - (-\sigma)\epsilon)ds + \int_0^h (-\frac{1}{2}(-\sigma)\epsilon - (-\sigma)(-\epsilon))ds$$

In a CED specimen, there are two independent cracks growing at either interface between the substrate and stiffener plate. Since the goal is to solve for the energy release rate around a single crack tip, the lower bound of the integral is set to be 0 so the path is taken along the center line of the samples. Taking the path along the center line, where applied tractions are equal to zero due to sample symmetry, ensures that only one crack tip is included in the path and the energy release rate of two independent crack tips are not combined. Solving for this gives the solution in Equation 2-8.

*Equation 2-8*

$$J_\Gamma = \sigma\varepsilon h$$

Assuming a linear elastic and isotropic system, Hooke's Law can be used to obtain the final solution for interfacial toughness shown in Equation 2-9.

*Equation 2-9*

$$G = \frac{\sigma^2 h}{E}$$

Where $E$ is the modulus of the stiffener plate and substrate, $h$ is the thickness of the stiffener plate, and $\sigma$ is the stress applied to the CED specimen, given by Equation 2-10.

*Equation 2-10*

$$\sigma_1 = \frac{P}{2h}$$

Where *P* is the applied load. From Equation 2-8 we can obtain the equation for the desired material property, interfacial toughness, seen in Equation 2-11 below.

*Equation 2-11*

$$G_c = \frac{\sigma_c{}^2 h}{E}$$

Where $\sigma_c$ is the stress associated with crack growth in the CED specimen obtained from Equation 2-10, and $G_c$ is the energy release rate also referred to as the interfacial fracture toughness.

### 2.2.3. *Previous CED Test Results*

Under the originally proposed CED test geometry, when loading a test specimen one loading platen would contact the substrate and both stiffener plates. If the stiffener plates were not adhered perfectly in line with the substrate on the loading surface, an asymmetric loading condition would result in non-Mode II loading. One stiffener plate could be loaded at a faster or slower rate than the substrate or the other stiffener plate, and premature delamination could occur. Additionally, since one loading platen would be contacting both stiffener plates and the substrate, that loading surface would also be in contact with all the different material layers (the substrate along with bond coat, TGO, topcoat, epoxy and stiffener plate on either side of the substrate). If any foreign material was present on the surface of the loading platen, there would be an increased risk of a stress concentration occurring at the interface and premature delamination occurring. To avoid these issues a modified CED test was developed (previously shown in Figure 2-1).

The geometry of the modified CED test is the same as that of the original CED test except that the stiffener plates have been moved from one edge of the substrate to the middle of the substrate. This mitigates the previous two issues discussed that arose because of loading the stiffener plates as well as the substrate. Performing the J-Integral of the original geometry in the same manner as above still gives the analytical solution in Equation 2-11 (Appendix A), showing that these two geometries can be used interchangeably. FE simulations detailing the differences in the loading conditions between these two geometries have been performed and are discussed in the following section.

The initial set of CED tests was performed by Lockyer-Bratton on a set of specimens provided by GE [1]. These specimens consisted of GE's standard diffusion aluminide/EBPVD TBC system deposited on a René N5 single crystal substrate oriented along a <001> crystal direction, which is the same standard commercial coating system provided by GE for the work in this study. The specimens were fabricated by GE to be the same size as the standard CED specimens mentioned in Section 2.1.1 ($L = 20$ mm, $w = 10$ mm, and $h = 3$ mm), and were coated by GE using the same fixture mentioned in Section 2.1.1. A number of the samples were thermally cycled using FCT protocols ($T_c = 36°C/97°F$, $T_H = 1150°C/2100°F$, $t_{heat\ up} = 10$ min, $t_{max\ temp} = 45$ min $t_{cool\ down} = 10$ min) to various fractions of their FCT lifetime. All CED samples were compressed in an MTS to induce delamination of the coatings and stiffener plates, while DIC was used to measure strain in the system and develop shear strain maps of the samples to identify the critical point of steady-state crack growth. Figure 2-11 below shows a set of DIC shear strain maps overlayed on an FCT CED specimen for one sample immediately before, during and after crack growth, along with the associated stress-strain curve for that sample.
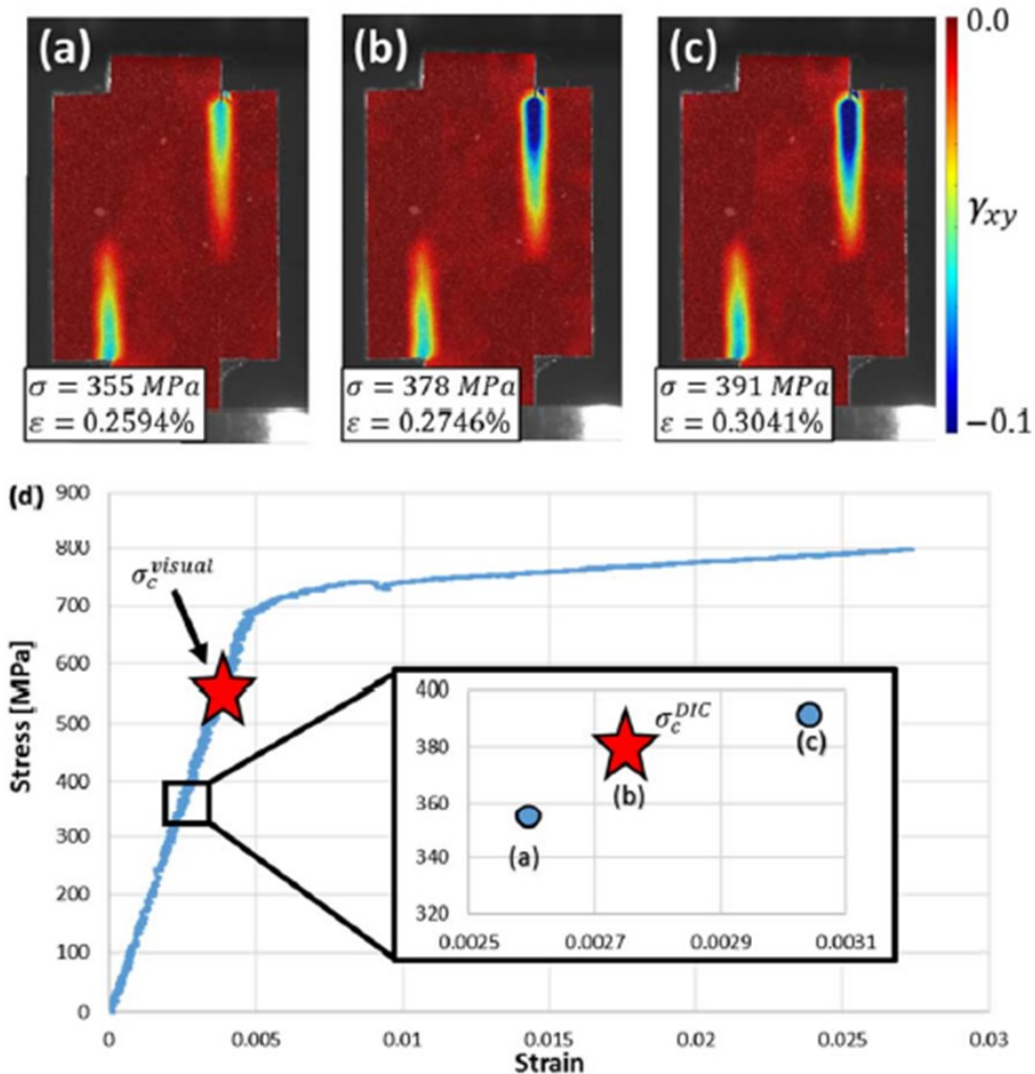
*Figure 2-1: Set of DIC images from Lockyer-Bratton's FCT CED specimens showing the shear strain maps immediately a) before, b) during and c) after delamination of, along with the associated stress-strain curve [1].*

In order to determine the point at which delamination began to occur, Lockyer-Bratton initially tried to mark the point where a visual crack can be seen during the test and use the stress associated with that point, shown by the red star labeled $\sigma_c^{Visual}$ in Figure 2-11. However, using the stress associated with that point gave interfacial toughness values that were significantly higher than expected. Instead, a method was developed where Lockyer-Bratton used DIC to identify a point of critical local shear strain that could be associated with the start of steady-state crack growth, as shown in Figure 2-11 b), and the stress associated with that point was used to measure interfacial

toughness. Lockyer-Bratton then tested a range of samples thermally cycled to various points in their thermal lifetime. Using this DIC method in conjunction with Equation 2-10 and 2-11, along with FEA to account for interfacial friction and the presence of TBC layers, Lockyer-Bratton was able to develop a curve showing how interfacial toughness decreases with percentage of FCT lifetime for GE's standard commercial TBC system, seen in Figure 2-12.
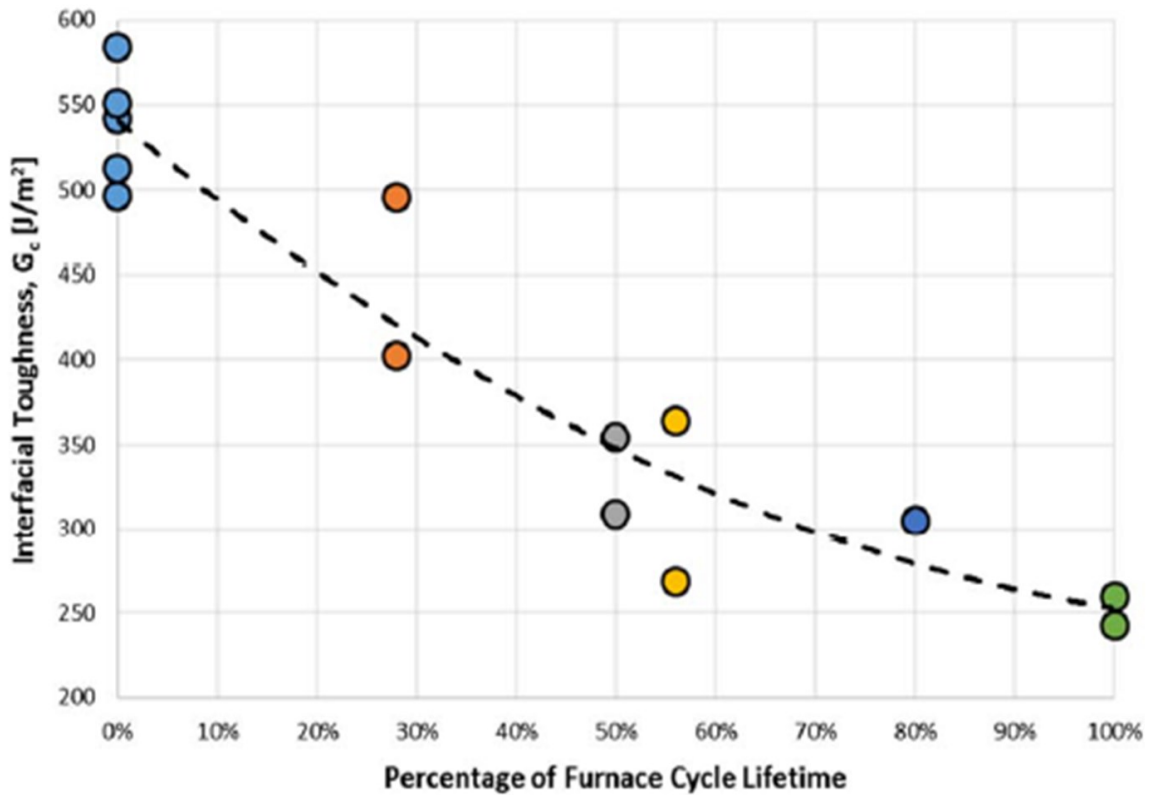


*Figure 2-12: Plot of interfacial toughness against percentage of thermal cycle lifetime for GE's standard commercial TBC system, developed by Lockyer-Bratton [1].*

For the "as-deposited" set of specimens Lockyer-Bratton measured an average interfacial toughness of 537 J/m$^2$, and that value dropped down to 252 J/m$^2$ for samples furnace cycled to 100% of their nominal FCT life, which corresponds to an interfacial toughness decrease of around ~55% [1]. This noticeable drop in interfacial toughness as a function of furnace cycle lifetime,

combined with the small scatter in the measured values at a given lifetime, confirmed both the efficacy and value of this novel test in measuring Mode II interfacial toughness.

As mentioned in Section 1.4.1, one of the purposes of this work was to understand whether phase angle impacts interfacial toughness. Figure 2-13 below shows of interfacial toughness measurements from various sources for "as-deposited" TBC systems plotted against the phase angle of the test used, with the results from this CED testing included.



The equation on the plot reads:

$$G_c = G_{I,c}\{1 + \tan^2[(1-\lambda)(\phi - \phi_0)]\}$$

Legend:
- Compression Edge-Delamination (JHU) - [Current]
- Micro-Bending (JHU) - [Eberl et al., Acta Mat. (2011)]
- Indentation - [Beuth et al., Eng. Fracture Mech. (2000)]
- 4-Point Bend - [Thery et al, Acta Mat. (2007)]
- 4-Point Bend (JHU) - [Current]
- Buckling - [Evans et al., J Mech. And Phy. Of Sol. (2000)]
- Barb Tests - [Evans et al., Acta Mat. (2006)]
- Pushout Tests - [Evans et al., Acta Mat. (2007)]
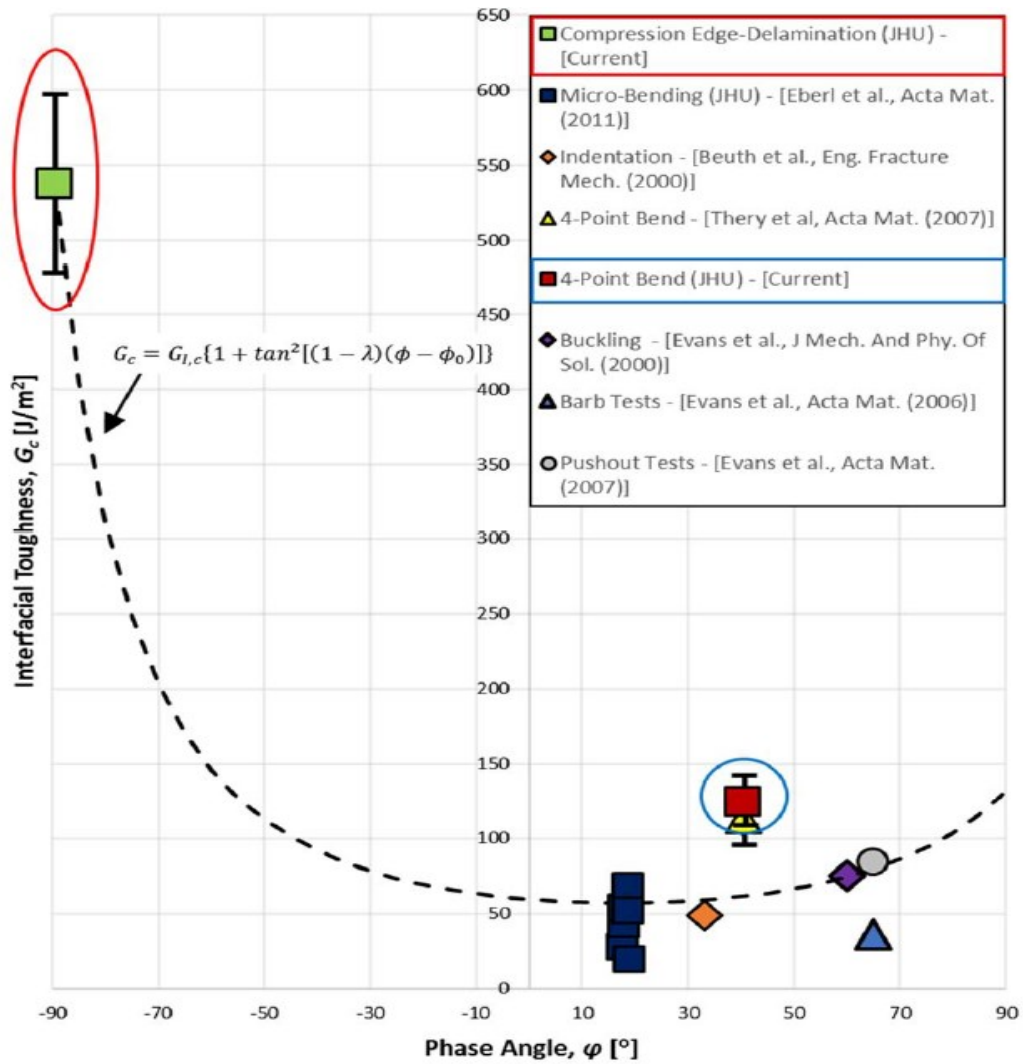
*Figure 2-13: Plot of interfacial toughness of TBC systems against the phase angle of the test used, highlighting the CED results from Lockyer-Bratton [1].*

It is clear from Figure 2-13 the dramatic effect phase angle has on the interfacial toughness of TBC systems. The results from Lockyer-Bratton's CED specimens are five to ten times higher than any other reported values. This clearly elucidates the need to measure interfacial toughness at the proper phase angle and with the proper loading conditions. This understanding motivated the work in Chapters 3 and 4 of this thesis, where CED tests were performed on a wide variety of EBPVD coatings to properly measure Mode II interfacial toughness of those systems.

### 2.2.4. A Finite Element Study of the CED Specimen

Changing the location and shape of the stiffener plates changes the geometry of the CED test, and thus modifies the loading conditions from those assumed by Hutchinson and Hutchinson. To account for these changes in the current study, FE modeling was performed using the engineering simulation software ANSYS Version 2020 R2. Models of both the original and modified CED specimens were built and loaded with the same axial loading conditions, matching those seen in the CED experiments. FE models of both CED specimens were meshed as one solid piece (ignoring interfaces and the TBC coating) and were uniaxially compressed in the $y$ direction. Experimental twins of these specimens were machined from 6061 aluminum and comparison between the FE simulations and experiments were facilitated by using the material properties for 6061 (E = 69 GPa, $\sigma_{yield}$ = 276 MPa, Poisson's Ratio $v$ = 0.33) in the FE simulations. Figure 2-14 shows the screenshots of the FE results for the $\varepsilon_{yy}$ strain distributions at a load of 16,200 N or a stress of 270 MPa, right before the onset of plasticity for each version of the CED geometry.
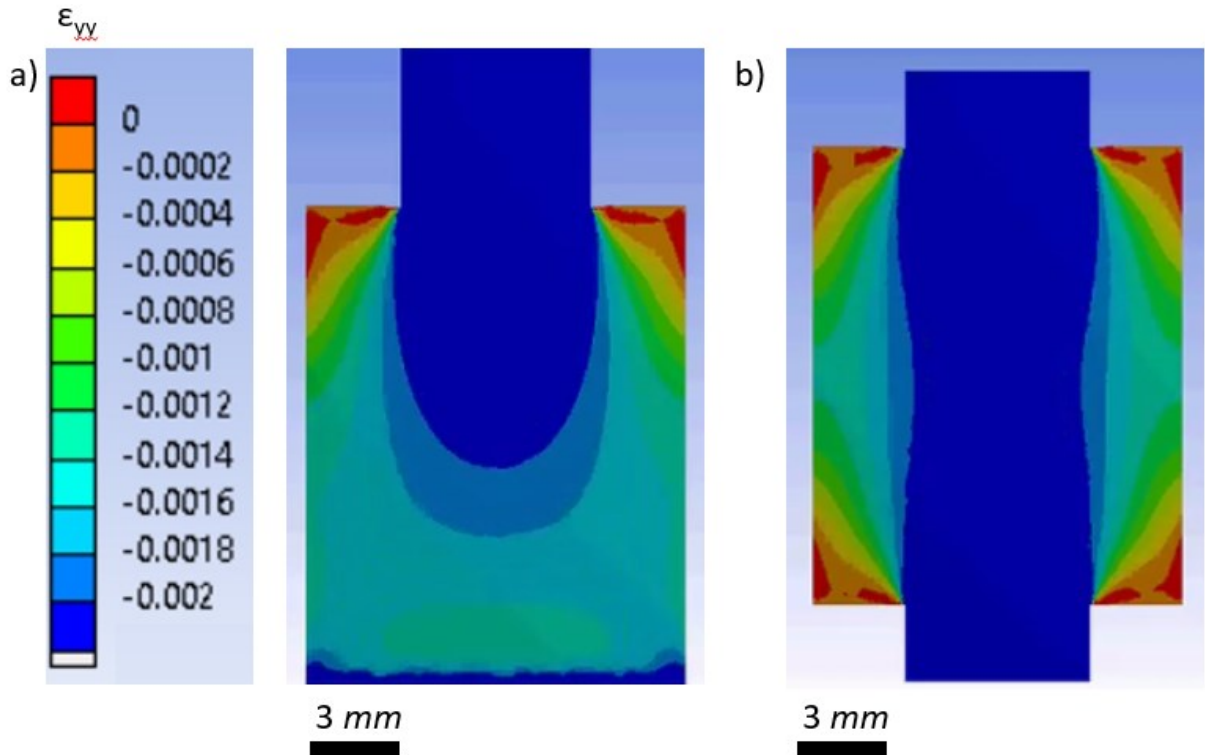
*Figure 2-14: FEM $\varepsilon_{yy}$ strain maps for a) the original CED geometry and b) the modified CED geometry where both are modeled as one piece with no interfaces.*

The most notable observation of these FE simulations is the reduced level of strain transfer from the substrate into the stiffener plate, even when the samples are modeled as one solid piece (as both samples are in Figure 2-14). In the original CED geometry, the strain is uniform and greatest in top portion of the substrate but trails off along the sides and bottom. In the modified CED geometry, the strain in the central region (nominally the region occupied by the substrate) is uniform at 0.2% $\varepsilon_{yy}$ strain but trails off along the sides. In neither case is the strain in the region that represents the stiffener plates equal to the strain in the substrate. In order to corroborate this result, the modified CED specimen EDM'd from 6061 aluminum was axially loaded to the same load/stress (16,200 N/270 MPa) as was used to make the ANSYS map. Figures 2-15 and 2-16 compares the $\varepsilon_{yy}$ strain map for the a) ANSYS model and b) the experimental specimen just before the onset of plasticity for the original and modified specimen respectively.
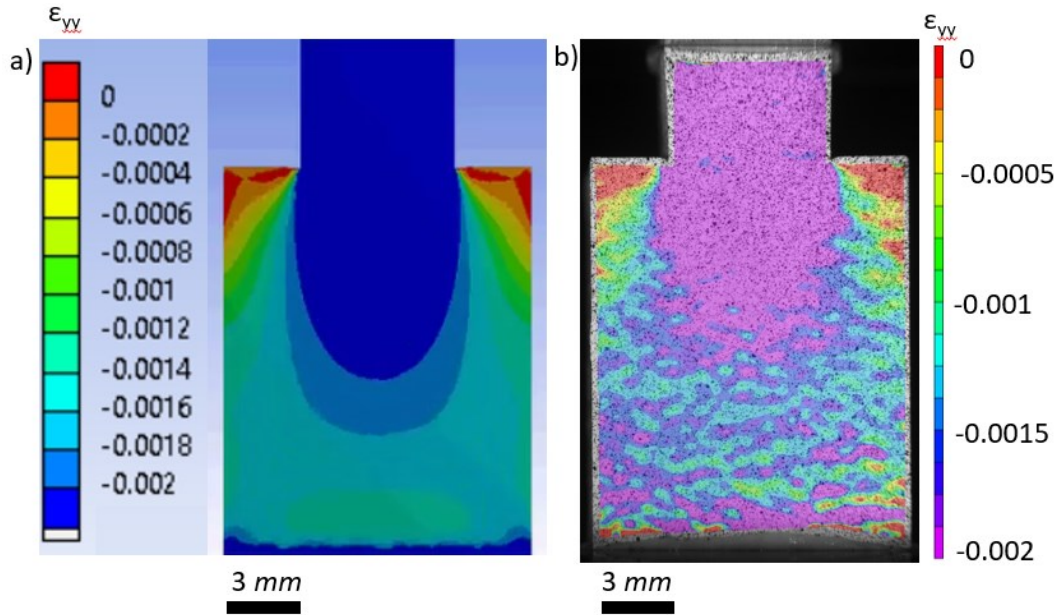
*Figure 2-15: FEM $\varepsilon_{yy}$ strain map for a) the original CED geometry compared to b) the strain map of the experimental original CED geometry.*
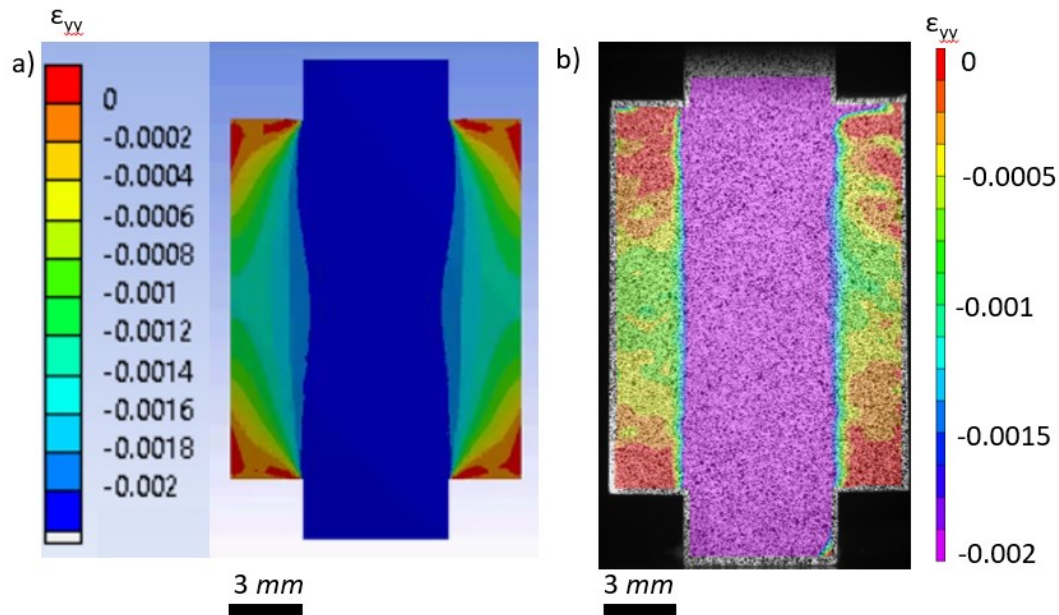


*Figure 2-16: FEM $\varepsilon_{yy}$ strain map for a) the modified CED geometry compared to b) the strain map of the experimental modified CED geometry.*

The agreement between the FEA and experimental results in Figures 2-15 and 2-16 confirms the lack of full strain transfer into the side regions, or what would be the stiffener plates in a

perfectly bonded CED specimen. This lack of full strain transfer, which is implied in the analytical solution that was used to derive the interfacial fracture toughness, suggests that Equation 2-11 will overestimate the interfacial fracture toughness. This is even more significant in the modified specimen as seen in Figure 2-16, since the strain transfer is reduced to a larger degree and thus will result in a larger overestimate of the interfacial fracture toughness. With reduced strain transfer, the applied stress must be greater to facilitate crack propagation. This calls into question the use of Equation 2-11 and favors the use of FE analysis to obtain the most accurate interfacial fracture toughness values from CED results.

2.3. Measuring Constitutive Properties of Disparate Coating Layers

An aspirational goal for jet engine manufacturers is to develop coating specification processes that are based on the material microstructures and/or attendant mechanical properties of the individual coating layers. Current topcoat specification processes only focus on the thickness of the coating, so reasonable next steps would involve cross-sectional observations of the columnar YSZ microstructure with SEM and measurement of the elastic response of the YSZ coatings. The studies and techniques that have been used to measure the elastic response of EBPVD YSZ topcoats have been reviewed as follows.

Instrumented indentation tests have frequently been used to measure topcoat "modulus", but these highly localized measurements have been shown to produce the largest scatter. The Young's modulus is an intrinsic material-specific property and is fundamentally different than the stiffness or compliance of a given structure, but the TBC literature uses these terms interchangeably. EBPVD topcoats have significant porosity and cracking that imparts highly desirable compliance in the topcoat, but the scale at which this compliance is accommodated must be considered.

Nanoindentation experiments are very attractive because sample preparation is easy, testing is highly automated and Dynamic Stiffness Measurement (DSM) heads now allow for rapid assessment of elastic modulus during each indent. However, the highly localized nature of nanoindentation cannot capture the more global elastic response of an EBPVD YSZ topcoat. To this point, reported in-plane modulus values for EBPVD YSZ coatings from indentation tests are widely inconsistent. Jang and Mastubara [13] reported in-plane modulus range for 4YSZ between 80-200 GPa. Vecchione et al. [12] measured a modulus value of 81 GPa, while Zotov et al. [14] and Wellman et al. [15] respective modulus values of 126 GPa and 130 GPa, which also fell in this wide range. Guo and Kagawa [16], however, measured and reported a much smaller modulus value of 53 GPa, highlighting the large scatter in this test method.

Compared to indentation tests, beam bending techniques measure a larger volume and can be more relevant to how coatings behave in service. However, the reported use of bending techniques to study EBPVD topcoat has been modest, variable and has not coalesced onto a common set of techniques. Much of the work has focused on the bond coat layer, including work by Jaya et al. [17] and Webler et al. [18] where focused-ion beam milling was used to create micro-cantilever beams. The same FIB milling technique was used to create micro-cantilever YSZ topcoats by Darnbrough et al. [19] and Liu et al. [20] measured modulus values between 60-90 GPa and 43 GPa respectively. However, like the indentation techniques, the FIB technique provides results on the micro-scale and different testing methods must be used to get macroscopic results.

Eberl et al. [21] developed a test in which modulus measurements can be obtained from bilayer microbeams of YSZ topcoat and a thin layer of bond coat. These microbeams were fabricated via a micro-EDM process where the substrate material was removed at various points along the circumference of a coated burner rig bar. The center of the beams were pulled on and modulus

values between 15-30 GPa were reported. Arai et al. [22] measured a topcoat modulus value of 41 GPa though a free bending vibration approach where Timoshenko beam theory was used to obtain modulus values via flexural vibrations produced by the impact of a hammer.

Recent attempts to measure topcoat modulus have focused on performing bend tests on free-standing topcoats specimens that are no longer attached to the substrate. Wang et al. [23] tested free-standing EBPVD 8YSZ topcoat beams using the 3-point bending technique and reported modulus values between 5-10 GPa. Pfeiffer et al. [24] tested free-standing as well as attached EBPVD YSZ topcoats using a 4-point bending method and measured a modulus value of 14 GPa. Wakui et al. [25, 26] also used a 4-point bend test to measure the compression-tension asymmetry of free-standing YSZ topcoats and measured modulus values of 16 GPa in compression and 6 GPa in tension.

In a recent study in the Hemker Group, Zhang [27] performed micro- to milli-scale experiments on free-standing and attached EBPVD topcoats in collaboration with P&W. The study was on a P&W NiCoCrAlY LPPS bond coat/7YSZ EBPVD topcoat system, and two sets of samples were studied: wedge-shaped burner rig bars with two flat surfaces machined onto them and a PW2000 2nd stage turbine vane. The bars and vane were cross-sectioned, polished to remove any damage. Various micro- and milli-scale bend tests were performed on cross sections of each.

Micro-EDM was used to cut small windows out of the substrate and bond coat at various points of interest around the circumference of the bars and the vanes. This resulted in doubly clamped bridge beams and cantilevers of YSZ (Figure 2-17 a)). These beams and cantilevers were pushed and pulled to reveal a tensile compression asymmetry and obtain representative values of topcoat modulus. The wedge bar specimens did not reveal an effect of substrate curvature on the topcoat modulus, but the modulus of the topcoat on the vane was found to be highly location dependent

and to vary with substrate curvature. From the micro-bend tests, Zhang measured topcoat modulus values of 50 GPa in compression and 30 GPa in tension on the straight edges of the wedge bar specimens. Modulus values of 47 GPa in compression and 28 GPa in tension were measured on the curved edges. On the vanes, the locations tested were of various radii of curvature on both the convex and concave side of the vane. The convex side had reported modulus values between 13 GPa and 20 GPa in tension, while values between 20 GPa and 29 GPa were reported in compression. The values reported on the concave side were notably higher however, with a tension modulus of 35 GPa and compression modulus of 60 GPa. These findings were interpreted as a clear indication that variations in processing parameters (power, temperature, curvature, line-of-sight angles, etc.) can have a significant influence on the topcoat microstructure and properties [27].

Wedge bar cross-sections were also fabricated into free-standing topcoats beam via acid etching of the underlying bond coat. These mm-scale free-standing topcoat beams were loaded in a 3-point bending (Figure 2-17 b)). For the 3-point bend tests of free-standing topcoats when loaded on the topcoat side, the modulus value of an "as-deposited" topcoat was reported to be between 58-61 GPa. When loaded on the bond coat side, the modulus dropped slightly and was reported to be between 52-54 GPa [27].
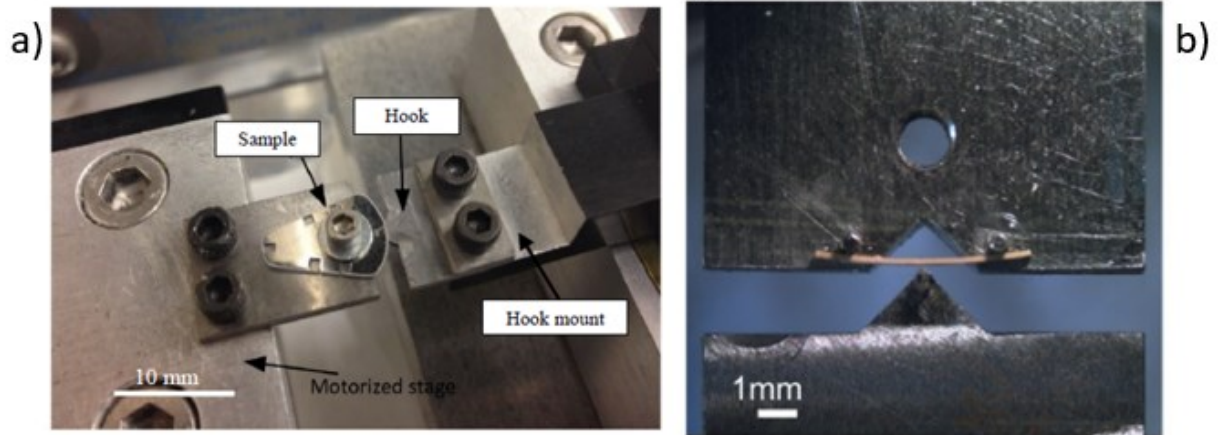
*Figure 2-17: Images showing a) the experimental setup for the micro-bend test of a wedge bar specimen and b) experimental setup for the 3-point bend of free-standing topcoats [27].*

### 2.3.1. 3-Point Bend Test

The 3-point bend test is similar to the previously mentioned 4-point bend test except there is only one inner loading point instead of two. Figure 2-18 below shows a schematic of a traditional 3-point bend test.
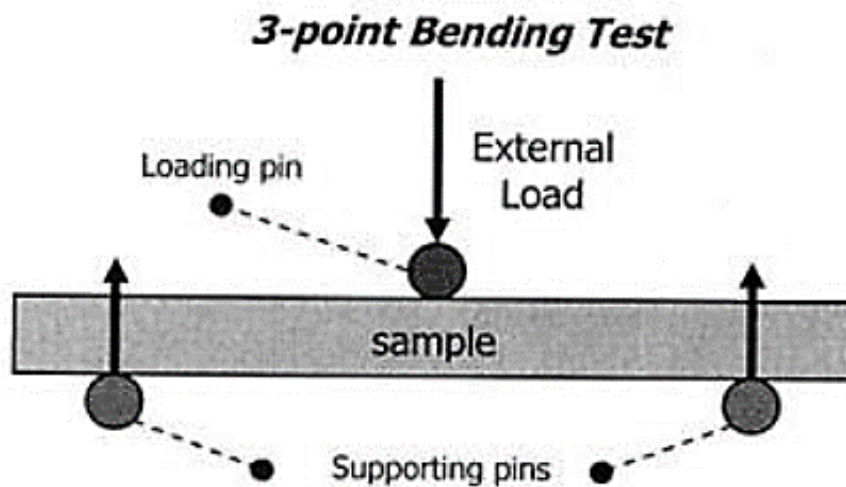


*Figure 2-18: Schematic of the traditional 3-point bend test [28].*

Compared to the 4-point bend test, a drawback of the 3-point bend test is that does not impart the same constant bending moment. However, since the goal of these tests is to measure modulus and not interfacial fracture toughness, this disadvantage is not an issue. Also, having only a single interior loading point makes the 3-point bend test a simpler test to run, and since the free-standing topcoats tested are fragile, the 3-point bend test is the preferred testing method for this study.

In order to solve for the modulus of the free-standing topcoats, Euler-Bernoulli beam bending assumptions can be made. Previous work by Zhang [27] compared Euler-Bernoulli solutions to the more rigorous Timoshenko beam bending theory [29] for these same free-standing topcoat specimens to determine if the Euler-Bernoulli assumption is valid. Due to the high aspect ratio of the topcoats, it was shown that the solutions from both theories converge such that the difference between the two is only 0.36%. By assuming small deflections and that the topcoats have a uniform, rectangular cross section that is loaded uniformly, Euler-Bernoulli solutions can be used to calculate the topcoat modulus. For a free-standing beam with no outer constraints, a uniform rectangular cross-section and is loaded at the midspan, Euler-Bernoulli solutions for beam deflection gives Equation 2-12.

*Equation 2-12*

$$W = \frac{FL^3}{48EI}$$

Where $W$ is the mid-span beam deflection, $F$ is the applied load, $L$ is the distance between the outer loading pins, $E$ is the elastic modulus of the topcoat, and $I$ is the 2nd moment of inertia, which for a rectangular cross-section is given by Equation 2-13.

*Equation 2-13*

$$I = \frac{bh^3}{12}$$

Where $b$ is the width of the topcoat and $h$ is the thickness of the topcoat. Using DIC during testing, the area around the loading pins can be imaged and deflection values can be obtained for the tested specimens. Combined with load data, a load-deflection curves can be created for each test, which can then be normalized by $b$ to get a normalized load-deflection curve. By normalizing this data, plugging Equation 2-13 into Equation 2-12 and rearranging the terms, Equation 2-14 is obtained.

*Equation 2-14*

$$E = \frac{KL^3}{4h^3}$$

Where $K$ is the slope of the normalized load-deflection curve. Chapter 5 details the specimen preparation, testing set-up and test parameters used for each 3-point bend specimen discussed in this study.

References:

[1]: Lockyer-Bratton, S., *Experimental measurements of thermal barrier coating interfacial fracture toughness as a function of mode-mix*. Ph.D. Thesis, Johns Hopkins University, 2016.

[2]: Hutchinson, R.G., Hutchinson, J.W., *Lifetime Assessment for Thermal Barrier Coatings: Tests for Measuring Mixed Mode Delamination Toughness.* Journal of the American Ceramic Society, 2011. **94**: p. s85-s95.

[3]: Lin, Z.X., et al., *In situ observation of fracture behavior of canine cortical bone under bending.* Materials Science and Engineering: C, 2016. **62**: p. 361-367.

[4]: Abdelhadi, O.M., L. Ladani, and J. Razmi, *Fracture toughness of bonds using interfacial stresses in four-point bending test.* Mechanics of Materials, 2011. **43**(12): p. 885-900.

[5]: Ključar, L., et al., *Effect of 4-point bending test procedure on crack propagation in thin film stacks.* Microelectronic Engineering, 2015. **137**: p. 59-63.

[6]: Fu, H., et al., *Plastic deformation behavior and bonding strength of an EBW joint between 9Cr-ODS and JLF-1 estimated by symmetric four-point bend tests combined with FEM analysis.* Fusion Engineering and Design, 2016. **102**: p. 88-93.

[7]: Kikuchi, S., et al., *Characterization of the hydroxyapatite layer formed by fine hydroxyapatite particle peening and its effect on the fatigue properties of commercially pure titanium under four-point bending.* Surface and Coatings Technology, 2016. **288**: p. 196-202.

[8]: Hutchinson, J.W., Suo, Z., *Mixed Mode Cracking in Layered Materials*, in *Advances in Applied Mechanics*, W.H. John and Y.W. Theodore, Editors. 1991, Elsevier. p. 63-191.

[9]: Charalambides, P.G., et al., *A Test Specimen for Determining the Fracture Resistance of Bimaterial Interfaces.* Journal of Applied Mechanics, 1989. **56**(1): p. 77-82.

[10]: Hofinger, I., Oechsner, M., Bahr, H.A. et al., *Modified four-point bending specimen for determining the interface fracture energy for thin, brittle layers.* International Journal of Fracture, 1998. **92**: p. 213-220.

[11]: Rice, J.R., *A Path Independent Integral and the Approximate Analysis of Strain Concentration by Notches and Cracks.* Journal of Applied Mechanics, 1968. **35**(2): p. 379-386.

[12]: Vecchione, N., Wasmer, K., Balint, D., Nikbin, K., *Characterization of EB-PVD yttrium-stabilised zirconia by nanoindentation*. Surface and Coatings Technology, 2009. **203**: p. 1743-1747.

[13]: Jang, B.K., Matsubara, H., *Influence of porosity on hardness and Young's modulus of nanoporous EB-PVD TBCs by nanoindentation*. Materials Letters, 2005. **59**: p. 3462-3466.

[14]: Zotov, N., Bartsch, M., Eggeler, G., *Thermal barrier coating systems—analysis of nanoindentation curves*. Surface and Coatings Technology, 2009. **203**: p. 2064-2072.

[15]:  Wellman, R., Dyer, A., *Nicholls, J., Nano and Micro indentation studies of bulk zirconia and EB PVD TBCs.* Surface and Coatings Technology, 2004. **176**: p. 253-260.

[16]: Guo, S., Kagawa, Y., *Effect of thermal exposure on hardness and Young's modulus of EB-PVD yttria-partially-stabilized zirconia thermal barrier coatings.* Ceramics International, 2006. **32**: p. 263-270.

[17]: Jaya, B. N., Jayaram, V. and Biswas, S. K., *A new method for fracture toughness determination of graded (Pt,Ni)Al bond coats by microbeam bend tests.* Philos. Mag., 2012. **92**: p. 3326–3345.

[18]: Webler, R., Krottenthaler, M., Neumeier, S., Durst, K. and Goken, M., *Local fracture toughness and residual stress measurements on NiAl bond coats by micro cantilever and FIB-based bar milling tests* Superalloys, 2012. p. 93-102.

[19]: Darnbrough, J. E., et al., *Micro-scale testing of ductile and brittle cantilever beam specimens in situ with a dual beam workstation.* Meas. Sci. Technol., 2013. **24**: p. 1-9.

[20]: Liu, D., Flewitt, P.E.J., *The Measurement of Mechanical Properties of Thermal Barrier Coatings by Micro-Cantilever Tests.* Key Engineering Materials, 2012. **525–526**: p. 13–16.

[21]: Eberl, C., Gianola, D. S., Wang, X., He, M. Y., Evans, A. G. and Hemker, K. J., *A method for in situ measurement of the elastic behaviour of a columnar thermal barrier coating.* Acta Mater., 2011. **59**: p. 3612–3620.

[22]: Arai, M., Kishimoto, K., *Estimation method of Young's modulus of thermal barrier coating layer based on free bending vibration.* J Soc Mater Sci, 2003. **52** (9): p. 1135-1139.

[23]: Wang, X., Tint, S., Chiu, M., Atkinson, A., *Stiffness of free-standing thermal barrier coating topcoats measured by bending tests.* Acta Materialia, 2012. **60**: p. 3247-3258.

[24]: Pfeiffer, C., Affeldt, E., Göken, M., *Miniaturized bend tests on partially stabilized EB-PVD ZrO$^2$ thermal barrier coatings.* Surface and Coatings Technology, 2011. **205**: p. 3245-3250.

[25]: Wakui, T., et al., *Strain dependent stiffness of plasma sprayed thermal barrier coatings.* Surface & Coatings, 2006. **200**: p. 4995-5002.

[26]: Wakui, T., et al., *Mechanical testing of thermally stressed materials with rough interfaces: Mechanically induced delamination cracking in thermal barrier composites.* Surface & Coatings, 2006. **200**: p. 5419-5426.

[27]: Zhang, B., *Experimental Characterization of Thermal Barrier Coatings Using Micro-Scale Bending Techniques.* Ph.D. Thesis, Johns Hopkins University, 2015.

[28]: Nagler, J., *Failure Mechanics of Multi Materials Laminated Systems Review Analysis-Based Project.* Book, 2013. Accessed: https://www.researchgate.net/figure/Schematic-of-flexure-tests-3-point-and-4-point-bending-test-36_fig2_331074946

[29]: Gere, J.M., Timoshenko, S., *Mechanics of Materials.* Book, 2001. p. 815-839.

**Chapter 3: Investigation of Gradient Thermal Exposure on TBC Interfacial Toughness**

This chapter focuses on the results of CED experiments performed on a GE commercial TBC after various exposures to thermal cycling. The previous work of Lockyer-Bratton [1] that involved CED specimens that had undergone various stages of furnace cycle testing (FCT) has been expanded by characterizing the interfacial toughness as a function of gradient thermal cycling. Extensions to blades pulled from service were also pursued. New protocols for CED testing needed to be developed to accommodate the buttons used for Jet Engine Thermal Shock (JETS) gradient cycling and the unique geometry of engine hardware. All coatings consisted of the same diffusion aluminide bond coat/8YSZ EBPVD topcoat TBC system and were provided by GE in both "as-deposited" and thermal cycled states. The sample preparation techniques prior to testing are reviewed, as well as the procedure used for CED testing. Loading curves for each test are presented, along with relevant DIC shear strain maps that facilitated crack tip tracking and identification of the critical stress associated with crack propagation. Analytical and FE methods were employed to calculate interfacial toughness, which is reported for various fractions of thermal cyclic life. SEM micrographs of specimen cross-sections and fracture surfaces were used to identify the delamination location and mechanism. The results collected in the current study provide a direct comparison for the work performed by Lockyer-Bratton [1] on the same GE TBC system at various stages of FCT testing.


3.1 JETS CED Specimen Preparation Procedure

Thermal gradient JETS testing at GE was done using 1 inch diameter buttons with the TBC deposited on one side. The buttons provided for the current study were coated with GE's standard ((Ni,Pt)Al) diffusion aluminide bond coat/8YSZ EBPVD topcoat TBC, and buttons were provided in the "as-deposited" state and after various stages of JETS testing. The buttons were cut into 10

mm x 6.5 mm x 3.2 mm CED specimens using a diamond wire saw at JHU and a high RPM semiconductor dicing saw at GE Research. The next preparation step was to trim the excess coating from the front surface of the JETS CED specimens. As mentioned in Section 2.2.3, Lockyer-Bratton modified the geometry of the CED test by moving the stiffener plates and coating away from the bottom edge of the sample, and instead positioned them so they covered the middle 75% of the substrate. This was done to avoid stress concentrations and premature delamination as a result from asymmetric loading that could occur if the coating or stiffener plates were not perfectly aligned with the substrate. As evidenced in Figure 2-4, which shows the coated JETS buttons along with their associated cut plans, the top surface of the JETS CED specimens were fully coated with topcoat extending to the edges. The topcoat was trimmed away from the top and bottom edge of CED specimens using an end mill with a diamond sintered dental tool from Starlite Dental Instruments. On both ends, 1.25 mm of coating was cut back at a depth of 175 µm, resulting in the removal of the entire topcoat and bond coat with no damage to the substrate. The cutting process was stepped down in intervals of 25.4 µm (0.001") to avoid chipping. Figure 3-1 shows: a) "early-in-life", b) "mid-life" and c) "late-in-life" JETS CED specimens with the excess coating removed.
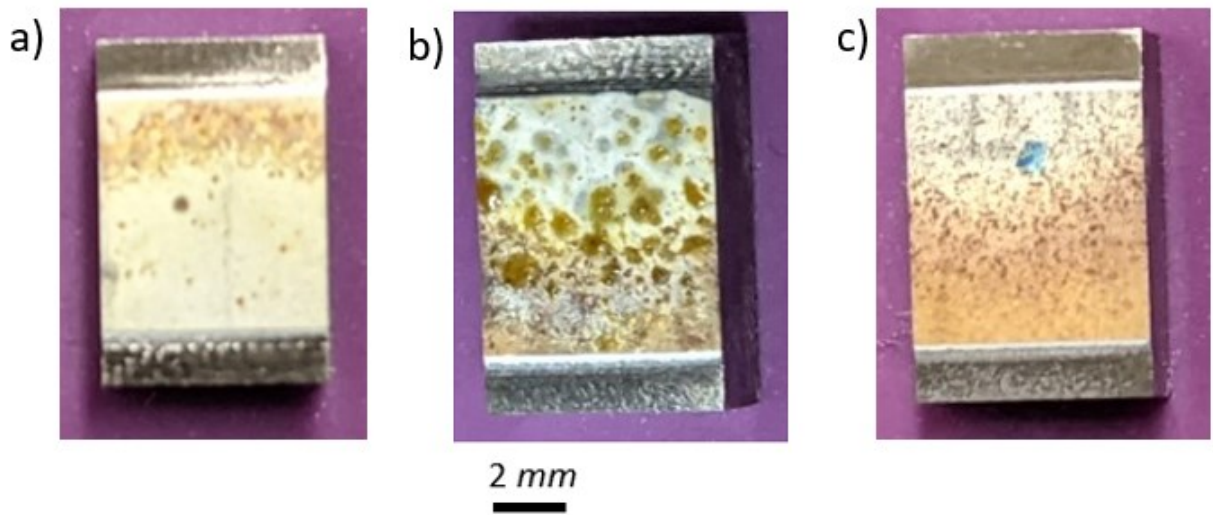
*Figure 3-1: Image of a) "early-in-life", b) "mid-life" and c) "late-in-life" JETS CED specimens with the excess coating removed on each side of the sample.*

Once the excess topcoat was removed, the next step involved creating a pre-crack at the bond coat/topcoat interface. Lockyer-Bratton [1] pre-cracked his original CED specimens by acid etching the bond coat. For the work in this thesis, the JETS buttons had $h = 1.6$ mm, which meant the cracks had to be at least 2.4 mm long to avoid end effects when measuring the critical stress associated with crack propagation. For the current study, multiple pre-cracking methods were considered including the use of femtosecond laser machining to selectively remove the bond coat. Preliminary attempts with the laser were made, but issues with laser reliability and difficulty in precise positioning of the laser beam resulted in this being abandoned. Parallel discussions with Potomac Photonics explored the use of traditional laser machining but it was determined that removing the bond coat via laser machining was prohibitively slow. In the end, the acid etching technique developed by Lockyer-Bratton was employed in this work. CED specimens were placed into a bath of 35% $H_2PO_4$, 30% HCl and 35% $H_2O$ and positioned such that 2.5 mm of bond coat was submerged in the acid. After one hour the sample was removed from the solution, placed in a

neutralizing solution of baking soda and water, and then cleaned in isopropyl alcohol in an ultrasonic bath for 10 minutes. Figure 3-2 shows an image of a CED specimen in the acid bath.
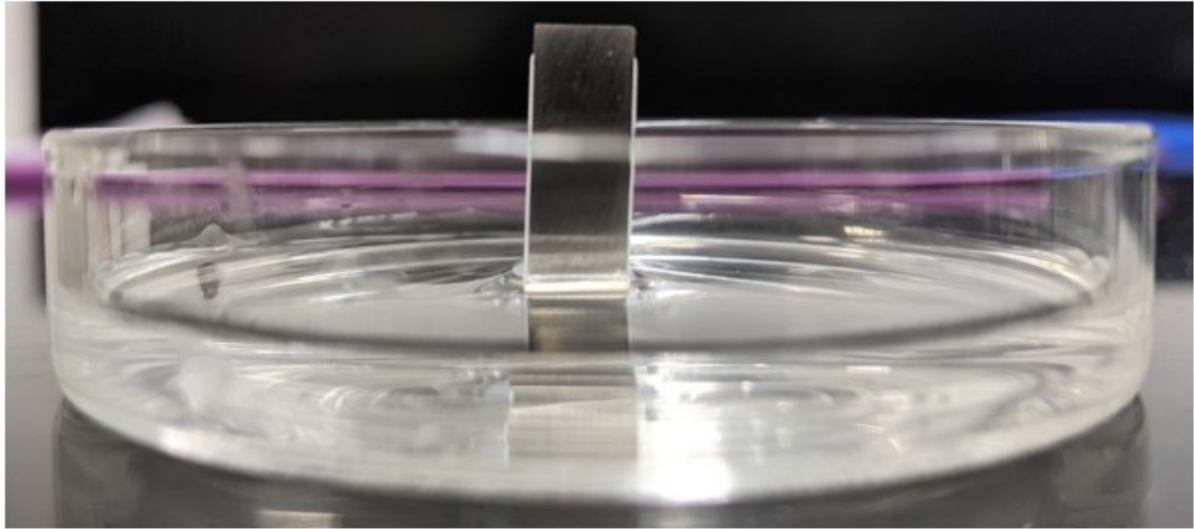


4 mm

*Figure 3-2: Image of a CED sample (without stiffener plates) that is partially submerged in 35H$_2$PO$_4$-30HCl-35H$_2$O acid bath for bond coat etching. The TBC topcoats are the white layers on either side of the sample.*

Bond coat removal was monitored with optical microscopy, and the sample was placed in the acid solution for two hours. In addition to initiating a starter crack, the acid etching also removed any excess bond coat that remained after the topcoat removal process. Figure 3-3 is an SEM collage of a CED button showing the effect that the acid etching had on the bond coat layer and the fact that the etchant did not alter the topcoat.
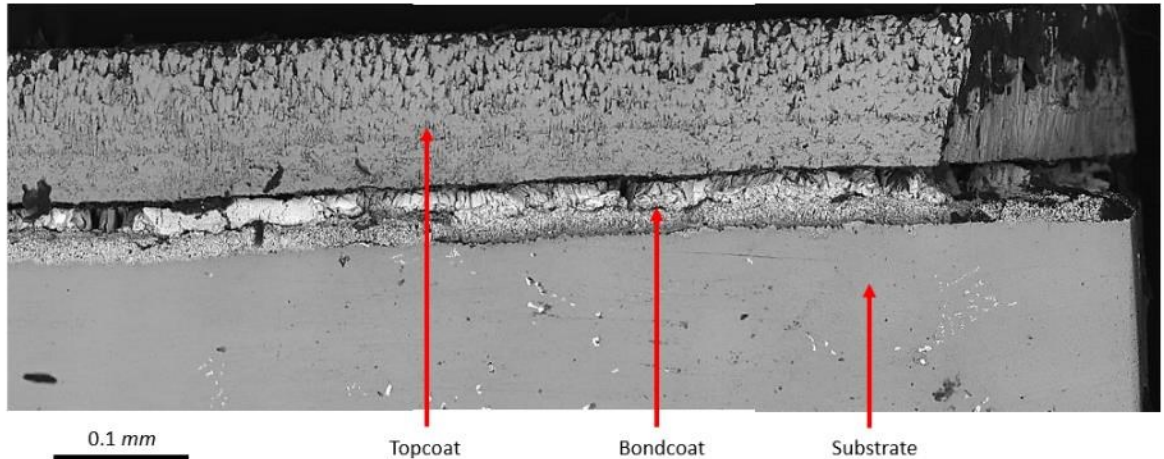
*Figure 3-3: Set of SEM images stitched together showing the effect of acid etching on the bond coat layer of the JETS CED specimens.*

Following the acid etching process, the next sample preparation step was to adhere the stiffener plates to the topcoat. The stiffener plates were used to increase the amount of strain energy in the system to ensure that delamination of the coating occurred before plastic yielding of the substrate. The stiffener plates had dimensions $L = 7.5$ mm, $w = 6.5$ mm, and $h = 1.6$ mm and were made from the same single crystal René N5 as the substrate. They needed to be adhered to the coating by a material that would not infiltrate the columnar gaps of the topcoat but was strong enough that the adhesive and the adhesive/topcoat and adhesive/stiffener plate interfaces had a higher shear strength than the TBC's topcoat/bond coat interface. Araldite 2011 was chosen due to its high viscosity (which reduced infiltration into the columnar gaps), its high shear strength, and its previous success in other studies [2, 3]. Equal parts of Araldite 2011 epoxy and curing agent were applied in a thin layer to the stiffener plate via a mixing gun. A glass slide was used to evenly spread a thin layer of epoxy over the surface of the stiffener plate. A wet film thickness gauge was used to ensure that the thickness of the epoxy was ~ 100 μm thick, the manufacturer recommended thickness [4]. The stiffener plate was placed on the coating surface and aligned with two custom 3D printed fixture guides in order to fit the stiffener plates perfectly flush with the coating. The

samples were left to cure for 24 hours in a desiccator pumped to 60 PSI. Although only one side of the JETS CED specimen was coated with TBC, stiffener plates were adhered to both sides of the specimen in order to keep the sample geometry symmetric. Figure 3-4 shows an image of a JETS CED specimen with an epoxy covered stiffener plate placed on top of the coating surface with the custom 3D printed fixtures prior to curing in the desiccator.



4 mm
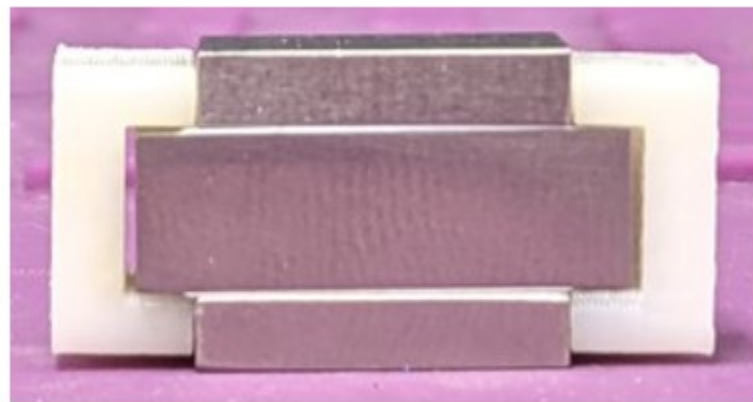
*Figure 3-4: Image of a CED specimen placed inside of the two 3D printed guide fixtures, along with the stiffener plates adhered to the side surfaces with epoxy.*

With the stiffener plates in place, the front and back surfaces of the CED specimen and stiffener plates were polished with SiC polishing paper to 1200 grit (P-4000) using an Allied Technology Tech-Prep 8 automatic polisher. Polishing these surfaces after the stiffener plates were adhered ensured that the stiffener plates were fully in-plane with the substrate, which facilitated better DIC as the substrate and stiffener plates were in the same imaging plane. The polished surfaces also provided better adherence when applying the DIC speckle pattern. The top and bottom loading surfaces of the CED specimen were then polished in the same manner, which ensured that the loading surfaces were both flat and parallel to each other.

The final sample preparation step before testing involved the application of a speckle pattern to one side of the CED specimen. DIC was used to monitor specimen displacements (and strain)

during the test, and to identify when TBC delamination occurred. The full details of the DIC process and how it was used in this thesis are detailed in Section 3.1.1. Images of the speckled surface taken by a camera facilitated direct tracking of the changes in the relative position of these markers over the course of the test. The in-plane displacement values were then used to obtain in-plane strain values. One of the most common ways to apply a speckle pattern, and the method used in this work, is by applying paint to the sample surface. An even and thin layer of white matte spray paint was applied to the specimen surface, and when this layer dried an Iwata CM-C airbrush sprayed at 80 PSI was used to apply a black speckle pattern with an average speckle size of ~ 50 µm. This procedure follows the work of LePage [5] who showed that the ideal speckle surface was black paint on a white background to reduce aliasing of the speckles and improve DIC tracking. Following the application of the speckle pattern, the JETS CED specimens were ready for testing

The JETS CED specimens were tested using an MTS servo-hydraulic machine with a 500 kN load cell. Details about the machine and control software can be found in Appendix B. The specimens were compressed under displacement control, with an applied displacement rate of $\dot{\delta}$ = .001 $mm/s$, which corresponds to a quasi-static strain rate of $\dot{\varepsilon}$ = 7 x $10^{-5}$ $\frac{1}{s}$. Both load and displacement data were logged at a rate of 10 Hz, or 10 data points every second. For imaging purposes, a PixelLINK PL-B781U black and white 6.6 MP camera with an Edmund Optics MMS Imaging Lens R-1 rear assembly and OBJ-11 front objective mounted on a tripod was used to take 1 image every second with the PixelLINK Capture OEM Software. DIC was used to obtain strain data for the JETS CED specimens from these images, and the process for this is briefly explained below.

### 3.1.1 Digital Image Correlation (DIC)

For all experiments performed in this study, non-contact DIC was used to make strain maps of the CED specimen and stiffener plates and to monitor shear displacements along the coating interface. First used by Sutton at the University of South Carolina in 1985 [6], DIC is an optical method to measure deformation in-situ that involves taking and comparing images of the tested specimen over the course of the experiment. Relative pixel intensities from these images are referenced back to the original image to generate displacement values, which are then used for strain calculations. The DIC analysis process consists of defining a recognizable speckle pattern (collection of dots) on the reference image, choosing subsets of this pattern to track, defining the center of the subsets from which displacements will be calculated, assigning a step size or distance between subset centers, matching the deformed subsets to the reference subsets and finally calculating the displacements. Figure 3-5 shows a schematic of this process.
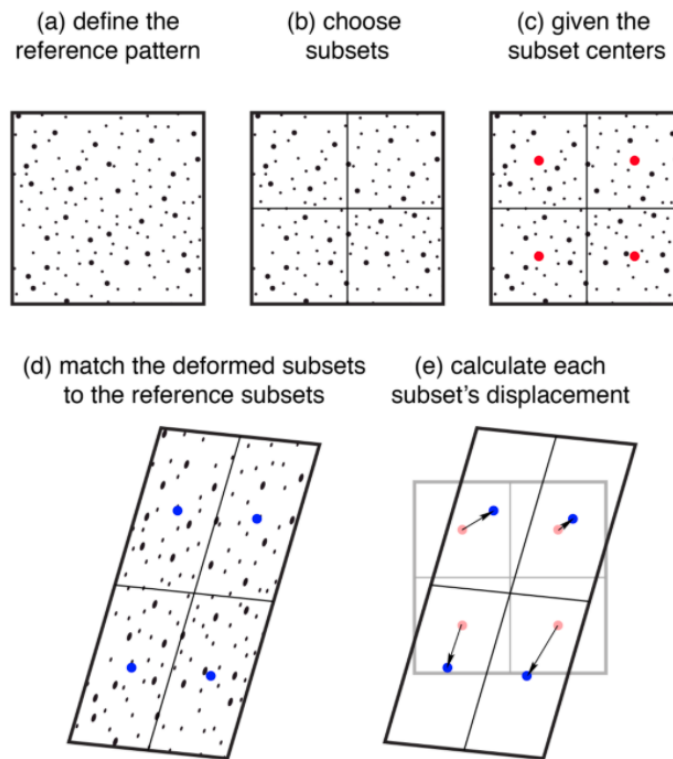


*Figure 3-5: Simplified schematic of the DIC analysis process [7].*

DIC was chosen over traditional contact strain measurement methods, such as the use of strain gauges, and other non-contact methods because DIC allows for the easy generation of 2D in-plane strain maps. For the CED tests, these strain maps can be used to track the local shear strain in the interface and especially at the crack tip, thus making it possible to identify the critical applied stress associated with crack growth. DIC also allows for high spatial resolution capable of resolving local variations in strain across the sample surface, as well as full-field displacement/strain measurement capabilities with the appropriate choices of imaging lens system.

For all the experiments conducted in this study, DIC was performed using the commercial software VIC-2D from Correlated Solutions. For the JETS CED tests, a subset size of 31x31 pixels was chosen for each test along with a step size of 5 pixels. Best practices for quality DIC [7] indicate that each speckle should be at least 3x3 pixels to avoid aliasing [8] and a maximum of 7x7 speckles to ensure a high density of DIC points [9]. With the PixelLINK camera setup, the images taken had a pixel size of 13 µm and an average speckle size ~ 50 µm corresponding to an average of 4 pixels per speckle, which fell within the range specified for high-quality DIC.

The use of VIC 2D served two purposes in this study. One was to measure uniaxial strain of the substrate in the $y$ loading direction to develop stress-strain curves for each test. The second was the fact that VIC 2D allowed for the easy creation of shear strain maps that could be overlayed on the sample surface during analysis. To calculate the load associated with crack propagation, Lockyer-Bratton used DIC to find the point at which a critical shear strain value was reached and used the load associated with that image to calculate interfacial toughness. The same method was used in this study to standardize selection of the critical stress. It is important to note that since only one side of the JETS buttons were coated with TBC, only the coated side of the specimen was used to determine the point of critical stress and any shear strain that developed in the glue of

the uncoated side was ignored. Shear strain maps were created using VIC 2D and the increase of

the shear strain at the substrate/stiffener plate interface was monitored over the course of the test.

Looking at the shear strain maps alone was not sufficient for determining the critical stress since

the shear strain maps are dominated by the viscoelastic strain of the glue which is not associated

with TBC crack growth. As a result, a 150 µm wide box starting from the edge of the substrate

was overlayed along the length of the coated interface and shear strain values were obtained from

this box. The TBC systems tested in this thesis were ~200-300 µm thick, so this ensured that the

shear strain values measured were from the TBC itself and not the epoxy. Figure 3-6 shows a

magnified schematic of a CED specimen at the top right interface along with the box used to

measure shear strain values.
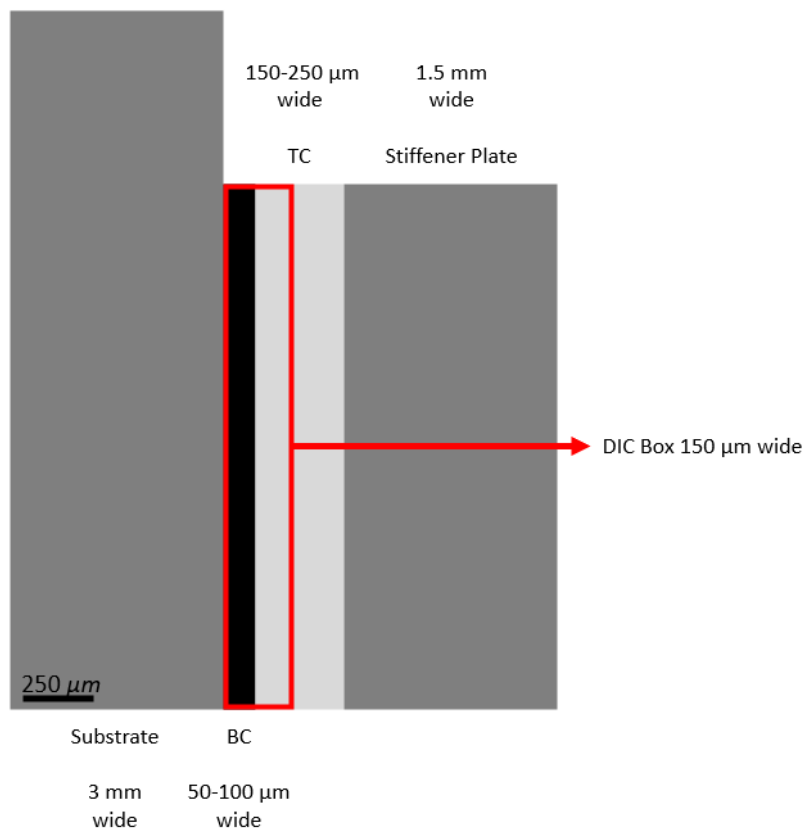


*Figure 3-6: Magnified schematic of the top right corner of a CED specimen showing the method used to measure shear strain via DIC. A 150 µm wide box (shown in red) was overlayed down the length of the coated substrate/stiffener plate interface such that it only contained the bond coat (black) and topcoat (light grey). Shear strain measurements were taken from this box to and used to identify the point associated with crack growth.*

Using this method, profiles of the shear strain along the coated substrate/stiffener plate interface were developed. As previously mentioned, a crack length of at least 1.5*$h$, which was 2.5 mm in the JETS specimens or 1/3$^{rd}$ the length of the stiffener plate, was needed to ensure steady-state crack growth. From the set of CED tests performed in this study, as well as the work performed by Lockyer-Bratton, it was seen delamination tended to occur around a shear strain value of 1%. To be consistent, the criteria was set that the first image at which the absolute value of the shear strain reached at least 1%, at a distance of at least 2.5 mm away from either the top or bottom edge of the stiffener plate, was determined to be the point associated with crack growth. The stress at this point was taken to be the stress associated with crack growth and used to calculate interfacial toughness. Figure 3-7 shows a shear strain profile plot for an "as-deposited" JETS specimen, JETS CED specimen #1 (the stress-strain curve for which is shown in Figure 3-8).
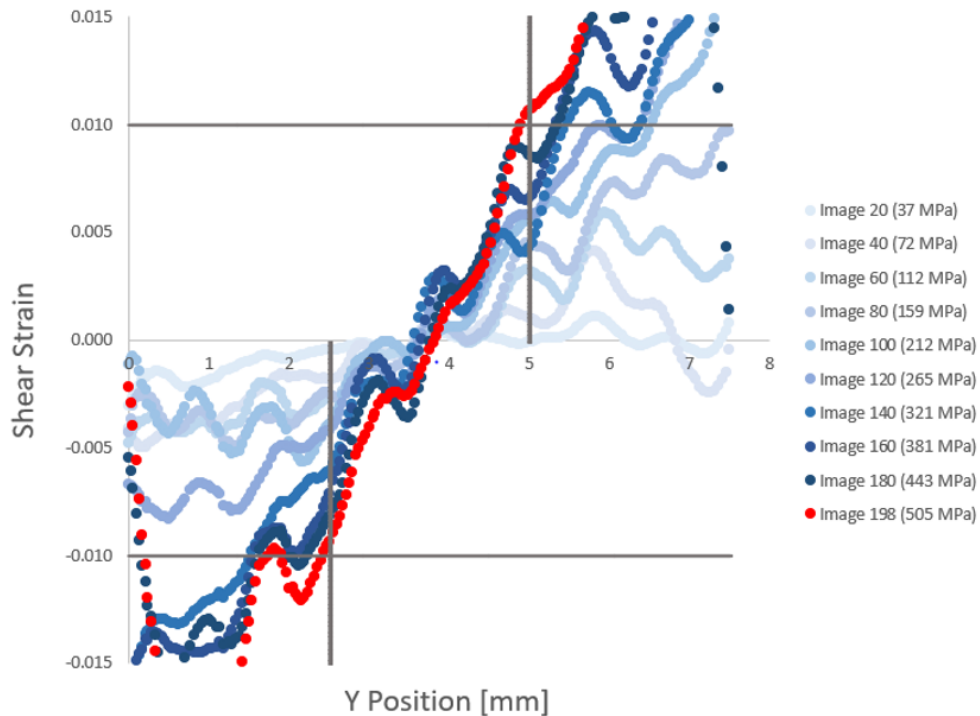


*Figure 3-7: Plots of shear strain along the coated interface between the substrate and stiffener for an "as-deposited" specimen, JETS CED specimen #1. Each curve represents an image from this test, while the gray lines represent the critical shear strain and length values. The red curve (Image 198) was the first to cross either critical shear strain line before the length value line, and thus the stress at this point (505 MPa) was determined to be the stress associated with crack growth.*

Each curve shown in Figure 3-7 represents the shear strain value along the coated interface between the substrate and stiffener at a different image during the test. The "Y Position" represents the position along the interface in mm measured from the bottom of the stiffener plate, where 0 mm is the bottom of the stiffener plate and 7.5 mm is the top. Gray lines were plotted along the relevant shear strain values ($\varepsilon_{xy} = \pm 1\%$) and length values (2.5 mm and 5 mm). The first image that had its curve intersect either the positive or negative 1% shear value gray line before the corresponding length value gray line was taken as the relevant point. In Figure 3-7 this is the red curve (Image 198), as it crosses the positive 1% gray line before the 5 mm gray line. The stress at this point was 505 MPa and determined to be the critical stress associated with crack growth. This process was repeated for each of the specimens tested.

## 3.2  JETS CED Results

Fifteen JETS CED specimens were tested including ten "as-deposited" samples, two "early-in-life" samples, two "mid-life" samples and one "late-in-life" sample. Figures 3-8 through 3-22 show a) the shear strain profile plots of each test for the image where the stress associated with crack growth was determined, along with image immediately preceding it and b) the stress-strain curves for each specimen, along with a callout (star) of critical stress associated with crack growth. The stresses are obtained by dividing the applied load by the cross-sectional area of the substrate, while the strain values are the DIC values for $\varepsilon_{yy}$ in the substrate. The VIC 2D shear strain map ($\varepsilon_{xy}$) corresponding to the critical stress for crack growth is also shown. The coated side of the JETS CED specimen is labelled as the "TBC-side" in each image and is always on the right side.
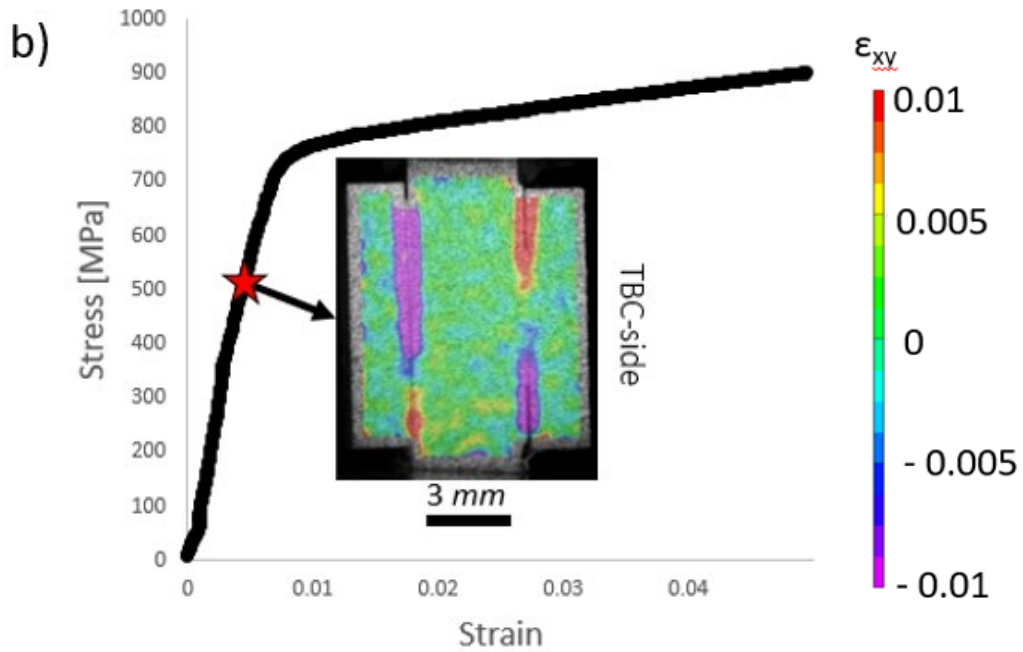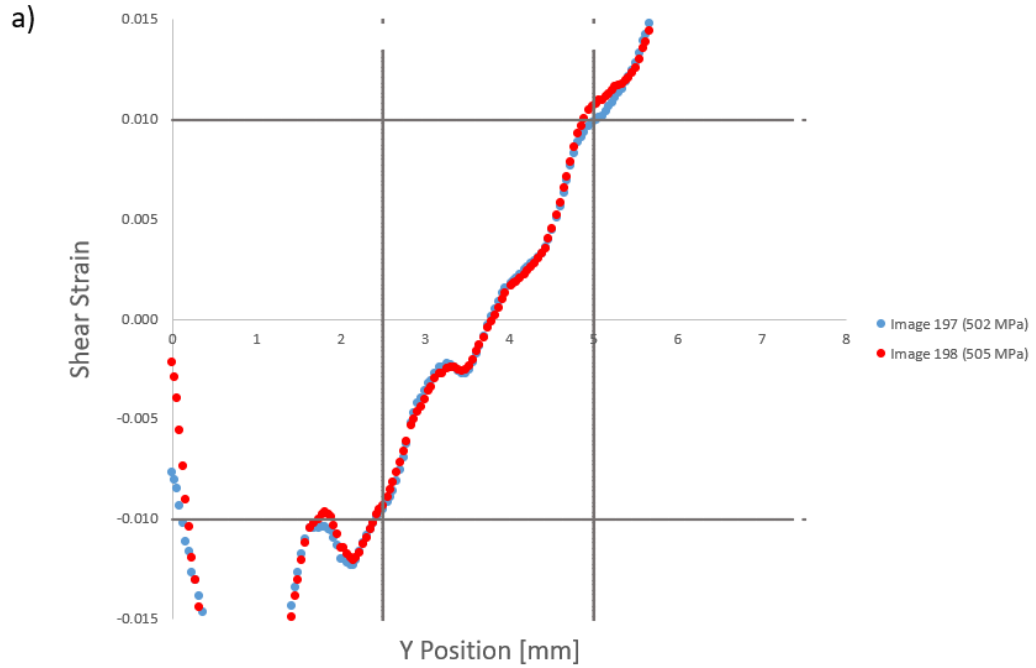
*Figure 3-8: Shown in a): Shear strain profile plot for an "as-deposited" (0% thermal gradient cycling) JETS CED specimen #1. The red curve marks the image were the criteria for critical stress associated with crack growth was met. Shown in b): Stress-strain plot for the specimen with the critical stress associated with crack growth (505 MPa) marked by a red star, with the shear strain map of the sample shown as well.*
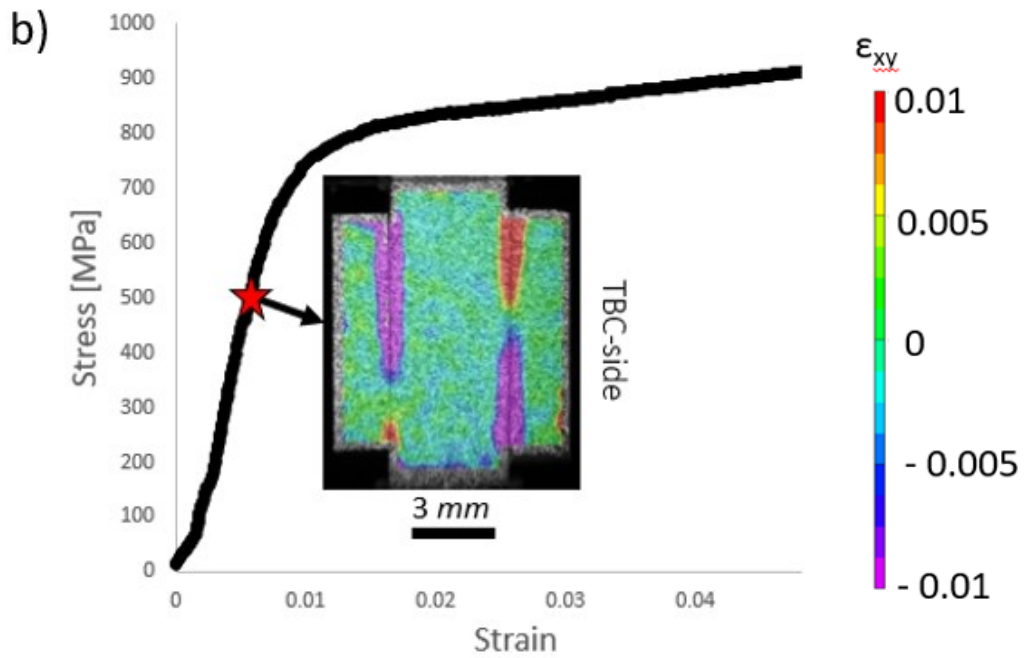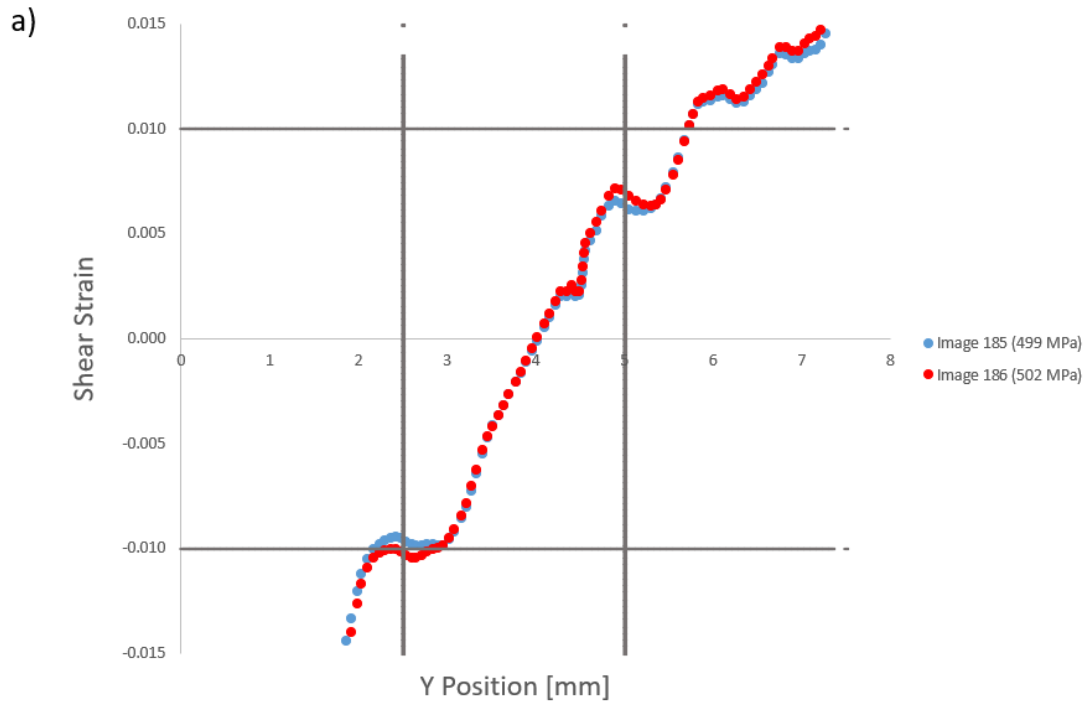
*Figure 3-9: Shown in a): Shear strain profile plot for an "as-deposited" (0% thermal gradient cycling) JETS CED specimen #2. The red curve marks the image were the criteria for critical stress associated with crack growth was met. Shown in b): Stress-strain plot for the specimen with the critical stress associated with crack growth (502 MPa) marked by a red star, with the shear strain map of the sample shown as well.*
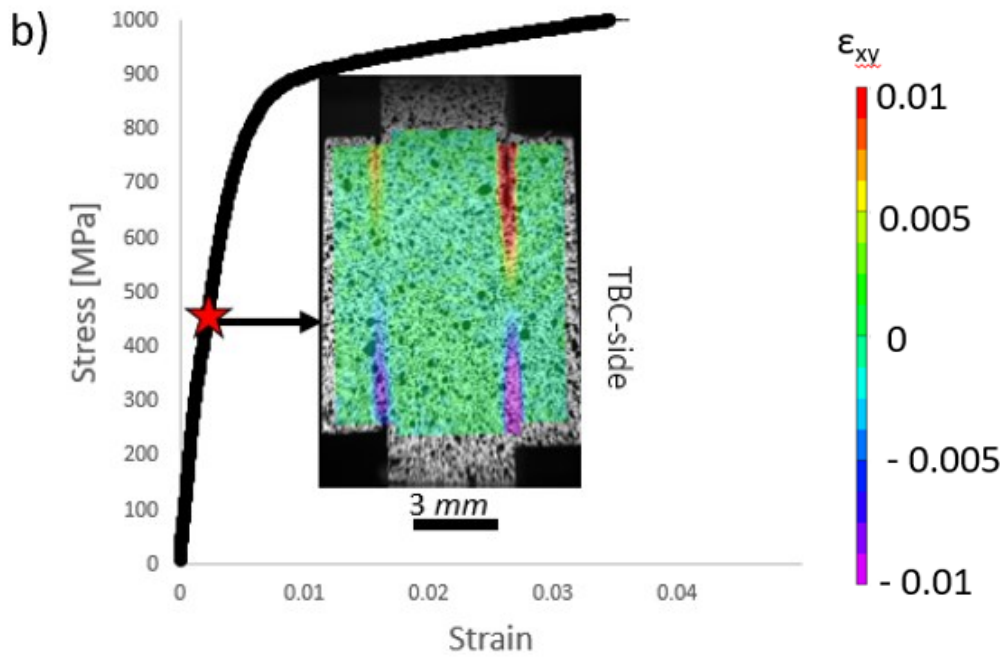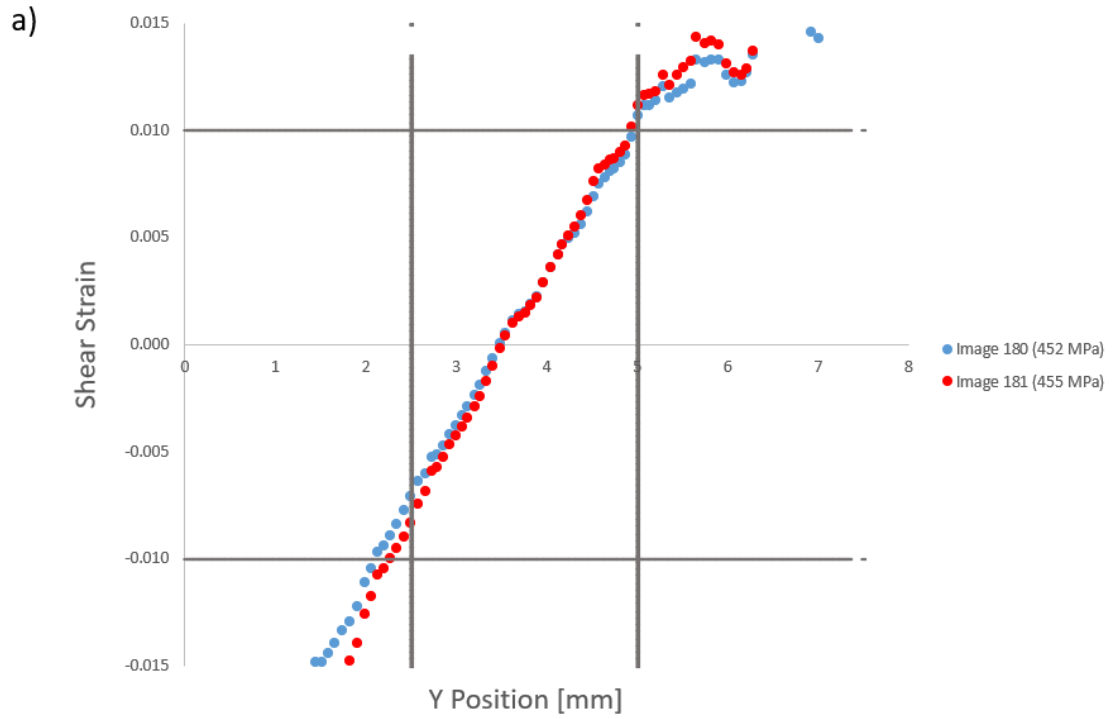
*Figure 3-10: Shown in a): Shear strain profile plot for an "as-deposited" (0% thermal gradient cycling) JETS CED specimen #3. The red curve marks the image were the criteria for critical stress associated with crack growth was met. Shown in b): Stress-strain plot for the specimen with the critical stress associated with crack growth (455 MPa) marked by a red star, with the shear strain map of the sample shown as well.*
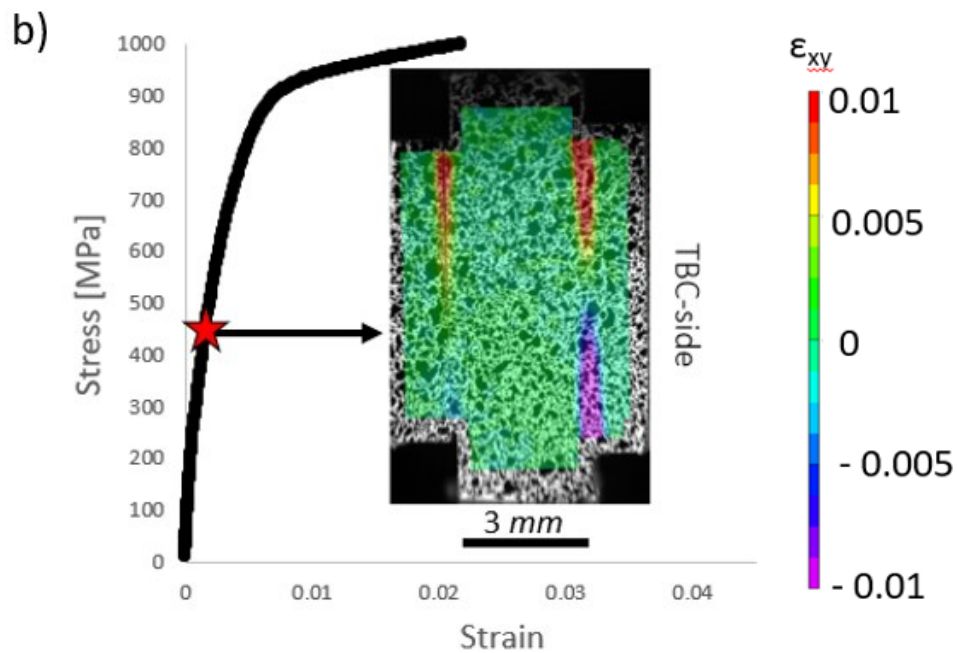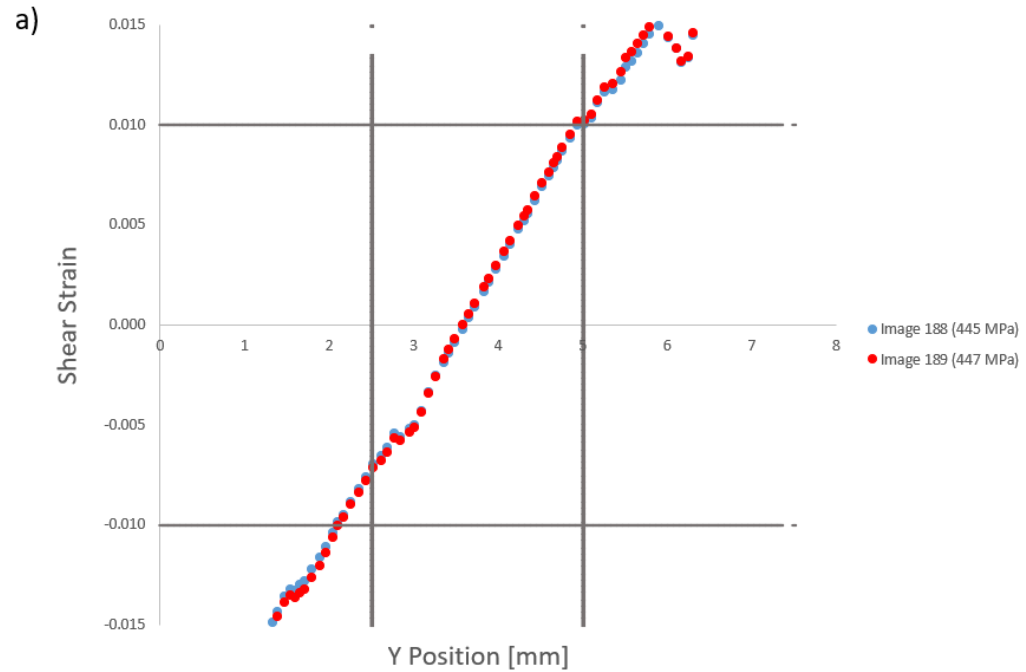
*Figure 3-11: Shown in a): Shear strain profile plot for an "as-deposited" (0% thermal gradient cycling) JETS CED specimen #4. The red curve marks the image were the criteria for critical stress associated with crack growth was met. Shown in b): Stress-strain plot for the specimen with the critical stress associated with crack growth (447 MPa) marked by a red star, with the shear strain map of the sample shown as well.*
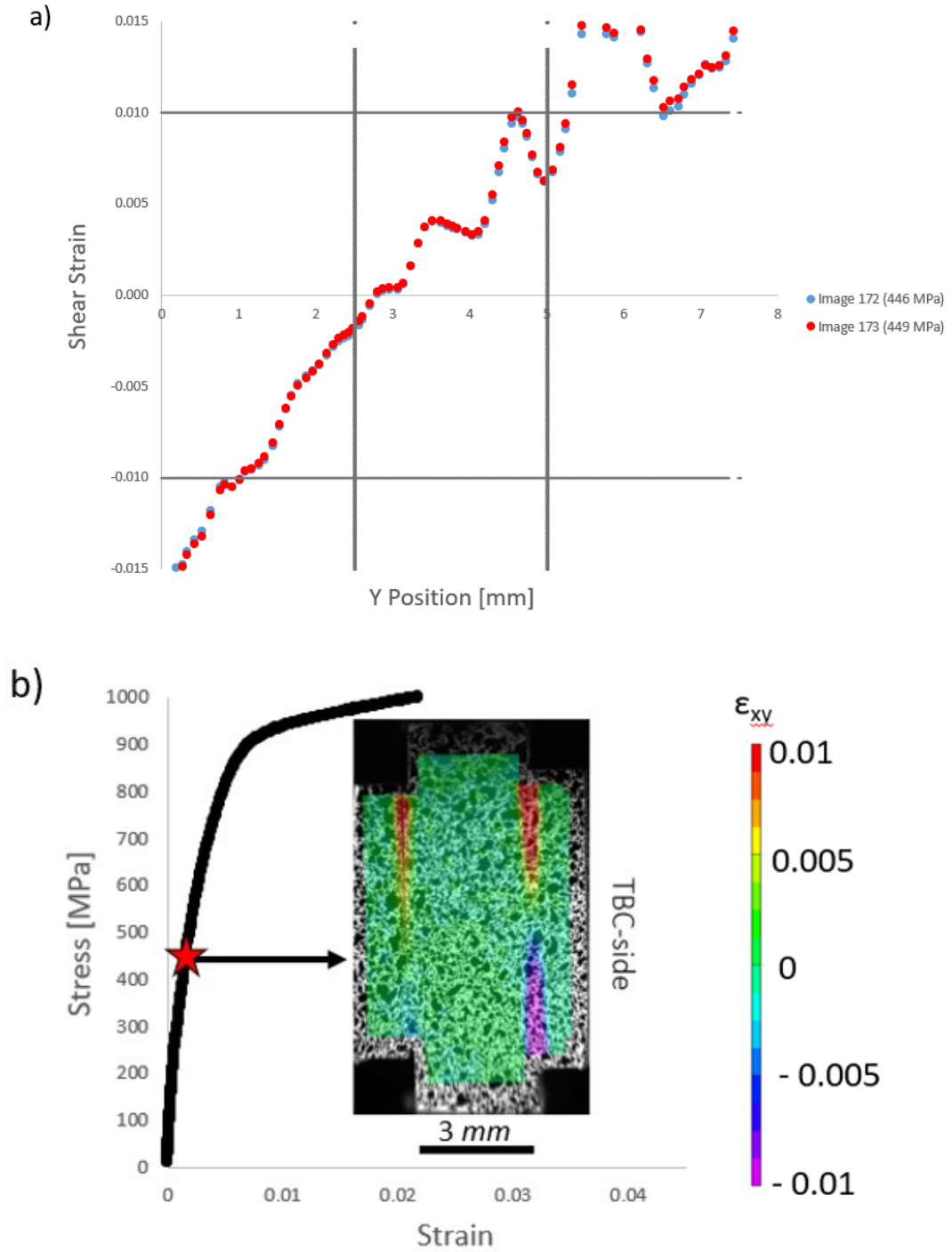
*Figure 3-12: Shown in a): Shear strain profile plot for an "as-deposited" (0% thermal gradient cycling) JETS CED specimen #5. The red curve marks the image were the criteria for critical stress associated with crack growth was met. Shown in b): Stress-strain plot for the specimen with the critical stress associated with crack growth (449 MPa) marked by a red star, with the shear strain map of the sample shown as well.*
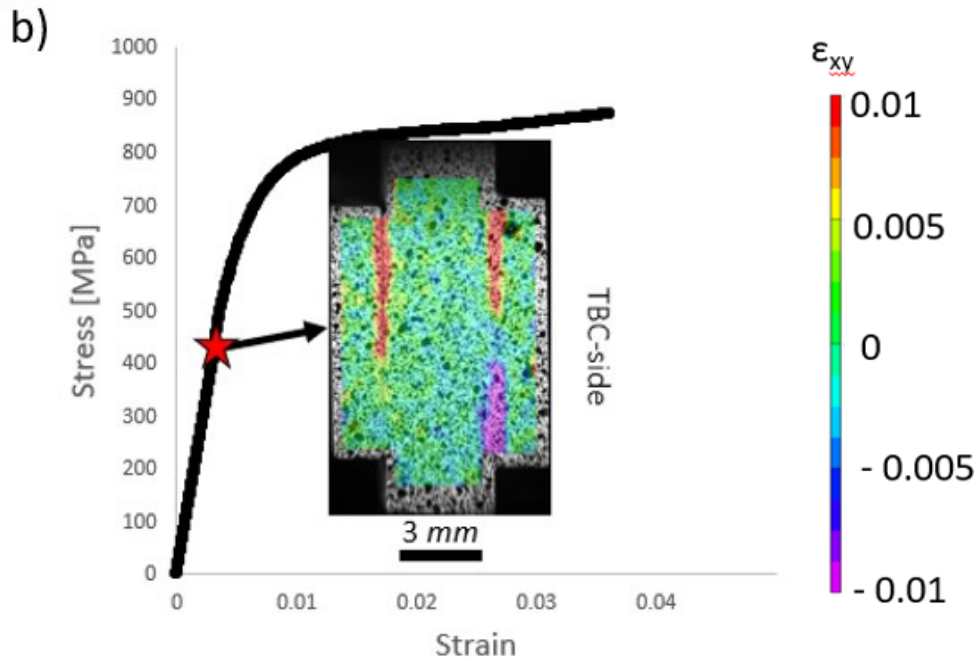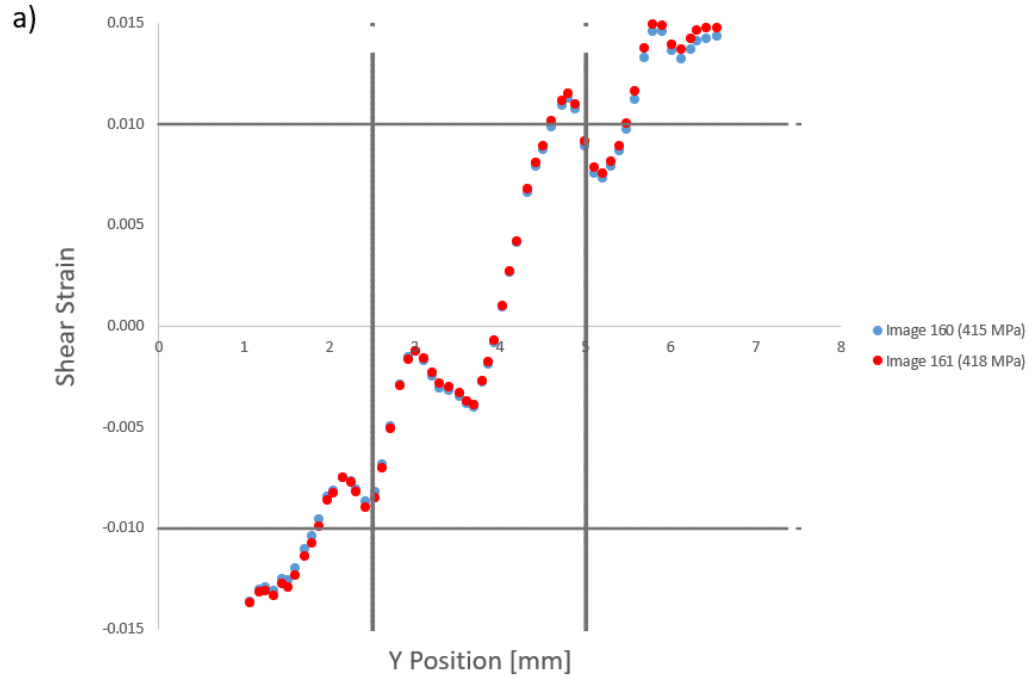
*Figure 3-13: Shown in a): Shear strain profile plot for an "as-deposited" (0% thermal gradient cycling) JETS CED specimen #6. The red curve marks the image were the criteria for critical stress associated with crack growth was met. Shown in b): Stress-strain plot for the specimen with the critical stress associated with crack growth (418 MPa) marked by a red star, with the shear strain map of the sample shown as well.*
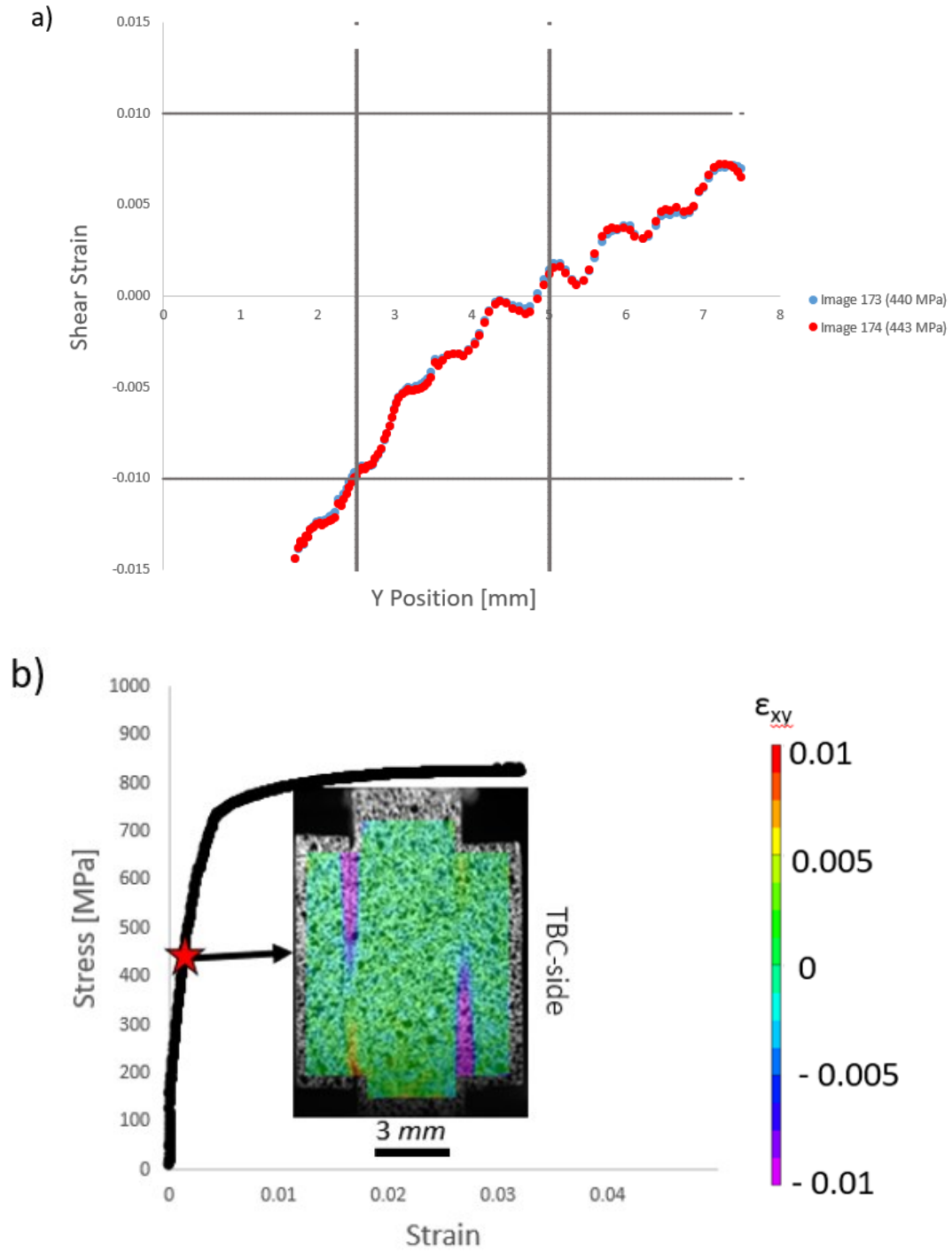
*Figure 3-14: Shown in a): Shear strain profile plot for an "as-deposited" (0% thermal gradient cycling) JETS CED specimen #7. The red curve marks the image were the criteria for critical stress associated with crack growth was met. Shown in b): Stress-strain plot for the specimen with the critical stress associated with crack growth (443 MPa) marked by a red star, with the shear strain map of the sample shown as well.*
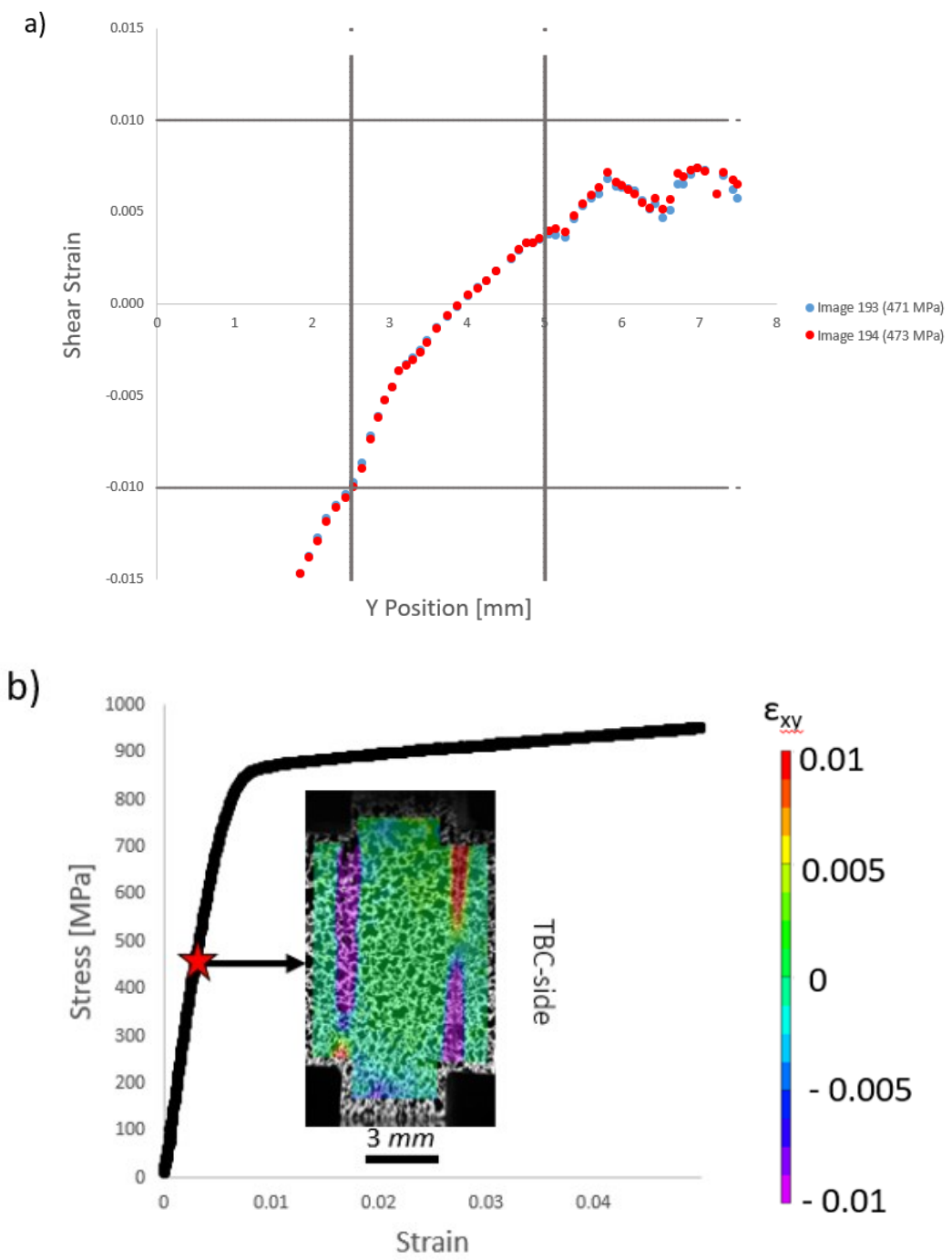
*Figure 3-15: Shown in a): Shear strain profile plot for an "as-deposited" (0% thermal gradient cycling) JETS CED specimen #8. The red curve marks the image were the criteria for critical stress associated with crack growth was met. Shown in b): Stress-strain plot for the specimen with the critical stress associated with crack growth (473 MPa) marked by a red star, with the shear strain map of the sample shown as well.*
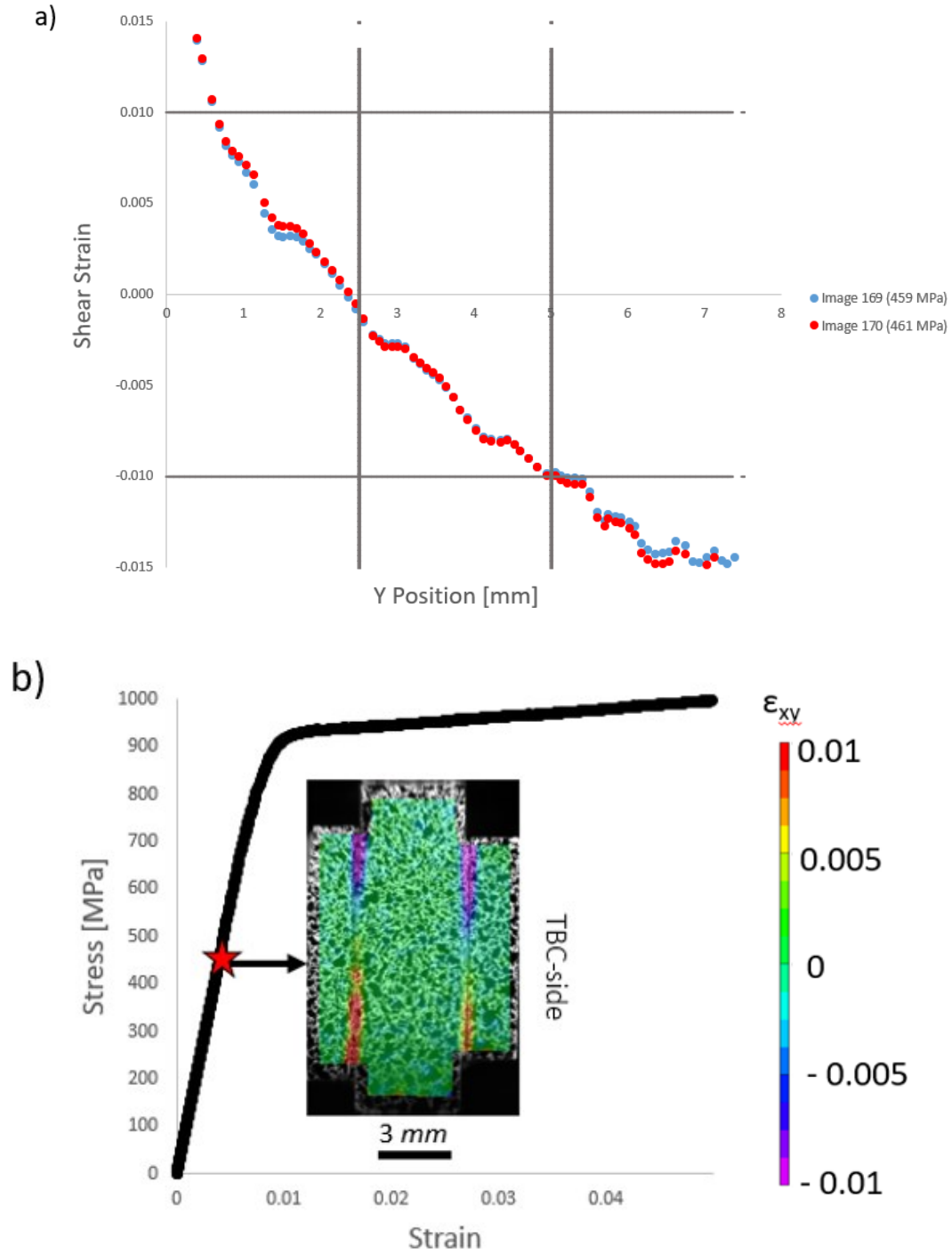
*Figure 3-16: Shown in a): Shear strain profile plot for an "as-deposited" (0% thermal gradient cycling) JETS CED specimen #9. The red curve marks the image were the criteria for critical stress associated with crack growth was met. Shown in b): Stress-strain plot for the specimen with the critical stress associated with crack growth (461 MPa) marked by a red star, with the shear strain map of the sample shown as well.*
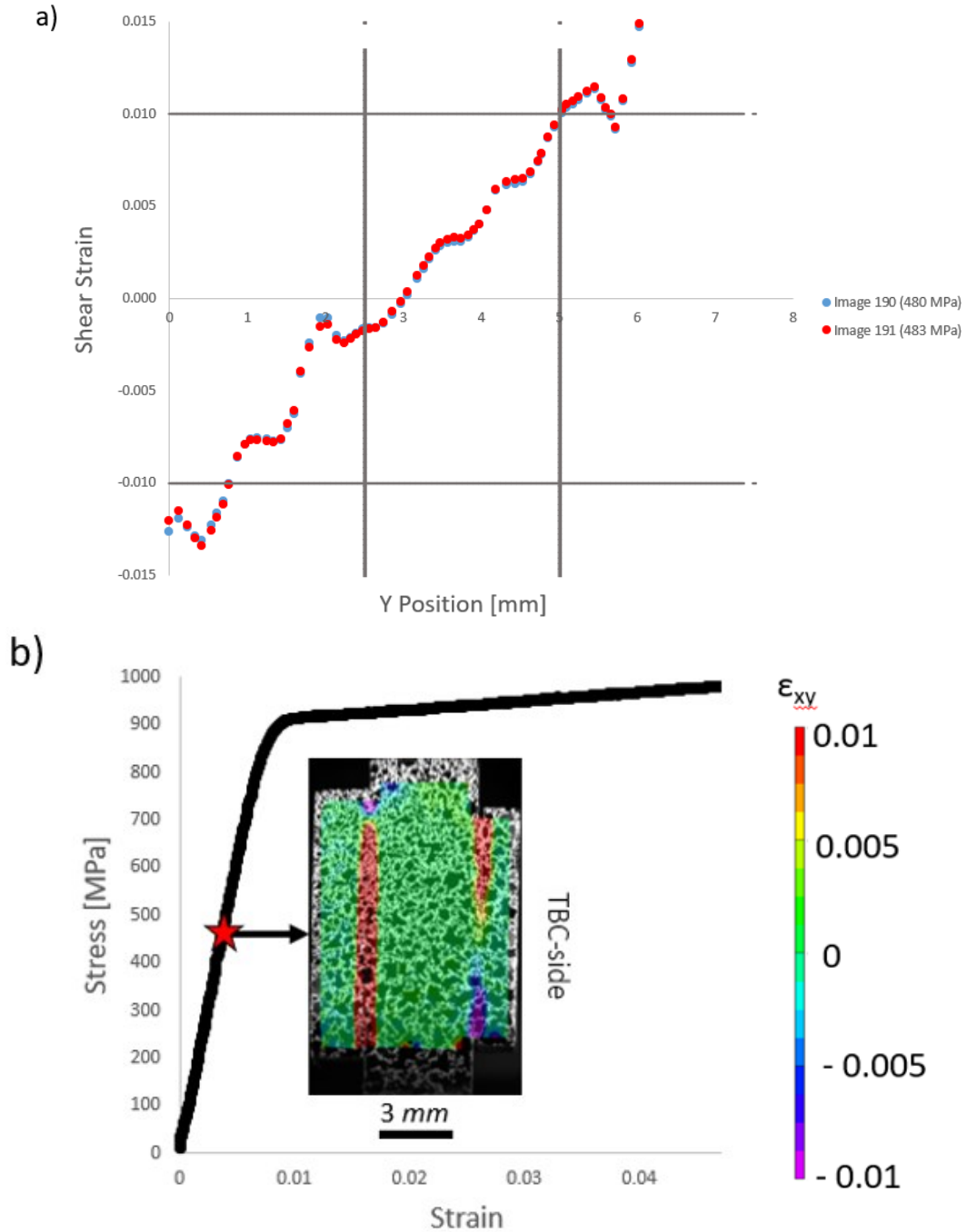
*Figure 3-17: Shown in a): Shear strain profile plot for an "as-deposited" (0% thermal gradient cycling) JETS CED specimen #10. The red curve marks the image were the criteria for critical stress associated with crack growth was met. Shown in b): Stress-strain plot for the specimen with the critical stress associated with crack growth (483 MPa) marked by a red star, with the shear strain map of the sample shown as well.*
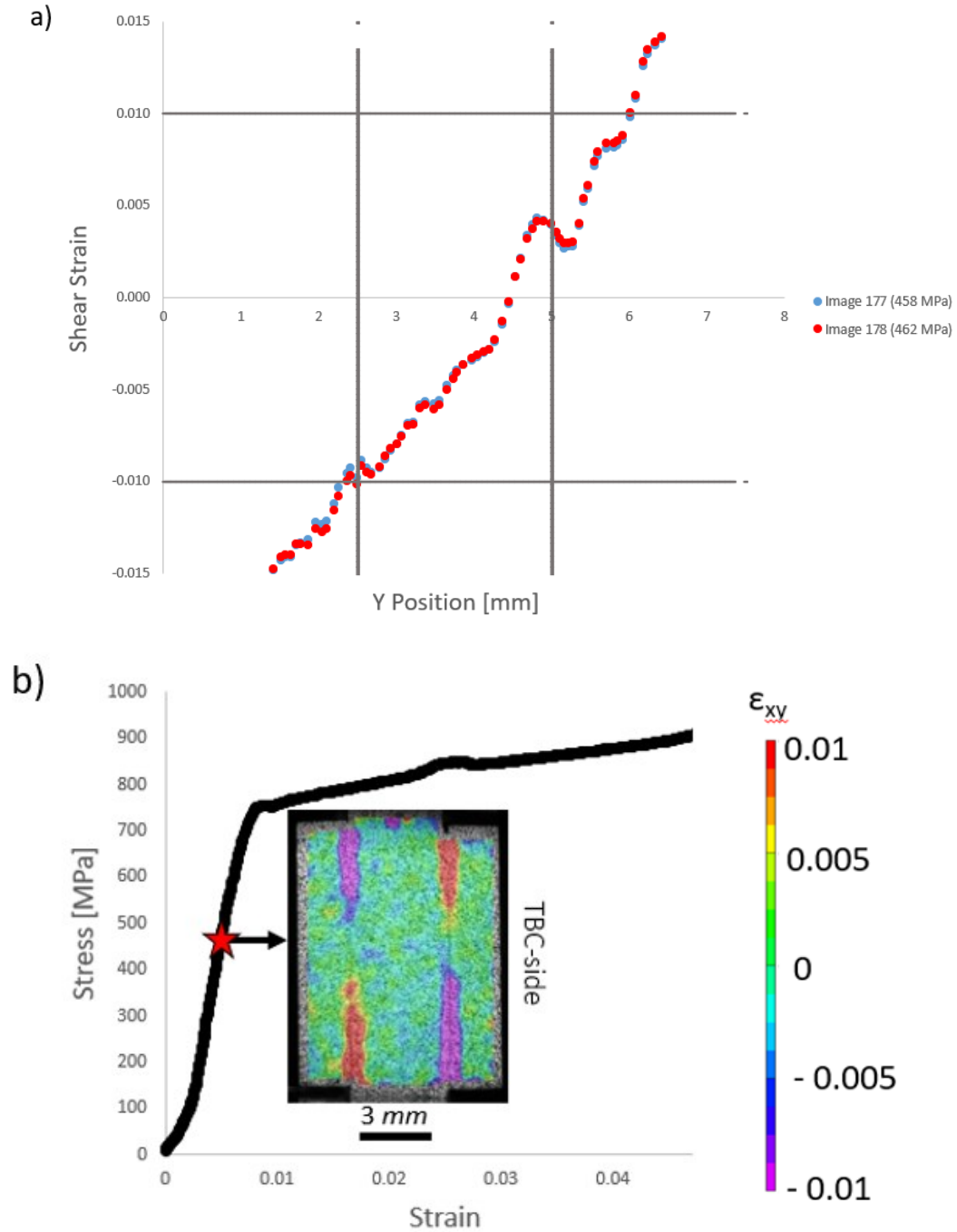
*Figure 3-18: Shown in a): Shear strain profile plot for an "early-in-life" (~30% thermal gradient cycling) JETS CED specimen #11. The red curve marks the image were the criteria for critical stress associated with crack growth was met. Shown in b): Stress-strain plot for the specimen with the critical stress associated with crack growth (462 MPa) marked by a red star, with the shear strain map of the sample shown as well.*
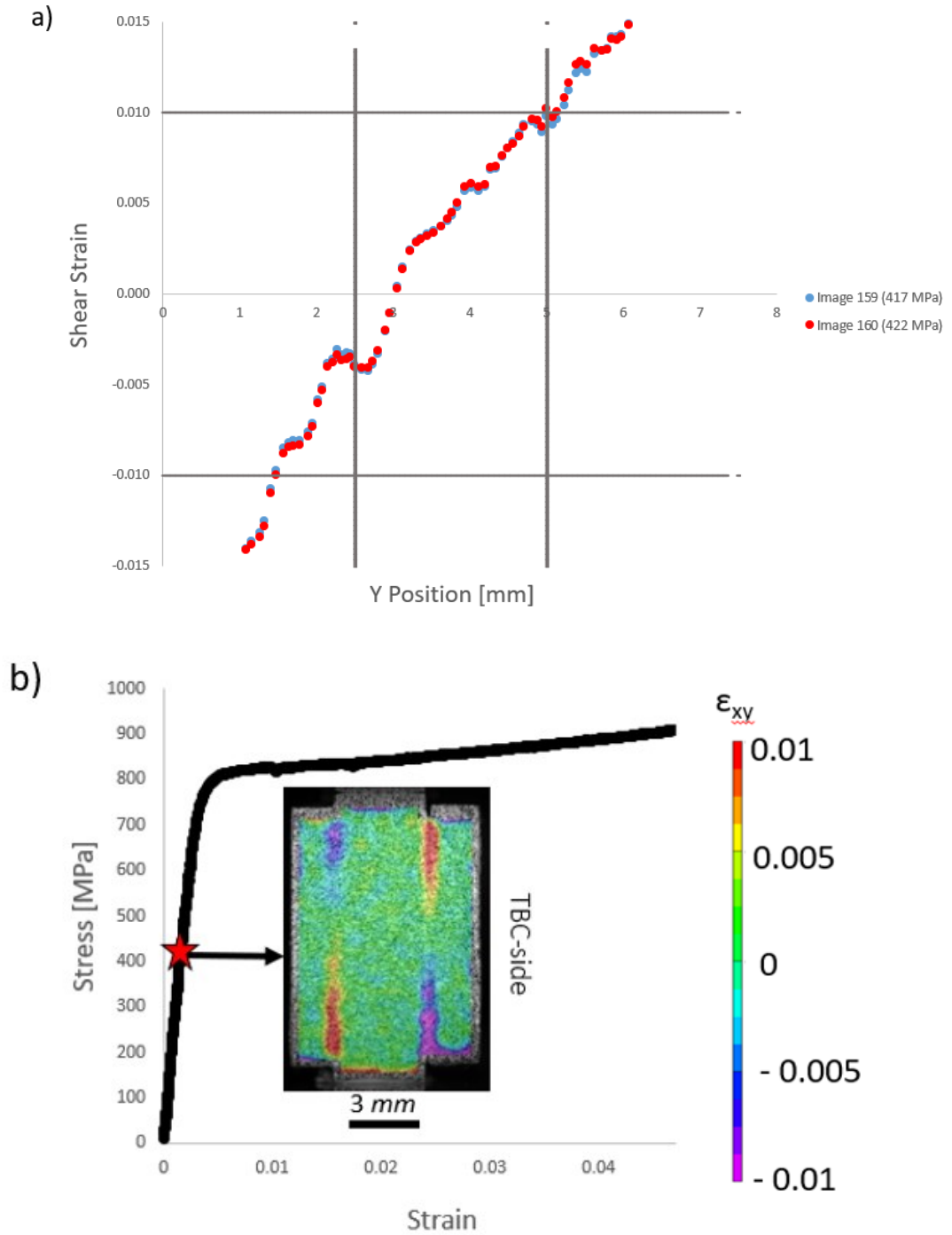
*Figure 3-19: Shown in a): Shear strain profile plot for an "early-in-life" (~30% thermal gradient cycling) JETS CED specimen #12. The red curve marks the image were the criteria for critical stress associated with crack growth was met. Shown in b): Stress-strain plot for the specimen with the critical stress associated with crack growth (422 MPa) marked by a red star, with the shear strain map of the sample shown as well.*
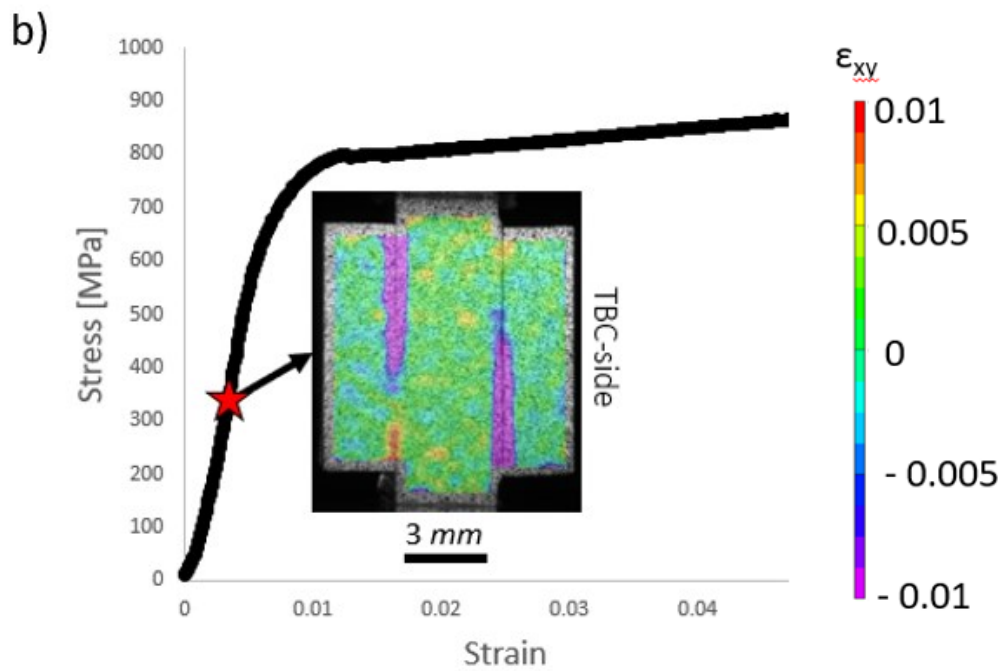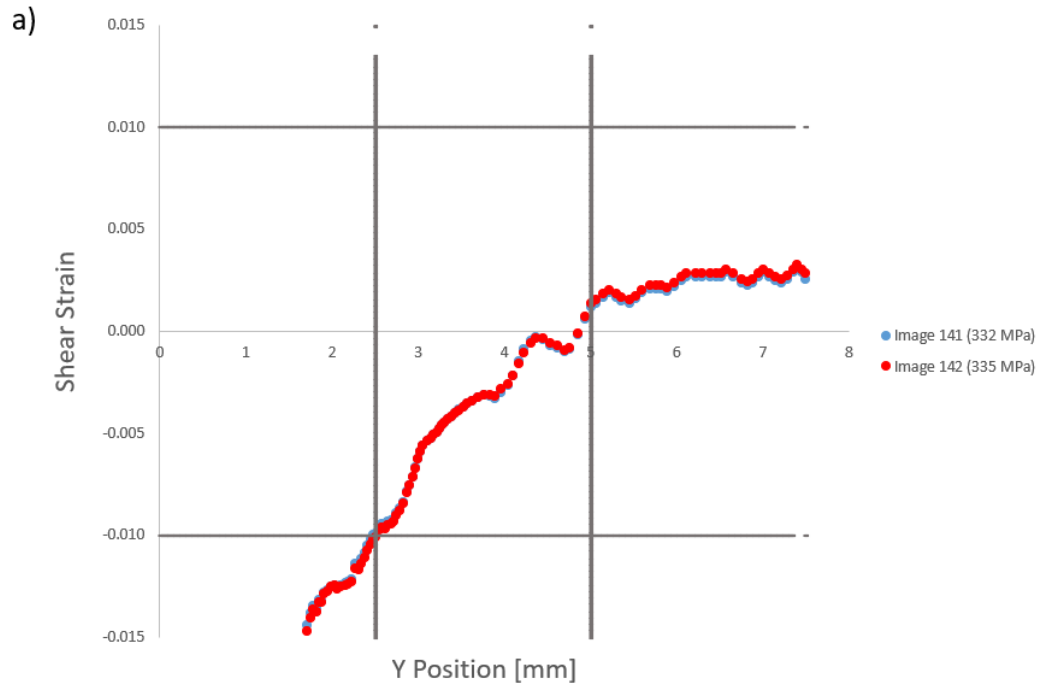
*Figure 3-20: Shown in a): Shear strain profile plot for a "mid-life" (~45% thermal gradient cycling) JETS CED specimen #13. The red curve marks the image were the criteria for critical stress associated with crack growth was met. Shown in b): Stress-strain plot for the specimen with the critical stress associated with crack growth (335 MPa) marked by a red star, with the shear strain map of the sample shown as well.*
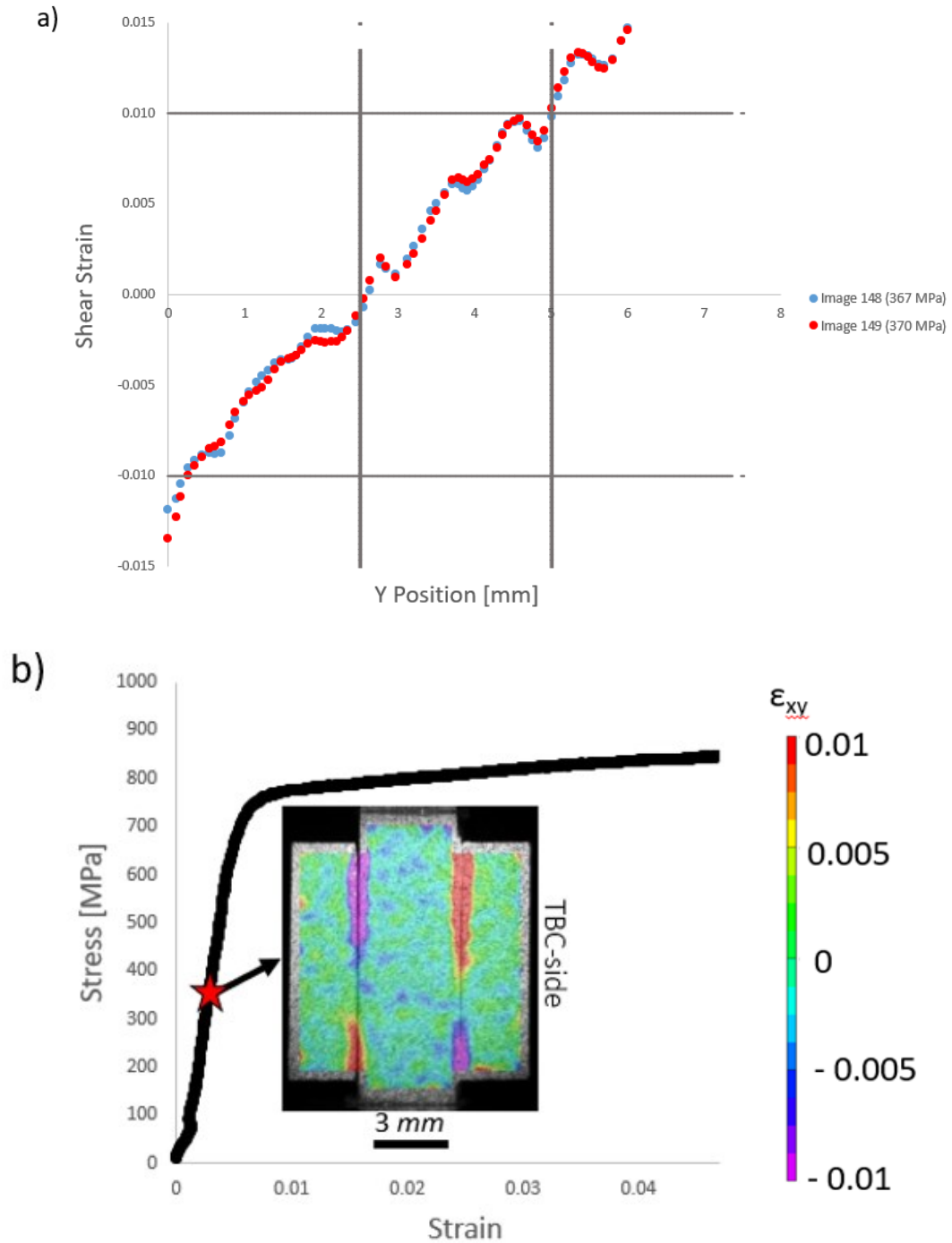
*Figure 3-21: Shown in a): Shear strain profile plot for a "mid-life" (~45% thermal gradient cycling) JETS CED specimen #14. The red curve marks the image were the criteria for critical stress associated with crack growth was met. Shown in b): Stress-strain plot for the specimen with the critical stress associated with crack growth (370 MPa) marked by a red star, with the shear strain map of the sample shown as well.*
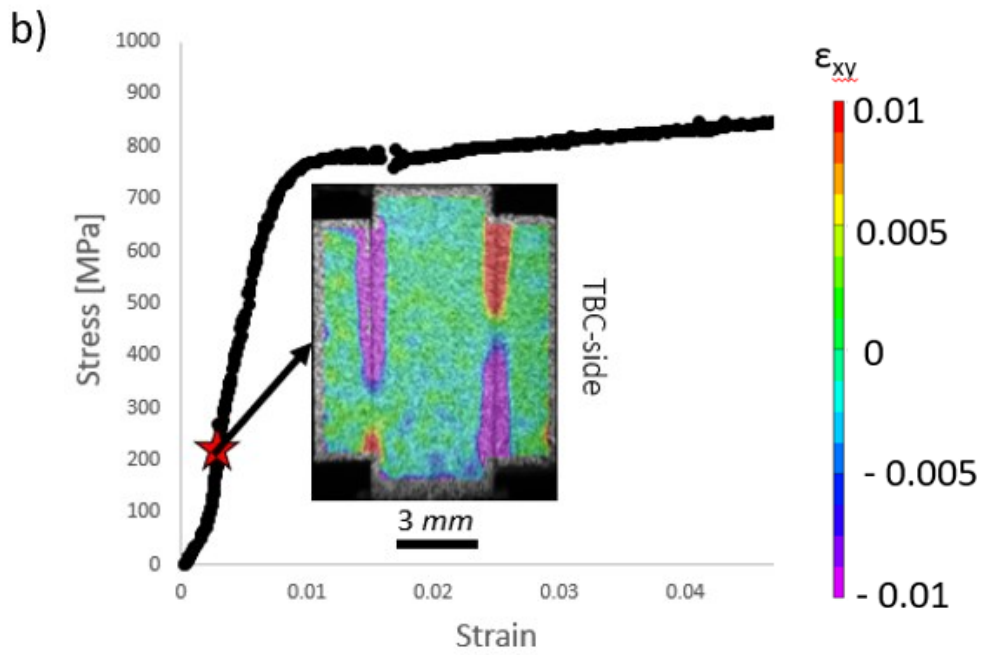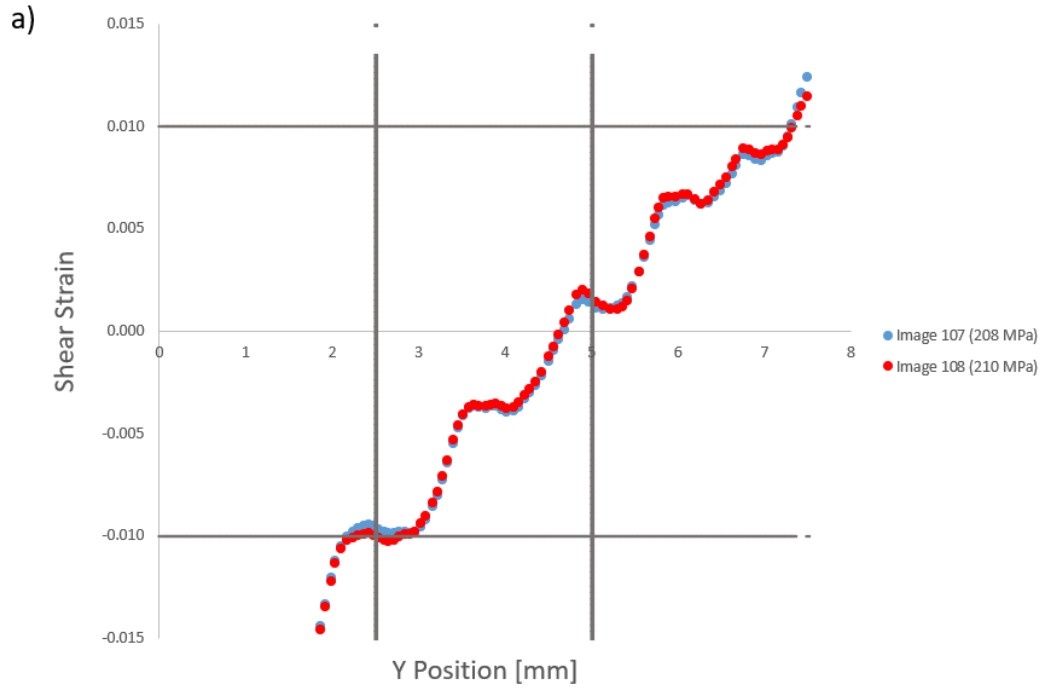
*Figure 3-22: Shown in a): Shear strain profile plot for a "late-in-life" (~90% thermal gradient cycling) JETS CED specimen #15. The red curve marks the image were the criteria for critical stress associated with crack growth was met. Shown in b): Stress-strain plot for the specimen with the critical stress associated with crack growth (210 MPa) marked by a red star, with the shear strain map of the sample shown as well.*

Consistent with Lockyer-Bratton's results for the FCT CED specimens, stable crack growth was observed in the elastic region of the test in every JETS CED specimen. It did not always begin on the side of the specimen that had been acid etched, which was taken to mean that the interface was weak enough for the cracks to nucleate under the applied stress and that the formation of pre-cracks was not really required. For the "as-deposited" specimens, the average critical stress for crack propagation was measured to be $463 \pm 27$ MPa. That value dropped to less than half (210 MPa) for the "late-in-life" specimen. The decrease in the nominal interfacial toughness (calculated using Equation 2-11) was from 2279 $J/m^2$ in the "as-deposited" state to 517 $J/m^2$ in the "late-in-life" state, which represents a drop of ~75%.

## 3.3  Discussion of JETS CED Results

Using the measurements of critical stress associated with crack propagation that are shown in the previous section, a plot of critical stress as an estimated percentage of thermal lifetime was developed for GE's standard commercial TBC system that had undergone JETS cycling to various stages of life. It is important to note that the thermal lifetime values are approximate ranges of thermal life, and thus are given a range of $\pm$ 10%, which is itself an estimate. Nevertheless, Figure 3-23 shows a clear decrease in the critical stress associated with crack propagation for increased thermal cycling.
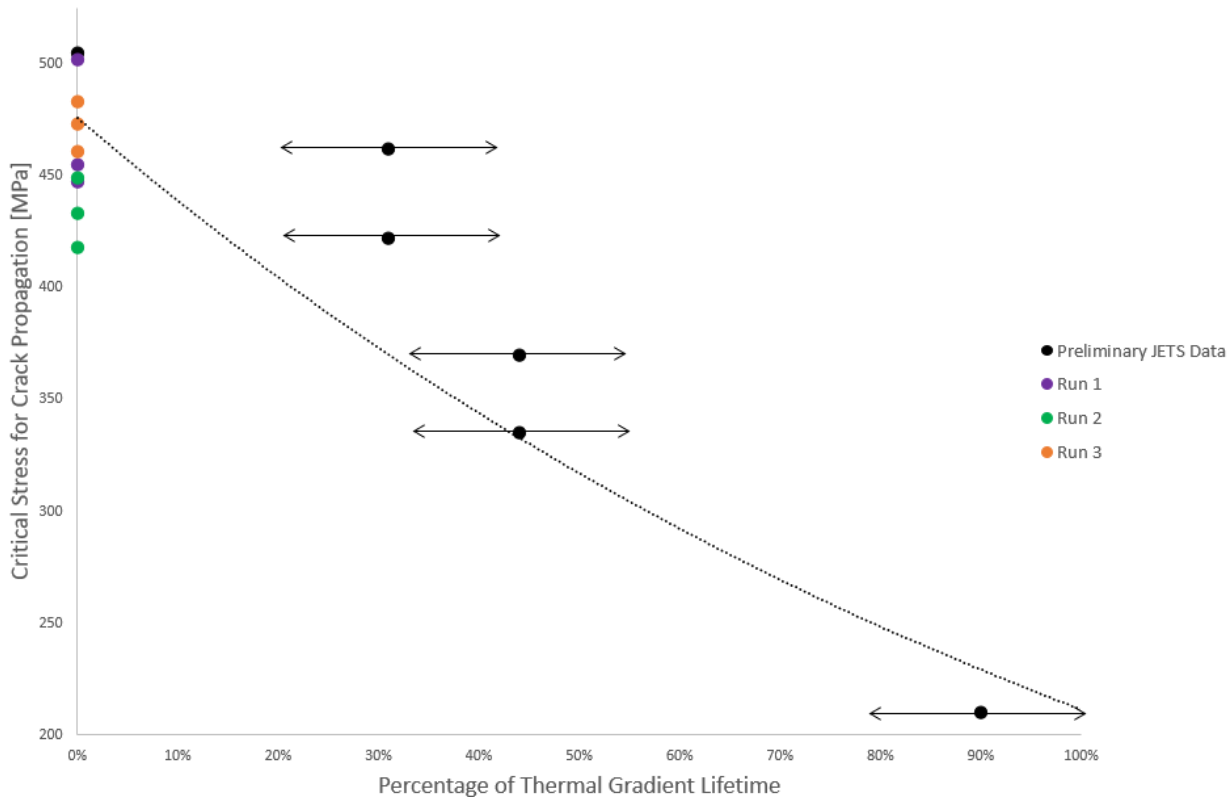
*Figure 3-23: Plot of critical stress associated with crack propagation as a function of JETS thermal cycling with an exponential fitted curve following the method from Lockyer-Bratton [1].*

When performing this work, an initial set of experiments were performed on an "as-deposited" (0% thermal lifetime) JETS CED specimen, two "early-in-life" (30 ± 10% thermal lifetime) JETS CED specimens, two "mid-life" (45 ± 10% thermal lifetime) JETS CED specimens and one "late-in-life" (90 ± 10% thermal lifetime) JETS CED specimen. After this, another nine "as-deposited" specimens from three different buttons, representing coating batches, were tested to investigate the variations that exist in the coatings on a run-to-run basis. These different coating runs are represented in Figure 3-23 by the purple "Run 1" data points, the green "Run 2" data points, and the orange "Run 3" data points. The average critical stress associated with crack propagation of Run 1, Run 2 and Run 3 respectively were 468 ± 24 MPa, 436 ± 13 MPa and 472 ± 9 MPa.

While the measured critical stress values from each run fell within small clusters (as seen in Figure 3-23 for the purple, green and orange data points) implying some amount of run-to-run variation, the differences between the runs were smaller than the decreases in critical stress measured as thermal exposure increased. When compared to the previously tested FCT CED specimens, the JETS CED specimens were approximately half the size (20 x 15 x 6 mm verses 10 x 6.5 x 3.2 mm) and were only coated on one side of the specimen as opposed to both. To confirm that the JETS CED specimens were viable test candidates that could be compared to the FCT CED specimens, it was important to have repeatable results for the "as-deposited" JETS specimens, as there was no thermal cycling involved and the only variable was the specimen geometry. The fact that the differences between the runs in the JETS test were on the same order of magnitude as those of the FCT tests (6% vs 3% respectively) gave confidence that the CED test performed on the JETS specimens was repeatable and accurate.

As shown in Figure 3-23, the critical stress associated with crack propagation dropped from an average of 463 MPa for the "as-deposited" specimens, to 442 MPa for the "early-in-life", to 353 MPa "mid-life" and 210 MPa in the "late-in-life" specimen. The total drop in the critical stress was measured to be 253 MPa or around ~ 55%. Using these data points, following the method from Lockyer-Bratton [1] an exponential curve of the form shown in Equation 3-1 was fit to the data.

*Equation 3-1*

$$\sigma_{Crit} = 475.8e^{-0.81t_{Life}}$$

Where $\sigma_{Crit}$ is the critical stress associated with crack propagation and $t_{Life}$ is the fraction of JETS thermal life. However, as shown in Figures 3-22, the measured critical stress values for the "early-in-life" JETS CED specimens were in the same range as the measured values for the "as-deposited" specimens. The first noticeable drop in the critical stress occurred in the "mid-life"

specimens, before falling significantly again with the "late-in-life" specimen. A more accurate curve for the CED data maybe the one shown in Figure 3-24.
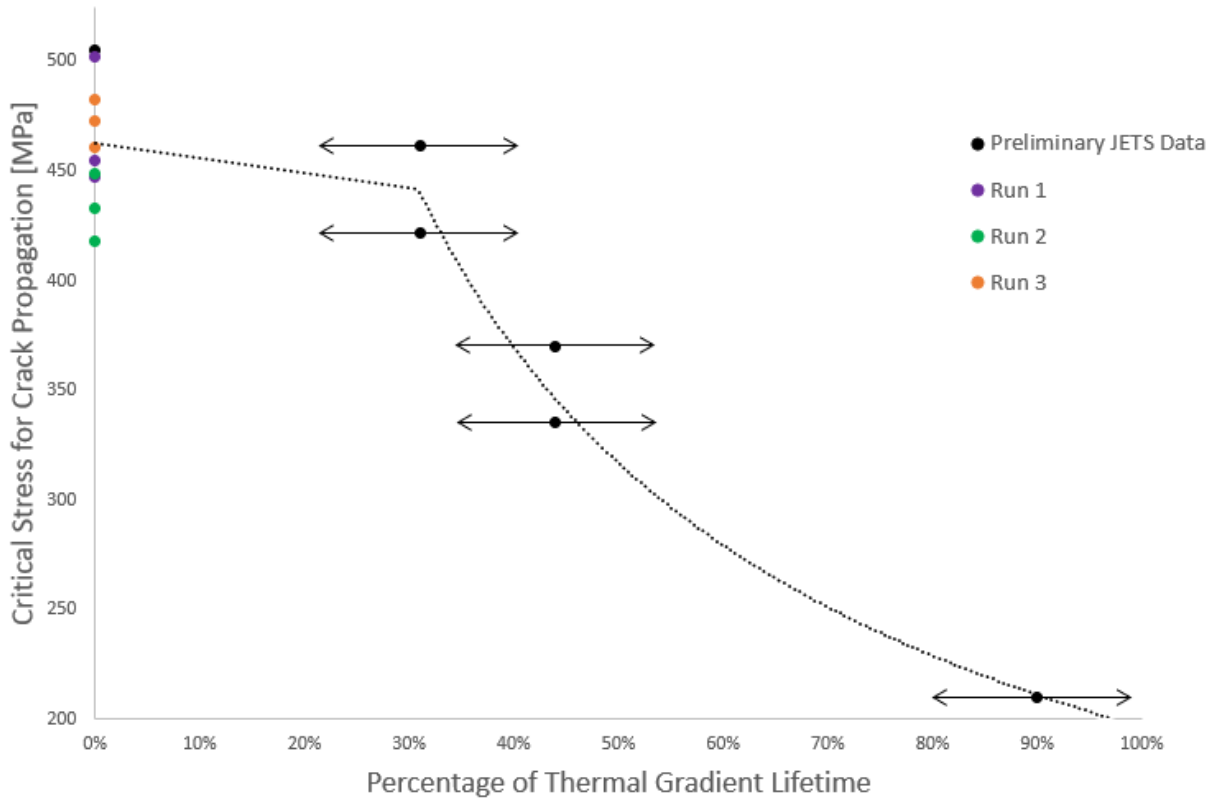


*Figure 3-24: Plot of critical stress associated with crack propagation as a function of JETS thermal cycling with a linear fitted curve following from the "as-deposited" to "early-in-life" specimens, followed by a power law curve.*

From the "as-deposited" to "early-in-life" specimens, a linear curve of the form shown in Equation 3-2 was fit to the data.

*Equation 3-2*

$$\sigma_{Crit} = 463 - 66.5t_{Life}$$

Following the linear curve, a power law curve of the form shown in Equation 3-3 can be used to describe the data.

*Equation 3-3*

$$\sigma_{Crit} = 196.2t_{Life}^{.69}$$

This modified curve provides a more accurate fit to the data and highlights the fact that a significant drop in critical stress is not observed until after the "early-in-life" specimens, indicating that there may be an incubation time before significant damage sets into the coating.

To better understand this behavior, high-resolution backscattered electron (BSE) SEM images of the fracture surfaces of the JETS CED specimens were taken. In each specimen failure occurred between the topcoat and bond coat (at either the bond coat/TGO interface or the TGO/topcoat interface) and observing the substrate fracture surface allowed for better understanding of how the delamination occurred. Figure 3-25 shows representative images of the fracture surface for each of the four thermal lifetimes that were tested.
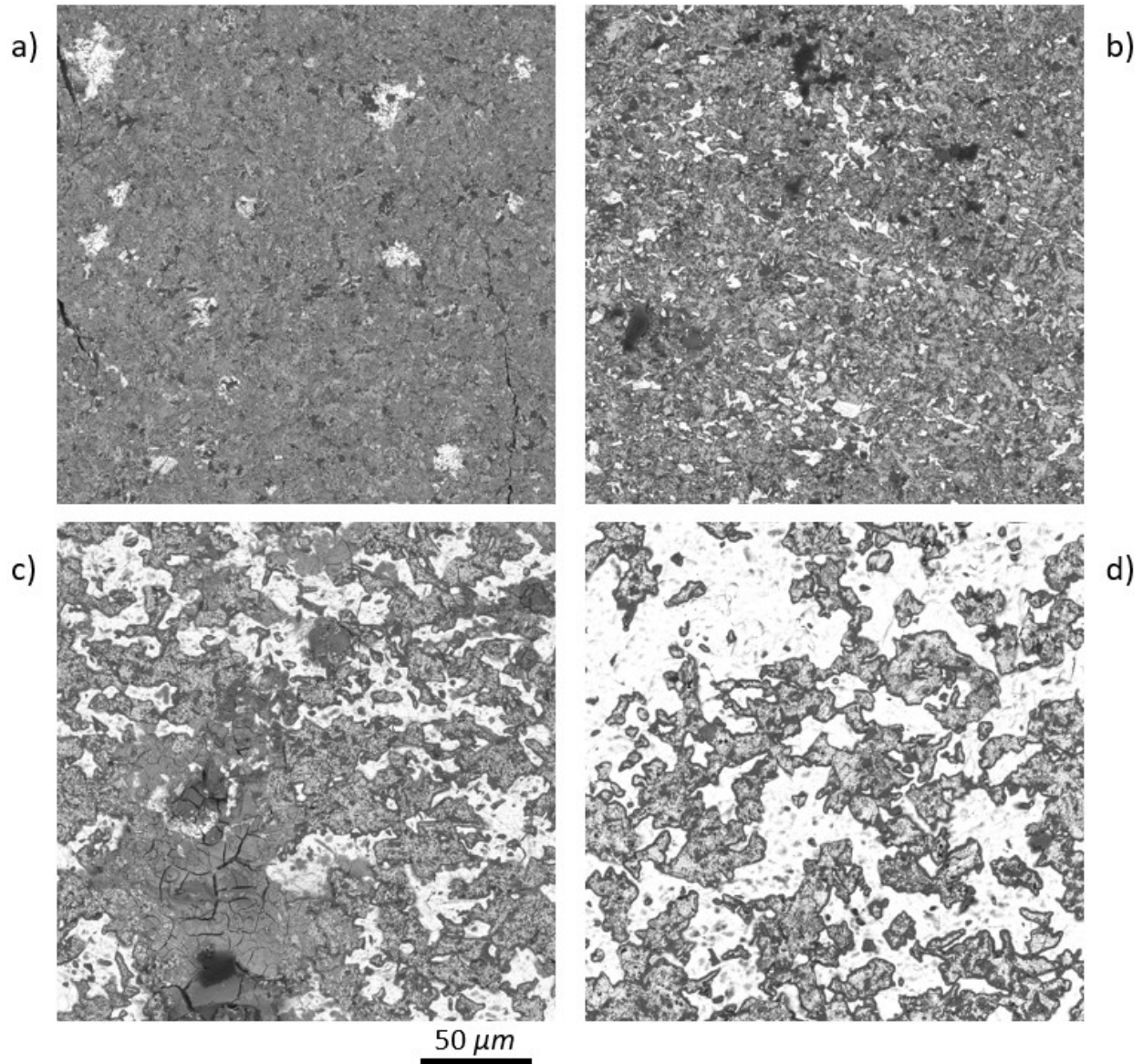
*Figure 3-25: Top-view BSE SEM images showing the substrate-side of the fracture surfaces for a) "as-deposited", b) "early-in-life", c) "mid-life" and d) "late-in-life" JETS CED specimens.*

A noticeable change in the substrate fracture surface as a function of thermal exposure is clearly visible in these SEM images. The fracture surface steadily transitioned from a mottled but uniform surface with a few dissimilar white pockets, to a wholly inhomogeneous surface with significantly larger and more frequent islands of white in the "late-in-life" state. To understand which of the four layers of the TBC these white areas were, energy dispersive X-ray spectroscopy (EDS) was used to measure the chemical composition of the fracture surface of each of the four

thermal conditions. Figure 3-26 shows a high-resolution BSE SEM image of the substrate-side of the fracture surface for the "late-in-life" specimen, as well the EDS results identifying the chemical composition of the fracture surface. It is important to note that the global EDS map shown in Figure 3-26 b) identifies the most prominent element present at that pixel, but the elemental maps below show that multiple elements can be detected in a single location.
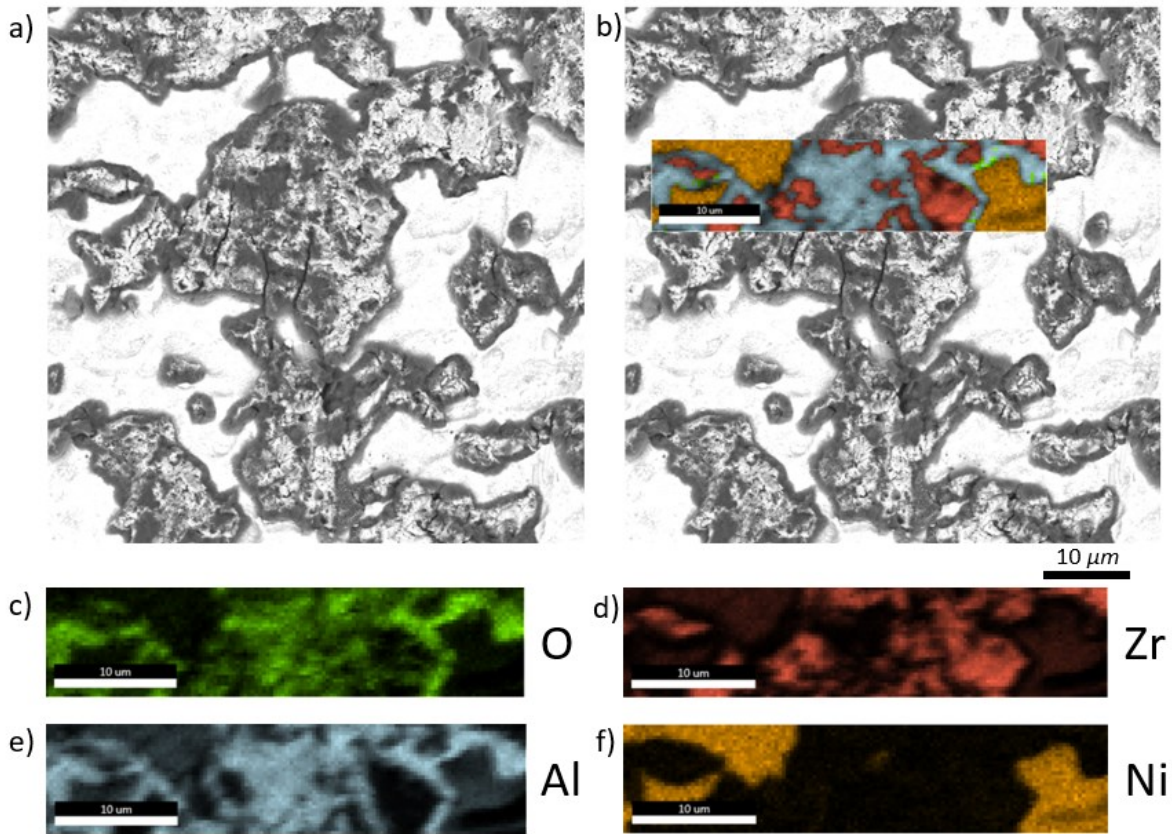


*Figure 3-26: (a) BSE SEM micrograph showing a high-res SEM image of the substrate side of the fracture surface for a "late-in-life" specimen. (b) same image overlayed with a color-coded EDS elemental map used to identify the bond coat (Ni-rich), TGO (Al-rich) and topcoat (Zr-rich) areas. (c-f) Individual elemental maps for the four elements (Al, Ni, O, Zr) detected.*

The EDS results from this "late-in-life" specimen showed that the large, high contrast white areas are Ni-rich, indicating the presence of the bond coat. Light gray islands are interspersed with the white islands and the interface between the white and light gray islands are delineated by dark gray lines. The light gray islands were determined to be a mixture of elements, mostly Zr and Al,

indicating a mixture of the topcoat and TGO. The dark grey lines that delineate between the area of metallic bond coat and ceramic TGO and topcoat are Al and O rich, indicating exposed TGO. Comparing this with Figure 3-25 suggests that, in the "as-deposited" state the substrate-side of the fracture surface is primarily TGO, but with increased thermal cycling the crack cuts through alternating regions of bond coat, topcoat and TGO. Moreover, the thin boarders of TGO suggests alternating mountains and valleys of topcoat and bond coat, which would be consistent with the onset of rumpling that has been reported in earlier studies [11, 12].

Qualitative observations indicate that the first significant change in the fracture surface occurred between the "early-in-life" and the "mid-life" specimen, while the largest change occurred between the "mid-life" and "late-in-life" specimens. The image analysis software ImageJ was used to quantify these changes. Histogram plots of the grey scale value for every pixel in these images were obtained, and the results show that the percent of Ni regions on the fracture surface grew from ~ 8% in the "as-deposited" and "early-in-life" stages to ~ 17% in the "mid-life" specimen, and again to ~ 42% in the "late-in-life" specimen. This implies that a mechanism activated by thermal cycling, possibly TGO growth accompanied by bond coat rumpling, resulted in local cracking of the topcoat [10], making delamination easier as thermal exposure is increased.

To further determine what the relevant mechanism controlling delamination was, SEM images of the cross-section of the fracture surface were also obtained to analyze the geometric changes in each layer as a function of thermal exposure. Approximately 150 μm of interface were observed for each fraction of life. Figure 3-27 shows representative cross-sectional images of the fracture surface at each of the four stages of thermal cycling.
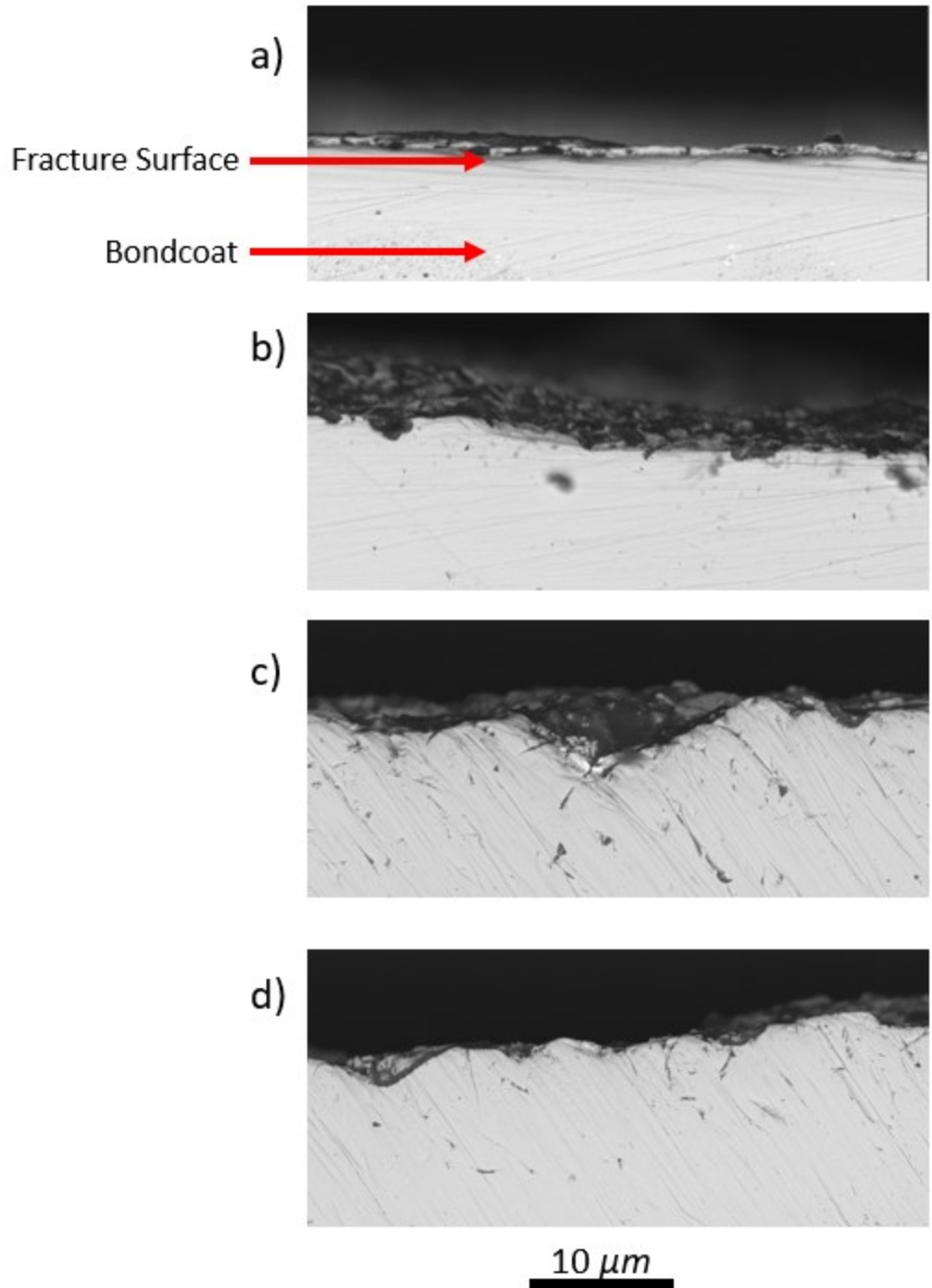
*Figure 3-27: Cross-sectional images of the fracture surfaces for an a) "as-deposited", b) "early-in-life", c) "mid-life" and d) "late-in-life" JETS CED specimen. The bond coat surfaces in the "as-deposited" and "early-in-life" states are flat while rumpling can be seen in the "mid-life" state and again with larger amplitudes in the "late-in-life" state.*

Consistent with Figure 3-25, failure in each specimen occurred between the topcoat and bond coat. The cross-sectional view of the "as-deposited" specimen shows a clean fracture above a flat surface bond coat with a very thin layer of TGO still present. In the "early-in-life" specimen, the bond coat remained relatively flat but was more rumpled than the as-received specimen. In this case, a thin layer of TGO was retained on the majority of the fracture but there are local regions where the TGO was breached and the bond coat exposed. The interface was significantly rougher and more noticeable in the "mid-life" specimen. The valleys on the fracture surface of the mid-life specimen contained both TGO and topcoat, the peaks had exposed bond coat and the transition regions were primarily TGO. In the "late-in-life" specimen, the amplitude of the undulations was even higher, consistent with work done by Mumm et al [11] and Tolpygo and Clarke [12], and the valleys were decorated with both TGO and zirconia, which explains and confirms the surface chemistries presented in Figure 3-25.

When looking at the results from the plot of critical stress associated with crack propagation as a function of JETS thermal exposure, the EDS of the substrate fracture surfaces, and the cross-sectional SEM images, the most significant change in the fracture behavior occurred between the "early-in-life" (30 ± 10% thermal lifetime) and "mid-life" (45 ± 10% thermal lifetime) specimens. The onset of significant bond coat and TGO rumpling resulted in the undulations imaged in the cross-sectional images and the change in the fracture path. The rumpling forced the crack to progress through multiple TBC layers, with local peaks and valleys leading to the islands that are observed in the fracture surface observations in Figure 3-25 d). The creation of a rough interface and the need to cut through multiple peaks might be expected to increase the interfacial toughness, but the rumpling led to local cracking of the topcoat which is visible in Figure 3-25, and with these added defects the critical stress and energy needed to grow the crack was reduced. When thermal

exposure was increased to the point of the "late-in-life" specimens, the behavior described above became even more severe, resulting in the larger drop in critical stress associated with for crack propagation.

Cross-sectional SEM images also provided an opportunity to measure TGO thickness as a function of thermal cyclic exposure. Cross-sectional images of the heat-affected zone of JETS buttons at various stages of thermal cycling life were used to measure TGO thickness. Figure 3-28 shows images of the bond coat, TGO and topcoat for "as-deposited", "early-in-life", "mid-life" and "late-in-life" buttons. The growth in TGO thickness can be readily seen in Figure 3-28, where the TGO was measured in 10 µm intervals along a 100 µm length. The TGO was measured to be $0.12 \pm 0.04$ µm thick in the "as-deposited" specimen, $0.97 \pm 0.14$ µm thick in the "early-in-life" specimen, $1.29 \pm 0.26$ µm thick in the "mid-life" specimen, and $2.31 \pm 0.35$ µm thick in the "late-in-life" specimen. Figure 3-29 shows a plot of TGO thickness as a function of JETS thermal exposure.
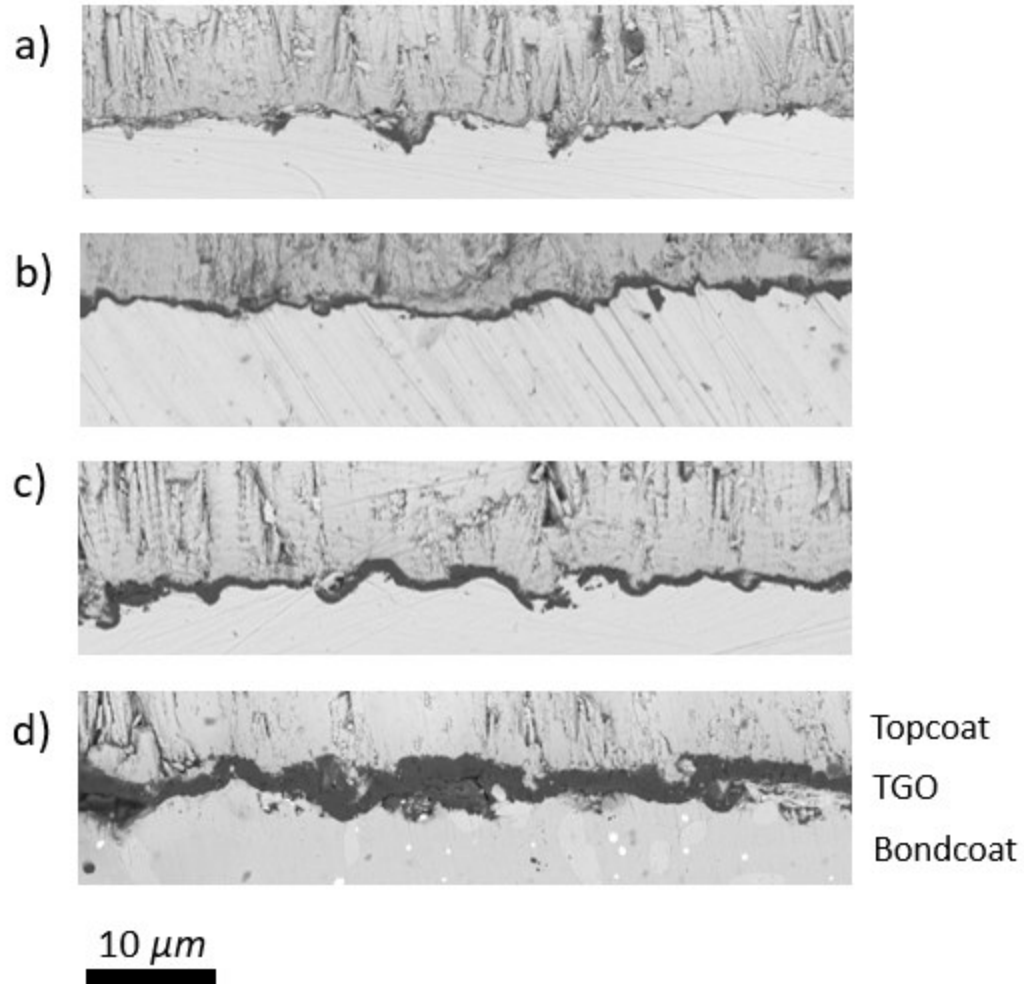
*Figure 3-28: Images showing the TGO thickness of an a) "as-deposited" specimen, b) a "early-in-life" specimen, c) "mid-life" specimen and d) "late-in-life" specimen. A very thin TGO layer is found in the "as-deposited" state and the thickness grows progressively larger with increased thermal exposure.*
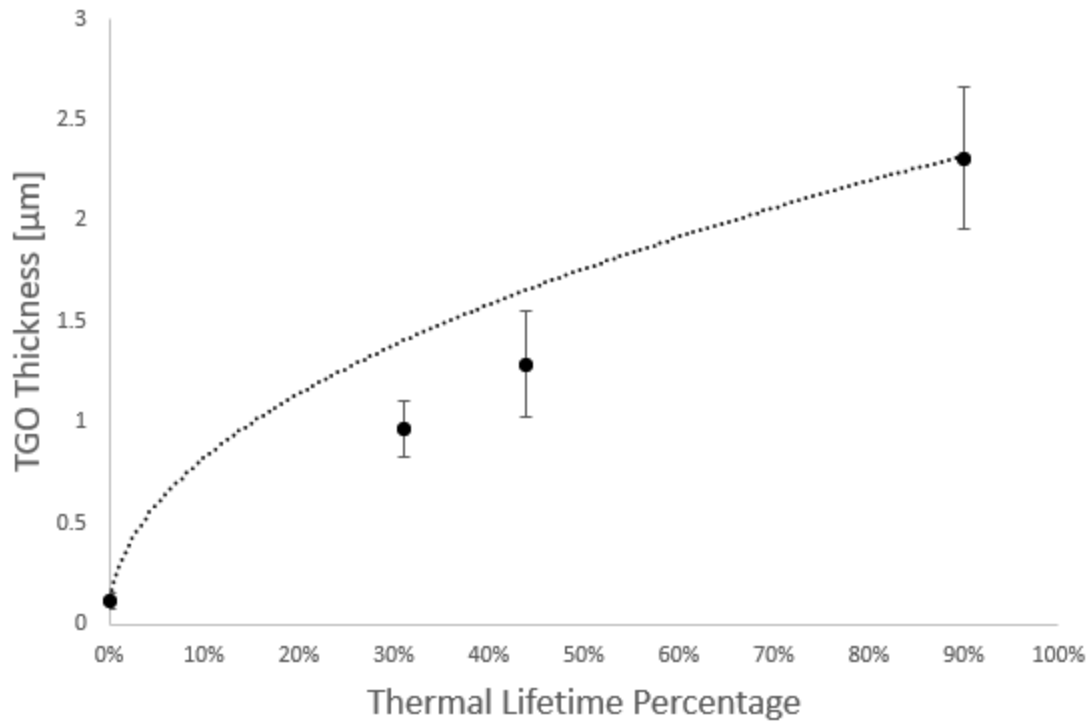
*Figure 3-29: Plot of TGO thickness as a function of percentage of JETS thermal exposure lifetime.*

The power law fit shown in Figure 3-29 was obtained and takes the form of Equation 3-4.

*Equation 3-4*

$$h_{TGO} = 2.44 t_{Life}{}^{.47}$$

Where $h_{TGO}$ is TGO thickness and $t_{life}$ is the fraction of JETS thermal life. This follows the generally accepted parabolic form of $h_{TGO}$ being a function of $t_{life}{}^{.5}$ as reported by Meier [13]. It can be seen that while TGO growth was most substantial in the "early-in-life", noticeable rumpling did not occur, and the critical stress associated with crack growth remained relatively constant. This suggests that failure in the JETS specimens was governed by bond coat rumpling rather than TGO growth and the associated increase in strain energy.

Rumpling of the bond coat has been reported in literature. Tolpygo and Clarke performed a series of studies from [12, 14, 15] on (Ni,Pt)Al bond coat systems cycled at 1150°C with no topcoat. These studies showed that oxidation at 1150°C led to significant rumpling of the bond

coat, that rumpling was much more pronounced for cyclic than isothermal oxidation, and that the amplitude of the undulations increased monotonically with thermal cycling. Hutchinson and Balint [16] developed a numerical model, that contained 23 independent parameters, for predicting TGO rumpling for four-layer TBCs and determined that undulation growth is determined by lateral growth strain in the TGO and the volume change in the martensitic transformation when it occurs [17]. Mumm and Evans [18] highlighted the formation of local micro-cracking in the topcoat induced by rumpling of the bond coat below. The TGO growth leads to buckling, which forces the bond coat to plastically deform. The topcoat cannot plastically deform so it cracks above the depressions that develop in the bond coat. These local cracks growth and link up and create a much easier fracture path for delamination [10].

The occurrence of micro-cracking is of particular interest, as the same behavior is seen in the JETS specimens. Micro-cracking was not visible in the "as-deposited" or "early-in-life" states and was first noticed in the "mid-life" specimens. Figure 3-30 shows a micro-crack that has formed in the topcoat above of an undulation in the bond coat from an "mid-life" specimen. The region shown is from a remnant piece of a "mid-life" button that was not mechanically tested.
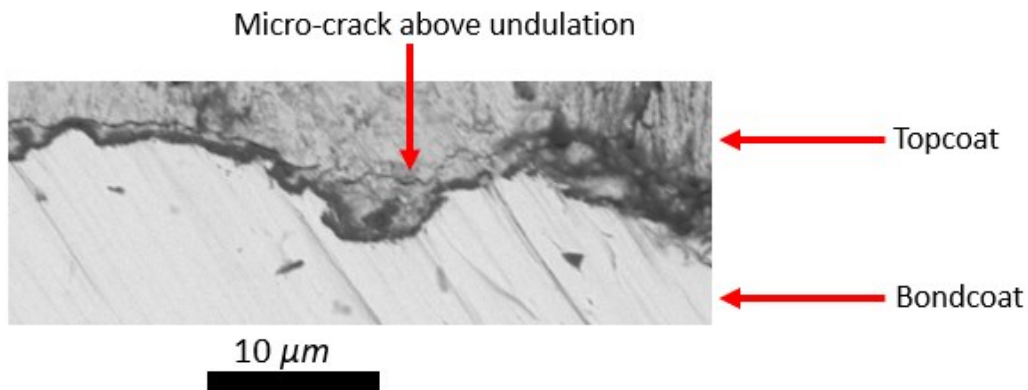


Figure 3-30: SEM image of a micro-crack formed in the topcoat of an untested "mid-life" JETS specimen. The micro-cracks form directly over undulations in the bond coat. Micro-cracking was not visible anywhere in the "as-deposited" or "early-in-life" specimens but are prevalent in the mid-life and late-in-life specimens and appear to be directly related to the reduction in interfacial toughness with thermal exposure.

The presence of rumpling in the bond coat and micro-cracking in the topcoat, along with the fact that the TGO thickness measured in the "late-in-life" specimens was only 2.3μm, while TGO thickness can grow to be 6-8μm at end of life [18], indicates that failure in the JETS specimens is driven by rumpling as opposed to TGO growth. This matches what is seen in the plot of critical stress associated with crack growth as a function of thermal lifetime in Figure 3-24, where the critical stress begins to fall noticeably after the "early-in-life" specimens.

### 3.3.1   Comparison of JETS CED Specimens to FCT CED Specimens

As previously stated, the work presented in this chapter was motivated by the work of Lockyer-Bratton [1] and his measurement of interfacial toughness values for FCT CED specimens that were made using GE's standard diffusion aluminide/EBPVD TBC. The present study was motivated, in large measure, by the desire to account for the thermal gradient that TBC's experience in service. The temperature in FCT tests cycles over time, but the temperature of the part in the furnace is isothermal.  Introduction of a thermal gradient was facilitated in two ways.  As described above, modified JETS CED specimens were machined from 1 inch (2.54 cm) diameter JETS buttons that had been cycled to various stages of life. As described in the next section, attempts were also made to make CED specimens from turbine blades that had been pulled from service.

The JETS CED specimens summarized above have the same standard TBC as Lockyer-Bratton's FCT CED specimens [1], making direct comparisons possible. Figure 3-31 shows a plot of the critical stress associated with crack propagation as a function of thermal lifetime for both sets of data.  It is important to note that the FCT tests were carried out with a maximum T of 1135°C (2075°F), while the surface temperature of the topcoat in the JETS tests was 1316°C

(2400°F) and the backside temperature was 36°C (97°F), which resulted in an approximate bond coat temperature of 1150°C (2100°F) based on 1-D heat transfer modeling conducted at GE.
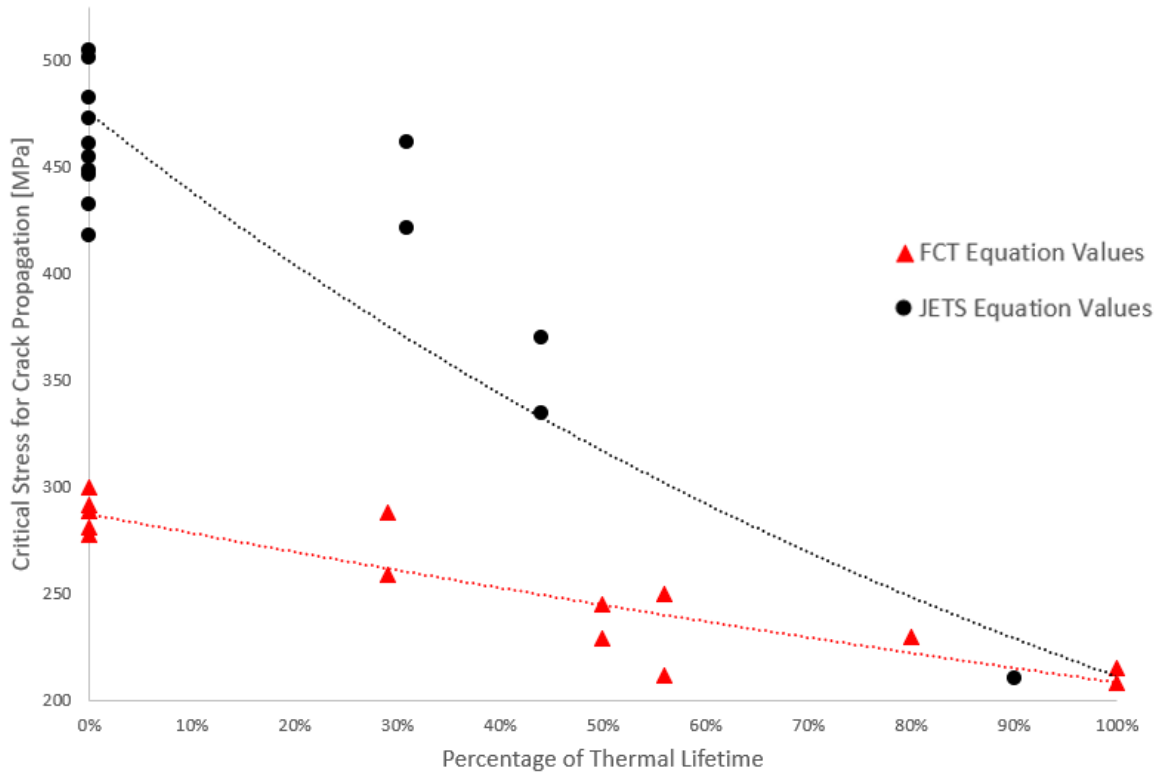


*Figure 3-31: Plot of critical stress associated with crack growth for as a function of thermal lifetime for both the JETS CED specimens and FCT CED specimens.*

The first major takeaway from Figure 3-31 is the disparity between the measured critical stress values for the "as-deposited" FCT and JETS specimens. Both sets both sets were in the "as-deposited" state, meaning no thermal cycling had occurred. Despite this, the measured critical stress associated with crack propagation of the JETS specimens was ~1.5 times larger than that of the FCT specimens. This discrepancy can be explained by the fact that the FCT CED specimens are around twice the size (20 x 15 x 6 mm vs 10 x 6.5 x 3.2 mm) of the JETS CED specimens. Critical stress associated with crack propagation is not a material property; it is related to the total strain energy in the substrate, coating and stiffener plate and is affected by the size of the specimen

and the stiffener plate. The relevant size independent material property is interfacial toughness, which can be estimated from the critical stress value in Equation 2-11. In this equation it is shown that the interfacial toughness $G_c$ is directly proportional to the energy release rate, which scales with the critical stress $\sigma_c{}^2$ as well as the thickness of the stiffener plate $h$. Using Equation 2-11, which is an estimate but sufficient for the current comparison, along with the critical stress values measured by Lockyer-Bratton and in the current study, Figure 3-32 was developed. This figure plots the analytical estimate for interfacial toughness of the JETS CED and FCT CED specimens as a function of thermal exposure lifetime.
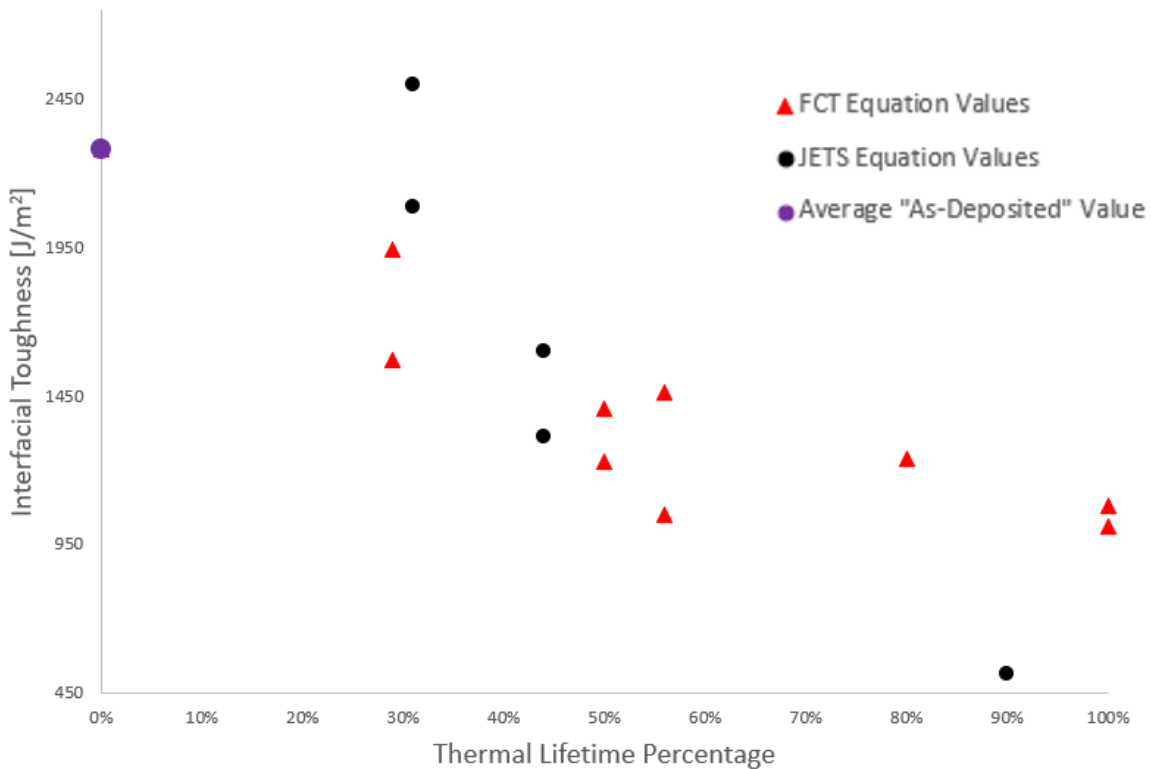


*Figure 3-32: Plot of the analytical estimate for interfacial toughness as a function of thermal exposure for both the JETS and FCT specimens.*

The average calculated interfacial toughness of all the "as-deposited" FCT and JETS specimens was used (2279 J/m²) as a singular interfacial toughness value for the "as-deposited"

specimens, shown by the purple data point in Figure 3-32. For the JETS specimens, interfacial toughness values of $2294 \pm 207$ J/m$^2$, $1460 \pm 145$ J/m$^2$ and 517 J/m$^2$ were measured at the "early-in-life", "mid-life" and "late-in-life" stages. From the "as-deposited" to "late-in-life" stages, this corresponded to a drop of 1762 J/m$^2$. For the FCT specimens at comparable points of life, values of $1758 \pm 186$ J/m$^2$, $1318 \pm 89$ J/m$^2$ and $1049 \pm 35$ J/m$^2$ were measured, along with a drop of 1230 J/m$^2$. Figure 3-32 shows that the interfacial toughness values between the JETS and FCT specimens agree with each other through ~50% of their lifetime, until the JETS specimens fall off more rapidly towards the end of life, although the caveat must be given that only one "late-in-life" JETS specimen was tested. The agreement between these values, even though the JETS specimens were smaller in size and only were coated on one side, gives confidence in the quality of the JETS CED test.

To better compare the FCT and JETS specimen results, each data set was replotted with the average "as-deposited" interfacial toughness of that data set. Figure 3-33 shows this plot, along with a best fit curve indicating interfacial toughness as a function of thermal lifetime.
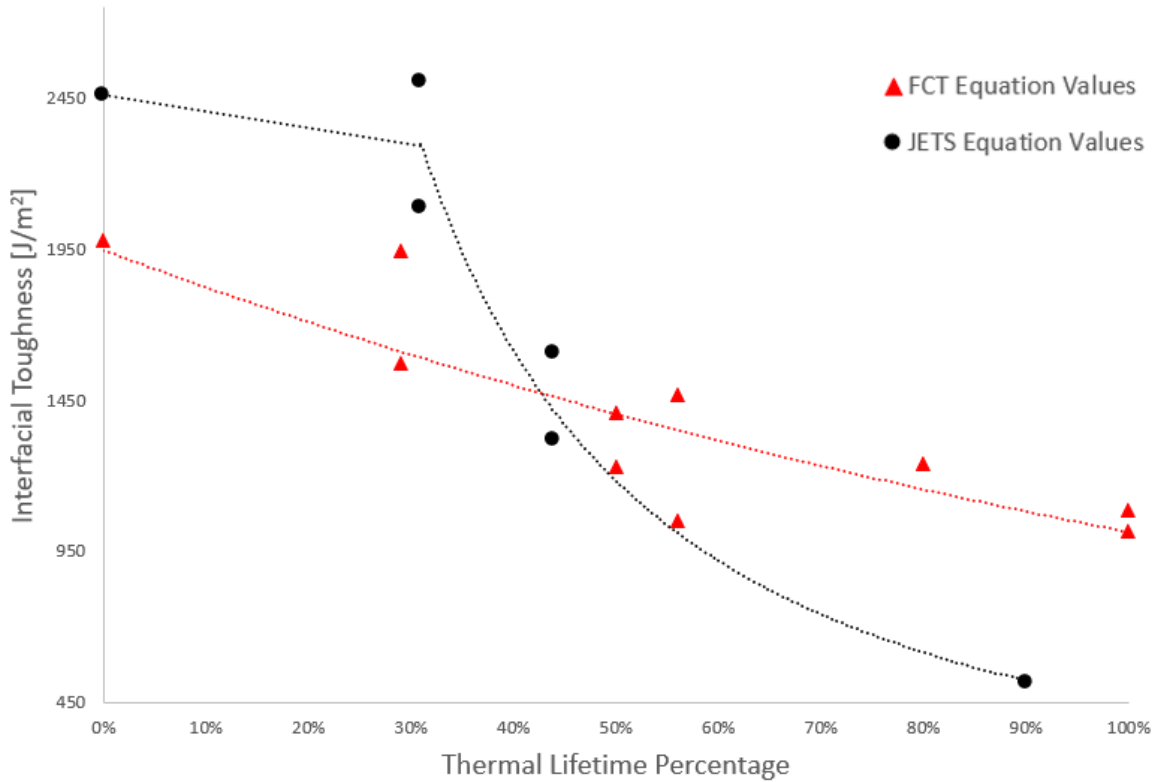
*Figure 3-33: Plot of the analytical estimate for interfacial toughness as a function of thermal exposure for both the JETS and FCT specimens along with best fit curves for each data set.*

For the JETS specimens this took the form of a linear curve early in life followed by a power law fit late in life. Equations 3-5 and 3-6 are for the JETS specimens, while 3-7 is the exponential equation for the FCT specimens.

*Equation 3-5*

$$G_C = 2463.9 - 547.6t_{Life}$$

*Equation 3-6*

$$G_C = 454.2t_{Life}^{-1.4}$$

*Equation 3-7*

$$G_C = 1948.8e^{-0.65t_{Life}}$$

The curve for the JETS specimens confirms the idea that there is a damage incubation period before a significant reduction in interfacial toughness occurs, leading to the higher interfacial

toughness values in the early stages of exposure. The linear portion of the curve shows a slight drop in interfacial toughness initially, after which a more pronounced drop in interfacial toughness occurs through the end of coating life for both sets of specimens. According to Karlsson et al. [19], a prerequisite for bond coat rumpling is the presence of a thermal expansion misfit between the TGO and the substrate, and Hutchinson and Balint [15] state that for (Ni,Pt)Al bond coat systems, the bond coat is susceptible to undulation growth as the result of thermal expansion mismatch. The comparable bond coat temperatures experienced by the FCT and JETS specimens means that both sets of specimens are expected to experience similar amounts of rumpling and TGO growth. This explains the similar calculated interfacial toughness values through "mid-life" for the FCT and JETS specimens. While the "late-in-life" interfacial toughness is lower in the JETS specimens, only one data point exists. Further testing must be done to elucidate whether JETS testing leads to lower "late-in-life" interfacial toughness values or whether the values will fall on top of the FCT values like they do through "mid-life".

The magnitude of the interfacial toughness values reported in Figures 3-30 and 3-31 are significantly higher than the values previously reported by Lockyer-Bratton [1]. These were obtained using Equation 2-11, while the values reported by Lockyer-Bratton were obtained using FE simulations of the FCT CED specimens that included multiple layers and accounted for TGO thickness and friction to develop a more accurate approximation for interfacial toughness. These simulations were only valid for the FCT sample geometry, and since the JETS CED specimens are half the size of the FCT specimens and only coated on one side, the adjustments Lockyer-Bratton made for the FCT specimens are not directly applicable in this study.

Instead, a similar set of FE simulations performed on the JETS CED specimen geometry would be necessary to properly adjust the interfacial toughness values. Thus, Equation 2-11 is used in

both cases to make a more direct comparison between the two sets of specimens. As stated in Section 2.2.4 of this thesis, Equation 2-11 overestimates the interfacial toughness of the specimens due to the inaccurate assumption of full strain transfer into the stiffener plates. Nevertheless, using Equation 2-11 still provides a size-independent approximation for interfacial toughness however and is useful in determining relative trends in the data such as the rate of decay of interfacial toughness as a function of thermal exposure lifetime.

3.4  Attempts to Extend the CED Tests to Jet Engine Blades

Along with the JETS buttons discussed above, GE also provided JHU with multiple sets of high-pressure turbine blades at various stages of life. The primary goal for this task was to prepare CED specimens from these blades and use CED testing to measure the interfacial toughness of engine hardware, in this case high-pressure turbine blades, over the course of their lifetime.  The temperature of the blades to be tested was not monitored and is not known, which limits direct comparison with the FCT and JETS CED specimens, but the merit of using blades was two-fold. It provided an opportunity to study trends regarding the drop in interfacial toughness with service life and the role of the thermal gradient.  Moreover, it provided an opportunity to assess the magnitude of the interfacial toughness of engine hardware.

Two important requirements of CED testing are that the specimens have flat surfaces onto which stiffener plates can be adhered and that they have a cross-sectional area that allows compressive loading without buckling. The vast majority of modern blades have complex geometries with curved surfaces, thin walls and cooling channels.  This greatly complicates the fabrication of CED specimens, but a trial effort involving an engine blade [20] yielded very promising results and served to motivate the current study.  GE identified a section of high-pressure

111

turbine blades that had relatively flat surfaces and cut the blades into sections that were both flat and masked proprietary geometries and design considerations. Challenges in the first set of samples arose because the cuts damaged or eliminated internal ribs and tips that are required to give the specimen a second moment of inertia that would resist buckling. The specimens split into two halves (pressure and suction side surfaces) that were too thin to support the needed compressive loads.

A second set of high-pressure blades consisting of one "as-deposited" blade and three thermally cycled blades were provided to JHU by GE. The specimen preparation procedure for the blades was the same as the procedure described for the JETS CED specimens, with one key difference. Each of these blades were cut from sections with a larger rib connecting the two sides, but these blades also had a more pronounced curvatures than the original set of blades. To account for this curvature, each of the blades was imaged using a Mitutoyo Toolsmaker optical microscope that documented the radius of curvature and geometry of each side of the blades. With this information in hand, computer aided design (CAD) software SolidWorks Professional was employed to design stiffener plates that matched the curved surfaces and a wire EDM was used to fabricate curved stiffener plates out of René N5. The stiffener plates were then adhered to the blades using the same epoxy and application technique as described earlier. Outside of the fabrication of the stiffener plates, the specimen preparation procedure for these blades was the exact same as the procedure for the JETS CED buttons. Following the adherence of the stiffener plates and application of the speckle pattern, the blades were ready for CED testing. The blades were tested using the same MTS system and camera setup that is described in Section 3.2.

It became clear upon loading that this second iteration of blades was better than the first iteration, but they still were not robust enough to properly perform CED testing. The second

iteration of blades had an additional support structure (rib) on one end that connected the two sides of the blade, but the connection was only on one end and this support structure was shaped more like a "U" than a block "O" and was not robust enough to prevent localized buckling of the tip during testing. This local buckling resulting in plastic deformation of the substrate and premature delamination of the coating. Figure 3-34 below shows two BSE SEM images of the tested "as-deposited" blade. The low magnification image of the blade shows the buckled portion of the blade near the tip. The higher magnification image was taken in the buckled portion of the blade; it shows the formation of a vertical crack that ran through the topcoat and into the underlying bond coat. This crack formed because of the local buckling and precluded testing the second set of specimens.



2 mm                                    20 µm
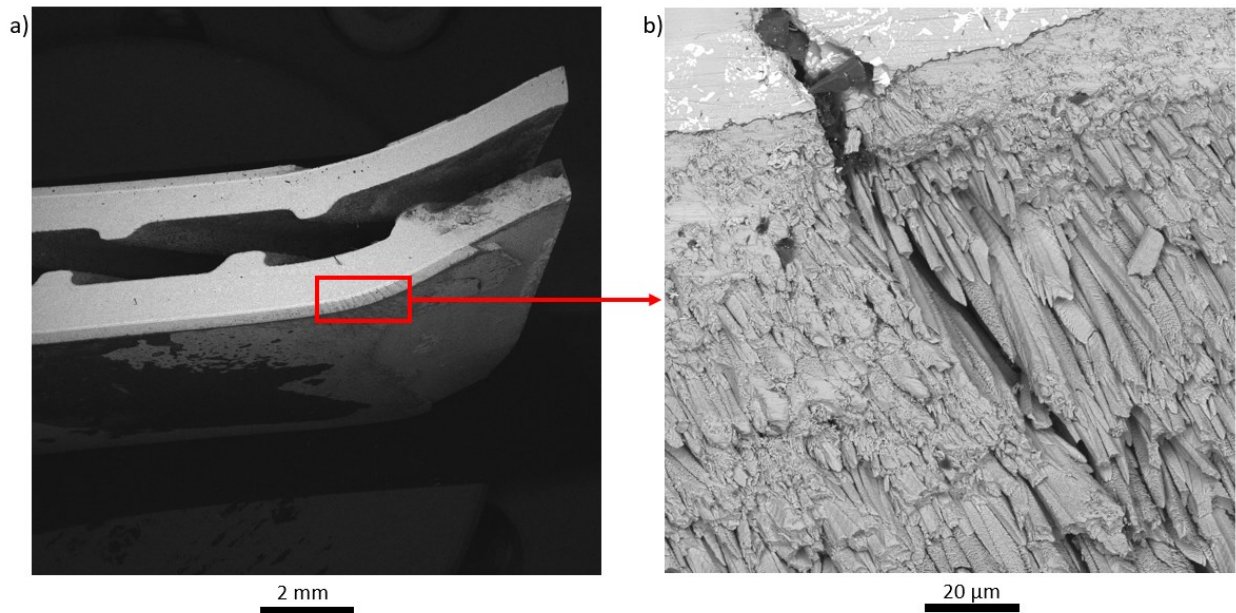
*Figure 3-34: Two SEM images of the buckled "as-deposited" blade. Image a) shows a low mag image of the full blade showing the buckled region, while b) is a high mag image showing cracking within the buckled region of the blade.*

These attempts to make CED specimens and to run CED tests on high pressure turbine blades uncovered the challenges that can arise when working with real engine hardware. The two

iterations of engine hardware that were provided by GE were either too fragile or too curved to be used as viable candidates for CED testing. This is not to say that such tests cannot be done, Lockyer-Bratton [20] previously showed CED testing of engine hardware is possible, but further iterations of blades and CED testing were not feasible within the scope of the current study. For future work, two guiding principles must be emphasized. First, the samples provided must be geometrically robust and thick enough to prevent buckling during compressive loading. Secondly the surfaces of the samples should be judiciously chosen to allow for adherence and nearly axial loading of the stiffener plates.

3.5  Chapter Summary

The work presented in this chapter highlighted the results of tests conducted on CED specimens coated with GE's standard (Ni,Pt)Al/8YSZ EBPVD TBC before and after various degrees of JETS thermal exposure. DIC maps were employed to identify the critical shear stress associated with crack growth. The critical stress was measured for consecutive stages of JETS thermal cycling and a value of 463 MPa was measured for the "as-deposited" JETS CED specimens.  The critical stress was measured to be similar (442 MPa) for the "early-in-life" specimens and to decay significantly in the later stages of life (353 MPa "mid-life" and 210 MPa in the "late-in-life") specimens. SEM observations and EDS analysis of the CED specimen fracture surfaces showed a transition from a predominantly TGO surface in the "as-deposited" state to mixed surface with interpenetrating metallic (bond coat) and ceramic (TGO and topcoat) islands in the "mid-life" and "late-in-life" specimens. Cross-sectional images of the CED substrates elucidated the onset of rumpling in the bond coat and micro-cracking in the topcoat as a result of transient thermal cycling. These observations, combined with the fact that the TGO thickness in

the late-in-life specimens was less than has been reported in previous studies, indicate that TBC failure in JETS specimens is controlled by bond coat rumpling that accelerates after an initial incubation period. This inference is supported by the measured critical stress values, which are relatively constant in the initial stages but decrease significantly in the latter stages.

Comparisons of the JETS CED results with Lockyer-Bratton's FCT CED results [1] highlight the fact that interfacial toughness degrades with thermal cycling in both cases. The initial toughness values are comparable in the early stages of life but appear to degrade more rapidly in the latter stages of life for the JETS CED specimens. The measurements reported in this study provide a relative measure of interfacial toughness and can be used to determine trends in the data such as the rate of decay of interfacial toughness as a function of thermal exposure.

Finally, attempts to test high-pressure turbine blades coated with GE's standard TBC have shown both the promise and the challenges of using the CED test on engine hardware. Two sets of blades were provided by GE but both were unsuitable for testing due to a lack of support between the two sides of the blades, leading to local buckling of the substrate. While previous efforts by Lockyer-Bratton [20] show that testing of real engine hardware can be done, the efforts in this study highlight the need for robust and thick blades to prevent buckling that also allow for adherence and nearly axial loading of the stiffener plates. This is at odds with the fact that modern blades have internal cooling channels and holes and contours that are anything but flat and straight.

References:

[1]: Lockyer-Bratton, S., *Experimental measurements of thermal barrier coating interfacial fracture toughness as a function of mode-mix*. Ph.D. Thesis, Johns Hopkins University, 2016.

[2]: Théry, P.Y., et al., *Spallation of two thermal barrier coating systems: experimental study of adhesion and energetic approach to lifetime during cyclic oxidation.* Journal of Materials Science, 2008. **44**(7): p. 1726-1733.

[3]: Théry, P.Y., Dupeux, M., Braccini, M., *Adhesion energy of a YPSZ EB-PVD layer in two thermal barrier coating systems.* Surface & Coating Technology, 2007. **202**: p. 648-652.

[4]: Materials, H.A. Araldite 2011 Technical Data Sheet. 2007.

[5]: LePage, W., Shaw, J., Daly, S., *Optimum Paint Sequence for Speckle Patterns in Digital Image Correlation.* Exp Tech, 2017. **41**: p. 557–563

[6]: Chu, T.C., W.F. Ranson, and M.A. Sutton, *Applications of digital-image correlation techniques to experimental mechanics.* Experimental Mechanics. **25**(3): p. 232-244.

[7]: https://digitalimagecorrelation.org/

[8]: Reu, P., *All about speckles: Aliasing.* Exp Tech, 2014. **38**(5): p. 1-3.

[9]: Reu, P., *All about speckles: Speckle Size Measurement.* Exp Tech, 2014. **38**(6): p. 1-2.

[10]: Evans, A.G., Mumm, D.R., Hutchinson, J.W., Meier, G.H, Pettit, F.S., *Mechanisms controlling the durability of thermal barrier coatings.* Progress in Materials Science, 2001. **46**(5): p. 505-553.

[11]: Spitsberg, I.T., Mumm, D.R., Evans, A.G., *On the failure mechanisms of thermal barrier coatings with diffusion aluminide bond coatings.* Materials Science and Engineering, 2005. **394**(1-2): p. 176-191.

[12]: Tolpygo, V.K., Clarke, D.R., *On the rumpling mechanism in nickel-aluminide coatings: Part II: characterization of surface undulations and bond coat swelling.* Acta Materialia, 2004. **52**(17): p. 5129-5141

[13]: Birks, N., Meier, G., & Pettit, F., *Introduction to the High Temperature Oxidation of Metals (2nd ed.).* Cambridge: Cambridge University Press, 2006.

[14]: Tolpygo, V.K., Clarke, D.R., *Surface rumpling of a (Ni, Pt)Al bond coat induced by cyclic oxidation.* Acta Materialia, 2000. **48**(13): p. 3283-3293

[15]: Tolpygo, V.K., Clarke, D.R., *On the rumpling mechanism in nickel-aluminide coatings: Part I: an experimental assessment.* Acta Materialia, 2004. **52**(17): p. 5115-5127

[16]: Balint, D.S., Hutchinson, J. W., *An analytical model of rumpling in thermal barrier coatings.* Journal of the Mechanics and Physics of Solids, 2005. **53**(4): p. 949-973.

[17]: Chen, M. W., Glynn, M. L., Ott, R. T., Hufnagel, T. C., Hemker, K. J., *Characterization and modeling of a martensitic transformation in a platinum modified diffusion aluminide bond coat for thermal barrier coatings.* Acta Materialia, 2003. **51**(14): p. 4279-4294.

[18]: Mumm, D.R., Evans, A.G., Spitsberg, I.T., *Characterization of a cyclic displacement instability for a thermally grown oxide in a thermal barrier system.* Acta Materiala, 2001. **49**(12): p. 2329-2340.

[19]: Karlsson, A. M., Hutchinson, J. W., Evans, A. G., *A fundamental model of cyclic instabilities in thermal barrier systems.* Journal of the Mechanics and Physics of Solids, 2002. **50**: p. 1565-1589.

[20]: Lockyer-Bratton, S., *Unpublished Work*

**Chapter 4: Application of CED Test to Furnace Cycled TBCs with LPPS Bond Coats**

This chapter details the work performed a P&W TBC system, which consists of an LPPS NiCoCrAlY bond coat and an EPBVD 7YSZ topcoat. The sample preparation procedures for the FCT CED specimens are reviewed, and the differences between the procedures used for GE's JETS CED specimens are noted. Five FCT CED specimens cycled to from 0-50% of their thermal lifetime were tested, and the topcoats delaminated in one large piece. The stress-strain curves and DIC shear strain maps associated with crack growth are shared for each. The results for the critical stress associated with crack propagation for each specimen are given, along with the dependence of the critical stress on thermal cycling. A combination of plane-view and cross-sectional SEM imaging and EDS was used to analyze the fracture surfaces of the CED specimens.

4.1 FCT CED Specimen Preparation Procedure

Although P&W's FCT CED specimens were twice the size of GE's JETS CED specimens with coating on both sides of the sample, the same general specimen preparation procedure was used for both. The key steps were to deposit a 7YSZ coating on CED substrates at Pratt & Whitney, trim the topcoat to a well-defined geometry, acid etch the bond coat to form a pre-crack, adhere stiffener plates to the topcoat, polish the ends of the specimen to ensure flat loading surfaces, and apply a speckle pattern to allow for the use of DIC.

The CED specimens used for the current study contained substrates made from <100> single crystals of P&W 1484 with dimensions $L = 20$ mm, $w = 10$ mm, and $h = 3$ mm that were coated with a LPPS NiCoCrAlY bond coat/YSZ EBPVD topcoat provided by P&W. Fabrication of the substrates and application of the coatings was performed by P&W before being sent to JHU. Application of the topcoat was done using the custom-built fixture described in Chapter 2 and

shown in Figure 2-2. The CED specimens were loaded into the fixture, which was tack welded to the base of a blade so that it could be mounted into the same EBPVD chambers used to coat engine hardware. The number of CED samples coated in a single run was chosen to match the thermal mass of actual engine hardware and shadowing brackets were added to ensure that the angle of topcoat deposition matched what blades see. Figure 4-1 a) shows an image of an "as-deposited" CED specimen.

Since the frame that held the CED substrates during coating shadowed them such that they were only coated in the middle 75% (15 mm) of the substrate, no excess coating on the front and back faces needed to be removed. However, the side surfaces contained excess coating, see Figure 4-1 b), and was removed by polishing the side surfaces with 1200 grit (P-4000) SiC papers using an Allied Technology Tech-Prep 8 automatic polisher, see Figure 4-1 c).
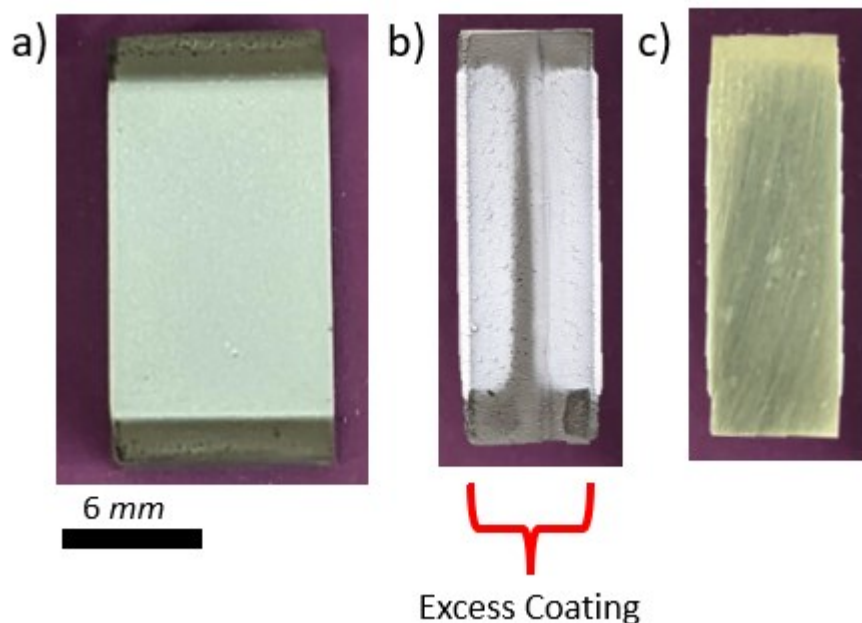


*Figure 4-1: Image a) shows the front face of a coated P&W FCT CED specimen while b) shows the excess coating on the side surface of the P&W FCT CED specimen and c) shows the polished side surface.*

A total of six CED specimens were coated in the first campaign; two were tested in the as-deposited state and four were thermal cycled in an FCT furnace at Pratt & Whitney using a standard 1-hour cycle. This process was repeated until a certain number of cycles were performed, corresponding to designated points of the coating's predetermined furnace cycled lifetime. Of the four thermally cycled FCT specimens that were provided to JHU by P&W, the coatings of one of the two "early-in-life" (25% of thermal lifetime) and both of the "mid-life" (50% of thermal lifetime) specimens were damaged during shipping. Based on the results from this first batch of specimens, a second campaign of CED was undertaken by Pratt & Whitney but were not received in time to include here. Partial delamination of the coating occurred on one side of the damaged "early-in-life" specimen and one side remained undamaged. For the "mid-life" specimens, one sample suffered partial delamination on one side and full delamination on the other, while full delamination occurred on both sides of the second sample.

To test the damaged specimens, the delaminated coating was machined away so that only a rectangular portion of coating that was fully adhered to the surface remained. The coating was removed using the same process and diamond sintered dental tool described in Chapter 3; however, the cutting process was iterated in steps of 12.7 µm (as opposed to 25.4 µm) to protect the coating from chipping during cutting. Figure 4-2 shows an image of the "mid-life" FCT CED specimen that had a) fully delaminated on one side and b) partially delaminated on the other, as well as c) an image of the partially damaged side with the stiffener plate epoxied to the topcoat.
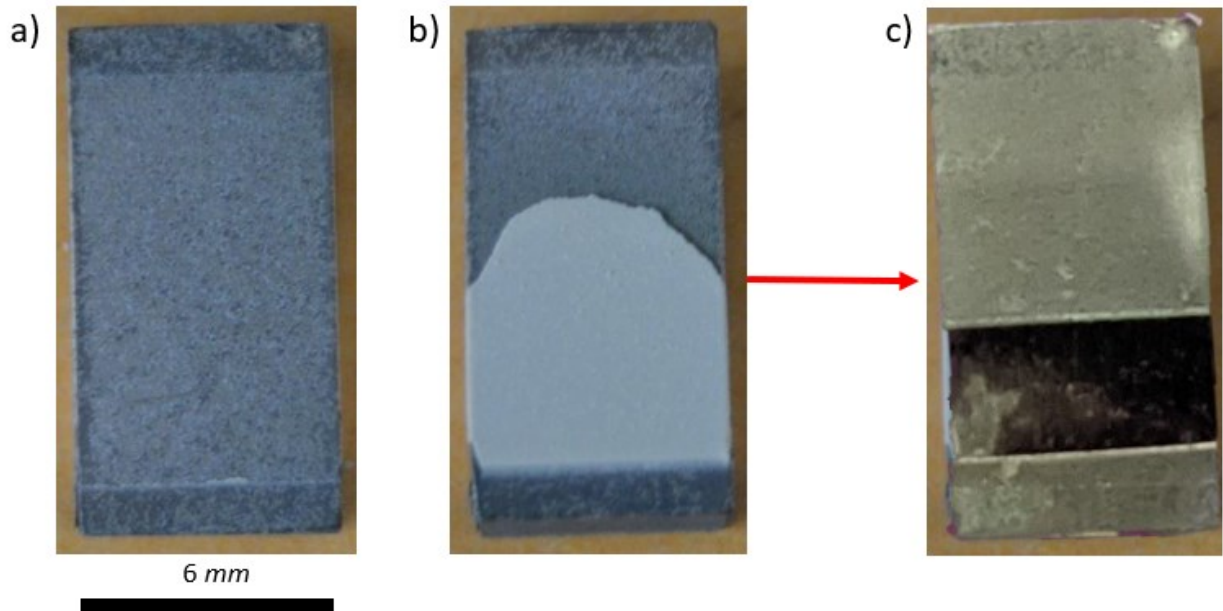
*Figure 4-2: Image a) shows the "mid-life" FCT CED specimen that was fully delaminated side, while b) shows the partially delaminated side and c) shows the partially delaminated side after removal of the damaged coating and attachment of a stiffener plate.*

Alternative methods for initiating a pre-crack were considered and explored. These included mechanical fatigue, laser machining, and elemental poisoning of a portion of the surface [1,2], but acid etching proved to be the most practical. The topcoat was too compliant for mechanical fatigue, accurate placement and creation of deep laser cuts was too difficult and introducing carbon or other impurity elements into Pratt & Whitney's coater was a non-starter.

The CED specimens with $L = 20$ mm and $h = 3$ mm require a crack length of $a = 4.5$ mm to avoid edge effects and assure steady-state crack propagation. In contrast to placing interfacial cracks at specific interfaces, removal of the bond coat provided a macro-scale stress concentration that allowed the delamination crack to form and propagate along the weakest fracture path. Acid etching and stripping of the bond coat is a common process in hardware refurbishment, and for the current study the etchant was chosen to be a 5-molar concentration of HCl heated to 80°C [3]. The specimens were placed in a 7 mm deep bath of HCl on a hot plate for one hour. Following this the samples were cleaned in isopropyl alcohol in a sonic bath for 10 minutes. Optical images of the

bond coat after etching showed that the bond coat was preferentially attacked with no visible damage to the substrate or topcoat. The attack occurred along the length of the bond coat at a position that was approximately 80 µm below the bond coat/topcoat interface, where SEM imaging revealed a region of elongated grains that may be result of stopping and restarting the deposition process that has been seen in the deposition of thin films [4]. At any rate, the acid etching process preferentially attacked this region. Figure 4-3 a) highlights the elongated grains while b) shows the effect of the etchant on this region. It should be noted that the elongated grains were primarily etched on the surface and were not fully etched through the thickness of the sample.
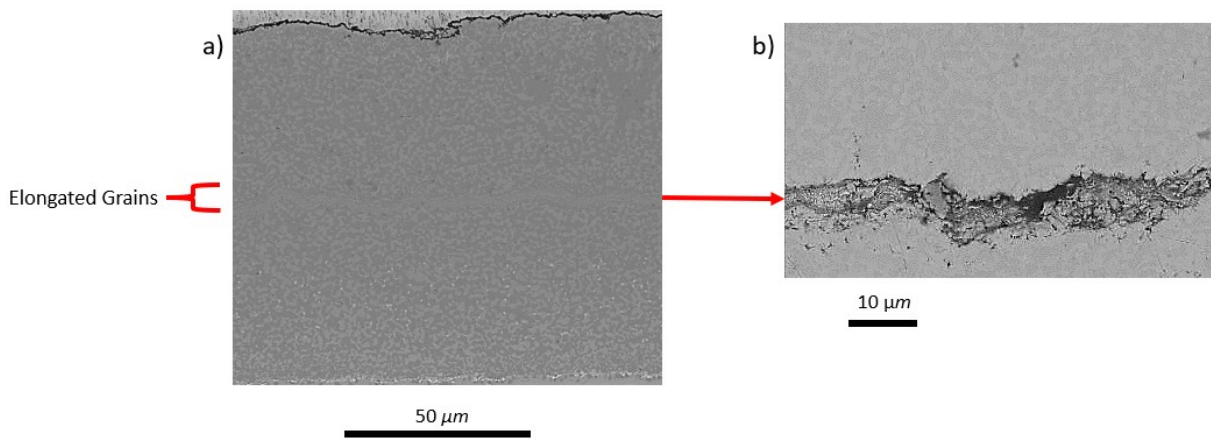


*Figure 4-3: SEM images showing a) the area of elongated grains before acid etching and b) showing the effect of acid etching on the elongated grains.*

Only the "as-deposited" P&W FCT CED specimens were acid etched. Due to the damage that occurred during the shipping, concern arose that acid etching the thermally cycled specimens would lead to premature delamination of the remaining coating. The results of the CED experiments for the "as-deposited" and thermally cycled specimens are presented in Section 4.2 and show that for all specimens, steady-state crack growth was initiated, and delamination occurred in the elastic loading region. This indicates that during CED testing cracks are able to self-nucleate and find the weakest fracture path even without pre-cracking or acid etching.

## 4.2 FCT CED Test Results

The P&W FCT CED specimens were loaded using an MTS servo-hydraulic machine with a 500 kN load cell. Details about the machine and control software can be found in Appendix B. For the P&W FCT specimens, a displacement rate of $\dot{\delta} = .002 \; {}^{mm}/_s$ was applied in order to impose a quasi-static strain rate of $\dot{\varepsilon} = 7 \times 10^{-5} \frac{1}{s}$. Load and displacement data were logged at a rate of 10 Hz, and images were taken one every second with a PixelLINK PL-B781U black and white 6.6 MP camera combined with an Edmund Optics MMS Imaging Lens R-1 rear assembly and OBJ-11 front objective mounted on a tripod. VIC-2D was used for DIC analysis of the CED experiments. A subset size of 31 x 31 pixels and a step size of 5 pixels chosen for each test. The P&W FCT CED specimens were coated on both sides allowing for crack growth on both sides of the substrate, but in practice the cracks did not advance symmetrically. The side and location (top or bottom) of crack initiation was random but once initiated the coating delaminated on one side and then the other. CED maps were used to monitor crack growth, and the analytical solution used in this study provides a qualitative measure of interfacial toughness for crack growth on one side of the CED specimen.

Consistent with Lockyer-Bratton's previous CED results [5], for each specimen crack growth began during the elastic portion of the stress-strain loading curve and on one side of the CED. The coating on the other face also delaminated but generally after the TBC detached from the first face and often only after the substrate was plastically deformed. The first interface to delaminate was used to define the interfacial toughness, and the images have been rotated such that it's the left side for for each test. The critical stress associated with crack propagation was defined as the point where the DIC shear strain reached at least 1% at a distance at least 1.5*$h$ (5 mm or 1/3$^{rd}$ of the length of the stiffener plate) away from the bottom or top edge of the stiffener plate. The critical

stress was determined from shear strain profile plots developed in the same manner as detailed for the previous CED experiments. Special note should be made of the "mid-life" sample, which was fully delaminated on one side prior to testing, so only the coated side (labelled "TBC-side) was monitored along a shorter length. Figures 4-4 through 4-8 show a) the shear strain profile plots of each test for the image where the stress associated with crack growth was determined, along with image immediately preceding it and b) the stress-strain curves for each specimen, along with a callout (star) of critical stress associated with crack growth. The stresses are obtained by dividing the applied load by the cross-sectional area of the substrate, while the strain values are the DIC values for $\varepsilon_{yy}$ in the substrate. The VIC 2D shear strain map ($\varepsilon_{xy}$) corresponding to the critical stress for crack growth is also shown.
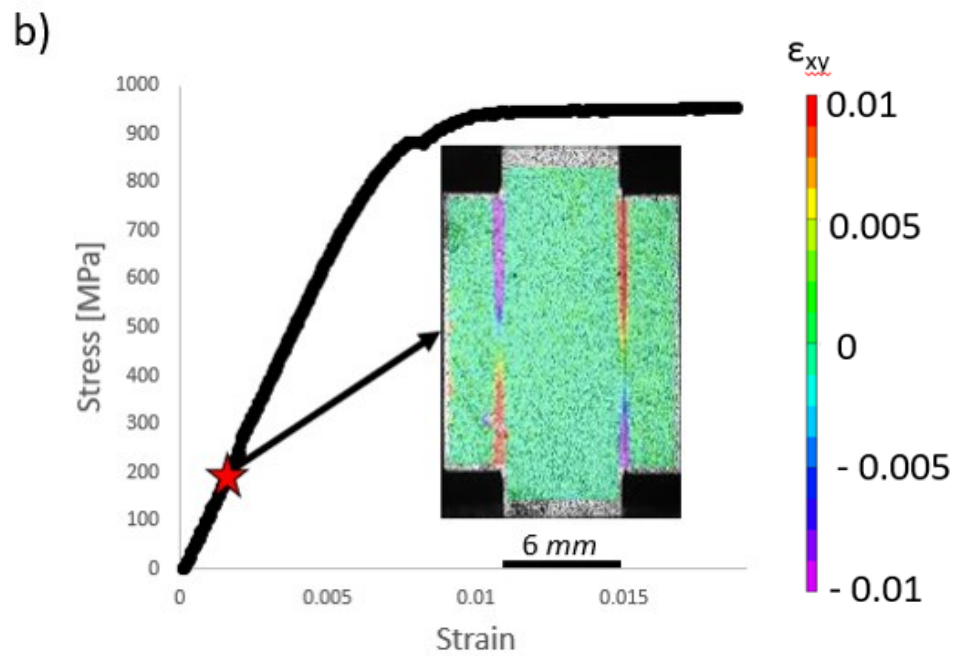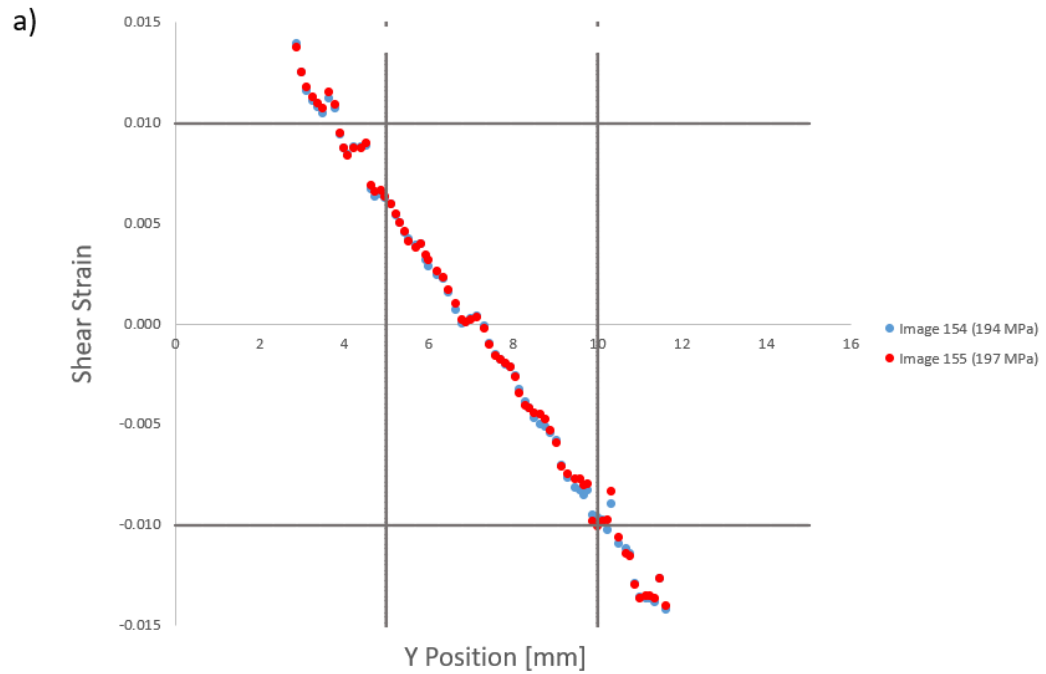
*Figure 4-4: Shown in a): Shear strain profile plot for an "as-deposited" (0% furnace cycling) FCT CED specimen #1. The red curve marks the image were the criteria for critical stress associated with crack growth was met on the left side of the sample. Shown in b): Stress-strain plot for the specimen with the critical stress associated with crack growth (197 MPa) marked by a red star, with the shear strain map of the sample shown as well.*
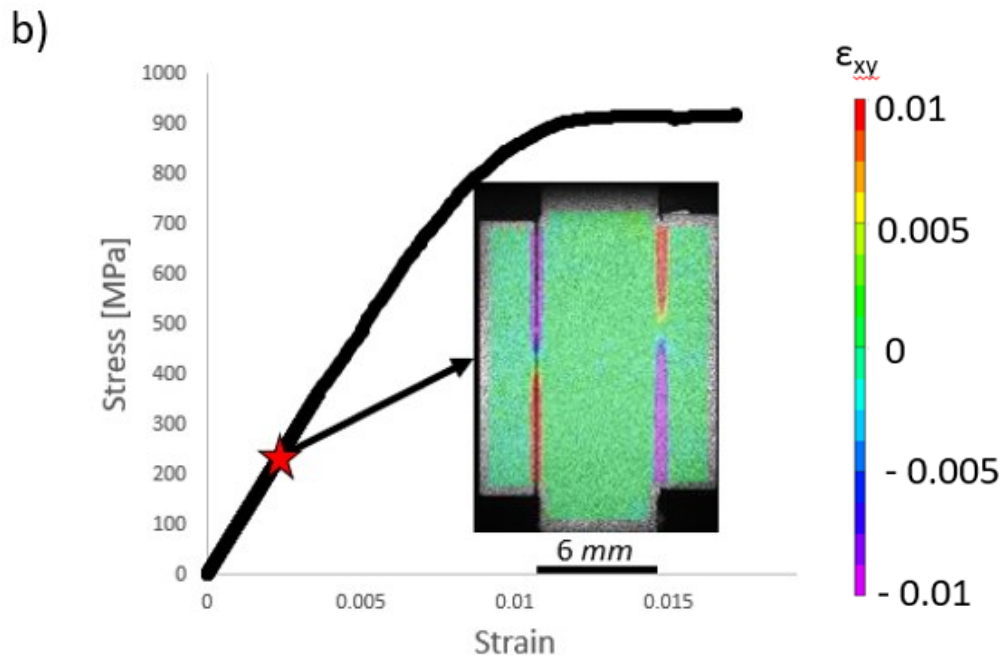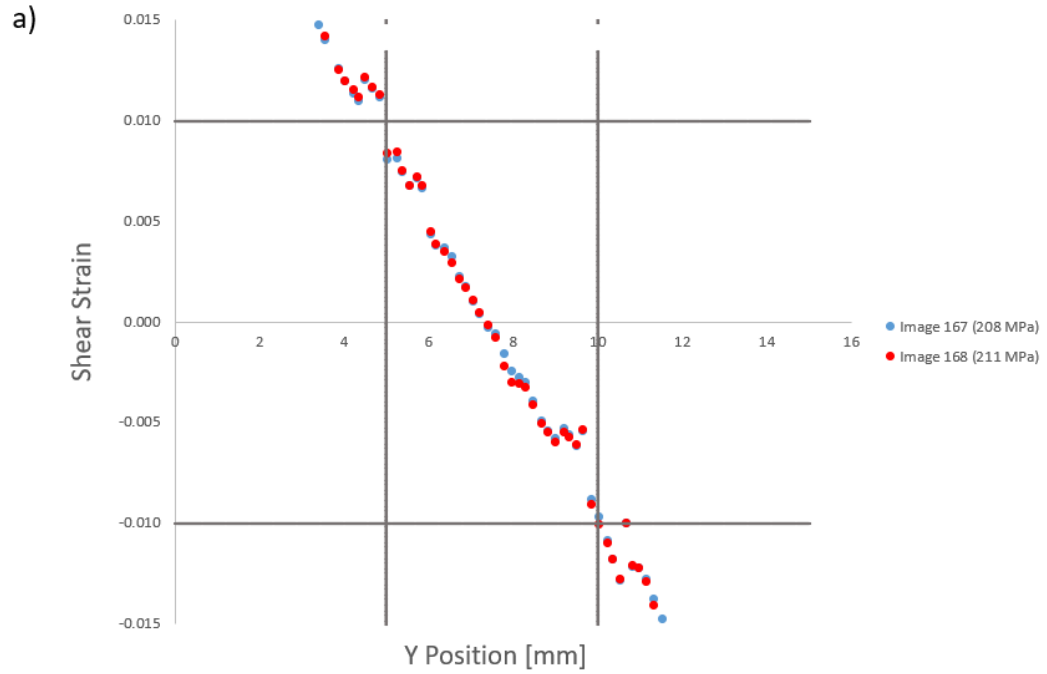
*Figure 4-5: Shown in a): Shear strain profile plot for an "as-deposited" (0% furnace cycling) FCT CED specimen #2. The red curve marks the image were the criteria for critical stress associated with crack growth was met on the left side of the sample. Shown in b): Stress-strain plot for the specimen with the critical stress associated with crack growth (211 MPa) marked by a red star, with the shear strain map of the sample shown as well.*
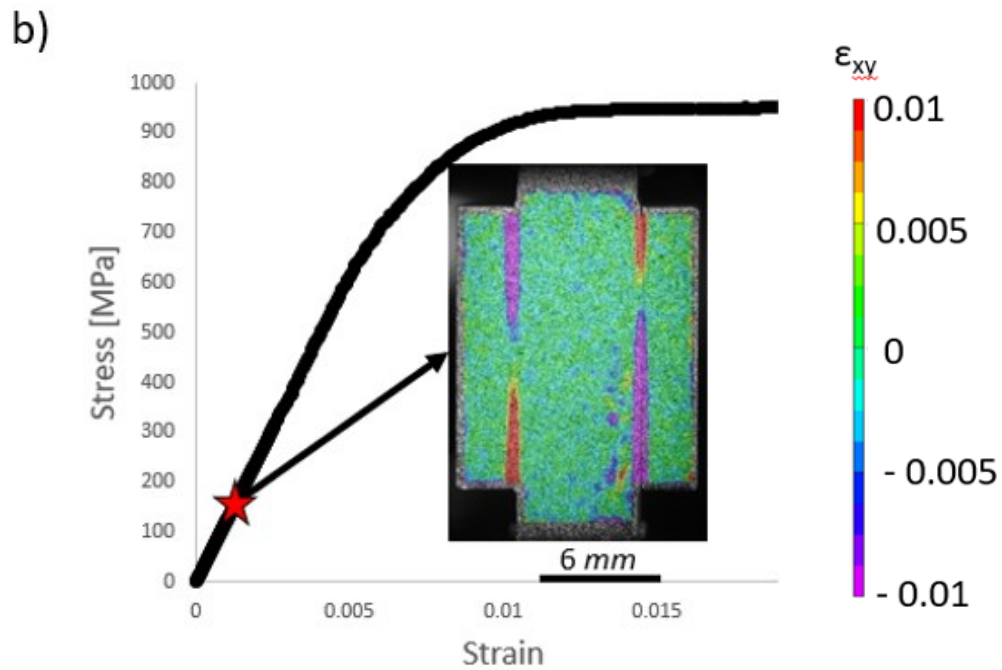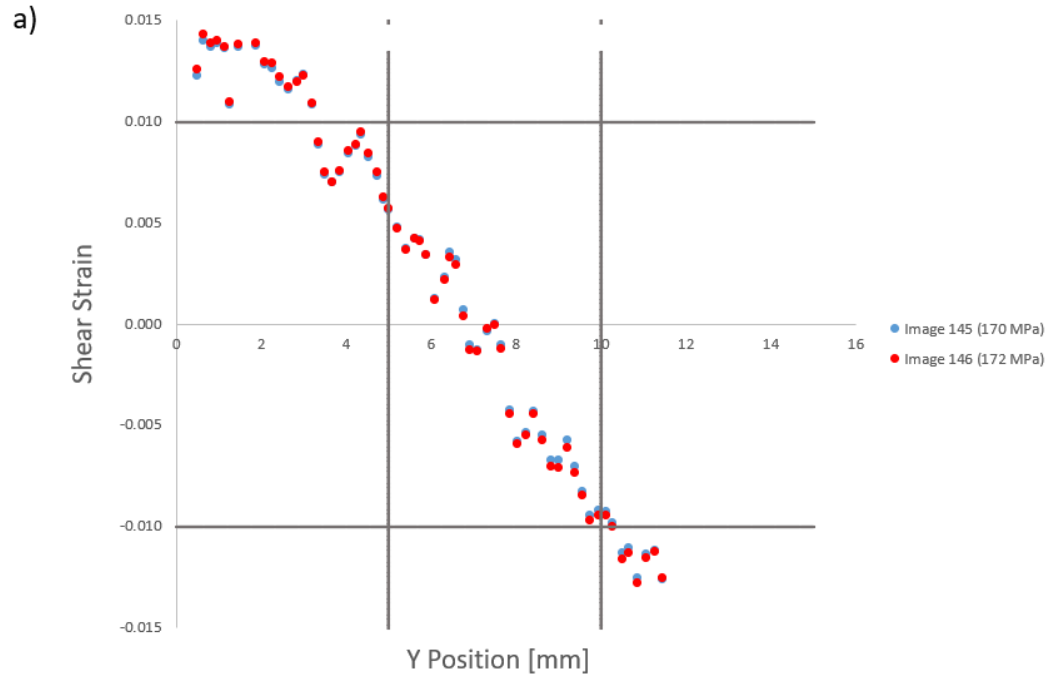
*Figure 4-6: : Shown in a): Shear strain profile plot for an "early-in-life" (25% furnace cycling) FCT CED specimen #3. The red curve marks the image were the criteria for critical stress associated with crack growth was met on the left side of the sample. Shown in b): Stress-strain plot for the specimen with the critical stress associated with crack growth (172 MPa) marked by a red star, with the shear strain map of the sample shown as well.*
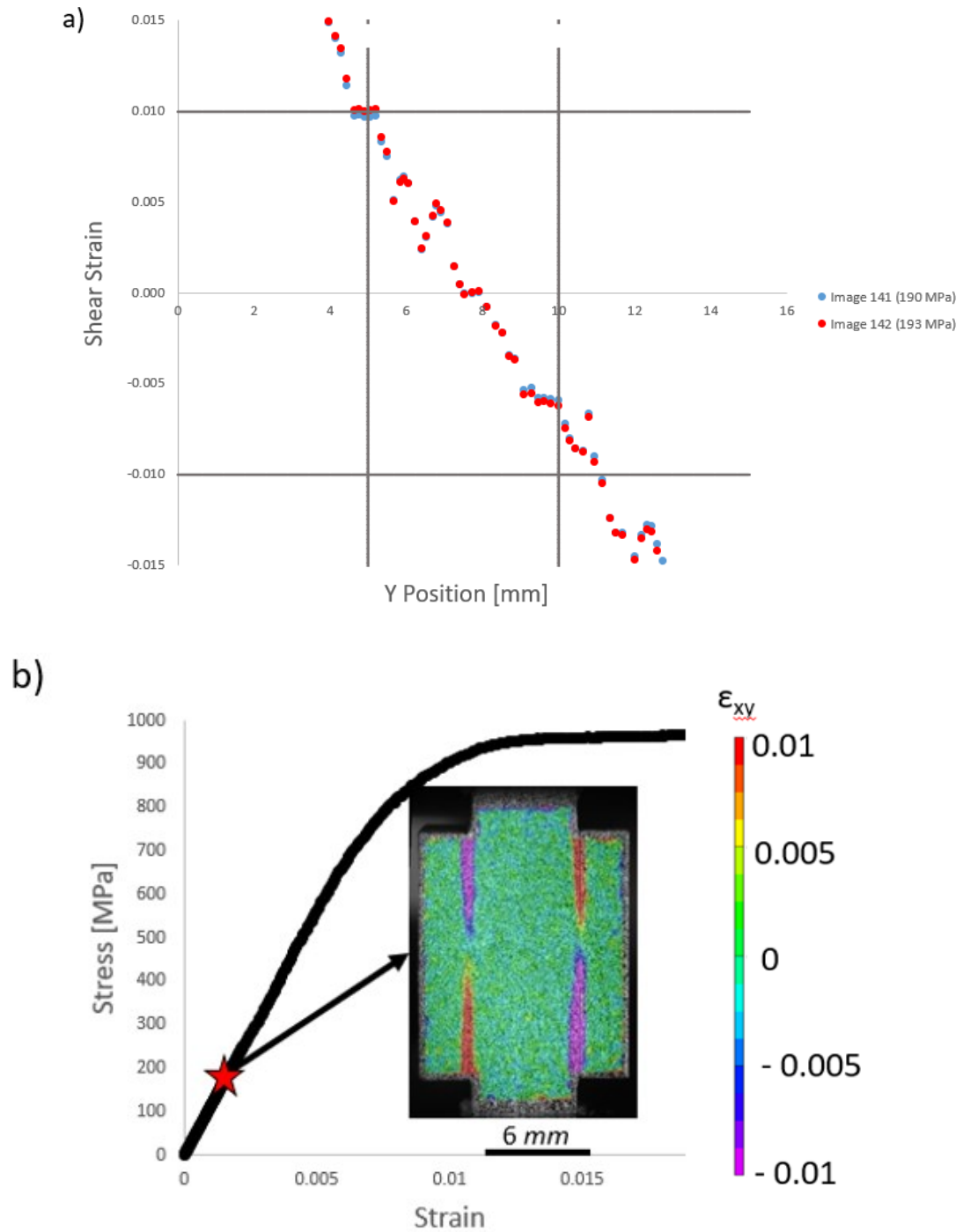
*Figure 4-7: Shown in a): Shear strain profile plot for an "early-in-life" (25% furnace cycling) FCT CED specimen #4. The red curve marks the image were the criteria for critical stress associated with crack growth was met on the left side of the sample. Shown in b): Stress-strain plot for the specimen with the critical stress associated with crack growth (193 MPa) marked by a red star, with the shear strain map of the sample shown as well.*
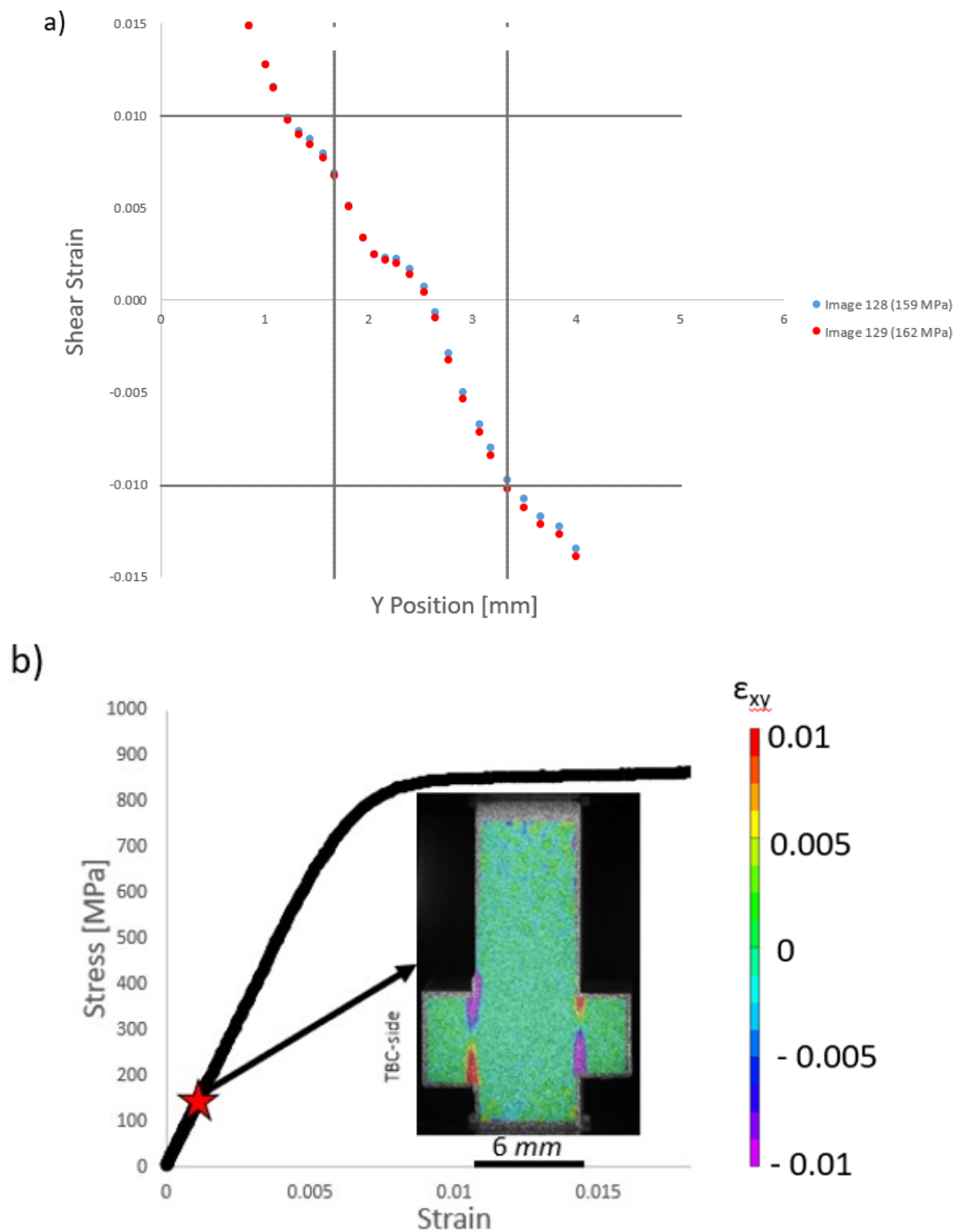
*Figure 4-8: Shown in a): Shear strain profile plot for an "mid-life" (50% furnace cycling) FCT CED specimen #5. The red curve marks the image were the criteria for critical stress associated with crack growth was met on the left side of the sample. Shown in b): Stress-strain plot for the specimen with the critical stress associated with crack growth (162 MPa) marked by a red star, with the shear strain map of the sample shown as well.*

Stable crack growth leading to delamination during the elastic region was observed on at least one side of every FCT CED specimen tested. For the specimens where both sides were coated, delamination did not occur on the second side until after the first side delaminated, and it usually occurred in the plastic region. For the "as-deposited" specimens that were acid-etched, delamination did not always begin on the end of the specimen that had been acid etched. For the thermally cycled samples that were not acid etched, stable crack growth was still seen. These results imply that the interface was weak enough for the cracks to nucleate under the applied stress and that the formation of pre-cracks was not really required. Delamination of the FCT CED specimens always occurred between the substrate and TBC and the topcoat always came off in one full sheet. Additionally, delamination of the stiffener plate from the TBC either did not occur or did not occur until the plastic region of the test. A compilation of all of the critical stress values measured in these CED tests is given in Table 4-1. For the "as-deposited" specimens, an average critical stress associated with crack propagation of $204 \pm 7$ MPa was measured. That value dropped to $183 \pm 11$ MPa for the "early-in-life" specimens and 163 MPa for the "mid-life" specimen. From "as-deposited" to "mid-life" this is a drop of 42 MPa, or a decrease of ~ 20%.

*Table 4-1: Critical stress associated with crack propagation for each of the five tested FCT CED specimens.*

| Sample # | Furnace Cycle Lifetime | Critical Stress Associated with Crack Propagation [MPa] |
|---|---|---|
| 1 | 0% | 197 |
| 2 | 0% | 211 |
| 3 | 25% | 172 |
| 4 | 25% | 193 |
| 5 | 50% | 162 |

4.3 FCT CED Discussion

The results of the FCT CED tests shown in Fig. 4.4-4.8, represent the first ever measures of values for critical stress associated with Mode II crack propagation and delamination for an LPPS NiCoCrAlY/EBPVD 7YSZ TBC system. The critical stress was measured as a function of thermal cyclic exposure (fraction of FCT lifetime) and the Mode II interfacial toughness was found to degrade with increased numbers of FCT cycles. Figure 4-9 shows a plot for critical stress as a function of furnace cycle lifetime up to 50% of furnace cycle lifetime.
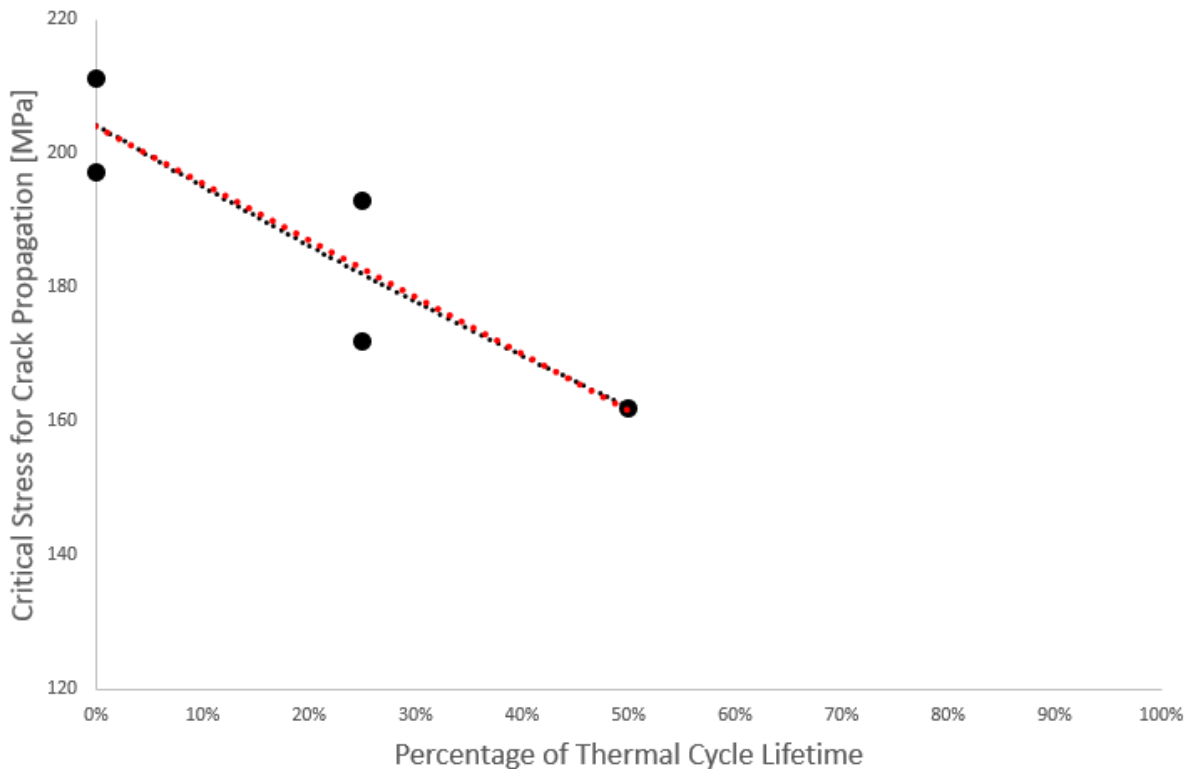


*Figure 4-9: Plot of critical stress associated with crack propagation as a function of furnace thermal cycling with an exponential fit curve shown in black and a linear fit curve shown in red.*

An exponential equation of the form in Equation 4-1 was fit to the data, shown in black in Figure 4-9.

*Equation 4-1*

$$\sigma_{Crit} = 204 \, e^{-0.46 t_{Life}}$$

131

Where $\sigma_{Crit}$ is the critical stress associated with crack propagation and $t_{Life}$ is the fraction of furnace cycle lifetime. A linear fit of the form shown in Equation 4-2 can also be applied to the curve, shown in red in Figure 4-9.

*Equation 4-2*

$$\sigma_{Crit} = 204 - 85t_{Life}$$

The differences between these two fit curves are minimal, so the exponential curve will be used moving forward to be consistent with Lockyer-Bratton's work [5].

Plugging the measured critical stress values into the analytical form of the solution for CED interfacial toughness (Equation 2-11) yielded estimates for interfacial toughness that are listed in Table 4-2. It is important to remember that Equation 2-11 overestimates the interfacial toughness of the specimens due to its simplified representation of the different layers, the fact that it does not account for interfacial friction, and its inaccurate assumption of full strain transfer into the stiffener plates. While full FE simulations would provide more accurate values for Mode II interfacial toughness, the analytical results can be used to determine trends in the data. A plot of interfacial toughness as a function of fraction of thermal cyclic (FCT) lifetime is given in Figure 4-10. In the "as-deposited" state an average interfacial toughness of $1254 \pm 86$ J/m$^2$ is measured. In the "early-in-life" state, the average measured value is $1003 \pm 115$ J/m$^2$. This falls to 787 J/m$^2$ in the "mid-life" state, or a drop of ~40% from the "as-deposited" interfacial toughness value.

*Table 4-2: Interfacial toughness values for each of the five tested FCT CED specimens.*

| Sample # | Furnace Cycle Lifetime | Interfacial Toughness [J/m$^2$] |
|----------|------------------------|----------------------------------|
| 1 | 0% | 1168 |
| 2 | 0% | 1339 |
| 3 | 25% | 888 |
| 4 | 25% | 1118 |
| 5 | 50% | 787 |
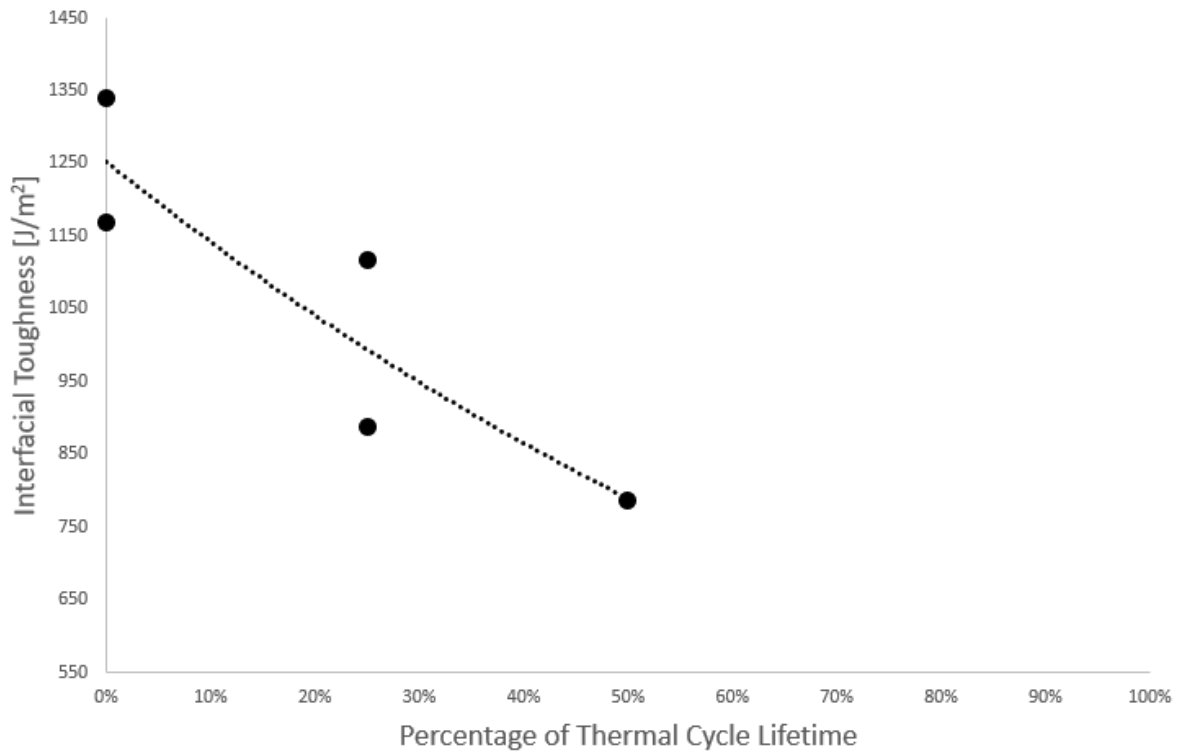


*Figure 4-10: Plot of interfacial toughness for P&W's FCT CED specimens with an LPPS NiCoCrAlY bond coat/YSZ EBPVD topcoat system as a function of furnace thermal cycling.*

An exponential fit was applied to the curve, shown in Equation 4-3.

*Equation 4-3*

$$G_C = 1250 \, e^{-0.92 * T_{Life}}$$

The manner in which delamination occurred for these FCT CED specimens was unique to other CED tests that have been run. As mentioned above, crack growth occurred at one interface during the elastic portion of the loading curve. In the CED specimens with a diffusion aluminide bond coat/EBPVD 8YSZ topcoat system, this led to a crack path that traversed through the topcoat, TGO, and bond coat with islands of each visible on the fracture surfaces. For the current set of FCT CED specimens with an LPPS NiCoCrAlY bond coat/EBPVD 7YSZ topcoat, full delamination of the coating occurred such that an entire layer of the coating detached from the substrate in one large piece. Figure 4-11 a) shows the last image shows the last image used for DIC from an "as-deposited" CED specimen test with the coating fully delaminated on both sides, while b) shows a fully delaminated coating after testing.
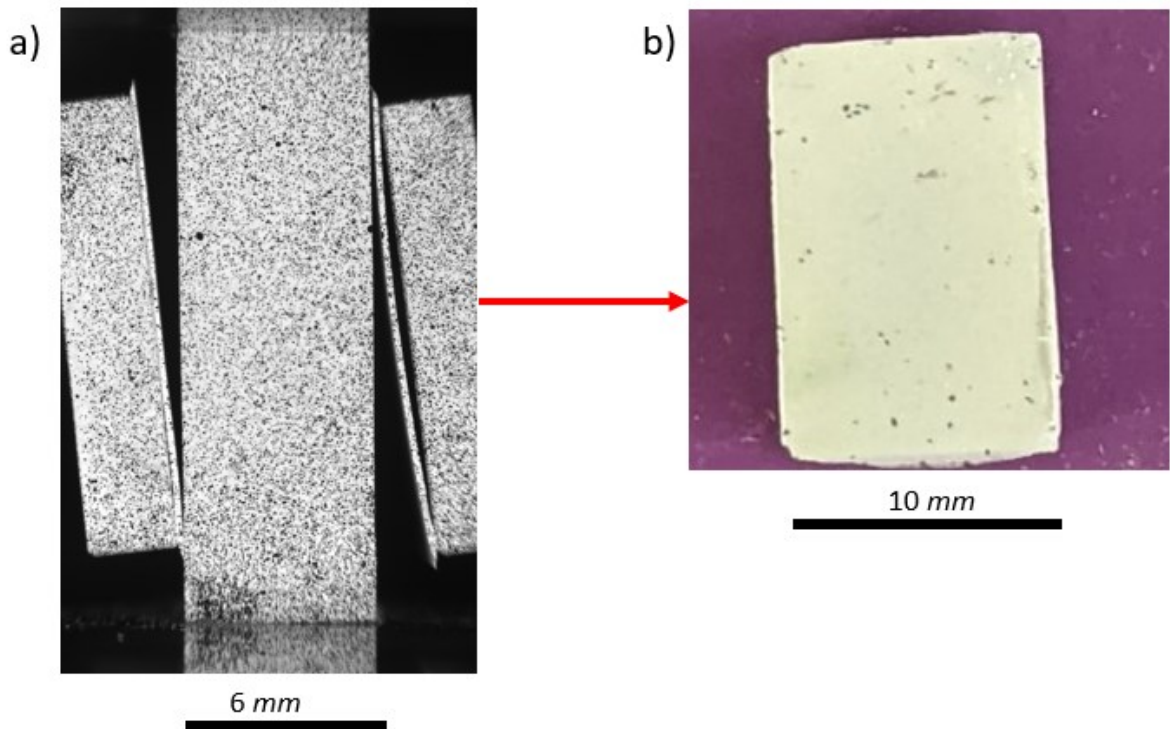


*Figure 4-11: Image a) shows the last DIC image from an "as-deposited" FCT CED specimen test with the coating fully delaminated on both sides, while b) shows a fully delaminated topcoat.*

A combination of BSE SEM imaging and EDS was used to understand the layer at which delamination occurred and to deduce why fracture occurred in the manner that it did. Cross-sectional SEM images of tested FCT CED specimens indicated that delamination occurred between the bond coat and the topcoat, see for example Figure 4-12 with images of the: a) "as-deposited", b) "early-in-life" and c) "mid-life" FCT CED specimens. These images show that in all cases fracture occurred between the bond coat and topcoat. Unlike the diffusion aluminide containing CED specimens, these images do not show any signs of bond coat rumpling; the fracture surface remained flat in all three specimens.
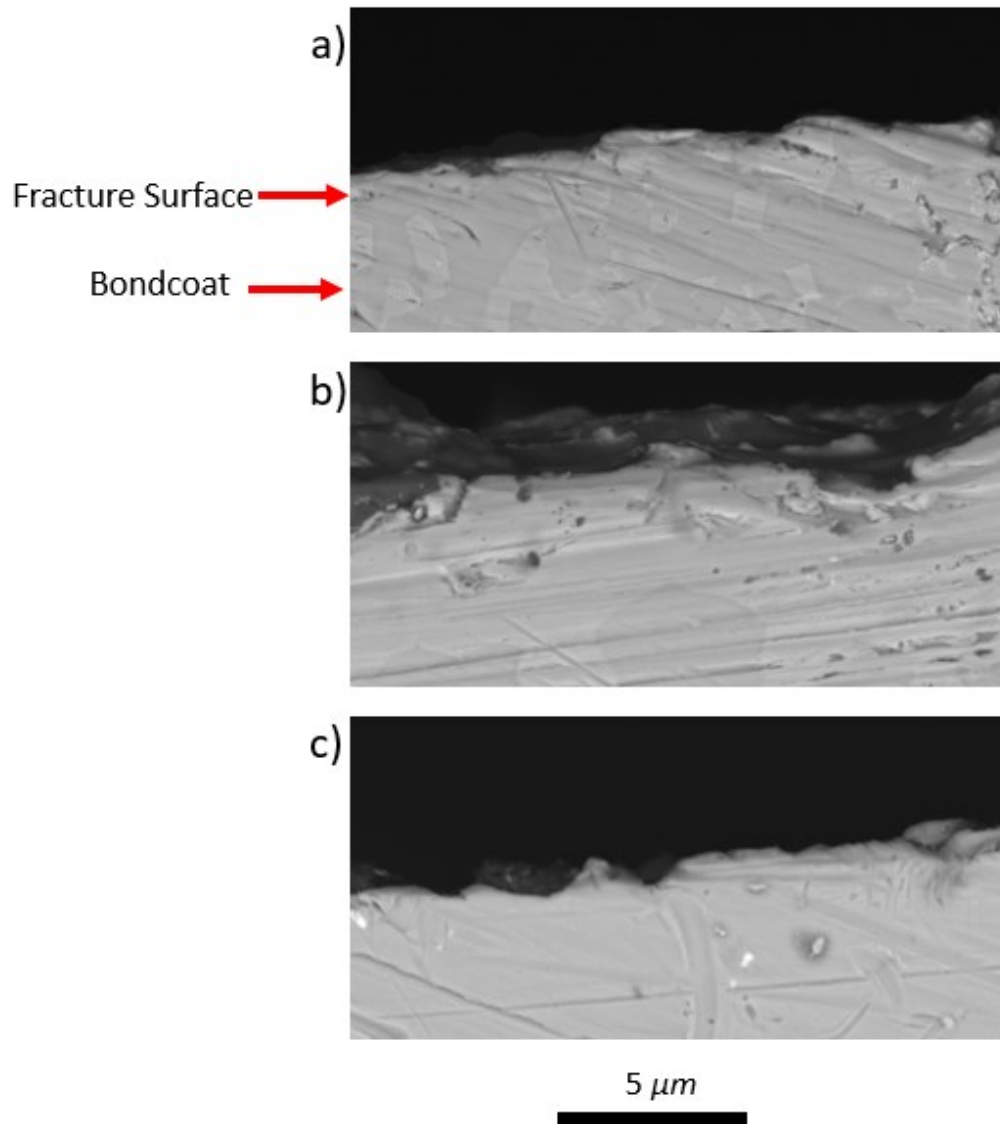
*Figure 4-12: Images showing the cross-sectional fracture surfaces for an a) "as-deposited", b) "early-in-life" and c) "mid-life" FCT CED specimen, with the bond coat and fracture surface labeled in a). In all three cases no rumpling is observed.*

The lack of rumpling in the bond coat provides an explanation as to why the topcoat delaminated in one large piece. The absence of undulations in the bond coat allows for a straight crack to propagate between the bond coat and topcoat without having to cut through different material layers. Once nucleated and grown to a critical length, the interfacial cracks were able to travel along the entire length of the interface, resulting in full delamination of the topcoat as

illustrated in Figure 4-11. SEM images of the fracture surfaces of a) "as-deposited", b) "early-in-life" and c) "mid-life" CED specimens are shown in Figure 4-13. Noticeable differences can be seen in the substrate fracture surfaces. In the "as-deposited" state, the fracture surface was finely mottled and uniform with an evenly distributed mix of white, grey and black areas. In the "early-in-life" specimens, large islands of white are apparent, and on the surface of the "mid-life" specimens these white regions increased in both size and volume fraction. The overall appearance of the mid-life specimens is that of interconnected white and light gray islands with dark gray lines along the borders.
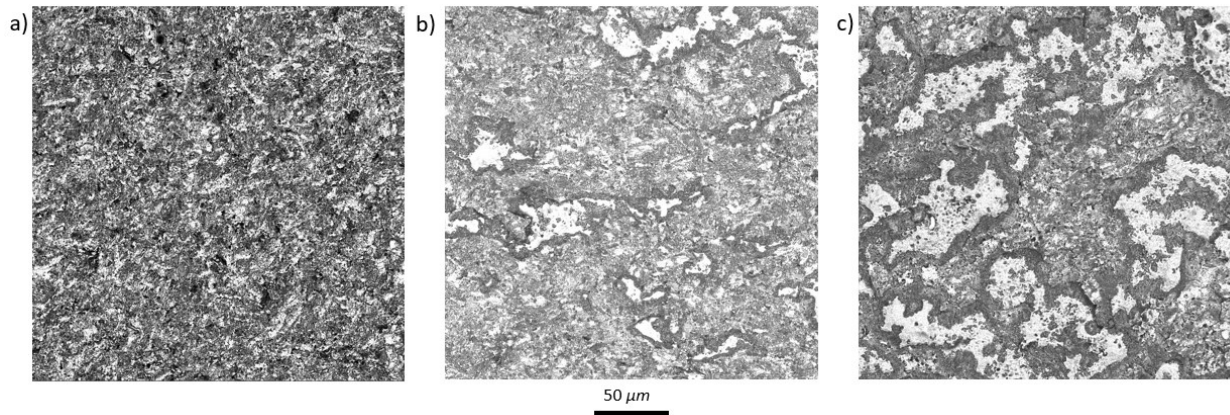


*Figure 4-13: Images showing the substrate fracture surfaces of a) "as-deposited", b) "early-in-life", and c) "mid-life" FCT CED specimens with P&W's LPPS NiCoCrAlY bond coat/EBPVD YSZ topcoat system.*

Chemical analysis (EDS) was performed on an "as-deposited" specimen to determine the elemental content and phases present on the fracture surfaces; the results are shown in Figure 4-14. Looking at these elemental maps, very little Ni was detected on the fracture surface on the substrate-side of the CED specimen. By contrast, significant amounts of O, Al and Zr were found on that surface. Moreover, the location of the Zr is inversely related to the location of the Al; the Zr content is low in the regions where Al is high and high in the regions where they are low. The O is found in both locations as both the TGO and topcoat are oxides. This implies that both the

TGO and the topcoat are present on the fracture surface of the CED specimens for the "as-deposited" specimens. With this and the absence of the bond coat, it can be inferred that for the "as-deposited" specimens the delamination progresses through the TGO or along the TGO/topcoat interface.
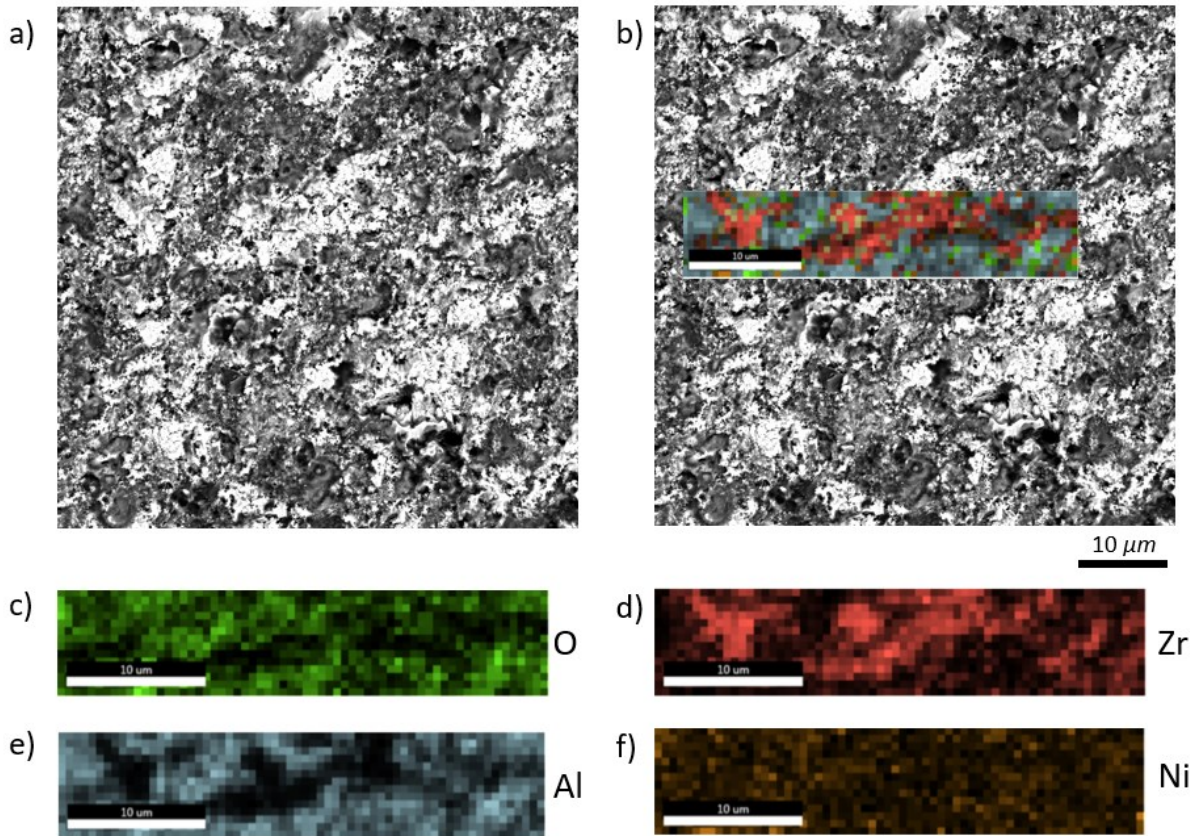


*Figure 4-14: Images showing a) a high-resolution SEM image of the substrate-side of the fracture surface for an "as-deposited" CED specimen and b) the same image with the EDS chemical analysis overlayed on the location where it was performed. The bottom images (c,d,e,f) show the individual elemental maps for the elements detected.*

EDS was also performed on the fracture surface of "mid-life" CED specimen, shown in Figure 4-15. Looking at these elemental maps, the presence of two distinct phases on the substrate-side of the fracture surface were identified. The first is the exposure of Ni-rich bond coat corresponding to the bright white regions in the SEM images and gold regions in the EDS map. The remainder of the fracture surface contains Al and O, meaning the dark grey areas in the SEM micrograph

(blue-green area in the EDS map) correspond to the alumina TGO. This can be confirmed when looking at Figure 4-13 c), where darker grey regions representing the TGO are seen decorating the edges of the white bond coat layer. Notably, the absence of Zr in the elemental EDS map indicates a lack of topcoat remaining on the substrate-side of the delamination in the specimens that were FCT cycled to approximately half of their life. This suggests that the delamination progressed along the bond coat/TGO interface in the "mid-life" specimens. This leads to the conclusion for P&W's FCT CED specimens, that delamination occurs below the TGO once furnace cycling resulted in a substantial TGO.
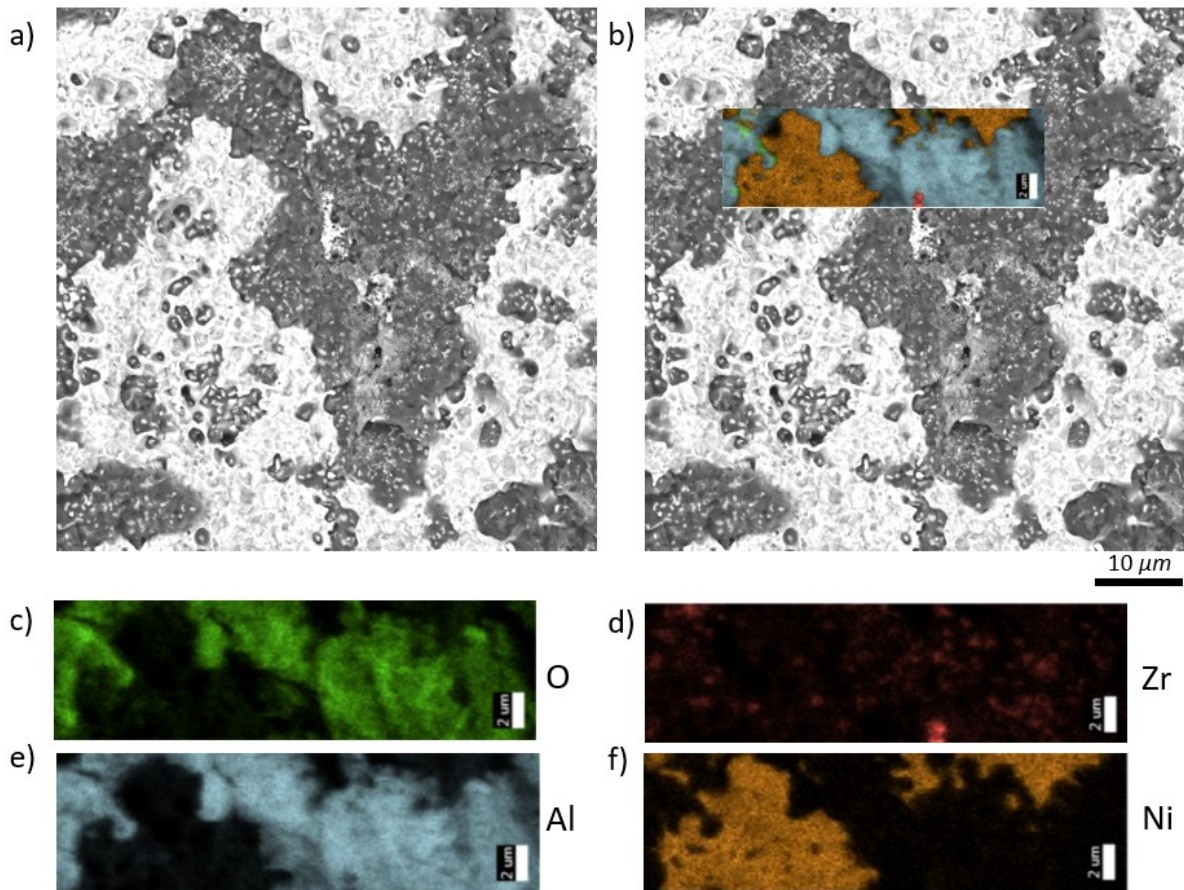


*Figure 4-15: Images showing a) a high-resolution SEM image of the substrate-side fracture surface for a "mid-life" CED specimen and b) with the EDS chemical analysis overlayed on the location it was performed. The bottom images (c,d,e,f) show the individual elemental maps for the elements detected.*

SEM imaging and EDS of the topcoat-side of the fracture surfaces (e.g. of the fully delaminated topcoat) were also taken in order to confirm this finding. Figure 4-16 shows the fracture surface for the a) "as-deposited" topcoat while b) shows a "mid-life" specimen. In both images the bulk of the fracture surface was white, representing the topcoat layer that has fully delaminated off the substrate. However, a noticeable change can be seen in the amount of dark grey pockets on the surface of each specimen. In the "as-deposited" state, very fine dark grey features speckle the fracture surface while in the "mid-life" specimen, the size of these dark grey features are greater, including the presence of several dark grey islands that are tens of microns in size.
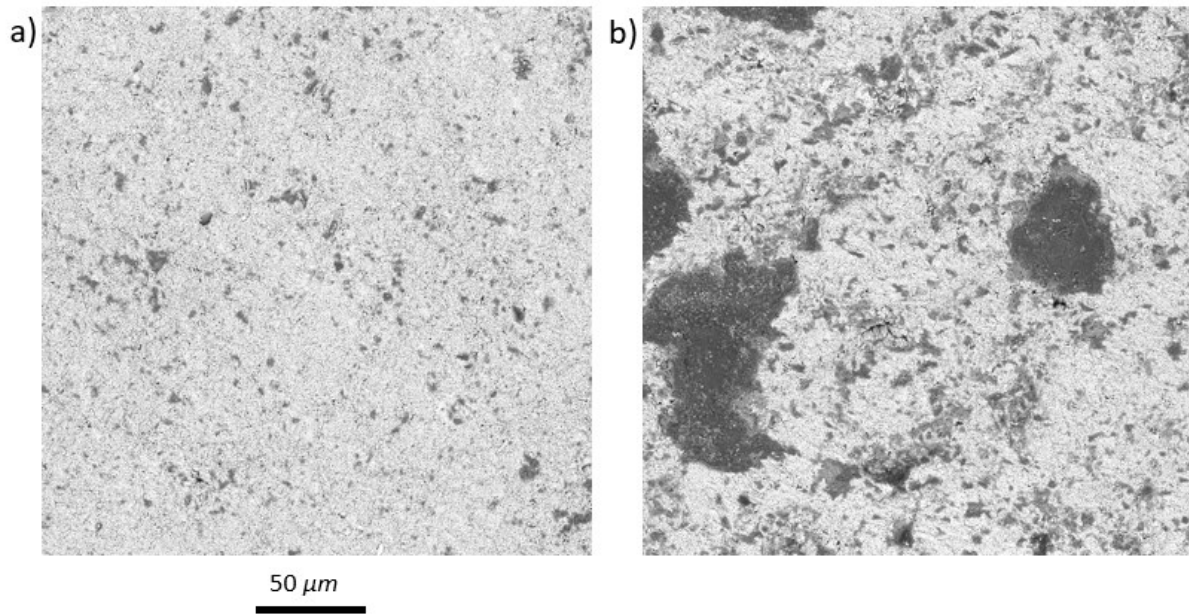


*Figure 4-16: Images showing the topcoat fracture surfaces of a) "as-deposited" and b)"mid-life FCT CED specimens with P&W's LPPS NiCoCrAlY bond coat/EBPVD YSZ topcoat system.*

In order to confirm the elements present on each fracture surface, EDS was performed on both specimens. Figure 4-17 shows the EDS results for the "as-deposited" topcoat fracture surface.
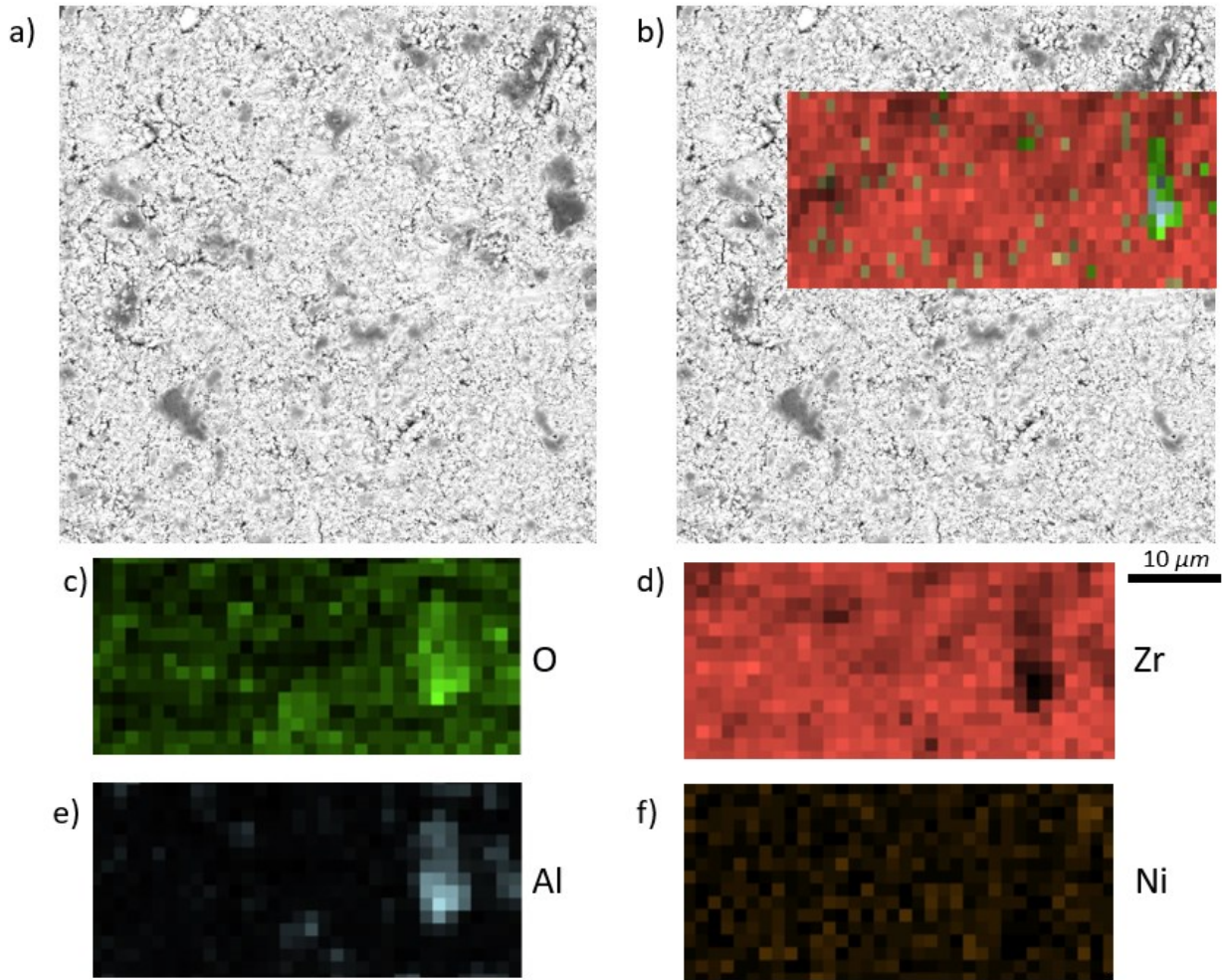
*Figure 4-17: Images showing a) a high-resolution SEM image of the topcoat-side of the fracture surface for an "as-deposited" CED specimen and b) with the EDS chemical analysis overlayed on the location it was performed. The bottom images (c,d,e,f) show the individual elemental maps for the elements detected.*

Looking at the elemental maps it can be seen that the fracture surface is almost entirely Zr and O, with nominally no Ni detected and a little bit of Al detected. This indicates that the fracture surface was almost entirely topcoat with a little bit of TGO on the surface, confirming prior observations about the crack path for the "as-deposited" FCT specimen. EDS was also performed on the fracture surface of "mid-life" CED specimen, shown in Figure 4-18.
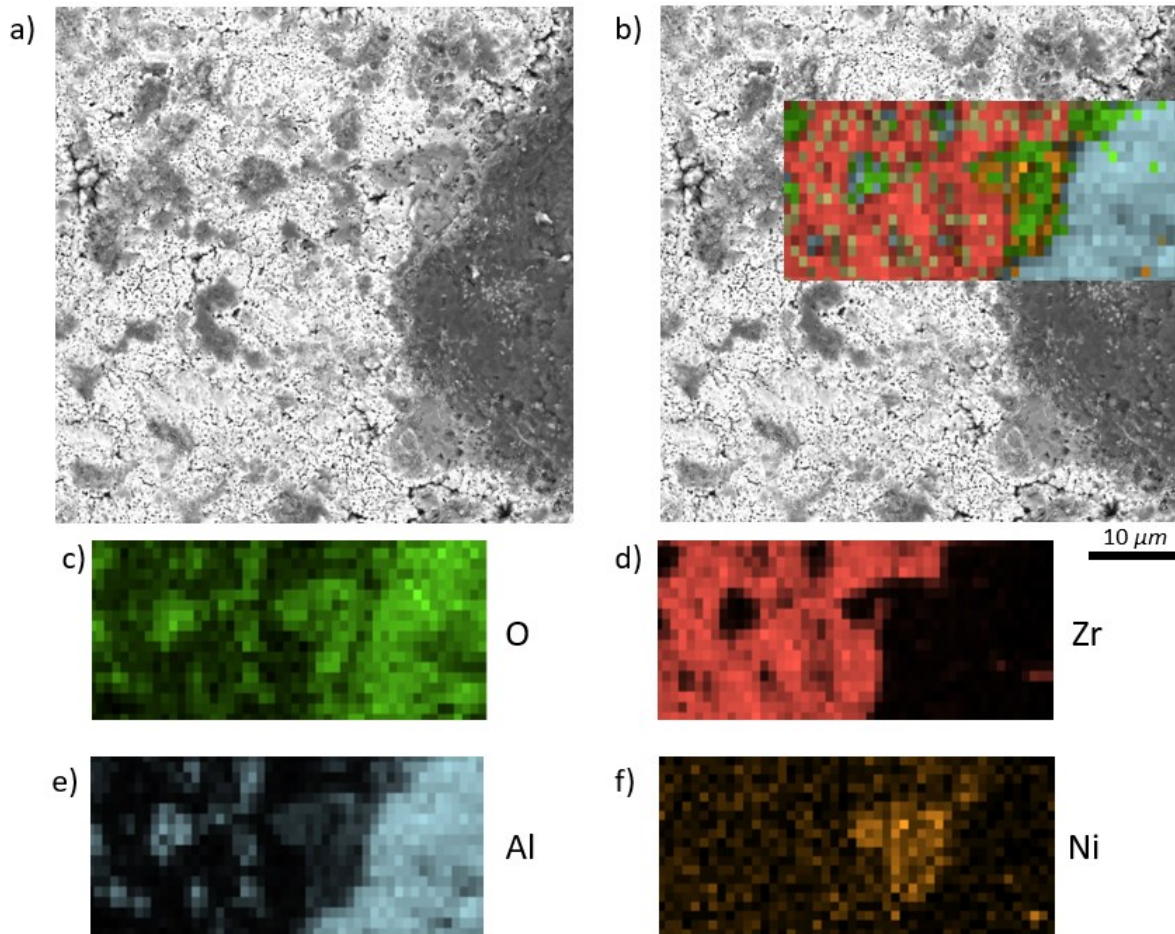
*Figure 4-18: Images showing a) a high-resolution SEM image of the topcoat-side fracture surface for a "mid-life" CED specimen and b) with the EDS chemical analysis overlayed on the location it was performed. The bottom images (c,d,e,f) show the individual elemental maps for the elements detected.*

The EDS shows a clear change in the topcoat fracture surface in the "mid-life" specimen. While the largest portion of the fracture surface was still Zr and O (which is to be expected as we are looking at the topcoat fracture surface), the dark grey islands contained no Zr and instead were entirely Al and O representing the TGO. Additionally, small pockets of Ni were found around the edges of the dark grey TGO islands, contrasting with the fact that no Ni was detected in the "as-deposited" specimen. All of this once again points to the fact that the fracture path in the "mid-life" state is through the TGO.

Looking at these results in summation, the failure of the P&W FCT specimens can be described as follows. Even as FCT thermal cycling increases, no rumpling of the TGO or bond coat is observed and a flat bond coat is maintained in the "mid-life" specimens. As a result, when fracture occurs the crack can grow unimpeded along the fracture plane, resulting in the full delamination of the topcoat as seen with these specimens. In the "as-deposited" specimens, the TGO is very thin and the fracture path cuts through both nascent TGO and the bottom of the topcoat. As FCT cycling is increased and the TGO thickens, the residual stresses in the TGO [6] contributes to the energy release rate and drives the fracture surface lower in the TBC, delaminating more of the TGO. This results in the fracture surface of the "mid-life" specimens occurring along the bottom of the TGO interface. The thicker TGO in the "mid-life" specimens provides energy release that promotes delamination and reduces the applied stress required for delamination.

4.4 Chapter Summary

The work presented in this chapter highlighted the CED tests performed on specimens coated with a P&W LPPS NiCoCrAlY bond coat/7YSZ EBPVD topcoat that had undergone various amounts of FCT cycling. DIC was used to identify the critical shear strain associated with crack growth. The critical stress was measured to be 204 MPa for "as-deposited" specimens, 183 MPa for "early-in-life" specimens and 163 MPa for the "mid-life" specimen. From "as-deposited" to "mid-life" this represents a drop of 42 MPa, or a decrease of ~ 20%, which corresponds to a drop of ~40% in interfacial toughness. Coating delamination for this TBC system occurred in a unique fashion whereby the entire coating delaminated in one large piece. SEM imaging and EDS of the CED specimen fracture surfaces showed no bond coat rumpling, even in the "mid-life" specimen. The lack of rumpling allowed for cracks to grow unimpeded along the fracture surface and resulted

in the full coating delamination. Moreover, SEM imaging and EDS analysis of the substrate-side of the fracture surface showed that the crack moved below the TGO, initially starting at the TGO/topcoat interface in the "as-deposited" specimens and going to the bond coat/TGO interface in the "mid-life" specimen. This was confirmed by SEM imaging and EDS of the topcoat fracture surface.

References:

[1]: Théry, P.-Y., et al., *Adhesion energy of a YPSZ EB-PVD layer in two thermal barrier coating systems.* Surface and Coatings Technology, 2007. **202**(4): p. 648-652.

[2]: Théry, P.-Y., et al., *Spallation of two thermal barrier coating systems: experimental study of adhesion and energetic approach to lifetime during cyclic oxidation.* Journal of Materials Science, 2009. **44**(7): p. 17-26.

[3]: Zhang, B., *Experimental Characterization of Thermal Barrier Coatings Using Micro-Scale Bending Techniques.* Ph.D. Thesis, Johns Hopkins University, 2015.

[4]: Chien-Min, L., et al., *Effect of grain orientations of Cu seed layers on the growth of <111>-oriented nanotwinned Cu.* Scientific Reports, 2014. **4**(1): p. 1-4.

[5]: Lockyer-Bratton, S., *Experimental measurements of thermal barrier coating interfacial fracture toughness as a function of mode-mix*. Ph.D. Thesis, Johns Hopkins University, 2016.

[6]: Evans, A.G., He, M.Y., Hutchinson, J.W., *Mechanics-based scaling laws for the durability of thermal barrier coatings.* Prog. Mater. Sci., 2001. **46**: p. 249–271.

## Chapter 5: The Effect of Off-Nominal Processing Conditions on YSZ Microstructures and Mechanical Properties

This chapter details a study of the effect of processing parameters on the microstructure and attendant mechanical properties of EPBVD 7 % YSZ topcoats provided by colleagues at P&W. Buttons, wedge bars and blades were intentionally deposited at "low run power", "nominal run power" and "high run power" processing conditions and provided to JHU for microstructural and mechanical characterization. Current manufacturing specifications for YSZ topcoats focus on thickness, and the overarching goal of this study is to identify microstructural or mechanical measures that might be used to enhance topcoat specification. Sample preparation procedures for the wedge bars were developed, including the fabrication of freestanding topcoat specimens deposited at "low", "nominal" and "high run powers". SEM imaging and EDS analysis of both cross-sections and freestanding topcoats were performed and the microstructure is compared at various locations and deposition powers. The anomalous behavior of the TGO in the "low run power" specimens is highlighted. The freestanding topcoats were tested via 3-point bend with the sample oriented to place the tips of the topcoat in both compression or tension. Force-deflection curves for the topcoats deposited at all three run power conditions were obtained and used to assess the compliance of the topcoats deposited at various run powers. Finally, initial efforts to perform the same set of tests and analysis on the blades are presented.

## 5.1 Wedge Bar Specimen Preparation Procedure

The first specimen preparation step was to mount each wedge bar in epoxy to limit any chipping of the coating during cutting [1]. The epoxy used was Allied High Tech's duel EpoxyMount resin and hardener, and the mounting was done in a vacuum impregnation system at 15 PSI to ensure that the epoxy fully infiltrated the columnar gaps in the topcoat. Each wedge bar

was sliced into multiple 1 mm thick cross-sections using a STX-202a Precision Diamond Wire Saw with a 0.225 mm diameter wire. These wedge bar slices were subsequently polished with SiC polishing papers to 1200 grit (P-4000) using an Allied Technology Tech-Prep 8 automatic polisher. In this step, each side was polished to remove 0.25mm of material and any damage from the diamond wire saw cutting process. This left a cross-sectional thickness of 0.5mm, and further polishing with Struers' 6 µm and 1 µm DiaDuo-2 diamond suspension fluid on largo polishing pads using a tripod polisher provided a high-quality final polish. The cross-sectional specimens that were examined with SEM imaging and EDS characterization, were sputter coated with 3 nm of Au-Pd (60:40 ratio) using a Leica EM ACE600 sputter coater to prevent charging while in the SEM [2].

Fabrication of the freestanding topcoat specimens required additional steps. These included using the diamond wire saw to cut off the curved top and bottom portions of the wedge bar specimens so that the only coated areas that remained were the flat edges of the wedge bar. The specimens were then burned out of the epoxy by placing them in a furnace at 650°C (1200°F) for half an hour. The trimmed and epoxy-free wedge bars were then acid etched for 1.5 hours using the same 5-molar concentration of HCl heated to 80°C [3] that was used for the P&W FCT CED specimens. For the wedge bars, the bond coat was completely etched away, leaving freestanding topcoats that were 8.5 mm long, 0.5 mm thick and 0.28 mm wide (the same as the topcoat). These topcoats consisted of a bond coat-side, the side formerly attached to the substrate before it was etched away, and the free surface, which contained the tips of the topcoat. After etching, the freestanding topcoats were placed in a bath of baking soda and water to neutralize any residual HCl and then cleaned in isopropyl alcohol in an ultrasonic bath for 10 minutes. Due to the fragile nature of the freestanding topcoats some of the initial topcoats fractured during the ultrasonic

vibration cleaning process, so subsequent iterations were handled with care to ensure that the coatings remained in-tact before testing. As will be shown later however, it seems likely that micro-cracking may still have occurred and that the freestanding topcoats were damaged prior to testing.

Figure 5-1 a) shows a slice of a "nominal run power" wedge bar specimen mounted in epoxy and Figure 5-1 b) a similar "nominal run power" wedge bar specimen after removal from epoxy with the top and bottom cut off and the bond coat etched away on the sides. The straight sections of the topcoat were released by etching away the bond coat, and higher magnification images of two freestanding topcoats (for a "nominal run power" wedge bar specimen) are shown in Figure 5-2.
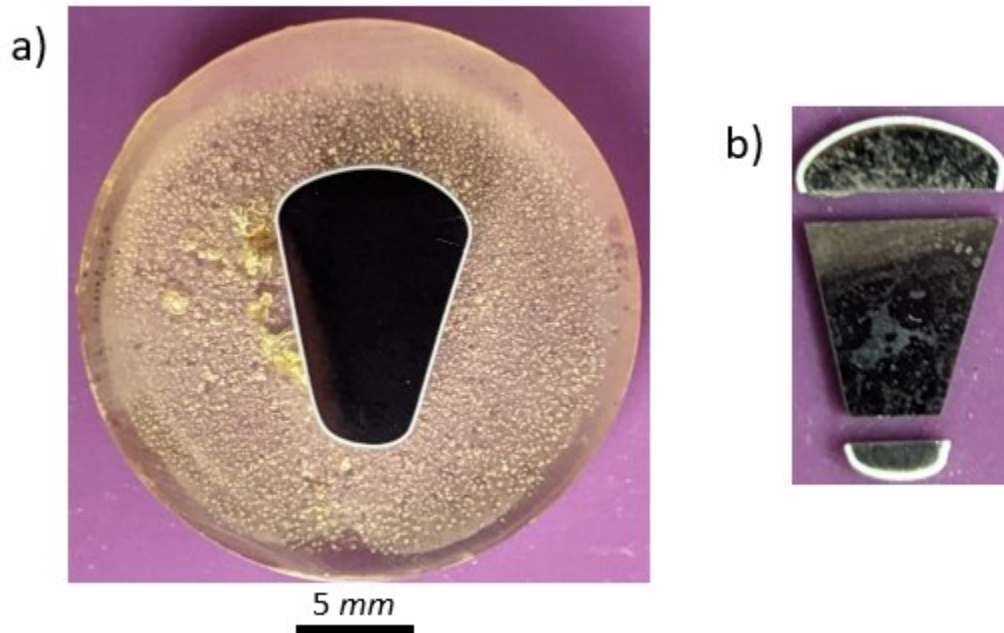


*Figure 5-1: Two images showing a) a "nominal run power" specimen mounted in epoxy for SEM use while b) shows the substrate of a "nominal run power" burned from epoxy with the curved top and bottom cut off and the bond coat etched away on the sides.*
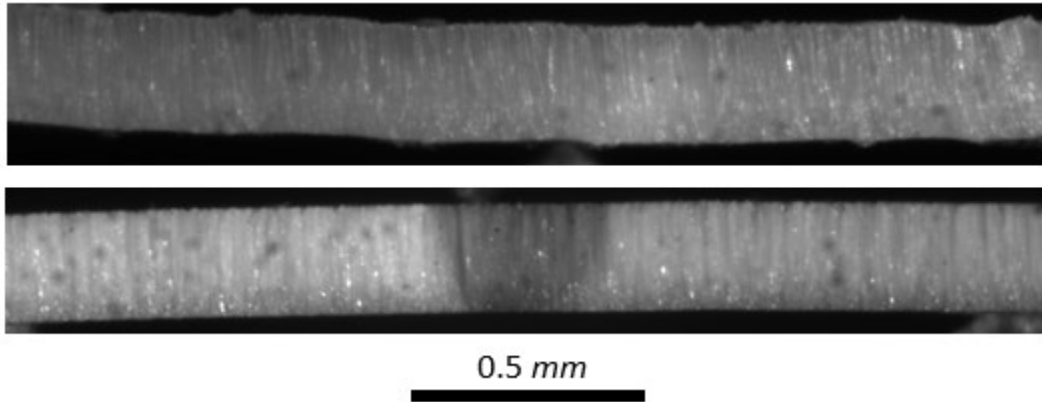
*Figure 5-2: Portions of two freestanding topcoats that were created by etching away the bond coat of a "nominal run power" specimen. The total length of the topcoat was 8.5 mm. In both images the bond coat-side is on the bottom and the free surface is on the top.*

Testing of the freestanding topcoats was done using the custom built 3-point bend test load frame shown in Figure 5-3. The freestanding topcoat beams rested on two pins that were 4.3 mm apart and served as the outer load points, while a groove in the middle of the fixture facilitated alignment of the central loading pin in the mid-span of the beam. The central pin was moved towards the freestanding topcoat beams at a rate of 150 nm/s using a Newport Model 8742 Picomotor actuator, while load data was monitored using a 250 g Futek Load Cell. The beams were tested in two configurations. The first configuration was with the center of the free surface pushed on by the central pin while the bond coat side was resting on the outer pins, resulting in the topcoat tips being placed in compression. The second configuration was the reverse, with the bond coat-side of the topcoat pushed by the central pin and the free surface against the outer pins, resulting in the topcoat tips being placed in tension.

Load and displacement data were both logged at a frequency of 10 Hz, or 10 data points per second. Specimens were loaded until a load of 0.075 N, the peak load used by Zhang [3] in his study of freestanding topcoat specimens via 3-point bend testing, or until failure of the beams occurred.
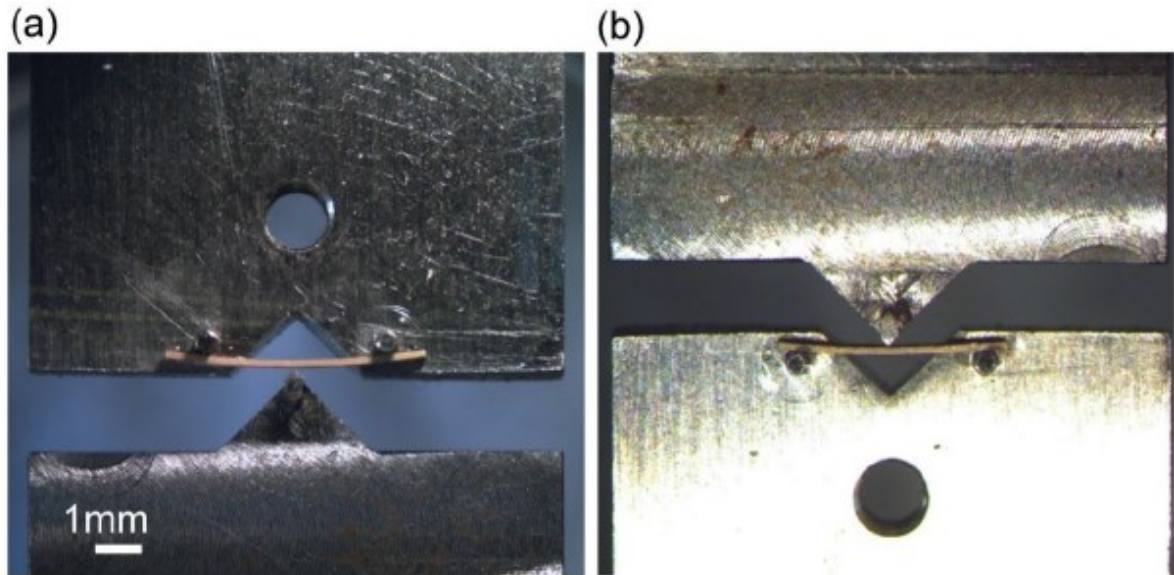
*Figure 5-3: Images of the 3-point bending test of freestanding topcoat beams on both sides showing: (a) the central pin pushing up on the bond coat-side of the freestanding topcoat, and (b) the central pin pushing down on the topcoat free surface [3].*

DIC was used to measure deflection of the freestanding topcoats during the 3-point bend tests. Images were taken using a PixelLINK PL-A782 black and white 6.6 MP camera with an Edmund Optics 4X Telecentric lens mounted above the specimen. This resulted in images having a pixel size of 1μm. Images were taken at a rate of 1 image every second using the PixelLINK Capture OEM Software. Unlike the CED specimens discussed in Chapter 4, no speckle pattern was applied to the freestanding beams, both to avoid damaging the fragile freestanding topcoats and because the columns of the topcoat provided enough contrast and inherent speckling to facilitate quality DIC. VIC-2D was used to analyze the DIC images using a subset size of 31 x 31 pixels and a step size of 5 pixels. A 50 x 150 pixel box around the central loading tip was used to measure the deflection of the freestanding coatings at this point. Use of a 4x lens allowed for a large enough field of view to monitor the edges of the opposing grip and adjusting for rigid body motion of the load frame facilitated measurement of the flexure of the freestanding topcoat during testing.

## 5.2 Topcoat Microstructural Variations as a Function of Variations in Processing Conditions

To determine how the topcoat microstructure changed as the processing conditions are varied, detailed electron microscopy was performed. Cross-sectional BSE SEM images were taken at various depths of the topcoats for each processing condition and compared against each other. Figure 5-4 shows an SEM image of the topcoat of a "low run power" specimen. The microstructure is columnar with ~6 µm wide columns and approximately 10% porosity. The vertical height of the columns in this image are truncated by the fact that the columns are tilted out of the image plane. Higher magnification images were taken at various locations through the thickness of the topcoat (~ 25µm, 125µm and 225µm from the TGO/topcoat interface) as indicated in Figure 5-4. Images were taken at the same depths through the thickness of the topcoat for the "nominal run power" and "high run power" specimens. Figure 5-5 is a 3 x 3 array of the high-res SEM images for each processing condition at each location through the topcoat thickness. The columns show the "low run power", "nominal run power" and "high run power" specimens moving from left to right, while the rows show the top of the topcoat, middle of the topcoat, and bottom of the topcoat moving from top to bottom.
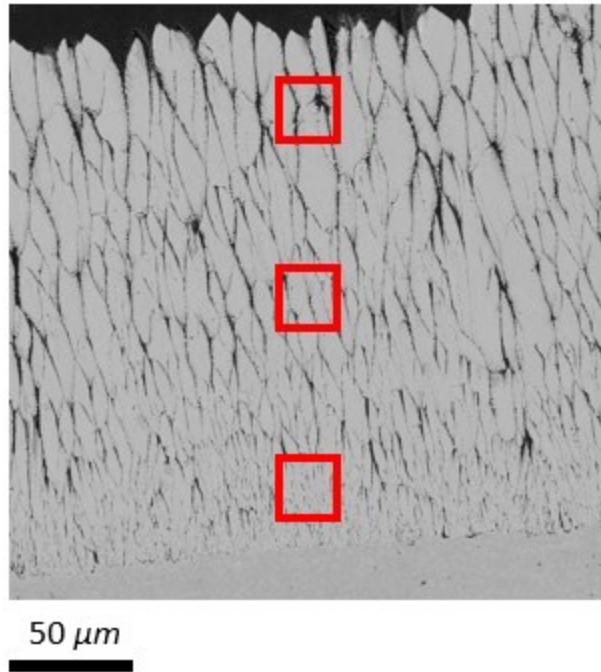
*Figure 5-4: SEM image of the YSZ topcoat of a "low run power" specimen with boxes indicating locations where higher magnification images were taken at the bottom, middle and top of the topcoat for each processing condition.*
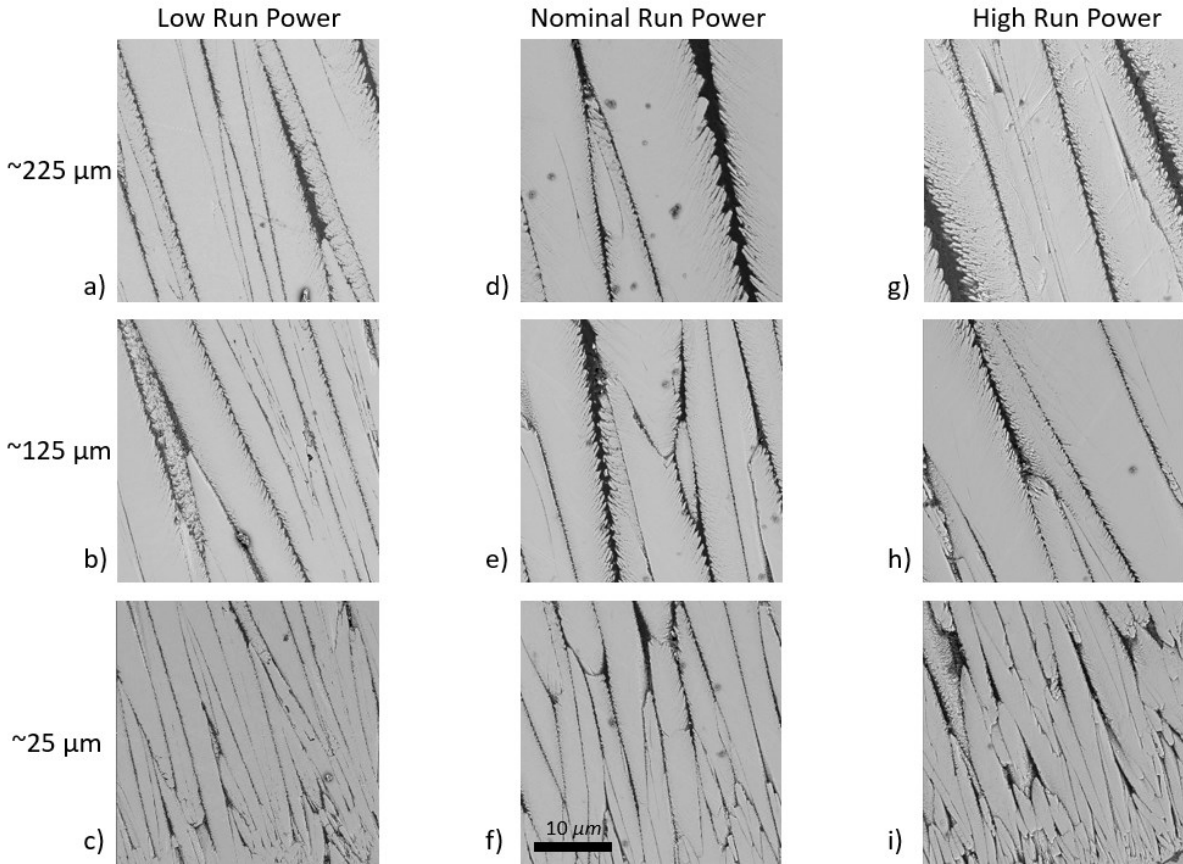
*Figure 5-5: A 3 x 3 array of the high-res SEM images for each processing condition at each location through the topcoat thickness. The columns show the "low run power", "nominal run power" and "high run power" specimens moving from left to right, while the rows show the top of the topcoat, middle of the topcoat, and bottom of the topcoat moving from top to bottom.*

The "low run power" specimen appears the most visually different of the three processing conditions. Towards the bottom of the topcoat, the columns are the smallest in width, have the least defined boundaries, and tend to coalesce into each other. Towards the top of the same topcoat, the grains are larger in size but are still smaller than the other two processing conditions and have a less feathery microstructure as well. Looking at the "nominal run power" and "high run power" specimens, coatings from the two processing conditions have similar appearances both in terms of grain size and definition. Towards the top of the topcoats, both coatings experienced grain growth to similar sized columns, and the edges of the column have a more feathery microstructure as compared to the "low run power" specimens.

The "low run power" coatings also exhibited unique behavior in the anomalous formation of the TGO. After the acid etching process, a thin black layer remained on the TGO/topcoat interface surface that did not exist for either the "nominal run power" or "high run power" specimens. The freestanding "low run power" topcoat specimens were fabricated with the same acid etching technique, HCl heated to 80°C, that was used to make freestanding topcoats from the "nominal run power" and "high run power" specimens. In the "nominal run power" and "high run power" specimens, the bond coat and TGO were fully etched away in 1.5 hours. By contrast, a thin layer of material was left on the TGO-side of the freestanding topcoat. Figure 5-6 consists of optical images of a top-down view of bond coat side of a freestanding a) "nominal run power" topcoat and b) "low run power" topcoat. In the "nominal run power specimen" the bond coat-side surface is white, like the topcoat. In the "low run power" specimen, however, no white can be seen and instead the surface is black.



100 μm
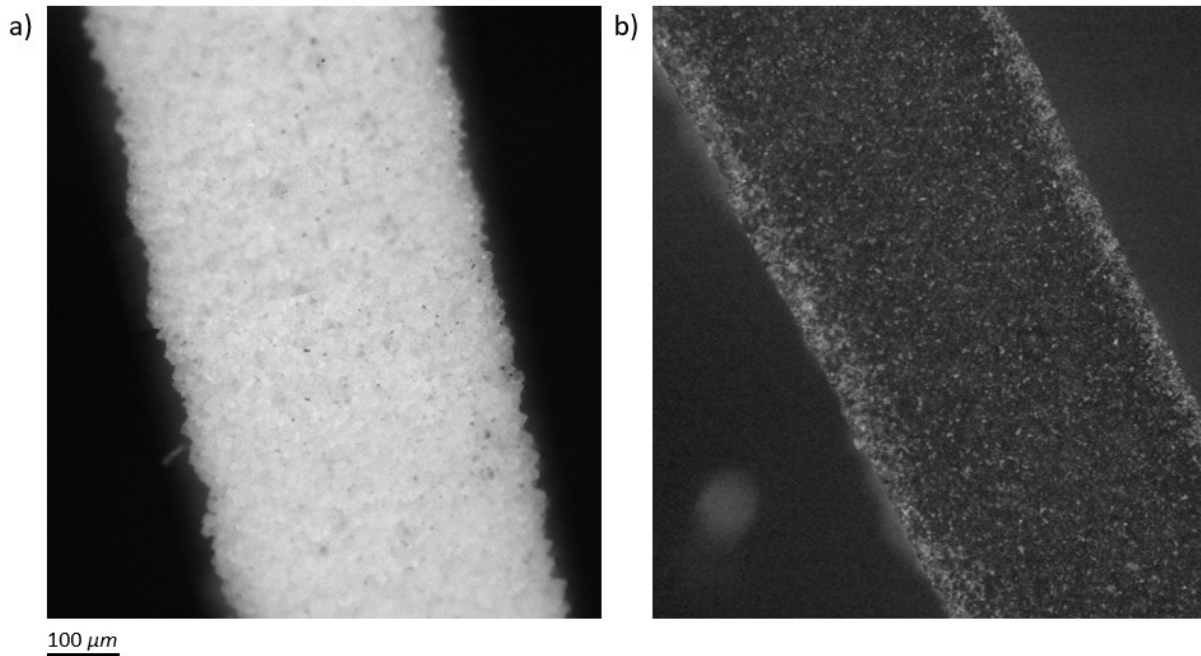
*Figure 5-6: Optical images showing the top-down view of the bond coat side of a) "nominal run power" and b) "low run power" freestanding topcoat specimens. In the "nominal run power specimen" the bond coat side is white representing the topcoat, while in the "low run power" specimen only a black layer is seen.*

SEM imaging combined with EDS analysis was performed to understand what was causing the formation of this black layer on the TGO/topcoat interface. In order to confirm that this layer was not formed as a result of acid etching, "low run power" topcoats that were still attached to the substrate were investigated, along with "nominal run power" specimens to compare against. In BSE SEM images of the "low run power" specimen, the TGO appeared as a thin, light grey layer instead of a darker grey layer as expected. BSE SEM imaging of the "nominal run power" specimen attached to the substrate showed the typical darker grey layer, and EDS showed a fully formed TGO consisting of Al and O as expected. By contrast, the EDS analysis of the "low run power" specimen, showed no clear formation of a TGO and instead showed Al in the bond coat and O in the topcoat, but no intermediate layer. Figures 5-7 and 5-8 show the SEM images and EDS results of the "nominal run power" and "low run power" specimens respectively.
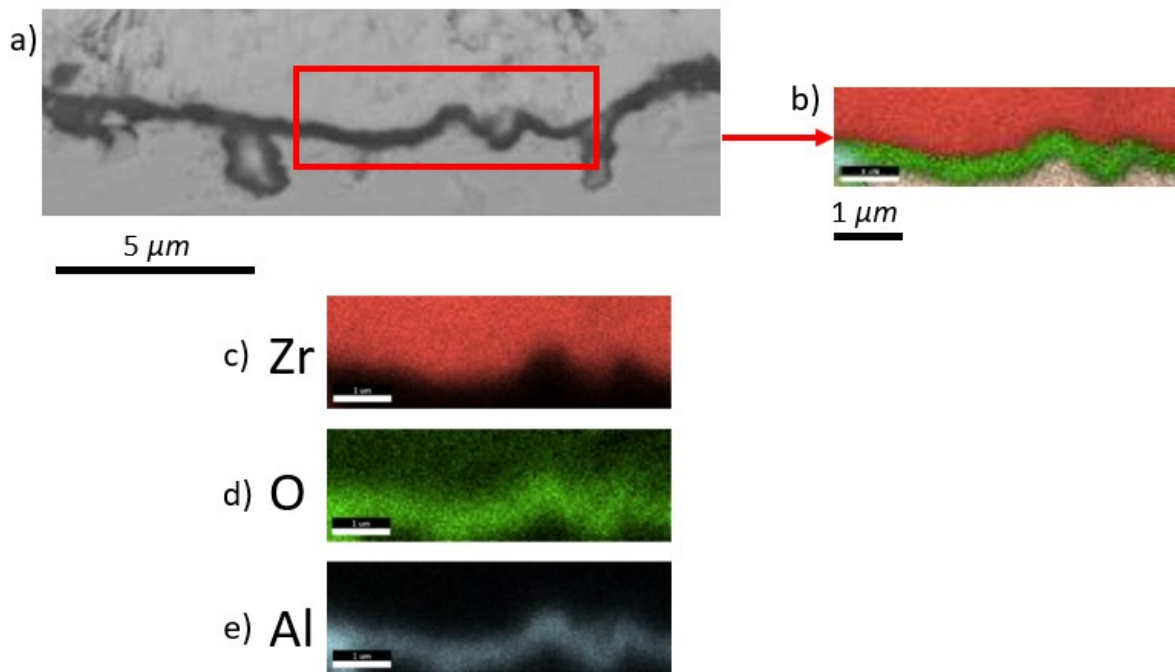


*Figure 5-7: Image a) shows a BSE SEM image of a "nominal run power" specimen with the dark grey TGO in a box, while b) shows the EDS of the region of interest, with the elemental results of Zr, O and Al shown in (c, d, e). A fully formed TGO with flashes of O and Al can be seen below a topcoat layer containing Zr.*
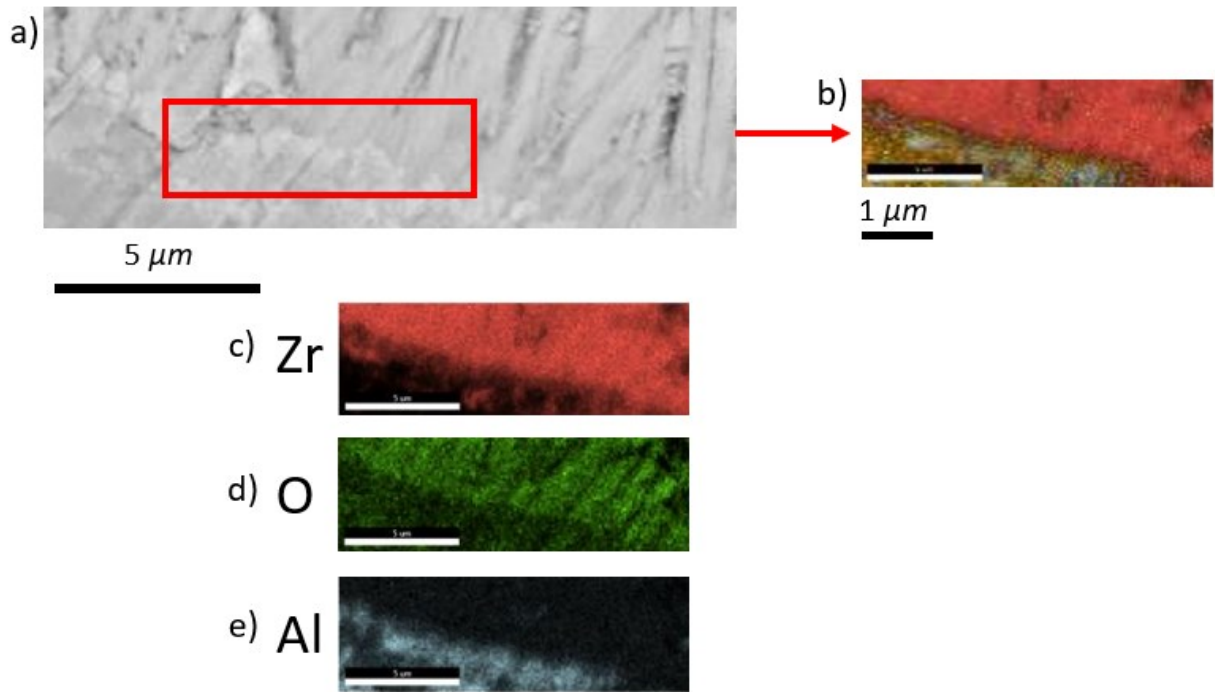
*Figure 5-8: Image a) shows a BSE SEM image of a "low run power" specimen with the thin light grey TGO in a box, while b) shows the EDS of the region of interest, with the elemental results of Zr, O and Al shown in (c, d, e). No fully formed TGO is visible as the O is seen in the topcoat layer and the Al in the bond coat layer.*

This very thin light grey layer was seen in every "low power run" wedge bar and blade specimen that was imaged. SEM imaging and EDS was also used on the bond coat-side surface of a freestanding "low run power" YSZ specimen, as shown in Figure 5-9. The results of this chemical analysis showed the presence of Al and O on a surface made predominantly of Zr, suggesting that this light grey layer is a transient oxide that was not full etched away by the acid.
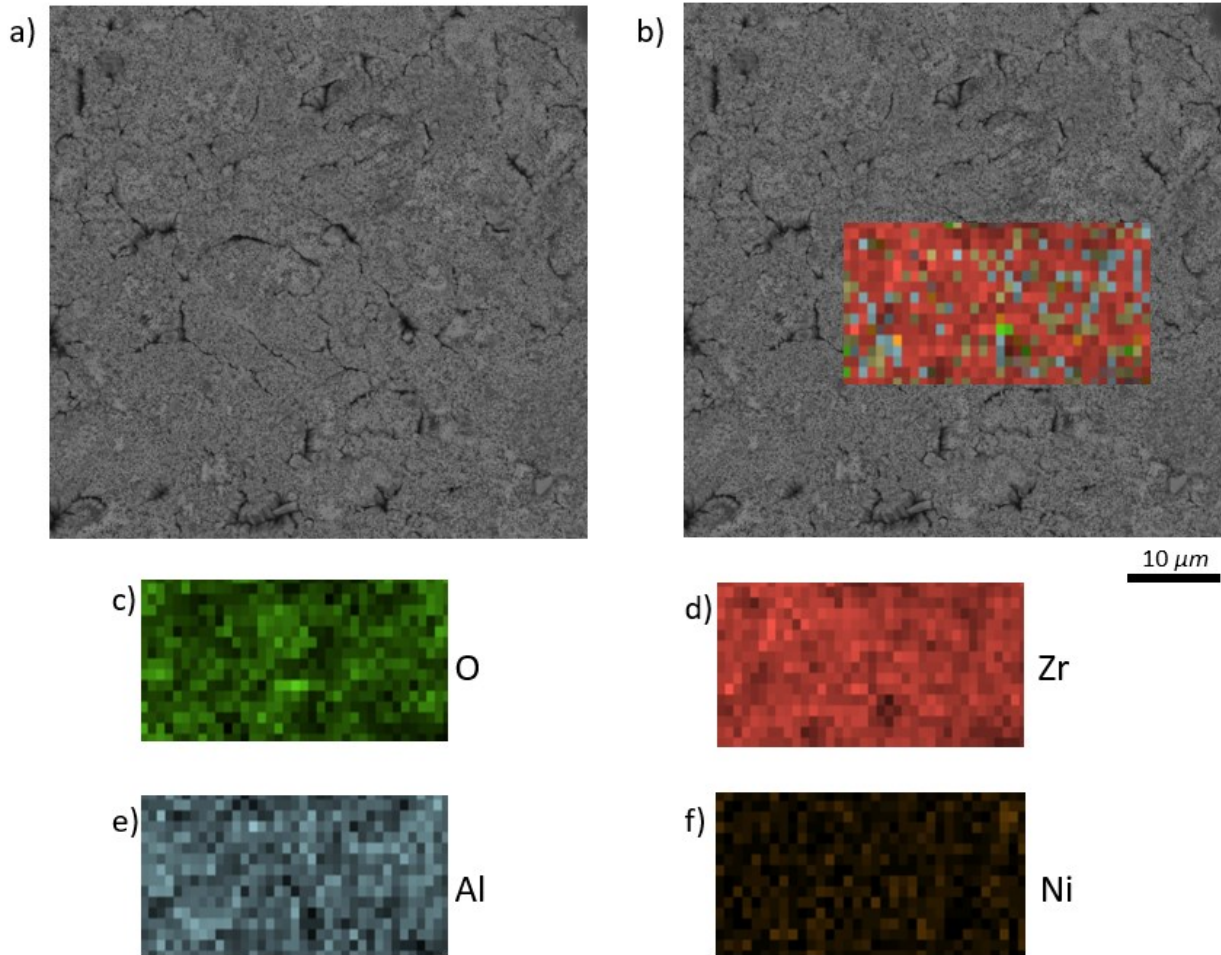
*Figure 5-9: Images showing a) a high-resolution SEM image of the topcoat fracture surface for an "as-deposited" CED specimen and b) with the EDS chemical analysis overlayed on the location it was performed. The bottom images (c,d,e,f) show the individual elemental maps for the elements detected.*

On the whole, imaging of the topcoats revealed few microstructural changes as a function of variations in the topcoat processing conditions. The most notable changes occurred in the "low run power" specimens, where the columns were the smallest in width, had the least defined boundaries, and tended to coalesce into each other. Also notable was the formation of a transient oxide instead of TGO, which remained on the surface of the topcoat after acid etching. The "nominal run power" and "high run power" specimens maintained visually similar appearances however, with any differences being too subtle to notice. To supplement this work, results of 3-point bend tests on

freestanding topcoats were examined to explore whether differences or trends in the mechanical response of the topcoat could be correlated with the processing conditions.

5.3 Wedge Bar 3-Point Bend Test Results

A total of 12 freestanding wedge bar specimens were tested using the 3-point bend setup. This included two "nominal run power" specimens with the topcoat tips in compression, two "nominal run power" specimens with the topcoat tips in tension, one "high run power" specimen with the topcoat tips in compression, two "high run power" specimens with the topcoat tips in tension, three "low run power" specimens with the topcoat tips in compression and two "low run power" specimens with the topcoat tips in tension. The force data from each tested was normalized by the width of each freestanding beam, and the deflection data was obtained by taking the DIC measured deflection of the freestanding beams adjacent to the central loading tip minus the motion of the opposing grip that held the two outer pins. Figures 5-10 through 5-21 show the normalized load-deflection curves for each test, while Figure 5-22 shows all of the tests plotted on one curve.
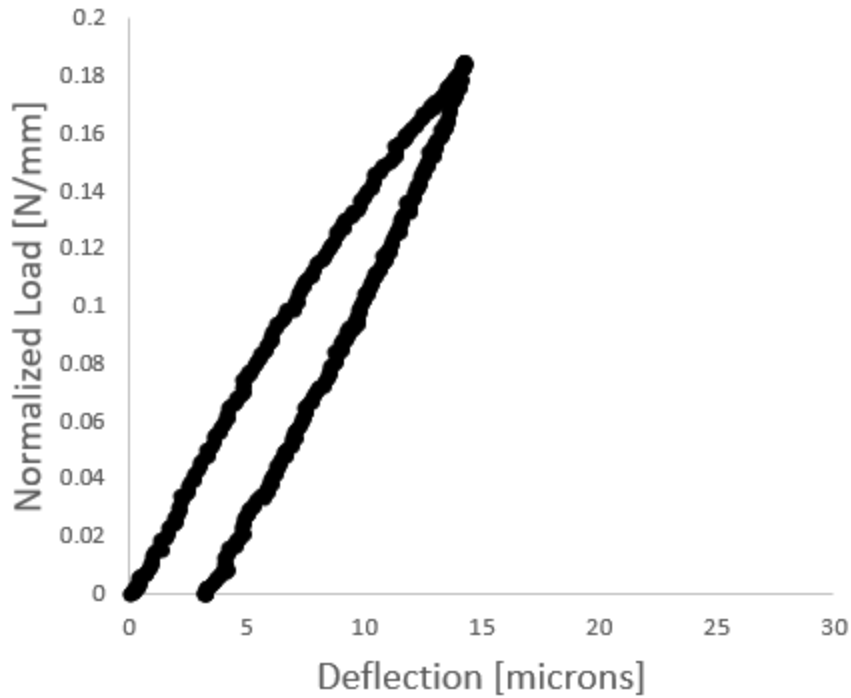
*Figure 5-10: Normalized load-deflection curve for a "nominal run power" specimen loaded so that the tips of the topcoat were in compression. A modulus value of 16.5 GPa was measured for this specimen.*
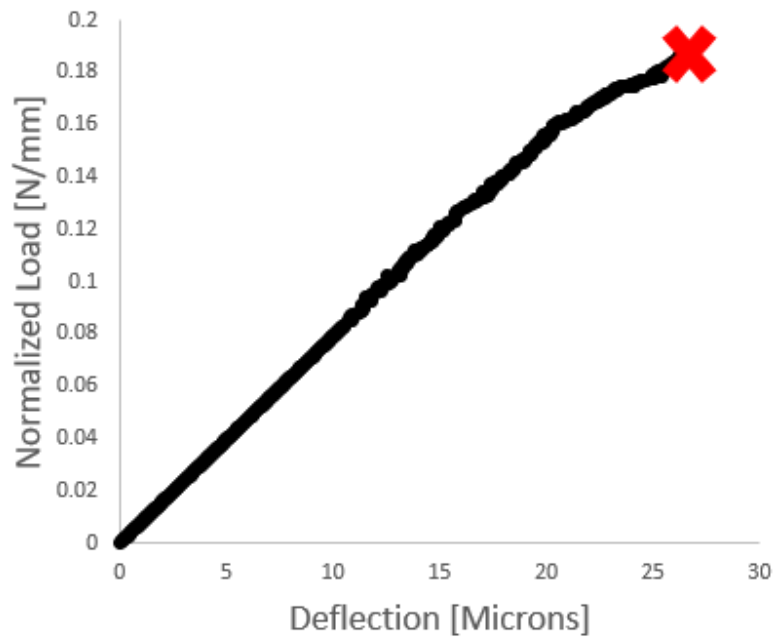


*Figure 5-11: Normalized load-deflection curve for a "nominal run power" specimen loaded so that the tips of the topcoat were in compression. A modulus value of 10.6 GPa was measured, and the red "X" indicates where failure of the specimen occurred.*
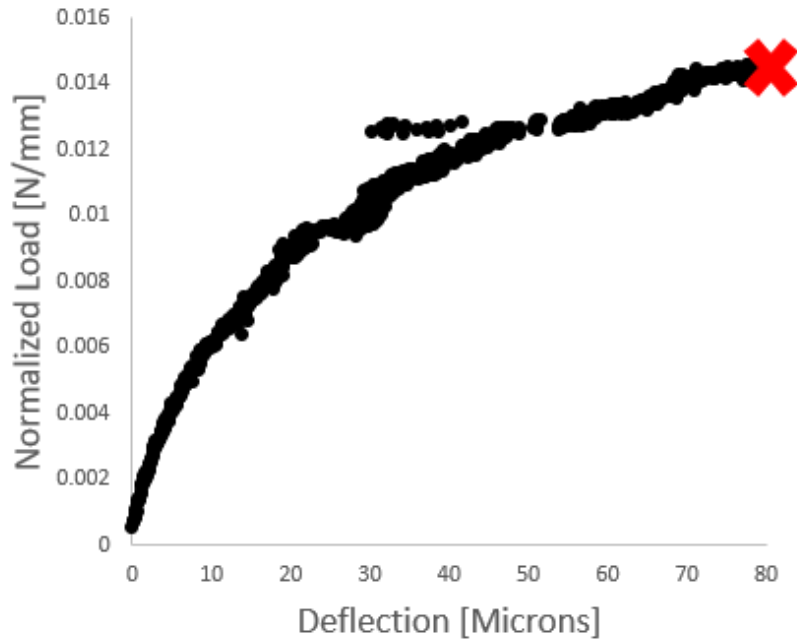
*Figure 5-12: Normalized load-deflection curve for a "nominal run power" specimen loaded so that the tips of the topcoat were in tension. A modulus value of 3.2 GPa was measured, and the red "X" indicates where failure of the specimen occurred.*
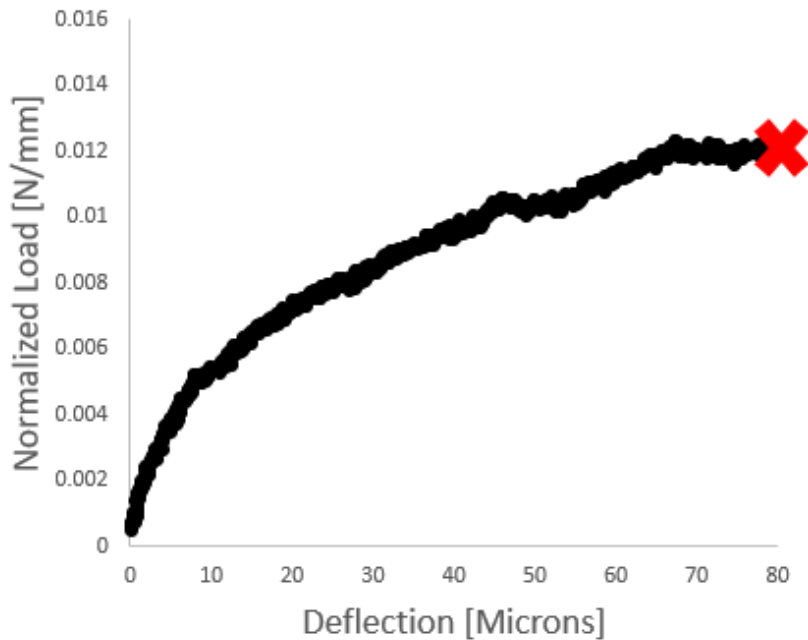


*Figure 5-13: Normalized load-deflection curve for a "nominal run power" specimen loaded so that the tips of the topcoat were in tension. A modulus value of 2.2 GPa was measured, and the red "X" indicates where failure of the specimen occurred.*
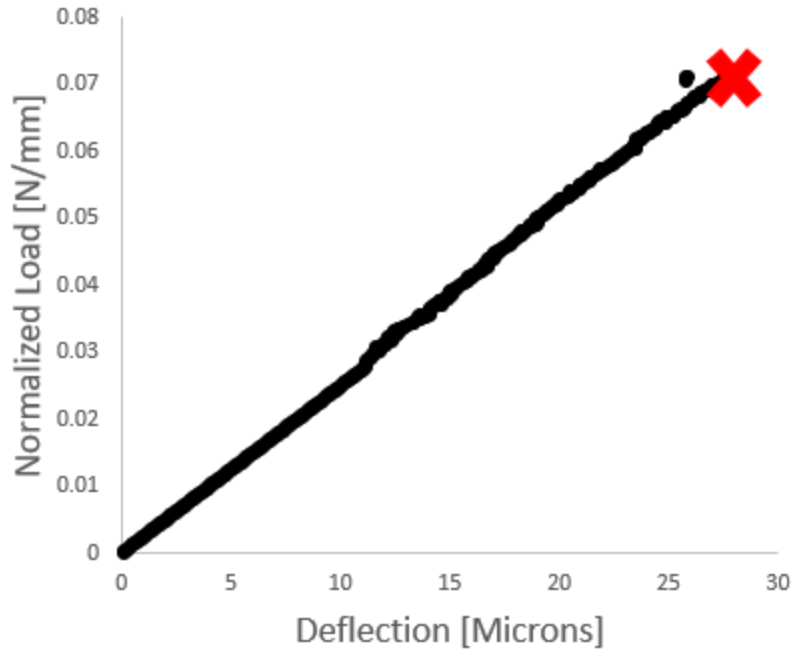
*Figure 5-14: Normalized load-deflection curve for a "high run power" specimen loaded so that the tips of the topcoat were in compression. A modulus value of 6.8 GPa was measured, and the red "X" indicates where failure of the specimen occurred.*
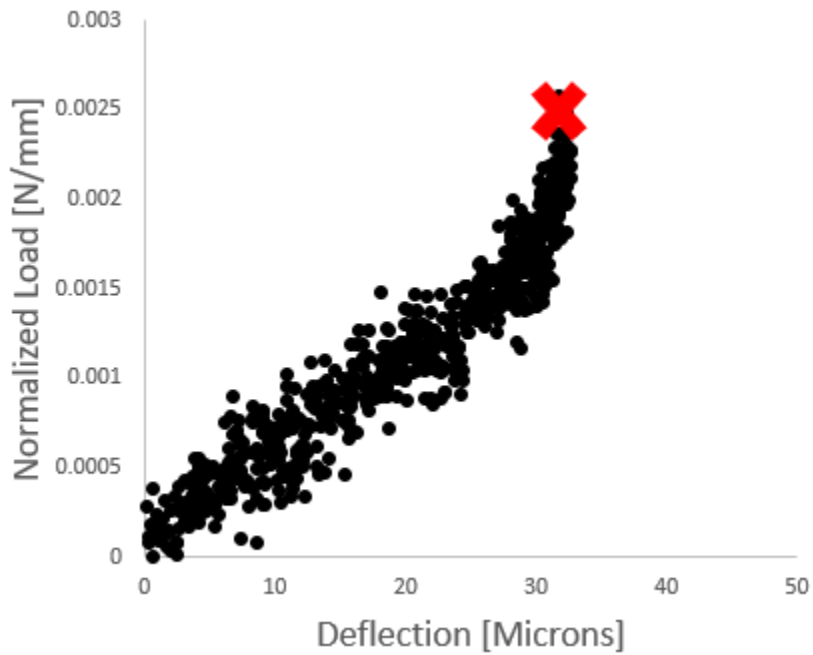


*Figure 5-15: Normalized load-deflection curve for a "high run power" specimen loaded so that the tips of the topcoat were in tension. A modulus value of 0.08 GPa was measured, and the red "X" indicates where failure of the specimen occurred.*
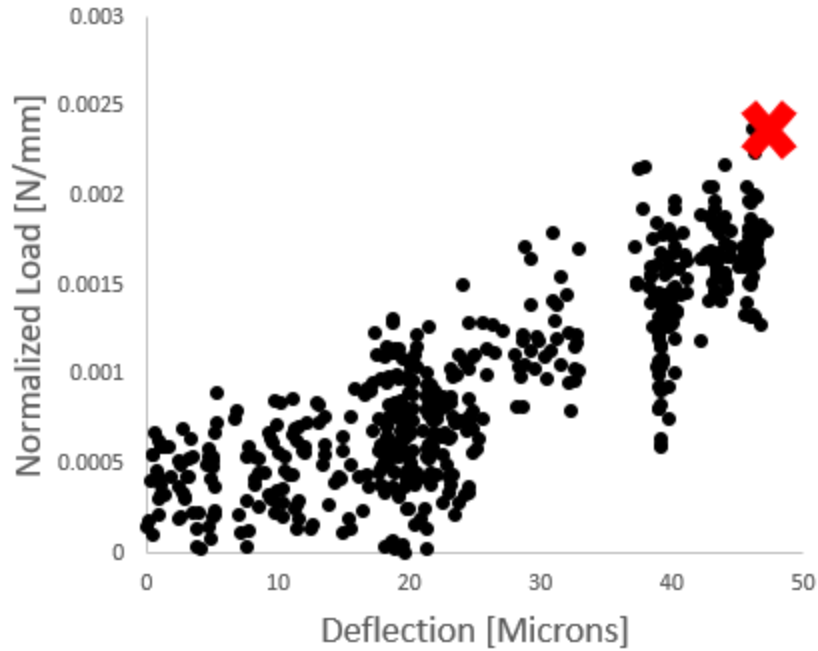
*Figure 5-16: Normalized load-deflection curve for a "high run power" specimen loaded so that the tips of the topcoat were in tension. A modulus value of 0.09 GPa was measured, and the red "X" indicates where failure of the specimen occurred.*
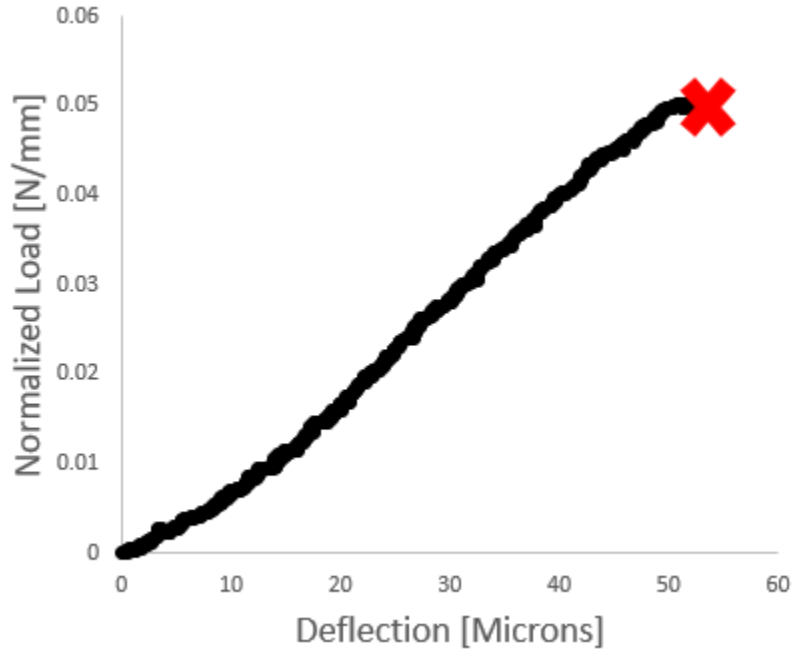


*Figure 5-17: Normalized load-deflection curve for a "low run power" specimen loaded so that the tips of the topcoat were in compression. A modulus value of 1.3 GPa was measured, and the red "X" indicates where failure of the specimen occurred.*

162
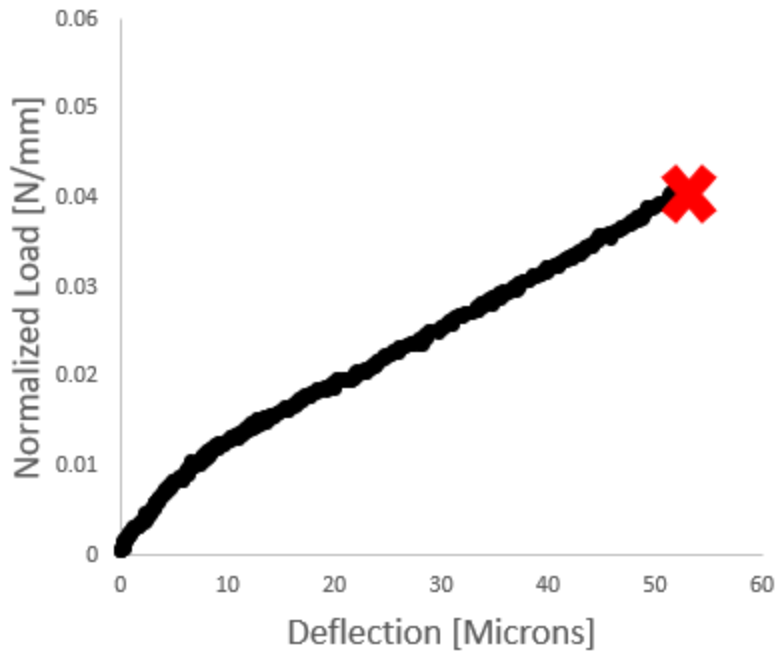
*Figure 5-18: Normalized load-deflection curve for a "low run power" specimen loaded so that the tips of the topcoat were in tension. A modulus value of 1.4 GPa was measured, and the red "X" indicates where failure of the specimen occurred.*
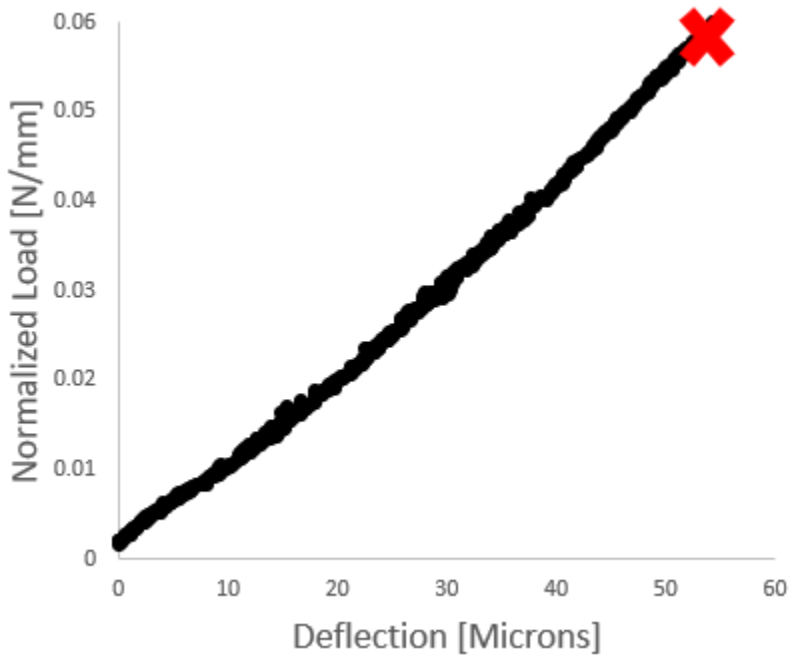


*Figure 5-19: Normalized load-deflection curve for a "low run power" specimen loaded so that the tips of the topcoat were in compression. A modulus value of 1.6 GPa was measured, and the red "X" indicates where failure of the specimen occurred.*
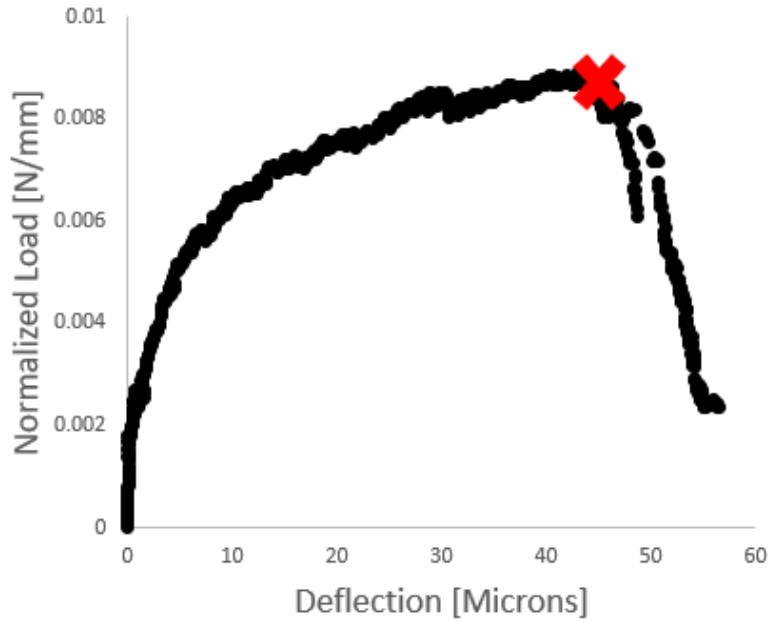
*Figure 5-20: Normalized load-deflection curve for a "low run power" specimen loaded so that the tips of the topcoat were in tension. A modulus value of 1.2 GPa was measured, and the red "X" indicates where failure of the specimen occurred. A crack was visible at the point of the red "X" and was deemed the point when failure occurred. However, the coating was still able to maintain a load after this point until the crack fully grew and split the specimen in half.*
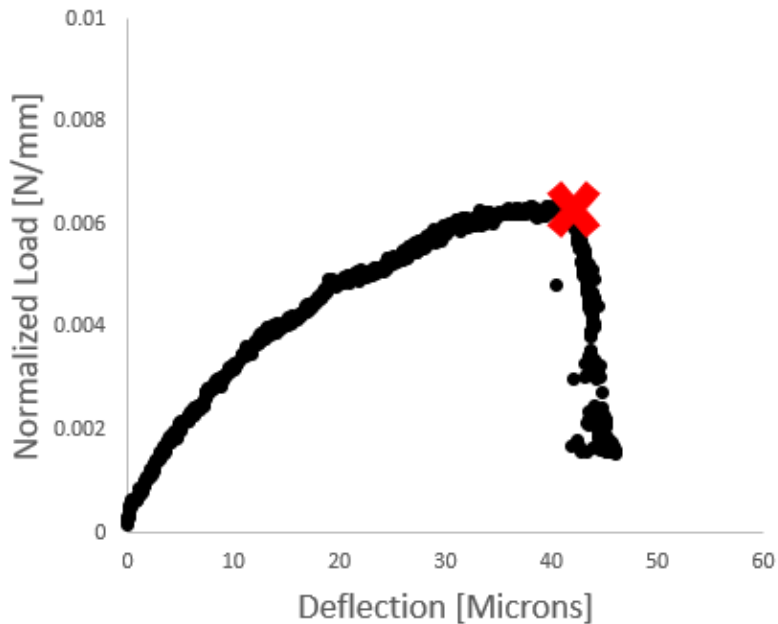


*Figure 5-21: Normalized load-deflection curve for a "low run power" specimen loaded so that the tips of the topcoat were in tension. A modulus value of 0.9 GPa was measured, and the red "X" indicates where failure of the specimen occurred. A crack was visible at the point of the red "X" and was deemed the point when failure occurred. However, the coating was still able to maintain a load after this point until the crack fully grew and split the specimen in half.*

164
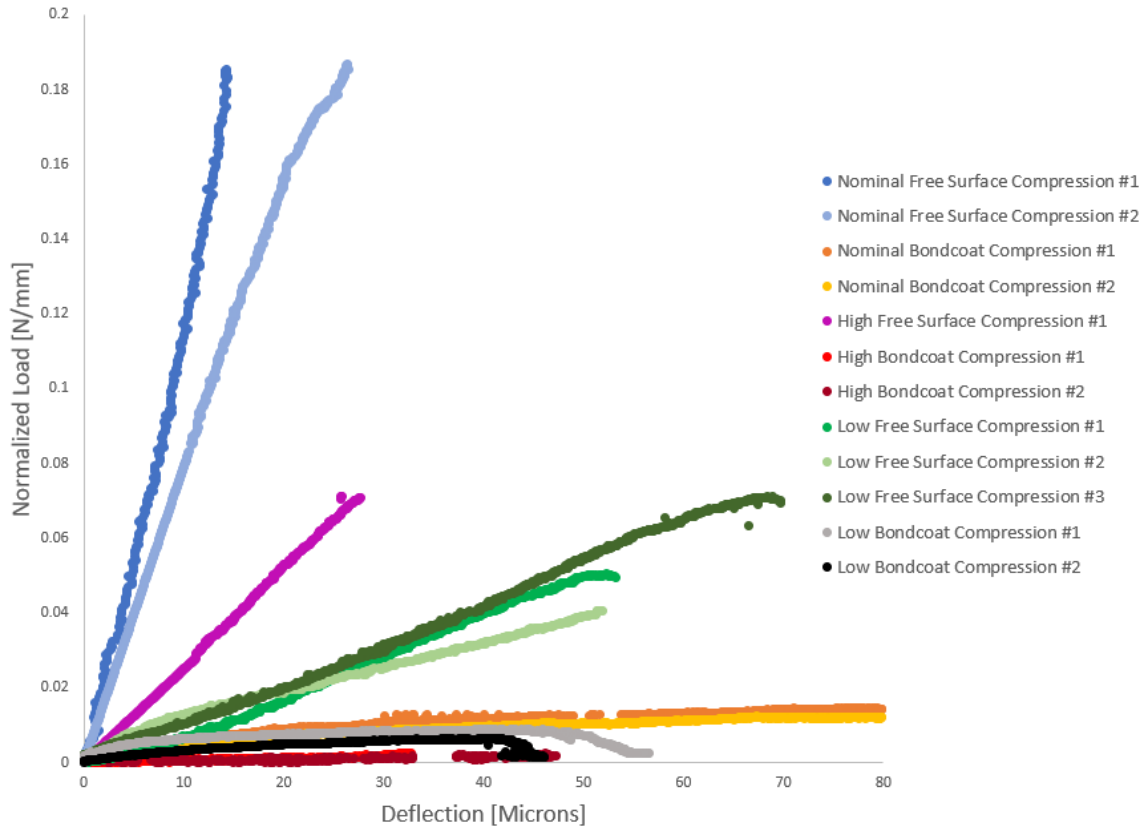
*Figure 5-22: Normalized load-deflection curve of all twelve 3-point bend tests of freestanding topcoats.*

The length between the outer pins was 4.3 mm while the topcoats had a thickness of 280 μm. These dimensions gave the tested freestanding beams a high enough aspect ratio that Euler-Bernoulli beam bending assumptions could be made. By making these assumptions such as small deflections and that the topcoats have a uniform, rectangular cross section that is loaded uniformly Equation 2-14 was obtained, which is shown again below.

*Equation 2-14*

$$E = \frac{KL^3}{4h^3}$$

Where $E$ is the elastic modulus of the topcoat, $K$ is the slope of the normalized load-deflection curve, $L$ is the distance between the outer loading pins (4.3 mm), and $h$ is the thickness of the

topcoats (280 μm). Table 5-1 gives the K value, deflection to failure and reported modulus for each tested specimen.

*Table 5-1: Values for the slope of the normalized force-deflection curve, deflection to failure and modulus for each tested specimen.*

| Specimen Run Power | Tips Loaded In: | K [N/mm] | Deflection to failure [μm] | E [GPa] |
|---|---|---|---|---|
| Low | Compression | 0.0014 | 55 | 1.3 |
| Low | Compression | 0.0015 | 52 | 1.4 |
| Low | Compression | 0.0018 | 53 | 1.6 |
| Low | Tension | 0.0013 | 48 | 1.2 |
| Low | Tension | 0.0010 | 42 | 0.9 |
| Nominal | Compression | 0.0182 | - | 16.5 |
| Nominal | Compression | 0.0117 | 26 | 10.6 |
| Nominal | Tension | 0.0035 | 76 | 3.2 |
| Nominal | Tension | 0.0024 | 79 | 2.2 |
| High | Compression | 0.0075 | 28 | 6.8 |
| High | Tension | $8*10^{-4}$ | 31 | 0.08 |
| High | Tension | $9*10^{-4}$ | 49 | 0.09 |

One specimen, the "nominal run power" specimen shown in Figure 5-10, did not fail during testing. This specimen was unloaded after reaching the target load of 0.075 N, and the modulus value for this specimen was taken from the unloading curve. In both of the "low run power" specimens where the tips were loaded in tension, a crack was visible at the point of the red "X" and was deemed the point when failure occurred. However, the coating was still able to maintain a load after this point until the crack fully grew and split the specimen in half, most likely due to

166

the fact that tests were run in a stroke control mode. For the "nominal run power" specimens loaded so that the tips were in compression, an average modulus value of $13.6 \pm 3.0$ GPa was measured compared to $2.7 \pm 0.5$ GPa when the load was reversed with the tips were loaded in tension. For the "high run power" specimens, a modulus value of 6.8 GPa was measured when the tips were placed in compression, while a modulus value of only $0.09 \pm 0.01$ GPa was measured when the tips were in tension. For the "low run power" specimens, modulus values of $1.4 \pm 0.1$ GPa and $1.1 \pm 0.2$ GPa were measured for the tips in compression and tension respectively.

5.4 Discussion of Wedge Bar 3-Point Bend Tests

Looking at the "nominal run power" specimens, the average modulus for when the tips are in compression was measured to be $13.6 \pm 3.0$ GPa, but $2.7 \pm 0.5$ GPa when the tips were loaded in tension. These values fall within the range of modulus values measured by Wang (5-10 GPa) [4] who performed 3-point bend tests on freestanding topcoats. Wakui et al. [6, 7] performed 4-point bend tests on freestanding topcoats and measured modulus values 16 GPa in compression and 6 GPa in tension, which match the values measured in this study as well as the asymmetry between them. A tension/compression asymmetry is also seen in the "low run power" and "high run power" specimens.

The tension/compression asymmetry phenomenon within the topcoat layer measured in this study has been seen in previous experiments [3, 5-7], and can be explained by the columnar microstructure of the topcoats. Loading the topcoat in tension enhances the space between the vertical columns, while loading in tension reduces the gap sizes. The effect of coating gaps and porosity on topcoat modulus was reported on by Strangman [8], who stated that coating density and modulus decrease as one gets further away from the substrate and was confirmed by Zhang's

[3] finding that porosity in the top 50 μm dominates the tension/compression asymmetry. Various attempts to model the modulus of various material systems as a function of porosity [9-11] highlight the impact that porosity can have on a material's stiffness response.

The most direct comparison for the "nominal run power" modulus results in this study can be found in Zhang's work, in which 3-point bend tests were performed on the same freestanding 7YSZ topcoat system. While the modulus when the tips are in compression falls within the lower range of modulus values measured by Zhang (13-20 GPa) [3], when loaded in tension the modulus values in this study are significantly lower than anything reported by Zhang. Additionally, the modulus values for the "low run power" and "high run power" specimens are lower than those of the "nominal run power", further highlighting the difference from Zhang's measurements. The significantly lower values measured in the current study must be called into question, and it must be considered whether the response being measured is representative of the "as-deposited" TBC. Potential sources for discrepancies include damage to the coating during the coating process, damage to the coating during specimen preparation, and differences in coating porosity between the different processing conditions as well as between the current study and the previous work by Zhang.

For the "low run power" specimens, an obvious source for the discrepancy comes from the transient oxide. It is likely that this oxide influenced the results of the 3-point bend tests, as the transient oxide would not be fully dense and could be a source for cracking and increased compliance. The modulus values for the "low run power" specimens have been omitted from the study.

Looking at the remaining samples, the fact that only one "nominal run power" specimen reached the intended peak load (0.075 N) without failing indicates that the unusually low modulus

values may be the result of damage to the topcoats. Any damage or micro-cracking in the coatings would artificially weaken the coating and result in a more compliant topcoat. Moreover, specimens that failed during loading meant that no unload curve was obtained, which would have been preferably used for modulus measurements since the sample is fully settled on the loading pins during the unload portion. For the one specimen that did not fail during loading, a modulus value of 12.3 GPa was measured during the load-up, while a modulus of 16.6 GPa was measured during the unload. While that difference alone does not account for the unusually low modulus values, it does indicate that larger moduli would have been measured during from unloading curves.

When looking at the SEM images that were taken of the topcoats, both before and after acid etching, no cracking or micro-cracking was obvious. The freestanding coatings were, however, very fragile and some broke during ultrasonic cleaning, so it is possible that the damage to the coating occurred but went undetected. It is also possible that micro-cracking occurred after the acid etching process while preparing the freestanding topcoats for testing. No micro-cracking was noticed during loading, and no hot spots were captured in the DIC displacement maps, but the DIC images were captured using a 4x lens to maintain a viewing area that included both grips. Future iterations of this work should be done at higher magnification to discount the presence of microcracks during testing.

In order to quantify changes in porosity, high-resolution BSE SEM images were taken, filtered in ImageJ and a binary threshold was applied. The porosity was measured by counting the dark contrast as pores and the light contrast as solid YSZ. Figure 5-23 contains an SEM image of a topcoat of a "low run power" specimen. Red boxes mark the locations ($z = 25$, 125 and 225 µm ) where higher magnification images were taken. Measurements were made at 5 locations for each height in the topcoat and for each processing condition. Measurements came from 30 µm by 30

µm areas, and representative images for each location and processing condition can be seen in Figure 5-5.



50 µm
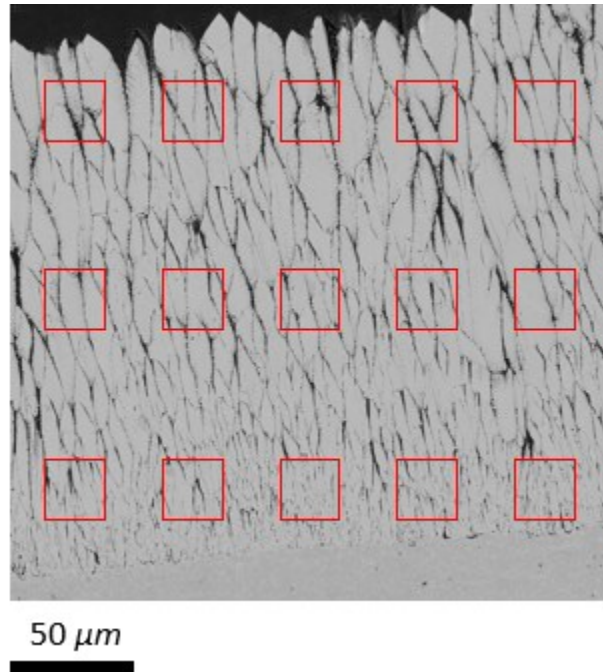
*Figure 5-23: SEM image of the topcoat of a "low run power" specimen with boxes indicating locations where higher magnification images were taken for porosity measurements at the bottom, middle and top of the topcoat for each processing condition.*

Table 5-2 gives the average porosity measurement for each topcoat processing condition at each depth through the thickness.

*Table 5-2: Values of coating porosity measurements, at various points through the coating thickness, for each processing condition*

| Specimen Run Power | Location Within Coating | Porosity [%] |
|---|---|---|
| Low | Bottom | 8.5 ± 0.9 |
| Low | Middle | 9.1 ± 1.0 |
| Low | Top | 10.2 ± 1.8 |
| Nominal | Bottom | 8.9 ± 1.5 |
| Nominal | Middle | 9.4 ± 1.2 |
| Nominal | Top | 11.8 ± 2.1 |
| High | Bottom | 9.3 ± 1.4 |
| High | Middle | 10.1 ± 2.0 |
| High | Top | 13.8 ± 2.6 |

Table 5-2 shows that the porosity increases in from the bottom of the topcoat towards the top for all topcoat processing conditions. It also shows that at each depth along the thickness, the "high run power" specimen had the greatest porosity. This is consistent with the findings by Schulz [12] that higher chamber operating pressures lead to less dense topcoat microstructures, as the higher adatom mobility at higher pressures lead to more particle collisions, resulting in lower energy states and an imperfect microstructure. The reported porosity values for Zhang's freestanding topcoats tested in a 3-point bend setup were 7.1% at the bottom, 7.5% in the middle and 9.2% at the top of the coating. While the porosity of the coatings in this study are larger than those seen in Zhang's study, the porosity differences do not appear to be large enough the explain the differences in modulus that were measured in the two studies.

Unlike the imaging results discussed in Section 5.2, significant differences in the mechanical response of the freestanding topcoat specimens were observed and appear to correlate with processing variations. However, the much lower-than-expected moduli call these results into question. Attempts were made correct these values for factors like topcoat porosity, however the most likely reason for these discrepancies is damage to the topcoat during sample preparation (e.g. ultrasonic cleaning) or handling (e.g shipping). Future iterations of this work must include extreme care at every step of fabrication, preparation and handling.

5.5 Attempts to Test P&W Blades

A set of blades, with the same variations in topcoat processing conditions, were also made for JHU by P&W to study the effect that substrate curvature has on the mechanical response of each of the three processing conditions. These blades were designed to be tested in the same manner as the vanes in Zhang's work [3], where small windows were micro-EDM'd at various points around the blade creating either double clamped micro-beams or cantilever micro-beams consisting of the topcoat with a small amount of bond coat as support. These samples can be tested using the same setup used for the 3-point bend tests, with a modified set of grips to allow for the central loading pin to push or pull on the topcoats into compression or tension.

The sample preparation procedure for these specimens were initially the same as for the 3-point bend specimens, which was to mount the blades in epoxy, cut them on the diamond wire saw, polish the slices to ~ 500 μm thick and burn epoxy out of the blades. Instead of acid etching the samples, they were sent to a micro-EDM shop (Viteris Technologies) in Utah for the fabrication of the windows. While the fabrication of the windows was initially successful, they all broke

172

during shipping and were unsuitable for testing. The loss of the micro-EDM'd beams can be attributed, at least in part, to the smaller size of the blades as compared to the vanes previously tested by Zhang and the increased presence of cooling holes in the blades. Future iterations and successful preparation of the micro-beams might have been possible with re-designed and smaller windows, but the disruptions and shutdowns caused by the COVID-19 pandemic made it impossible to micro-EDM and test the blades in the current study.

5.6     Chapter Summary

The work presented in this chapter focused on efforts to understand the effect topcoat processing conditions have on topcoat microstructure and mechanical response. Wedge bars, blades and buttons were provided with topcoats deposited at "low run power", "nominal run power" and "high run power" conditions. The wedge bar specimens were sliced and prepared for SEM imaging and used to fabricate freestanding topcoat specimens for 3-point loading. No significant variations in topcoat microstructure were observed. The formation of a transient oxide was noted in the "low power specimen" where it formed in lieu of the TGO and did not get fully removed during acid etching.

Significant variations were noted in the measured compliance of the beans, but the reported modulus values were significantly lower than expected and were called into question as a result. Efforts were made to reconcile these values, but the most likely reason for the lower values seems to be damage to the topcoats that occurred during specimen preparation or handling. Future iterations of this work can be done but great care must be taken to ensure no damage occurs to the coatings before testing.

References:

[1]: Sauer, J.P., Leonhardt, T., Gear, A.R., *The Effect of Mounting Technique on the Microstructure of Thermal Barrier Coatings.* International Thermal Spray Conference Proceedings, 1997. p. 959-964.

[2]: Höflinger, G., *Brief Introduction to Coating Technology for Electron Microscopy.* Leica Microsystems, 2013. Accessed: https://www.leica-microsystems.com/science-lab/brief-introduction-to-coating-technology-for-electron-microscopy/

[3]: Zhang, B., *Experimental Characterization of Thermal Barrier Coatings Using Micro-Scale Bending Techniques.* Ph.D. Thesis, Johns Hopkins University, 2015.

[4]: Wang, X., Tint, S., Chiu, M., Atkinson, A., *Stiffness of freestanding thermal barrier coating topcoats measured by bending tests.* Acta Materialia, 2012. **60**: p. 3247-3258.

[5]: Zolochevsky, A., *Damage Development in Thermal and Environmental Barrier Coating Systems for Aerospace Applications.* Stability of Structures, Kharkov Polytechnic Institute, 2015.

[6]: Wakui, T., et al., *Strain dependent stiffness of plasma sprayed thermal barrier coatings*. Surface & Coatings, 2006. **200**: p. 4995-5002.

[7]: Wakui, T., et al., *Mechanical testing of thermally stressed materials with rough interfaces: Mechanically induced delamination cracking in thermal barrier composites*. Surface & Coatings, 2006. **200**: p. 5419-5426.

[8]: Strangman, T.E., *Thermal Barrier Coatings for Turbine Airfoils.* Thin Solid Films, 1985. **127**: p. 93-95.

[9]: Spriggs, R., *Expression for effect of porosity on elastic modulus of polycrystalline refractory materials, particularly aluminum oxide.* Journal of the American Ceramic Society, 1961. **44**: p. 628 629.

[10]: Wang, J.C., *Young's modulus of porous materials.* Journal of Materials Science, 1984. **19**: p. 801-808.

[11]: Krstic, V., et al., *Effect of porosity on Young's modulus of nanocrystalline materials.* Scripta Metallurgica et Materialia, 1993. **29**: p. 1501-1504.

[12]: Kaden, U., Muenzer, J., Schulz, U., *Influence of Deposition Conditions on Density and Microstructure of EB-PVD TBCs.* Ceramic Engineering and Science Proceedings, 2002. **23**(4): p. 353-360.

# Chapter 6: Summary and Future Work

The work in this dissertation was performed with two main goals. The first was to employ the novel CED test, recently developed by Lockyer-Bratton [1], on a variety of EBPVD TBC systems and to measure the Mode II interfacial toughness of those systems. The second was understanding how variations in processing conditions for an EBPVD topcoat effect both its underlying microstructure and its mechanical response. This chapter summarizes the results of this work and gives suggestions for future areas of related work.

6.1 Summary of Results and Conclusions

*6.1.1 Investigation of Gradient Thermal Testing on TBC Interfacial Toughness*

The work presented in Chapter #3 highlighted the results of tests conducted on CED specimens coated with a standard (Ni,Pt)Al/8YSZ EBPVD TBC. GE provided coated buttons in the "as-deposited" state and gradient cycled to "early-in-life", "mid-life" and "late-in-life" states. The key results of this study were as follows:

- The stress associated with delamination was measured for consecutive stages of JETS thermal cycling. An average value of $463 \pm 27$ MPa was measured for the "as-deposited" specimens. The delamination stress (442 MPa) for the "early-in-life" specimens was similar but significant deficits were observed in the "mid-life" (353 MPa) and "late-in-life" (210 MPa) specimens.

- SEM observations and EDS analysis of the CED fracture surfaces evidenced a transition from a predominantly TGO surface in the "as-deposited" state to a mixed surface with interpenetrating metallic (bond coat) and ceramic (TGO and topcoat) islands in the "mid-life" and "late-in-life" fracture surfaces. Cross-sectional images of the CED

substrates elucidated the onset of TGO and bondcoat rumpling and localized micro-cracking in the topcoat. The degree of rumpling increased with transient thermal cycling.

- These observations, combined with the fact that the TGO thickness in the late-in-life specimens was less than has been reported in previous studies, indicate that TBC failure in JETS specimens was controlled by TGO and bond coat rumpling that leads to accelerated after an initial incubation period. This conclusion is supported by the measured critical stress values, which are relatively constant in the initial stages but decrease significantly later in life.

- Comparing the JETS specimens in this study with the previous FCT CED results of Lockyer-Bratton [1] indicate that the interfacial toughness is similar in both sets of specimens in early to mid lifetimes, but the toughness appeared to degrade more rapidly for the transient thermal test.

- For the JETS specimens, the calculated interfacial toughness values dropped 75% from the "as-deposited" state to "late-in-life." These values were calculated using the analytical equation provided by Hutchinson and Hutchinson [2] and are known to be overestimates; nevertheless, comparisons of these nominal interfacial toughness estimates do provide valuable trends in the interfacial delamination behavior of these specimens. For one, the interfacial toughness was observed to degrade with thermal cycling in both cases. This degradation is similar at first but occurs more rapidly in the latter stages of life during transient thermal cycling.

- Attempts to test high-pressure turbine blades pulled from service showed both the promise and the challenge of using the CED test on engine hardware. Two sets of blades were provided by GE but both were unsuitable for testing due to the onset of buckling

before delamination. Previous efforts by Lockyer-Bratton [1] demonstrated that CED testing of real engine hardware is possible, but the results of the current effort highlight the need for robust and relatively flat blades to prevent buckling and allow for adherence and axial loading of the stiffener plates. This is at odds with the fact that modern blades have internal cooling channels and holes and contours that are anything but flat and straight.

### 6.1.2  Application of CED Test to Furnace Cycled TBCs with LPPS Bond Coats

The results presented in Chapter #4 presented Mode II CED tests for a P&W LPPS NiCoCrAlY bond coat/7YSZ EBPVD TBC. The thermally cycled CED specimens were damaged and partially delaminated during shipping, viable tests were conducted and DIC was employed to identify the critical stresses associated with delamination and the fracture surfaces were examined after the tests. The key findings of this study were as follows:

- A critical stress of 204 MPa was measured for the "as-deposited" specimens, and this decreased to 183 MPa for "early-in-life" and 163 MPa for "mid-life" specimens, or a drop of 20% which corresponds to a drop of ~40% in interfacial toughness.

- Coating delamination for this TBC system was unique in that coating delaminated in one large piece. SEM imaging and EDS of the fracture surfaces showed no bond coat rumpling. The lack of rumpling allowed cracks to propagate unimpeded along the fracture surface, facilitating the full coating delamination.

- SEM imaging and EDS analysis of the substrate-side of the fracture surface showed that the delamination occurred below the TGO, initially starting at the bottom of the topcoat when the TGO was very thin and then traversing the bond coat/TGO interface once the TGO had grown.

### 6.1.3 The Effect of Off-Nominal Processing Conditions on YSZ Microstructures and Mechanical Properties

The work presented in Chapter #5 focused on efforts to understand the effect that topcoat processing conditions have on the EBPVD microstructure and its mechanical stiffness. Wedge bars were prepared for SEM imaging and 3-point bend tests, and the key findings were as follows:

- SEM imaging was performed at various regions for each of the processing conditions, but no noteworthy variations in topcoat microstructure were observed. The "low run power" specimens varied the most; the topcoat columns were slightly thinner, less feathery and coalesced into each other more than the "nominal run power" and "high run power". The "nominal run power" and "high run power" specimens maintained a similar visual microstructure throughout.

- SEM imaging and EDS analysis indicated that the TGO was not fully formed in the "low run power" specimens.

- Significant differences in the compliance of the freestanding EBPVD 7%YSZ beams were measured, and the reported modulus values were significantly lower than expected [3], low enough to call into question these results. The most likely explanation seems to be damage to the topcoats that occurred during specimen preparation or handling. Future iterations of this work are possible, but great care must be taken to ensure that the topcoat is not damaged before testing.

6.2 Recommendations and Opportunities for Future Work

- The interfacial toughness values reported in this thesis were all obtained using the proposed analytical solution. This solution provides a reasonable initial approximation but does not account for interfacial friction, reduced strain transfer to the stiffener plates of finite sized specimens, or the multiple layers (substrate, bond coat, TGO, topcoat, epoxy, stiffener plate) that make up the CED specimen. Detailed FE work accounting for the proper strain transfer, presence of the various layers, as well as friction between them would be a valuable next step. Models of TGO thickening and rumpling (similar to Balint and Hutchinson [4]) and topcoat cracking would be more challenging but would also provide greater insight into the failure mechanisms.

- Expanding on the method used to determine critical stress associated with crack growth is another potential area for future work. In both this study and Lockyer-Bratton's work [1], the stress associated with crack growth was determined based on a level of critical shear strain at the interface as measured using DIC strain maps. Improvements made to the DIC in the current study suggest that monitoring changes in axial strain across the substrate-stiffener plate interface may be a viable and more accurate method for determining and tracking the location of the advancing crack tip. This would allow for more accurate measurements of interfacial toughness.

- Performing 3-point bend and CED tests of TBCs infiltrated with CMAS is another avenue for future work. Infiltration of columnar EBPVD coatings changes the stiffness and the interfacial chemistry. Quantifying the effect that CMAS has on the constitutive mechanical behavior of the topcoats in different coating systems would better enable the engine companies to gauge the deleterious effects of CMAS.

- Attempts were made to expand the tests in this study beyond laboratory specimens to real engine hardware. While these attempts were unsuccessful due to the increased geometric complexity of modern blades and vanes, (and complications associated with the COVID-19 pandemic), the potential and payoff of this test remains. Future work should focus on performing CED and 3-point bend testing. Judicious selection of jet engine blades and vanes should provide meaningful comparisons between laboratory tests and thermal exposure to the engine environment. Expansion of this work to other coating systems remains an opportunity as well, especially to other EBPVD topcoat systems like for example GZ.

References:

[1]: Lockyer-Bratton, S., *Experimental measurements of thermal barrier coating interfacial fracture toughness as a function of mode-mix*. Ph.D. Thesis, Johns Hopkins University, 2016.

[2]: Hutchinson, R.G., Hutchinson, J.W., *Lifetime Assessment for Thermal Barrier Coatings: Tests for Measuring Mixed Mode Delamination Toughness.* Journal of the American Ceramic Society, 2011. **94**: p. s85-s95.

[3]: Zhang, B., *Experimental Characterization of Thermal Barrier Coatings Using Micro-Scale Bending Techniques.* Ph.D. Thesis, Johns Hopkins University, 2015.

[4]: Balint, D.S., Hutchinson, J. W., *An analytical model of rumpling in thermal barrier coatings.* Journal of the Mechanics and Physics of Solids, 2005. **53**(4): p. 949-973.

## Appendix A: Original CED Specimen J-Integral

The J-integral is a contour path integral that can be used to calculate the strain energy release rate for elastoplastic materials as well as materials with complicated geometries that do not have simple, analytical solutions. A typical J-integral solution takes the form shown in Equation A-1.

*Equation A-1*

$$J = \int_{\Gamma} (W\, dy - T_i \frac{du_i}{dx} ds)$$

Where $T_i$ are the surface tractions acting on the boundary $\Gamma$, $u$ is the displacement vector, $dx$ is the change in the $x$ position along a path, $dy$ is the change in the $y$ position along a path, $ds$ is the is an element of the arc length along $\Gamma$ and $W$ is the strain energy density shown in Equation A-2.

*Equation A-2*

$$W = \int \sigma_{ij} d\epsilon_{ij}$$

One benefit to the J-integral is that the analysis is independent of the path taken around the crack, and thus the path can be chosen to best simplify the calculations. This means that the J-integral result can be re-written such that the final J-integral result is the sum of $n$ different J-integrals, each one representing a subset of the total path taken around the crack, as shown in Equation A-3.

*Equation A-3*

$$J_{\Gamma} = J_{\Gamma}{}^1 + J_{\Gamma}{}^2 + \cdots J_{\Gamma}{}^n$$

Figure A-1 shows a schematic for the breakdown of paths used for the J-integral analysis of the modified CED specimens.
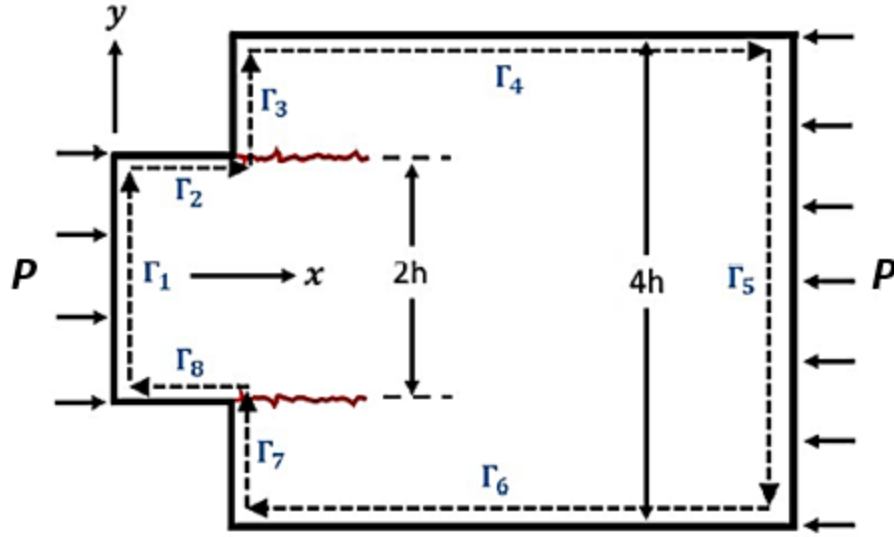
*Figure A-1: Schematic showing the breakdown of the different paths chosen for the J-integral analysis of the original CED specimen.*

For the path chosen for the CED specimens, the J-integral is represented by Equation A-4.

*Equation A-4*

$$J_\Gamma = J_\Gamma{}^1 + J_\Gamma{}^2 + \cdots J_\Gamma{}^8, \Gamma = \sum_1^8 \Gamma_i$$

From Equation A-1, it can be seen that $J_2, J_4, J_6$, and $J_8 = 0$, since there are no surface tractions and no changes in $y$, meaning all $T$'s and $dy$'s = 0. $J_3$, and $J_7 = 0$ since there are no surface tractions and no applied load on these faces, meaning all $T$'s and $W$'s = 0. This leaves two remaining J-integrals, $J_1$ and $J_5$. On $\Gamma_1$, the loading conditions are:

$$W = \frac{1}{2}\sigma_1 \epsilon \qquad\qquad dy = ds$$

$$T_1 = -\sigma_1 \qquad\qquad \frac{du_1}{dx} = \epsilon$$

Where $\sigma_1 = \frac{P}{2h}$ is the stress applied on $\Gamma_1$ where the load $P$ is applied over a length of *2h*. And on $\Gamma_5$, the loading conditions are:

$$W = \frac{1}{2}(-\sigma_2)\epsilon \qquad\qquad dy = -ds$$

$$T_2 = -\sigma_2 \qquad\qquad \frac{du_2}{dx} = -\epsilon$$

Where $\sigma_2 = \frac{-P}{4h}$ is the stress applied on $\Gamma_2$ where the load $P$ is applied over a length of *4h*.

Plugging back into Equation A-1, Equation A-5 is obtained.

*Equation A-5*

$$J_\Gamma = \int_0^h (\frac{1}{2}\sigma_1\epsilon - (-\sigma_1)\epsilon)ds + \int_0^{2h}(-\frac{1}{2}(-\sigma_2)\epsilon - (-\sigma_2)(-\epsilon))ds$$

In a CED specimen, there are two independent cracks growing at either interface between the substrate and stiffener plate. Since the goal is to solve for the energy release rate around a single crack tip, the lower bound of the integral is set to be 0 so the path is taken along the center line of the samples. Taking the path along the center line, where applied tractions are equal to zero due to sample symmetry, ensures that only one crack tip is included in the path and the energy release rate of two independent crack tips are not combined. Solving for this gives the solution in Equation A-6.

*Equation A-6*

$$J_\Gamma = \sigma_1 \varepsilon h$$

Assuming a linear elastic and isotropic system, Hooke's Law can be used to obtain the final solution for interfacial toughness shown in Equation A-7.

*Equation A-7*

$$G = \frac{\sigma_1{}^2 h}{E}$$

Where $E$ is the modulus of the stiffener plate and substrate, $h$ is the thickness of the stiffener plate, and $\sigma$ is the stress applied to the CED specimen, given by Equation A-8.

*Equation A-8*

$$\sigma_1 = \frac{P}{4h}$$

Where $P$ is the applied load. From Equation A-6 we can obtain the equation for the desired material property, interfacial toughness, seen in Equation A-9 below.

*Equation A-9*

$$G_c = \frac{\sigma_c{}^2 h}{E}$$

Where $\sigma_c$ is the stress associated with crack growth in the CED specimen obtained from Equation A-8, and $G_c$ is the energy release rate also referred to as the interfacial fracture toughness.

## Appendix B: MTS Servo-Hydraulic System Overview

The system used to conduct the compression edge-delamination test is an MTS servo-hydraulic test machine. The system includes a servo-hydraulic driven actuator with a linear variable displacement transducer (LVDT) used for displacement control and a 500 kN tension/compression load cell. The software used to control the test setup is MTS MultiPurpose Elite (MPE) and Station Manager package. Image capture is accomplished through the use of a PixelLINK camera coupled with the PixeLINK Capture OEM image capturing software. Descriptions of the key components are given, which is followed by an overview of the software and programs used to conduct the tests.

A close-up image of the key testing equipment is shown in Figure B-1. The sample is placed between 1" diameter tungsten carbide inserts in the loading platens to align the sample. A square enclosure made from Plexiglass Acrylic panels is used to protect the operator from any debris that might become ejected from either the sample or the tungsten carbine inserts during failure. A PixelLINK PL-B781U black and white 6.6 MP camera with an Edmund Optics MMS Imaging Lens R-1 rear assembly and OBJ-11 front objective was used for imaging purposes. This combination allows for a field of view capable of capturing the entire sample with working distances between 100 mm to 200 mm. The entire imaging assembly is mounted on a tripod and positioned at an appropriate working distance.
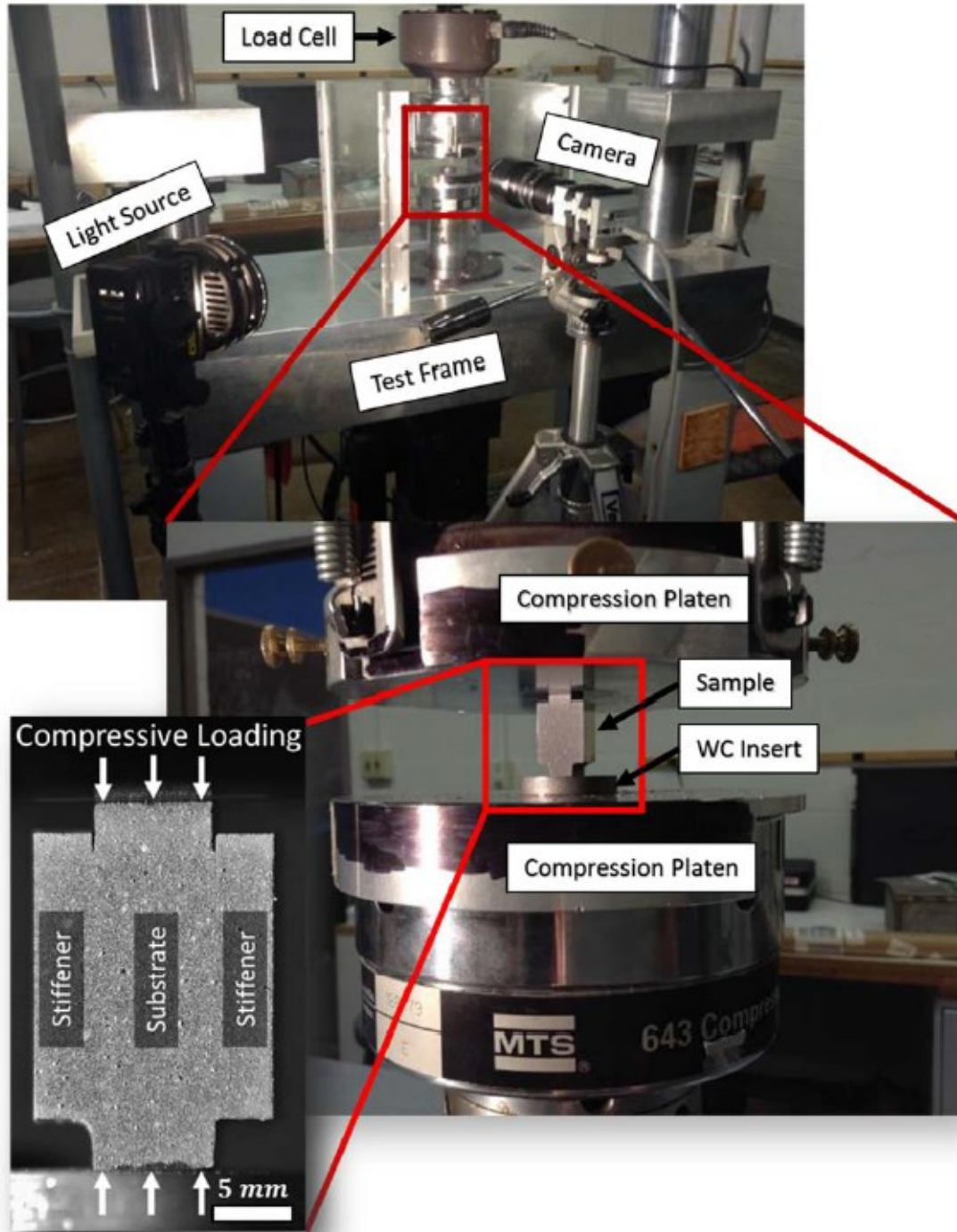
*Figure B-1: Photos of the MTS servo-hydraulic machine used for CED testing with callouts indicating key components and specimen orientation [1].*

Lighting is accomplished through the use of a DiCon LED light source coupled with a dual branch adjustable light guide. The machine is controlled using a computer running the MTS MultiPurpose Elite software, which is capable of providing raw control of the system as well as run custom programs for the testing procedure. The program steps are constructed from a series of distinct task types with editable parameters. These tasks can additionally have start and interrupt commands linked to them to allow for complex program structures. The program used for compression of the CED samples consists of the following steps:

1. Moving the actuator such that the sample is touching both of the compression

platens with a 300 N preload force.

2. A step where the system is commanded to maintain the constant preload of 300 N

to ensure any settling of the sample on the platens occurs before additional loading.

3. A compression step where the sample is taken up to a specified maximum displacement

while recording load data and capturing images.

4. Subsequent unloading of the sample until completely unloaded.

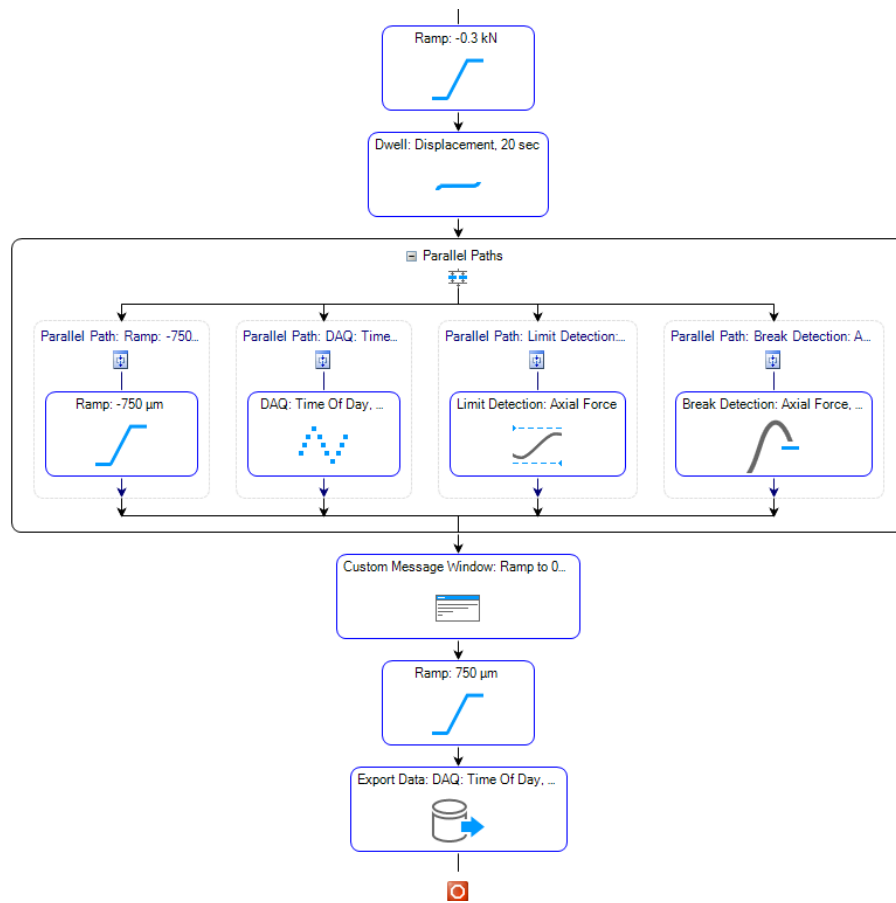A more detailed flow chart of the sample is show in Figure B-2.

*Figure B-2: The workflow used to run CED tests in the MultiPurpose Elite software.*

References:

[1]: Lockyer-Bratton, S., *Experimental measurements of thermal barrier coating interfacial fracture toughness as a function of mode-mix*. Ph.D. Thesis, Johns Hopkins University, 2016.

**Curriculum Vitae**

Jalil Alidoost was born in New York City, New York on August 5<sup>th</sup>, 1994. He grew up in Montclair, New Jersey and graduated from Montclair High School in 2012. Jalil then attended the University of Michigan in Ann Arbor, Michigan and majored in mechanical engineering. He completed his undergraduate studies in April of 2016 and earned a Bachelor of Science in Engineering degree in Mechanical Engineering. In August of 2016, Jalil moved to Baltimore, Maryland to pursue his graduate studies under the guidance of Professor Kevin J. Hemker in the Department of Mechanical Engineering at Johns Hopkins University. In May of 2019 he earned a Master of Science in Engineering degree in Mechanical Engineering. In October of 2021, Jalil fulfilled the requirements for a Doctor of Philosophy in Mechanical Engineering.